Influence of geometry and wettability on two-phase flow in porous media

Dissertation
zur Erlangung des akademischen Grades
eines Doktors der Naturwissenschaften
der Naturwissenschaftlich-Technischen Fakultäten
der Universität des Saarlandes

von
Weiwei Li

Saarbrücken, 2020

Tag des Kolloquiums : 23.11.2020
Dekan: Prof. Dr. Jörn Walter
Berichterstatter: Prof. Dr. Ralf Seemann
Prof. Dr. Manfred Lücke

Vorsitz: Prof. Dr.-Ing. Michael Vielhaber
Akad. Mitarbeiter: Dr. XianLin Zeng

Hiermit versichere ich an Eides statt, dass ich die vorliegende Arbeit selbstständig und ohne Benutzung anderer als der angegebenen Hilfsmittel angefertigt habe. Die aus anderen Quellen oder indirekt übernommenen Daten und Konzepte sind unter Angabe der Quelle gekennzeichnet. Die Arbeit wurde bisher weder im In- noch im Ausland in gleicher oder ähnlicher Form in einem Verfahren zur Erlangung eines akademischen Grades vorgelegt.

Saarbrücken, 12, August, 2020

Weiwei Li

Kurzzusammenfassung

Das Verdrängungsmuster für Zweiphasenströmung in porösen Medien wird von vielen Faktoren bestimmt. In dieser Arbeit konzentrieren wir uns auf die Einflüsse von Benetzbarkeit und Geometrie auf das Einstehen der Verdrängungsmuster. Ausgehend vom klassischen Cieplak & Robbins' Modell wurde gezeigt, dass im kapillardominierten Regime eine Verringerung der Porosität zu einer Änderung des dominierenden Verdrängungsmodus, dem sog. "touch-event", für mittlere Kontaktwinkel führt. Die wichtige Rolle von "touch-events" wurde weiter gezeigt, als die Benetzungsheterogenität dem Modellsystem hinzugefügt wurde. Zur Quantifizierung des Flüssigkeits-Verdrängungsmusters wurden drei verschiedene Methoden entwickelt, die nicht nur das von der Benetzbarkeit abhängige Verdrängungsmuster mit einer kompakten Domäne für niedrige fortschreitende Kontaktwinkel und einer verzweigten Struktur bei hohen fortschreitenden Kontaktwinkeln darstellten, sondern auch ein Invasionsregime für den Drainageprozess in der späteren Phase der Flüssigkeitsinvasion in den Experimenten mit sphärischen Glaskugeln identifizierten. Dieses Regime wurde mit einem Modell weiter untersucht, das das 2D Cieplak & Robbins' Modell auf den dreidimensionalen Raum erweitert. Weitere Verdrängungsexperimente in Sanden mit unterschiedlichen Kornformen und Oberflächenrauhigkeiten mittels Röntgentomographie zeigten die wichtige Rolle der makroskopischen und mikroskopischen Geometrie bei der Veränderung des Flüssigkeits-Verdrängungsmusters. Mit den in dieser Arbeit vorgeschlagenen Quantifizierungsmethoden konnte ein neues Verdrängungsmuster für den Imbibitionsprozess in Ottawa-Sand identifiziert werden. Im letzten Teil wurden zwei verschiedene Algorithmen entwickelt, um das Schnittvolumen zwischen kugelförmigem Partikel und Polyeder zu evaluieren, das im 3D Cieplak & Robbins' Modell verwendet wurde.

Abstract

Fluid invasion pattern for two-phase flow in porous media is controlled by many factors. In this thesis, we focus on the influences of wettability and geometry on the evolution of fluid invasion pattern. Starting from the classical Cieplak & Robbins' model, it was illustrated that in the capillarity-dominated regime, decreasing the porosity leaded to a change of dominating invasion mode, touch events, for intermediate contact angles. The important role of touch events was further shown when wetting heterogeneity was added to the model system. To quantify the fluid invasion pattern, three different methods were developed, which not only illustrated the wettability-dependent invasion pattern with a compact domain for low advancing contact angle and a fingering structure in high advancing contact angle, but also identified an invasion regime for the drainage process during the later stage of fluid invasion in the experiments with spherical beads. This regime was further investigated with a model which extends the 2D Cieplak & Robbins' model to three dimensional space. Further liquid imbibition experiments in sands with different grain-shapes and surface roughness with X-ray tomography revealed the important role of macroscopic and microscopic geometry in altering the fluid invasion pattern. With the proposed quantification methods in this thesis, a new invasion pattern for imbibition process in the Ottawa sands was identified. In the last part, two different algorithms were developed to evaluate the intersection volume between spherical particle and polyhedron, which was employed in the 3D Cieplak & Robbins' model.

Acknowledgment

First and foremost, I would like to thank my supervisor Prof. Dr. Ralf Seemann. Thanks for giving me the opportunity to do my research under ideal conditions in a harmonious working atmosphere. Thanks for being tolerant and giving me enough freedom to try many ideas, especially when I was lost in the magnetic monopole. Without your continuous supports, I would not be able to finish the work presented in the current thesis. Thanks for fixing the big fan for our in-house CT, which is an important lesson I learned during my Phd journey.

I would also like to thank Dr. Martin Brinkmann. Without the insightful discussion, a lot of work presented in this thesis would not be possible. Especially your extensive knowledge and unfailing passion in the fields of physics and mathematics impressed me deeply. Finding the connection between the gauge theory and intersection volume calculation together with you is really a wonderful and unforgettable moment during the past five years. In addition, thanks for your magic hands to fix the moving stage in our in-house CT.

Furthermore, I would like to thank the members of AG Seemann and AG Jacobs for creating a harmonious working environment. I would like to thank Dr. Hagen Scholl, who helped me get familiar with our CT machine and taught me how to use the software for image analysis. Also I would like to thank Dr. Michael Jung for proofreading my thesis and correcting the Kurzzusammenfassung. Thanks for Dr. Menglin Li taking care of me when I just arrived in Saarbrücken. Thanks to Dr. Tak Shing Chan for inviting me to cook with his apartment mates, which gave me a lot of comforts and fun when I was not working.

I would like to acknowledge generous support from BP Exploration Operation Company Ltd. within the GeoMorph research project.

Lastly, to my parents. Thank you for your constant supports and belief in me. Also thanks for my sister, who took the responsibility to take care of my parents when I was far away from home.

“What is the use of these results? The answer is that I don’t know. We are studying these topics because they are interesting in their own right as mathematical problems, and that is what science is all about.”
-Allan MacLeod Cormack

Contents

Chapter 1

Introduction

Virtually the majority of the solid and semisolid materials are porous to different degrees. Materials containing small voids and being permeable to fluids are referred to as permeable porous media. We encounter these permeable porous materials in our daily life. Even the tissues of our body could be treated as a permeable porous medium because they are made of cells separated by connected voids and these voids provide channels for transportation of nutrients or minerals. Studying two phase immiscible fluid displacement in permeable porous media is of great importance in diverse fields of industrial or natural processes including soil science, proton exchange membrane (PEM) fuel cells, CO_2 sequestration and oil recovery. For example, nearly half of the original oil in place is not recovered by primary and secondary productions. To improve the efficiency of fuel cells and to facilitate the recovery of oil, a better understanding of the fundamental displacement mechanism is in need.

Displacement processes in the porous media cover a wide range of length scales. On the one hand, within the confinement of solid space formed by grains or some other materials, fluids flow through a tortuous path with only a few microns in diameter. The morphology of local void space, surface properties of the porous media and properties of the fluids strongly influence the displacement process occurring on the length scale several orders below the field-scale. On the other hand, displacement on reservoir scales from meters to kilometers provides the basis for the evaluation of important factors in oil industry, such as the final oil recovery. To characterize the macroscopic fluid displacement process, empirical relationships are required while the pore-scale invasion process is not delineated. Macroscopic displacement processes ranging from meters or kilometers are naturally a result of combinations of pore-scale fluid displacements. In this sense, the connection between the pore-scale fluid displacement processes and macroscopic fluid displacements is meaningful but elusive. Questions like how to characterize pore-scale displacement processes under various influencing parameters such as wettability and how to link the pore-scale invasion processes within microns to the fluid displacement pattern with an extension of several kilometers are still not tractable. Despite the importance of fluid displacement processes in the porous media, there is limited understanding of the processes connecting the pore-scale displacement with the macroscale displacement pattern. Actually fluid displacement processes are controlled by a plethora of factors, such as the physical parameters of fluids including flow velocity, viscosity, the properties of porous media comprised of geometry and surface roughness. Also the properties governed by both of the porous media and fluids such as wettability, which is the relative affinity of the fluids to the solid, are also of the same importance.

The aim of this work is to explore the factors that affect the displacement process at pore scale. Given so many factors, the focus of the thesis is to display how the geometry and wettability govern the fluid displacement process at pore scale via simulation and experiments for the purpose of expanding the understanding of two phase immiscible fluid flow in two- and three-dimensional model systems.

Chapter 2

Scientific Background and Literature Review

To investigate the phenomena in two-phase flow of porous media and further characterize the liquid invasion process, a plethora of parameters and their mutual relationships are in need. Due to the complexity of the liquid invasion process, many parameters and relationships are empirical such as the relationship between the capillary pressure and saturation [Leverett et al., 1941; Hassanizadeh and Gray, 1993]. Before we delve further into more details, the definitions of some fundamental parameters behind two-phase flow in porous media are introduced. On top of that, open questions are discussed, which lead to the main work of this thesis.

2.1 Wettability

Wettability plays an important factor in controlling fluid displacement processes in permeable media and the distribution of fluids within reservoir [Anderson et al., 1986; Abdallah et al., 1986; Singh et al., 2017b; Zhao et al., 2016]. The concept of wettability characterizes the affinity of a liquid to a solid in the presence of other immiscible fluids [Anderson et al., 1986]. In practical quantification of the wettability, a contact angle between the fluids and the solid surface as a result of the balance of forces in a three phase system consisting of vapor/liquid/solid system is frequently employed [Abdallah et al., 1986; De Gennes, 1985]. To describe the concept of contact angle, we firstly introduce the Young's equation [Young, 1805].

2.1.1 Young's equation

In Fig.2.1(a), given a flat surface with a droplet, a certain contact line of the invading liquid is formed with the surface of the solid phase. The three involved phases (solid-S, liquid-L and vapor-V) will generate three interfaces (solid/liquid, solid/va-

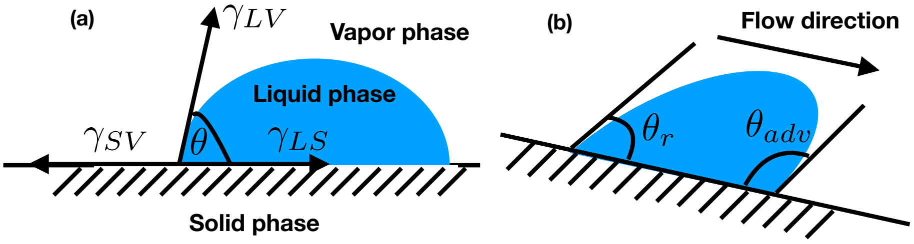

Figure 2.1: (a) An illustration for Young's contact angle; (b) An illustration of the advancing and receding contact angle. The blue phase indicates a sliding droplet on a tilted surface.

por, liquid/vapor) with corresponding surface energies of γ_{SL}, γ_{SV}, γ_{LV}. According to Young's law, the surface energies satisfy in equilibrium the following condition [Young, 1805; De Gennes, 1985]:

$$\gamma_{SV} - \gamma_{SL} - \gamma_{LV} \cos\theta = 0 \ . \tag{2.1}$$

where θ is the contact angle, which is defined as the angle between the tangent to soild/liquid interface and the tangent to the liquid/vapor interface at the point where the three phases are in contact as shown in Fig.2.1(a).
After reaching mechanical equilibrium for each phase, a liquid with $\theta < 90°$ is preferentially wetting the solid, while the other liquid with $\theta > 90°$ is nonwetting. For the case when $\theta \approx 90°$, the surface is named as intermediate (or neutral)-wetting [Anderson et al., 1986]. We employ "wetting" when the liquid tends to spread over the solid surface and otherwise "nonwetting". Further with the definition of wetting and nonwetting phase, drainage is defined as the situation when the nonwetting phase displaces the wetting phase and the reverse process is called imbibition.

2.1.2 Contact angle hysteresis

In the natural world, it is always found that the contact line is either pinned and immobile whenever θ satisfies [De Gennes, 1985]:

$$\theta_r < \theta < \theta_{adv} \ . \tag{2.2}$$

where, θ_{adv} is the advancing contact angle and θ_r is the receding contact angle as shown in Fig.2.1(b) [De Gennes, 1985; Dullien, 2012]. The source of the hysteresis mainly comes from the surface roughness, chemical contaminations and a film deposited by solutes in the liquid [De Gennes, 1985]. Even though the contact angle hysteresis is everywhere in our daily life and attracts many research interests, there is still no predictive theory on how to quantify the influence of the inhomgeneities on the wettability [Priest et al., 2007]. To characterize the contact angle hysteresis, models such as the pore-network model [Valvatne and Blunt, 2004], employed Morrow's experimental results [Morrow et al., 1975], in which $\theta_{adv,r}$ (the advancing and receding contact angle) is measured as a function of the intrinsic contact angle on a rough surface [Dullien, 2012]. The intrinsic contact angle here is the contact angle measured at a smooth PTFE (Polytetrafluoroethylene) surface and the roughness is produced by roughening PTFE with particulate solids. It should be noted that Morrow's model is only an approximation for contact angle hysteresis quantification and the real world is much more complicated [Morrow et al., 1975; Blunt, 2017].

2.1.3 Surface roughness

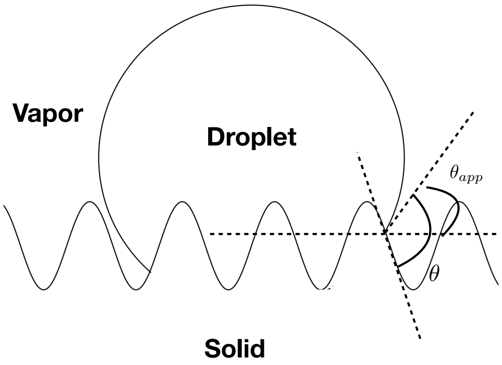

Figure 2.2: Fluid distribution in accordance with the Wenzel model [Wenzel, 1936]. θ is the material contact angle and θ_{app} is the apparent contact angle measured from the average surface plane, which can differ greatly from the true contact angle.

The understanding of wetting properties of rough solid substrates is limited due to the wide ranges of scales a surface roughness covers, which extends from sub-micron scales to millimeter scales [Herminghaus, 2012]. The surface roughness not only influences the contact angle hysteresis as mentioned in the previous part, but also contributes to influence the contact angle. Wenzel provides a relationship between the apparent contact angle θ_{app} and the material contact angle θ [Wenzel, 1936] as shown in Fig.2.2:

$$\cos\theta_{app} = f\cos\theta \ . \tag{2.3}$$

where, f is the ratio of the true surface area to the projected surface area of the solid.

It is worth noting that Eq.2.3 reveals one aspect about how surface roughness influences the contact angle. In other words, the material contact angle is not the same as the apparent contact angle, as a result of the different surface roughness.

In literature, there are already some research works targeting the influence of surface roughness on a fluid invasion process. For example, during the imbibition process, the wetting fluid is able to flow mainly through surface roughness, which corresponds to the edges of the ducts with rectangular cross sections and in the duct bulk in the 2D model system used by [Lenormand et al., 1984]. And it was further shown in experiments with packs of smooth and etched glass bead packs [Dullien et al., 1989], where the wetting liquid occupies the grooves in the surface of the beads. In addition, when we consider flowing fluid, the grain surface roughness creates ”grooves”, which might provide open channels for liquid to creep [Lukyanov et al., 2012].

2.2 Capillary pressure

Capillary pressure (P_c) is an inherent pore-scale phenomenon [Armstrong et al., 2012]. This phenomenon features a discontinuity in pressure occurring across the interface, which separates the two immiscible fluids in contact with a porous media. This capillary pressure depends on the local interface curvature and is defined as the Young-Laplace equation [Young, 1805; Laplace, 1806; Bear, 2013]:

$$P_c = P_{nw} - P_w = \gamma(\frac{1}{r_1} + \frac{1}{r_2}) = 2\gamma\kappa \ . \tag{2.4}$$

where, P_{nw} is the pressure in the nonwetting phase; P_w is the pressure in the wetting phase; γ is the surface tension between the two liquid interfaces and r_1, r_2 are the principal radii of curvature of the liquid/liquid interface; κ is the mean curvature.

2.2.1 Capillary pressure saturation curve

Capillary pressure (P_c) is measured at the macro-scale by assuming that it is a function of saturation of one fluid (S) only. The resultant capillary pressure function P_c (S) lays the foundation for the theory of multiphase flow in porous media [Brooks and Corey, 1963; Hassanizadeh and Gray, 1979, 1993; Gostick et al., 2009; Pini and Benson, 2013]. However, this simplified empirical relationship gives rise to a hysteretic capillary pressure saturation curve (CPS) [Bear et al., 2011; McClure et al., 2018] as shown in Fig.2.3. The hysteresis in CPS curve is influenced by the geometry of pores combined with the processes of imbibition and drainage. The potential reasons for hysteresis is summarized as follows:

- Firstly, the hysteresis of contact angle already causes the hysteretic phenomenon CPS curve, which is illustrated in an experiment with microfluidic cells containing a single wedge-shaped channel that simulates individual pore throats [Liu et al., 2011].

- Secondly, the pore-scale instability events play a significant role for the hysteresis observed in a CPS curve. It is shown that Haines jumps (as later explained in section 2.5.2) accounts for nearly 64% of the energy dissipation during the drainage process in an experiment with Berea sandstone [Berg et al., 2013]. For an imbibition process, according to the recent experimental results for a quasi-2D model [Jung et al., 2016], the dominating events are cooperative overlap events. These cooperative events lead to smoothing front when two advancing fronts merge. In 3D networks of pores, the snap-off (as later explained in section

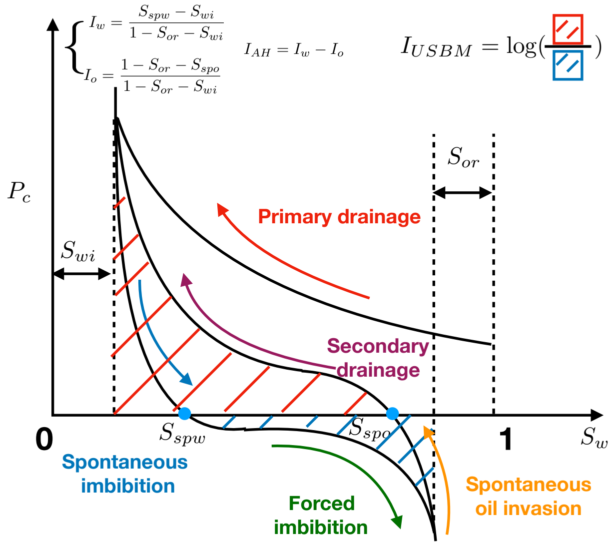

Figure 2.3: Capillary pressure saturation curve. Initially, the porous media is saturated with water. Then a primary drainage process is performed until the saturation of the water reaches initial water saturation (S_{wi}). The subsequent imbibition process is call spontaneous imbibition due to the fact that $P_c > 0$ when $S_w < S_{spw}$. S_{spw} is the water saturation for a zero capillary pressure during the imbibition process. The following process is named as forced imbibition due to negative capillary pressure. At the end of the water flooding the residual oil saturation (S_{or}) is reached. After that, a secondary drainage process is performed. Similar to the imbibition process, we have the spontaneous oil invasion before the S_w reaches S_{spo} and then a secondary drainage follows [Blunt, 2017; Abdallah et al., 1986]. The USBM index I_{USBM} [Donaldson et al., 1969] and the Amott Harvey index I_{AH} [Amott et al., 1959; Morrow et al., 1990] are are also shown respectively.

2.5.2) of wetting fluids within narrow throats are also significant in additional dissipation [Hiller et al., 2019]. In addition, fluid interfaces meeting an obstacle and splitting into separate interfaces are also irreversible and dissipate energy [Murison, 2014]. How important the contributions of the respective pore-scale events is to the energy dissipation (during an imbibition or drainage process) are still not clear and it is still in need of further investigation. Therefore, a better understanding of the energy dissipation for different pore-scale events becomes very meaningful to explain the hysteretic CPS curve.

- In addition, the choice of path taken by the moving interfaces during the drainage and imbibition process also influences the hysteresis showing up in the CPS curves [Liu et al., 2011; Murison, 2014]. For example, Schlueter et al. showed that the shape of the displacement fronts is an additional source of hysteresis with the help of X-ray tomography [Schlüter et al., 2016]. The selectivity of the flowing path contributes to the corresponding different capillary pressure for the same given saturation of the invading phase. To be more specific, for an imbibition process, faster filling of a small tube in preference to a larger one is observed in microfluidic branched networks [Sadjadi et al., 2015]. While for a drainage process, it is found that the non-wetting fluid invades larger throats leading to a ramified morphology [Singh et al., 2017b]. The choice of path taken by the invading liquid leads to different invasion pattern and can be characterized by Euler characteristics.

2.2.2 CPS curve measurement

The CPS curve in the continuum scale can be determined experimentally by such as mercury intrusion [Purcell et al., 1949; Pini and Benson, 2013]. And recent developments in X-ray tomography allow us to build a link between the pore-scale interfacial curvature and column-scale capillary pressure [Armstrong et al., 2012]. The reason to target the pore-scale interface curvature is as follows. Because the external pressure measurements in the CPS curve can only determine interface pressure differences around phase clusters connected to a pressure transducer, which leads to a loss of characterization on capillary pressure distribution present in disconnected nonwetting phase clusters [Andrew et al., 2014].

To further study the source of the hysteretic effect for the CPS curve, a model system in this thesis is developed to illustrate the influence of contact angle heterogeneity, which will be discussed in details later.

2.3 Reservoir wettability

After clarifying the definitions of wettability, and capillary pressure curve, we are able to further discuss the reservoir wettability. Reservoir wettability is shown to affect the rate of oil recovery from a waterflood by changing the pore-scale displacement [Al-Futaisi and Patzek, 2003; Hiller et al., 2019; Anderson et al., 1986; Salathiel et al., 1973]. Typically, surfaces of reservoir rocks are composed of various minerals with different capacity to adsorb surface active materials leading to different wettabilities. Thus Brown et al. suggested abandoning the concept of a contact angle for the reservoir rocks [Brown et al., 1956]. Instead, they proposed that a reservoir should be stated with fractional wettability, where a fraction of the pore surface area is preferentially oil-wet or water-wet [Fatt et al., 1956, 1959]. Salathiel coined the term ”mixed wettability”, where the oil-wetted surfaces are distributed in a way that a continuity of oil is permitted, where oil-wet film spans from pore to pore, even when the residual saturation of oil is low [Salathiel et al., 1973; Kovscek et al., 1993]. And situations where continuous paths for oil flow are not implied in the fractional wettability [Salathiel et al., 1973; Dullien, 2012]. Recent experiments [Singh et al., 2016] have demonstrated the existence of pore-scale oil layers in a mixed-wet carbonate rock under reservoir condition. Given the complexity in describing the wettability of a reservoir and the strong influence of wettability on capillary pressure and waterflood behavior [Anderson et al., 1986], there are two commonly used classifications of wettability indices relying on the capillary pressure saturation curve including the Amott Harvey index (AH index) [Amott et al., 1959; Morrow et al., 1990] and the U.S. Bureau of Mines (USBM) index [Donaldson et al., 1969].

2.3.1 Amott-Harvey index

The Amott test does not require the measurement of capillary pressure [Morrow et al., 1990; Blunt, 2017]. As shown in Fig.2.3, the porous media is fully saturated with water and water is displaced by the oil until it reaches to the initial water saturation S_{wi} ($= S_{spw} - S_{wi}$). Then the core is immersed in the water for the purpose of spontaneous imbibition. We record the change of water saturation ΔS_{ws} ($= 1 - S_{or} - S_{wi}$) when the capillary pressure falls to zero. When the residual oil saturation is reached by continuation of forced displacement, an overall increase ΔS_{wt} is recorded. The wettability index to water is given by [Amott et al., 1959; Morrow et al., 1990]:

$$I_w = \frac{\Delta S_{ws}}{\Delta S_{wt}} = \frac{S_{spw} - S_{wi}}{1 - S_{or} - S_{wi}} \tag{2.5}$$

An analogous oil index is obtained:

$$I_o = \frac{\Delta S_{os}}{\Delta S_{wt}} = \frac{1 - S_{or} - S_{spo}}{1 - S_{or} - S_{wi}} \tag{2.6}$$

The difference $I_w - I_o$ is known as Amott-Harvey index. Water-wet media $I_w \simeq 1$ and $I_o = 0$, while oil-wet systems have $I_o > 0$ but $I_w = 0$. For neutral wettability, $I_w \approx I_o \approx 0$, while a mixed-wet one is characterized with $I_w \approx I_o > 0$.

2.3.2 USBM numbers

Another frequently used index to quantify the wettability is the USBM method [Donaldson et al., 1969; Morrow et al., 1990]. As shown in Fig.2.3, the wettability number is defined by:

$$N_w = \log(\frac{A_1}{A_2}) = \log(\frac{\int_{S_{wi}}^{1-S_{or}} P_c dS_w}{\int_{1-S_{or}}^{S_{spw}} P_c dS_w}) \ . \tag{2.7}$$

where A_1 is the area under the secondary water-drainage curve (red hatched area) and A_2 is the area under the imbibition when $P_c < 0$ (blue hatched area). For water-wet systems, $N_w > 0$ and $N_w < 0$ is characterizing oil-wet rock.

The relation of surface energies, as given by Youngs contact angle and the characterisation of wettability of porous media has already illustrated the general difficultly to connect pore-scale properties to the properties of the fluid displacement on a larger scale. It is already shown with pore-network modeling that the Amott-Harvey index may give misleading results when the sample is fractionally wet [McDougall et al., 1995]. Other interesting attempts to investigate how the pore scale wettability influence the CPS curves include the pressure-controlled displacement experiments in dense packings of glass beads with well defined wettability correlation [Murison et al., 2014]. In theses experiments, the distribution of different surface energies on the displacement characteristics in the porous media has been systematically investigated of a controlled model system with the help of X-ray tomography. In addition, recent simulation results [Hiller et al., 2019] indicate that USBM and AH indices can not identify the different wetting distributions and their corresponding impact on the fluid invasion pattern. The hysteresis opening of a CPS curve should be added to complete the information. To further investigate the impact of heterogeneity on the capillary pressure hysteresis, the experiments focusing on symmetric heterogeneity, where the contact angles that are formed by the fluid interfaces with the oil-wet and the water-wet beads add up to π, were conducted, which indicates that the enhanced heterogeneity will decrease the hysteresis instead of increasing the hysteresis [Moosavi et al., 2018]. These new findings indicate that the empirical parameters such as Amott-Harvey index might eclipse the influencing factors like wetting heterogeneity.

2.4 Darcy's law

Similar to the philosophy of developing a macroscopic empirical parameter to characterize the wettability, Darcy's law is introduced as an empirical relationship to describe flow in sand filters for fountains [Darcy, 1856; Nutting, 1930]:

$$v = -\frac{K}{\mu}(\nabla P - \rho g) \ . \tag{2.8}$$

where, v is the Darcy velocity, which is defined by volume average of the flow field. K is the permeability with units of length squared. μ is the viscosity of the fluid. ∇P is the pressure gradient over a distance that covers the representative volume of the porous media. ρ is the density of the liquid. g is the gravity of the earth.

With the postulations that the capillary equilibrium between the fluids exists to establish the capillary pressure saturation curve and saturation-dependent relative permeabilities, Darcy' law is further extended to multi-phase flow [Dullien, 2012; Yortsos et al., 1998]. The resulting non-linear differential equations including Buckley-Leverett equation [Buckley et al., 1942] or Richards equation [Richards, 1931] are based on the aforementioned assumption [Bear, 2013]. However, it is pointed out that the continuum scale model is not able to characterize the ramified and chaotic aspect of capillary and viscous fingers [Lenormand et al., 1986] and the corresponding homogenization or volume-averaging requires that the capillary equilibrium to exist over a sufficiently large length scale [Yortsos et al., 1998; Whitaker, 1986]. Consequently, models based on a microscopic description of the porous medium or displacement of interfaces between fluids are developed over years [Lenormand et al., 1986; Joekar-Niasar et al., 2010]. More details about models based on microscopic description will be detailed in the following.

2.5 Pore-scale invasion process and the global invasion pattern

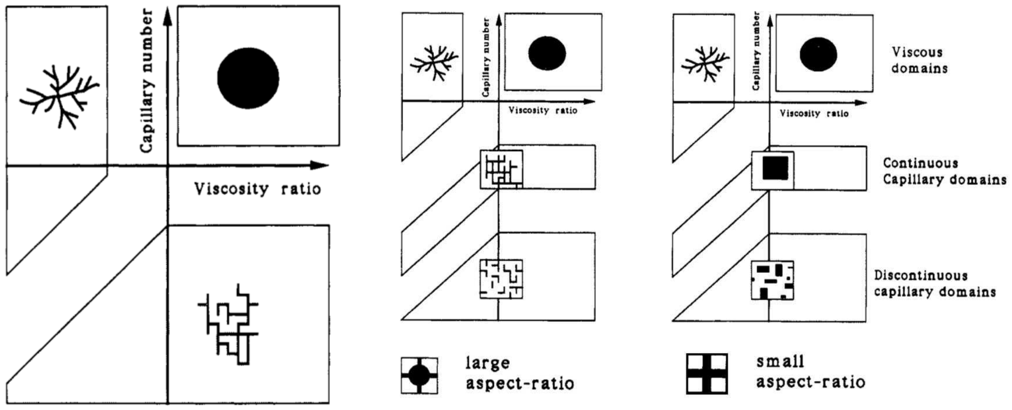

(a) phase diagram for drainage **(b) phase diagrams for imbibition**

Figure 2.4: Drainage and imbibition phase diagram adpated from Lenormand's results [Lenormand, 1990]. The viscosity ratio M and capillary number is defined in Eq.2.9. Figures adapted with permission from Lenormand et al. [Lenormand, 1990], copyright IOP Publishing.

When the focus is drawn on the pore-scale displacement process or evolution of interfaces between fluids, phase diagrams together with corresponding statistical models are frequently employed to establish a link between pore-scale invasion processes and global invasion pattern [Lenormand et al., 1988; Lenormand, 1990; Yortsos et al., 1997, 1998; Medici and Allen, 2009; Mukherjee et al., 2009; Ewing and Berkowitz, 2001; Alava et al., 2004; Tsuji et al., 2016]. As stated in the work of de Gennes and Patzek et al. [de Gennes, 2009; Patzek et al., 2000], "Many phenomena are made of random islands and in certain conditions, among the islands, one macroscopic continent emerges". These phase diagrams and statistical models give us a convenient tool to study how "the microscopic islands" form "a macroscopic continent" and facilitate the investigation of the influences from various dominating physical parameters on different invasion patterns. In the following part, we summarize some key results of a seminal phase diagram constructed by Lenormand [Lenormand, 1990], which is shown in Fig.2.4. Before we further discuss the phase diagrams, several key dimensionless numbers describing the competition between different forces should be clarified.

2.5.1 Dimensionless number for forces quantification

Viscous, capillary and gravitational forces control the dynamics of two-phase immiscible flow. To address the relative magnitude of different forces, viscosity ratio (M), capillary number (Ca) and Bond number (Bo) are usually employed, which are defined as follows [Dullien, 2012; Or, 2008; Batchelor, 2000]:

$$M = \frac{\mu_i}{\mu_d}, \quad Ca = \frac{\mu_i Q}{A\gamma}, \quad Bo = \frac{\Delta\rho g d^2}{\gamma} \ . \tag{2.9}$$

where, M is the ratio between the viscosity of the invading liquid (μ_i) and the viscosity of defending liquid (μ_d); for defining the capillary number (Ca), Q is the flow rate through a perpendicular area of A in the porous media, γ is the surface tension. $\Delta\rho$ is the density difference between the invading and defending fluid. d is the characteristic length scale of the considered situation and g is the acceleration as a result of gravity. The capillary number (Eq.2.9) measures the ratio of viscous to capillary forces. And Bond number is the ratio between buoyancy and capillary forces. The interplay between these three forces lead to complex flow phenomena influencing the morphology of wetting and drainage fronts [Or, 2008].

2.5.2 Pore-scale events

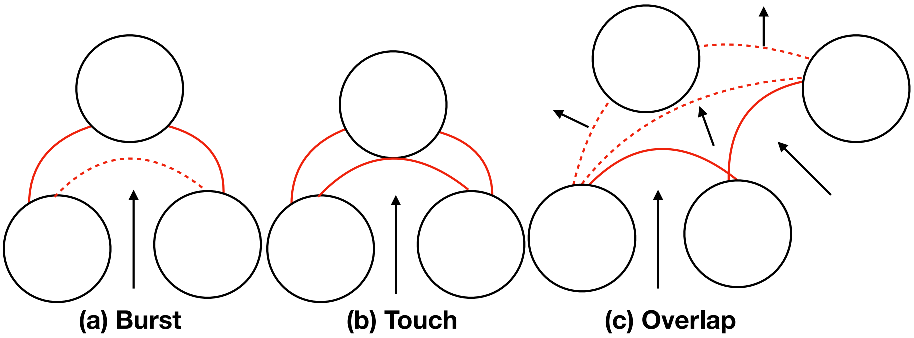

Figure 2.5: Local mechanisms of interface growth. The arrows indicate the flow direction for the invading liquid. (a) The dashed line indicates the meniscus having the maximum capillary pressure and the meniscus will become unstable and decomposes into two or more other menisci; (b) The meniscus will touch the upper disk, leading to two new arcs; (c) Two neighboring arcs overlap and they are replaced by a new arc.

Pore-scale events play a central role in connecting the pore-scale invasion process with the global invasion pattern and these events are the cornerstones for various numerical models, such as grain-based model and pore-network model [Lenormand et al., 1983; Cieplak and Robbins, 1988; Holtzman and Segre, 2015; Motealleh et al., 2013; Blunt, 2017; Primkulov et al., 2019; Hu et al., 2019]. In the following, different pore-scale events are briefly introduced starting from the pore-scale instabilities in the classical

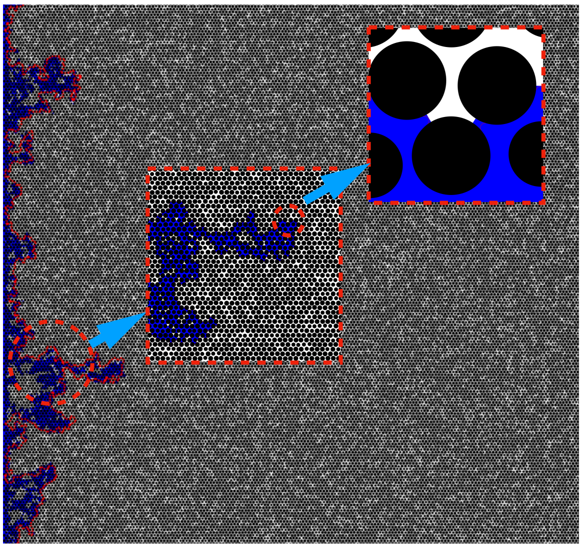

Figure 2.6: An illustration of a typical fluid invasion process in a disk packing. The disks are positioned based on a triangular lattice. There are 100 disks per row and the same amount for the column. The red dashed square represents the magnified part of the region surrounded by the circular dashed line. The connected blue phase indicates the invading fluid and the white phase is defending fluid. Contact angle of the invading fluid is 170°.

model [Cieplak and Robbins, 1988, 1990], which decompose the propagation of the interface into a sequence of three local meniscus instabilities as sketched in Fig.2.5. In this model, the porous media is made of circular disks. In Fig.2.6, a snapshot of a 2d numerical two-phase displacement process in a disk packing is presented, which gives us an impression about how the pore-scale picture is connected to a larger scale.

Burst event

A burst event [Cieplak and Robbins, 1988; Motealleh et al., 2013; Holtzman and Segre, 2015], also known as Haines jump [Haines, 1930] or rheon [Melrose, 1970], features sudden jumps of the fluid interface when the capillary pressure exceeds a certain threshold. Haines jump could be easily observed by air displacing a liquid phase or vice versa by packing consisting of small glass beads or glass micromodels [Melrose, 1970; Moebius and Or, 2012]. With recent development of synchrotron-based X-ray tomography, such an event can be imaged in porous rocks in real time [Berg et al., 2013]. The importance of these pore-scale events is that they are essential to upscale multiphase flow because they account for a large portion of the energy dissipation, affect the global displacement patterns, and also hysteresis in porous media [Melrose, 1970; Melrose et al., 1974; Berg et al., 2013; Singh et al., 2017b; Moosavi et al., 2018]. The criterion for the occurrence of Haines jumps is better explained by a thermodynamic approach because this way is not restricted to the specific geometry and wettability of the porous media [Melrose et al., 1974; Payatakes, 1982], as shown in Fig.2.7. When the non-wetting liquid (oil) is displacing the wetting liquid (water) [Melrose et al., 1974; Payatakes, 1982], the interface is stable if the pressure difference between the oil reservoir (P_0) and the water reservoir (P_w) satisfied the following condition: :

$$P_o - P_w = \gamma J, \quad \frac{dJ}{dV_o} \geq 0\ . \tag{2.10}$$

where V_o is the volume of the oil in the neighborhood of the interface, i.e. when the pressure difference increases for an advance of the fluid meniscus. It is worth noting that J is described as Gaussian curvature of the interface in the work of Payatakes [Payatakes, 1982]. However, based on Eq.2.10 and 2.4, J should be twice of the mean curvature.

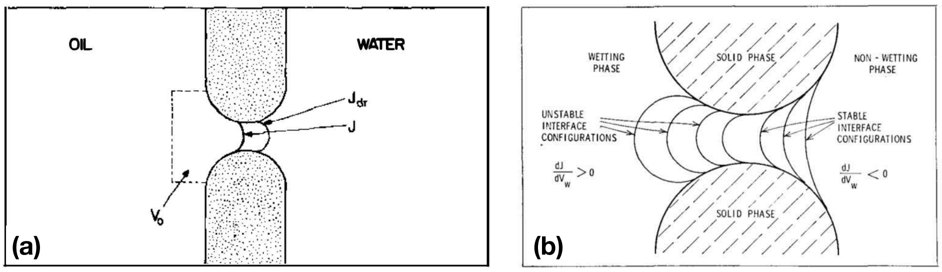

Figure 2.7: Equilibrium and stability of the meniscus (a) Meniscus separating two pools of oil and water adapted from the work of Patayakes [Payatakes, 1982]. Figures adapted with permission from Patayakes [Payatakes, 1982], copyright Annual Reviews, Inc.. (b) Illustration of the stable and unstable meniscus adapted from the work of Melrose et al. [Melrose et al., 1974]. Figures adapted with permission from Melrose et al. [Melrose et al., 1974], copyright PETROLEUM SOCIETY OF C.I.M. [ETC.].

If we employ the same thermodynamic point of view to describe Haines jumps, we can find a Haines jump in the break-up of a liquid bridge or pendular ring [Melrose, 1970; Erle et al., 1971], even though the void region formed by the two spheres does not display a converging-diverging geometry, which will be further explained in Chapter 5 . Even though Haines jumps have been investigated for nearly one century, this phenomenon is not fully understood [Edery et al., 2018; Sun and Santamarina, 2019]. For example, it has been shown that a Haines jump event can be cooperative and the advancement of one meniscus affects the nearby interconnected menisci [Armstrong and Berg, 2013; Sun and Santamarina, 2019]. In addition, the presence of surfactants will alter dynamically the interfacial tension and modify the invasion process caused by a Haines jump [Jang et al., 2016; Edery et al., 2018]. The current thesis focuses on the influence of the interplay between geometry and wettability on the fluid invasion process because combining these two factors are already very complex, which will be described in more details in the following chapters. A large number of questions remain unsolved, such as how wetting heterogeneity and geometrical heterogeneities influence Haines jumps locally and how the change in local invasion process leads to corresponding various global invasion pattern even though in an ideal porous media formed by spherical beads [Moosavi et al., 2018].

Touch event

As shown in Fig.2.5, touch events happen when a meniscus intersects a third particle. Touch events are employed in various models, but for an analysis of the competition between different pore-scale events, touch event is always ignored [Motealleh et al., 2013; Holtzman and Segre, 2015; Hu et al., 2019]. However, in the work of Cieplak et al. [Cieplak and Robbins, 1990], it is shown that in some packings, touch events rise rapidly in terms of the probability of modes when the contact angle is below 120° and the global invading pattern loses all similarity to the non-wetting invasion pattern. In the current thesis, the touch dominating regime is further explored and will be described in details later.

Overlap event

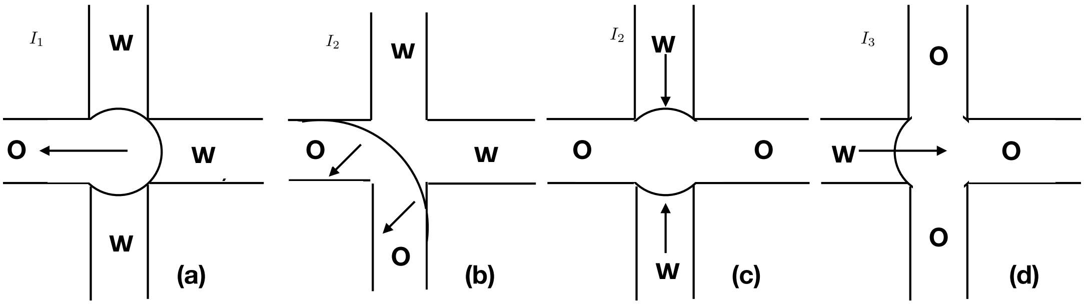

Figure 2.8: An illustration of pore filling in imbibition. The number n in I_n indicates the number of throats connected to the pore with non-wetting fluid (Oil-wet). In this plot, O represents oil-wet as well as non-wetting phase and W represents wetting phase. These plots are adpated from Lenormand's results [Lenormand et al., 1983, 1984].

The overlap of adjacent menisci is a nonlocal, cooperative mechanism as shown in Fig.2.5 [Cieplak and Robbins, 1988; Holtzman and Segre, 2015]. In the work of Lenormand and the subsequent pore network models, there is a cooperative pore filling process, which has the equivalent smoothing effect compared with the overlap event in the model presented in the work of Cieplak et al. [Lenormand et al., 1983; Blunt, 2017]. However, the models in the work of Cieplak et al. and Lenormand et al. [Cieplak and Robbins, 1988; Lenormand et al., 1983] are partially equivalent. During an imbibition process for the work of Lenormand et al. [Lenormand et al., 1983], the pore filling mechanism is named as I_n, where n is the number of throats connected to the pore with non-wetting phase as shown in Fig.2.8 [Lenormand et al., 1984, 1983; Blunt, 2017]. In Fig.2.8, we notice that I_1(a) and I_2(b) can be seemed as an overlap event as shown in Fig.2.5. Either in the work of Cieplak et al. and Lenormand et al. [Cieplak and Robbins, 1990; Lenormand et al., 1983], this cooperative event happens for the imbibition process. However, it is also pointed out that during a drainage process, an overlap event can also happen [Lee et al., 2017; Primkulov et al., 2018] and this process will entrap isolated liquid chambers.

Piston-type motion

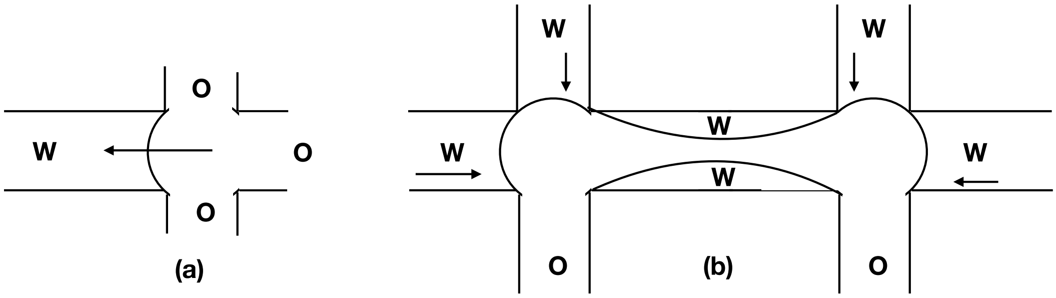

Figure 2.9: (a) Piston-type motion characterized by the non-wetting fluid enters the duct filled with the wetting fluid. (b) Snap-off event.

As shown in Fig.2.9(a), only when the capillary pressure between the non-wetting phase and wetting phase is equal to or greater than the given 'threshold pressure', the interface will advance [Lenormand et al., 1983]. When the interface is moving inside the duct, this piston-like motion is reversible [Lenormand et al., 1983, 1984]. To determine the threshold pressure, it is assumed that this pressure reaches its maximum when the liquid is passing through the narrowest pore space [Blunt, 2017]. However, if we resort to the burst event as described in the work of Cieplak et al. [Cieplak and Robbins, 1990], only when the contact angle is 180°, the maximum capillary pressure to penetrate the narrow region formed by the disks is reached. For other contact angles, this threshold pressure is not reached when the meniscus passes through the narrowest pore space.

Snap-off event

As shown in Fig.2.9(b), the wetting liquid moves along the edge of the duct instead of displacing the non-wetting liquid directly. Further addition of wetting phase leads to swelling of these "liquid fingers", which might lead to the breakup of the oil phase into ganglia and this process is called snap-off, also known as choke-off [Mohanty et al., 1987]. During drainage, a snap-off also occurs as a result of a Haines jump [Roof et al., 1970], where the drop of local pressure allows the wetting layer in the corners of the pores to swell. A snap-off event is influenced by the geometry and wettability [Wardlaw et al., 1982; Singh et al., 2017a]. In addition, a snap-off event

Flow type	Flow regime	Large pores	Small pores
One-phase flow	Bulk flow	Effective medium approach	
Drainage	Bulk flow	Invasion percolation (IP)	
Imbibition	No film flow	IP in dual network	Frontal drive compact growth
	Flow by film through roughness	Bond percolation	Compact cluster growth
Viscous flow	Stable	Flat interface	
	Unstable	Gradient governed growth Diffusion limited aggregation	

Table 2.1: Displacement mechanism and the related statistical models, adapted from the work of Lenormand et al. and Patzek [Lenormand, 1986; Patzek et al., 2000].

leads to further coalescence caused by the fluid redistribution between two clusters that are close to each other [Rücker et al., 2015].

2.5.3 Phase diagrams and statistical models

In Fig.2.4, Lenormand proposed phase diagrams to characterize the pattern formed by a fluid pushing an immiscible fluid [Lenormand, 1990]. For a drainage process, three different types of invasion patterns are identified:

- Capillary fingering develops when the fluid injection rate is low, where the capillary force dominates over the viscous force;
- Stable displacement for large viscosity ratio (M) between the invading and defending liquid;
- Viscous fingering for small viscosity ratio (M), also known as Saffman–Taylor instability [Saffman and Taylor, 1958].

For imbibition at high Ca, the global invasion pattern behaves as stable and unstable viscous cases, which is similar to drainage. A continuous capillary domain develops without film flow at intermediate Ca and discontinuous capillary domain is observed with flow by film at a lower Ca.

Accompanied with the phase diagram, an adapted table based on Lenormand's results [Lenormand, 1986] is shown in Tab.2.1, where statistical models are matched to different displacement mechanism. Tab.2.1 presents the main approach adopted to understand the underlying physics in two-phase immiscible fluid flow which is briefly summarized in the following. When capillary forces dominate over viscous forces, percolation theory has already been used to describe the displacement process [Lenormand, 1986; Patzek et al., 2000].

- Drainage. By taking into account the transport process, Wilkinson et al. [Wilkinson and Willemsen, 1983] developed the invasion percolation (IP) based on the standard theory of percolation [Broadbent and Hammersley, 1957]. Compared with usual percolation model, IP characterizes that the invading fluid can only reach regions connected to the places where it enters the medium [Cieplak and Robbins, 1990]. In addition, a trapping rule is employed to describe the phenomenon of 'residual oil', which is a great economic problem in oil industry [Wilkinson and Willemsen, 1983; Cieplak and Robbins, 1990]. Since then, the invasion percolation model gradually becomes the standard model to describe the drainage process in the two-phase immiscible flow for an ensembles of connected pores of a certain size. The benefits of statistical models is obvious because the computation is much less demanding and it is very convenient to derive the global invasion pattern in a much larger scale by connecting the pore-scale displacement. The bulk flow represents that the flow happens in the bulk of the ducts or channels and flow occurs only when a continuous path of channels or pores filled with this phase exists towards the entrance or the exit of the network [Lenormand, 1990].

- Imbibition. When the wetting fluid could not flow via the roughness of the walls, the mechanism can be described by IP in a dual network when the pores are large, while the invasion pattern displays a compact growth for small pore. When the film develops, the wetting fluid will develop film along the roughness of the walls. For large pores, bond percolation is enough to describe the global invasion pattern. Here bonds represent the cylindrical capillaries or ducts and the sites are pores for the volumes of the intersections [Lenormand, 1986]. However for small pores, compact cluster growth is dominating because the meniscus inside a pore will be unstable when the two adjacent ducts are filled.

- Viscous flow. When viscous forces dominate over the capillary force, the viscosity dependent invasion pattern has been described in the phase diagram with graident governed growth [Sherwood and Nittmann, 1986] to account for the stable case and Diffusion Limited Aggregation [Paterson, 1984; Witten and Sander, 1981] for the unstable case.

2.5.4 Progress and remaining questions

As pointed out by Homsy et al. [Homsy, 1987], Lenormand's morpholgy diagram [Lenormand, 1990] of fluid displacement differentiates only wetting and non-wetting invading fluids without quantifying their wettability. And the micromodels to perform the corresponding experiments are quasi-2D system, which lead to specific geometry of flow paths within the porous region where fluid flows. In addition, the experimental and numerical results of Fernández et al. and Ferer et al. [Fernández et al., 1991; Ferer et al., 2004, 2007] indicate the existence of crossover length scale where the invasion pattern is controlled by capillary-force for small-length-scale and viscous fingering for large-length-scale. As a result, we need to take great care when we interpret the results for the phase diagrams. In the following part, we focus on the impact of geometry and wettability of the porous media on the two phase fluid immiscible displacement process.

Geometry

The influence of geometry of the porous media on the fluid invasion pattern is not well characterized in Lenormand's diagram. For example, it is stated that I_3 only takes place when "snap-off" happens in Lenormand's results [Lenormand et al., 1983, 1984]. However for the case of I_3 in the work of Zacharoudiou et al. [Zacharoudiou et al., 2017], the pore-scale invasion mechanism differs between a quasi-static imbibition process and dynamic imbibition process. For the quasi-static process, where the pressure of the invading fluid is gradually increased, snap-off events occur in the narrowest throats in accordance with the prediction based on the Young-Laplace equation. For the dynamic process, where the invading fluid is injected at constant flow rate, the wetting phase invades the neighboring throat firstly. This difference occurs because the advancing wetting films needs the time to develop [Bico and Quéré, 2003] and the dynamic process do not allow for the development of a wetting film ahead of the advancing film [Zacharoudiou et al., 2017]. As a result, the pore geometry becomes pivotal in the case of fast spontaneous imbibiton. In addition, the results of Zacharoudiou et al. [Zacharoudiou et al., 2017] provide a potential interpretation for the invasion pattern recognized in the work of Singh et al. [Singh et al., 2017b], where only compact interfaces are developed even when the contact angle of the invading fluid is around 20°, because the experiments were also performed with a constant flow rate. These experiments [Zacharoudiou et al., 2017; Singh et al., 2017b] naturally raise questions like how to describe and quantify the influence of the development of a wetting film and the role that this wetting film plays in altering the invasion pattern on a scale larger than the pore-scale.

Even though that the drainage is fairly well understood after a century of intense research and with pore-network modeling and the fluid displacement at the field scale can be predicted with satisfactory results [Lenormand et al., 1983; Blunt et al., 2013; Odier et al., 2017; Zacharoudiou et al., 2017], recent new findings challenge our understanding of the drainage process. Even for a combination of parameter spaces where M and Ca favoring capillary fingering, Lu et al. found that by controlling the gradient of the pore size, the capillary fingering is either suppressed or promoted [Lu et al., 2019]. This invasion pattern governed by the pore geometry is another interpretation of Homsy' comment [Homsy, 1987] on the diagram of Lenormand [Lenormand, 1990]. Similarly, a gradual reduction of the pore sizes leads to restraining viscous fingering [Rabbani et al., 2018]. Even in the quasi-2D system, if the circular pillars are replaced with triangular pillars or some other shapes, it is questionable that the invasion pattern obtained based on experiments with circular pillar or square channels for given Ca and viscosity ratio remain unchanged. For instance for a regular arrays of triangular posts, the wetting liquid will preferentially choose a direction for the wicking or imbibition [Liu et al., 2019]. Even though the system of Liu et al. [Liu et al., 2019] is not closed from the top, it already indicates the potentially strong influence of geometry on the fluid displacement. In 3D, the influence of geometry on the invasion pattern might become even more important because the pore space in a 3D medium is much more connected than the pore space of a 2D medium [Sahimi, 2011; Datta et al., 2014].

Wettability

Cieplak & Robbins [Cieplak and Robbins, 1988] provided a classical model to investigate the influence of wettability on a quasi-static fluid invasion process. It was shown that increasing the affinity of the invading fluid to the surface will promote the cooperative smoothing mechanism and the invasion pattern turns from a fingering to a compact structure [Cieplak and Robbins, 1988, 1990]. This smoothing effect for low capillary number has been observed again in recent experiments [Trojer et al., 2015] using a radial Hele-Shaw cell packed with glass beads. Similar to the experiment in the work of Trojer et al. [Trojer et al., 2015], by combining grain-based models and pore-based models, Holtzmann et al. [Holtzman and Segre, 2015] showed that increasing the wettability of the invading fluid promotes cooperative pore filling and this effect is reduced with increasing flow rate. In addition, recent experimental results in microfluidic Hele-Shaw cells [Jung et al., 2016] and bead packs [Singh et al., 2017b] further investigated the influences of the wettability on the invasion pattern. For the experiments conducted in bead packs [Singh et al., 2017b], it is shown that the contact angle dependent invasion pattern can be predicted on the basis of local instabilities that control the progression of the fluid interfaces and a cross-over from a compact front morphology to a fingered morphology is identified, which is similar to the numerical model by Cieplak & Robbins [Cieplak and Robbins, 1988, 1990]. Apart from that, some new invasion patterns are found. For example, it is found that for sufficiently small contact angle, there is a strong imbibition process induced by the fluid invasion along the corners [Zhao et al., 2016]. Here, the phenomenon of corner flow means that the invading liquid preferentially flows along the corners where top and bottom surfaces of the flow cell meet instead of going through the pore body [Primkulov et al., 2018; Zhao et al., 2016]. Actually, this phenomenon has already been studied extensively for spontaneous imbibition in angular capillaries [Concus and Finn, 1969; Dong and Chatzis, 1995]. However, the experiments in the work of Zhao et al. [Zhao et al., 2016] are again performed in a quasi-2D microfluidic cells with vertical posts. The corner flow is a phenomenon occuring under the combination of specific geometry and wettability. Whether the invasion pattern identified in this quasi-2D system could be extended to 3D system, where the flowing channels are formed by 3D bead packs, still remains elusive. At least, for the capillarity-dominated experiments of the bead pack [Singh et al., 2017b], no trace of corner flow is found when the contact angle is around 20°, which will be further explained by the quantification method developed in this thesis. And this difference between 2D and 3D naturally raises the question about what determines the fingering invasion pattern for the strong imbibition in 3D. In the diagram of Lenormand's work [Lenormand, 1990], film flow is induced by the surface roughness of the walls and it is different from the corner flow described in Zhao's work [Zhao et al., 2016]. If there is film flow in 3D, is it a result of the wall roughness or specific combination of geometry and wettability? The answer could be a combined influence of surface roughness and geometry for a given wettability. In that case, quantification of the influence of surface roughness and pore space geometry becomes pivotal. Apart from that, natural porous media is often heterogenous wet. And recent experimental and simulation work [Murison et al., 2014; Moosavi et al., 2018; Hiller et al., 2019] provide new insights in characterizing heterogeneous wet porous media. If the natural reservoir is heterogeneous wet, how to interpret the phase diagram of Lenormand's work [Lenormand, 1990]?

The aforementioned experimental and numerical simulation results naturally raise questions such as how geometry and wettability of the porous media influence the invasion process on different scales and despite the importance of the fluid invasion process, there is only limited understanding of the processes connecting the pore-scale invasion to the global invasion pattern. With the advent of more sophisticated tools like X-ray tomography, we are able to answer more questions on the interaction between different parameters on fluid invasion process for 3D porous media. Among many factors influencing the fluid invasion process, the current thesis focuses on the pore scale geometry and precisely adjusted wettability of the porous media.

Chapter 3

Influence of wettability and geometry on fluid invasion in disk packing

3.1 Introduction to the Cieplak Robbins model

The influence of wettability on the immiscible fluid displacment has been studied in a two-dimensional porous medium by Cieplak and Robbins [Cieplak and Robbins, 1988, 1990]. Considering the somehow artificial situation of a two-dimensional system offers the advantage that the equilibrium configurations of the interface between the two fluid phases are simply collections of circular arcs. In addition to the condition of the same curvature in every point of the interface, these circular arcs need to intersect the surface of the porous solid at a given material contact angle which itself is controlled by surface energies.

A simple pore geometry that permits an explicit construction of equilibrium configurations of the menisci are given by regular arrays of circular disks. In the original Cieplak Robbins (CR) model, geometrical disorder of the porous medium is achieved through randomizing the radii of the disks while their centers are arranged on regular triangular or square lattice defining 'pores' delimited by three or four disks, respectively. The fluid displacement process itself is described by a sequence of equilibrium configurations for an increasing curvature of the circular arcs representing the interface of the invading fluid. By virtue of the Laplace equation, the curvature is controlled by the pressure difference between the fluid phases which is slowly ramped up by small increments.

While, for most of the time, the new interfacial configuration after a small pressure increment is almost identical to the previous configuration, a number of capillary instabilities may trigger a sudden progression of the interface. The three basic capillary instabilities leading to local fluid invasion considered in the CR model were already described in section 2.5.2. A local 'burst' of the interface in the adjacent pore occurs once the curvature of a meniscus exceed the largest possible curvature of a menisci between two neighboring disks which intersect both disks with the given contact angle. Bursts can be precluded either by a 'touch' instability where the meniscus touches the surface of a third disk or by a 'coalescence' instability. The latter type of capillary instability occurs if two neighboring menisci touch in a point of the free interface or touch in the point where they intersect the disk in common.

Every time a capillary instability has been detected in the CR model, the involved menisci are removed from the configuration while new menisci are added to correctly represent the state of the invaded pore. This process is repeated, if necessary, until the new menisci are not anymore subject to one or more instabilities. It has been noticed in Ref. [Hecht and Taitelbaum, 2004] that the order in which the new interface configuration is generated matters for the evolution of invading interface. Although the rules to generate new configurations may appear artificial, the systematic comparison between the interfacial advance predicted by the CR model and the observed displacement in experiments with quasi-two dimensional microfluidic cells in Sec. **??** demonstrates that the rules correctly reproduce the evolution of the invading interface in the vast majority of cases.

Central aim of the work presented in this chapter is to employ and extend the original CR model to quantify the impact of combined wetting and geometrical disorder on the emerging fluid displacement pattern. To this end, we first need to develop the methodology and tools to construct the equilibrium meniscus configurations for a given curvature between two disks while allowing each disk to have an arbitrary radius and contact angle. Based on this construction, we will derive closed form expression for the conditions of burst and touch in the two-dimensional CR model. Here, we are going to make repeated use of the Cayley Menger determinant (CMD) in two and three dimensions [Menger, 1928]. The value of the CMD represents the signed volume of a n-dimensional simplex with given side-lengths. This novel method to find closed form expression for burst and touch conditions allows us to give straightforward generalisations for three and more spatial dimensions. Later in chapter 5 of this thesis, these expressions will be valuable to formulate a model for three-dimensional packs of spherical beads that is fully analogous to the two-dimensional CR model.

3.1.1 Geometrical construction of menisci

In this section we are going to describe the geometrical construction of menisci between two circular disks of arbitrary radii r_i and contact angles and θ_i where the index $i = 1, 2$ refers to the disks. Since the applied pressure difference P is identical to the Laplace pressure and, thus, controls the radius of the meniscus, we need to construct segments of circular arcs with radius $R = \gamma/|P|$ that intersect the disks with the given contact angle. Throughout this thesis, we will adopt the widespread convention that the curvature of the meniscus is positive if is curved to the invading

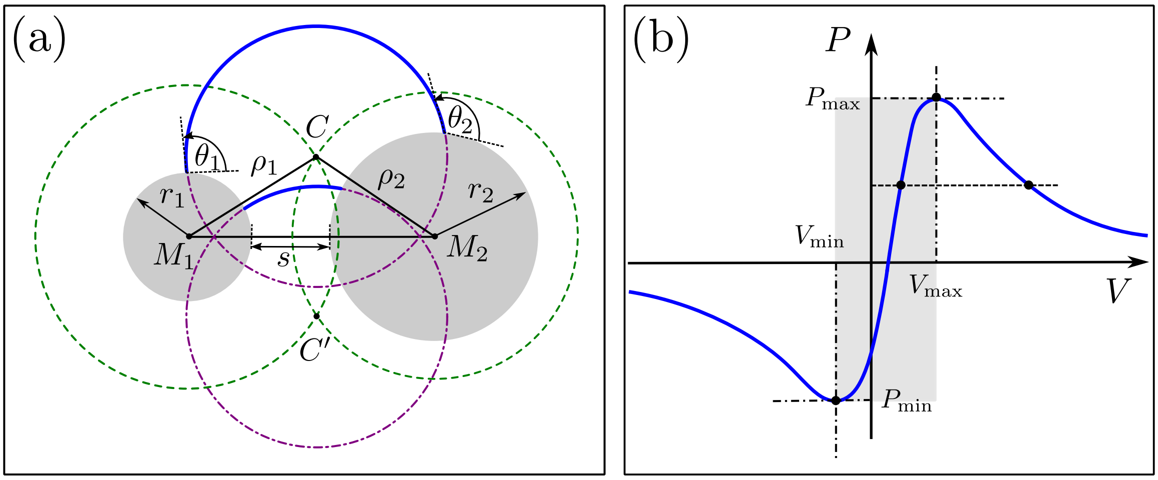

Figure 3.1: (a) Construction of a meniscus intersecting two disks with different radii r_i and contact angles θ_i. (b) Sketch of the Laplace pressure P of a meniscus as a function of the volume V. The region volumes of the invading fluid and Laplace pressures corresponding to mechanically stable menisci are highlighted in grey.

fluid and negative if it is curved to the defending fluid.

In the following, we will first consider the case $P > 0$ of a positive Laplace pressure and discuss the case $P < 0$ later. Employing the condition of a given contact angle θ_i on disk i, we conclude from a simple geometrical construction shown in Fig. 3.1 that the center of the circle which contains the segment that represents the meniscus lies at a distance

$$\rho_i = \sqrt{R^2 + r_i^2 - 2Rr_i \cos\theta_i} \tag{3.1}$$

from the center of disk i. We observe that the radius ρ_i for a finite contact angle $0 < \theta_i < \pi$ lies in between the two extreme values $\rho_i = |R - r_i|$ for $\theta_i = 0$ and $\rho_i = R + r_i$ for $\theta_i = \pi$.

To describe a meniscus that intersects both disks with the given contact angle, the condition Eq. (3.1) must be satisfied for $i = 1, 2$ simultaneously. This implies that the center of the circle of radius R representing the meniscus, must be located in an intersection of two circles with radius ρ_i around the center of disk i. Now, depending on the separation distance $s > 0$ between the surfaces of the two disks, we may find two, one, or no intersection of the circles. Using the quantity

$$G = \rho_1 + \rho_2 - d \tag{3.2}$$

where $d = r_1 + r_2 + s$ is the distance between disk centers, we have two solutions for $G > 0$, one solution for $G = 0$ or no solution for $G < 0$. Obviously, each of the two possible solutions for $G > 0$ can be obtained by a reflection from the other solution with respect to the line passing through the centers of disks 1 and 2. Hence, for $G > 0$, we find two possible segments of a circular arc which represent a meniscus with a positive curvature which can be distinguished their arc-length and by the volume of the invading fluid that is enclosed by them. The menisci are represented by the two upper circular arcs, as indicated as blue solid lines in Fig. 3.1(a). In the following, we will refer to the circular arc of the upper circle as the 'large solution' and the circular arc of the lower circle as the 'small solution'.

To construct menisci with a negative Laplace pressure $P < 0$, i.e. which are curved away from the invading fluid, we can follow the procedure for a positive Laplace pressures $\bar{P} = -P$ but for complementary contact angles $\bar{\theta}_i = \pi - \theta_i$, $i = 1, 2$. Since the orientation of the interface has changed in respect to the case $P > 0$, the meniscus is now represented by the lower segments of the circle.

To find an explicit parameterisation of the circular arcs which allows to compute the enclosed volume and other physical quantities, it is useful compute the distance of the center of the circle representing the meniscus and the line passing through the two disk centers. At this point, we can employ Heron's formula to compute the area $A_\triangle$ of the triangle $\triangle\overline{M_1 M_2 \mathcal{C}}$ that is formed by the two disk centers and the center of the circle representing the meniscus. Using the total perimeter of the triangle, $l = \rho_1 + \rho_2 + d$, we have

$$A_\triangle = \sqrt{l\left(l/2 - \rho_1\right)\left(l/2 - \rho_2\right)\left(l/2 - d\right)/2}\ . \tag{3.3}$$

With the knowledge of the triangle area $A_\triangle$, we can easily compute the height of the triangle

$$h = \frac{2A_\triangle}{d}\ . \tag{3.4}$$

From this point on, it is rather straightforward to compute the angles of the triangle $\triangle\overline{M_1 M_2 \mathcal{C}}$. Using elementary geometrical relation this allows us to calculate the area of the invading fluid enclosed by the meniscus, the perimeter of the disks and the line passing through the centers of the disks. The procedure to compute the area and the interfacial energy associated to the meniscus configuration can be found in the appendix C.1.

The typical plot of the Laplace pressure as a function of the enclosed volume for given radii r_i of the disks and contact angles θ_i shown in Fig. 3.1(b) reveals a numbers of generic features. First of all, the Laplace pressure is bound between a maximum value $P_{\mathrm{max}} > 0$ and a minimum value $P_{\mathrm{min}} < 0$. Both, the maximum and the minimum value are attained at finite volumes V_{max} and V_{min}, respectively. Since the function $P(V)$ is smooth, the Laplace pressure crosses zero at a certain finite volume. At this point, the meniscus is straight line as expected from the the small solutions in the limiting case of of an infinitely large absolute radius of curvature. However, in the limit $|V| \to \infty$ the magnitude of the Laplace pressure tends to zero, $|P| \to 0$ and meniscus configurations with a volume V in range of $]V_{\mathrm{max}}, \infty[$ and $]-\infty, V_{\mathrm{min}}[$ always correspond to large solutions.

Burst criterion

Only menisci corresponding to the small solutions found for volumes between $V_{\min}$ and $V_{\max}$ are mechanically stable and need to be considered in the CR model. Because of the derivative $\mathrm{d}P/\mathrm{d}V > 0$, any small increase or decrease of the volume enclosed by the meniscus leads to an increase or decrease of the Laplace pressure, respectively, which allows for a stable mechanical equilibrium with a volume reservoir that fixes pressures difference between the invading and defending fluids. In cases where the applied pressure P falls outside of the range $[P_{\min}, P_{\max}]$, the derivative is now $\mathrm{d}P/\mathrm{d}V < 0$ and no stable meniscus configuration between the two neighboring disks exists.

If the pressure is raised from a value $P < P_{\max}$, one observes a sudden "burst" of the fluid meniscus at constriction formed by the two disks and filling the adjacent pore once P has reached $P_{\max}$. The pore that was initially filled with the defending fluid will be filled with the invading fluid after the burst. Similarly, one observes a 'reverse burst' of the meniscus if P falls below $P_{\min}$. During the reverse burst, the pore that was initially filled with the invading fluid will be suddenly invaded by the defending fluid. As the applied pressure difference is slowly ramped up to larger values in the CR model, the latter situation does not occur and can be discarded.

The largest possible Laplace pressure $P_{\max} > 0$ or, equivalently, the smallest radius $R_{\max} = \gamma/P_{\max}$ allowing for a mechanically stable meniscus can be expressed either through the condition $G = 0$ or, alternatively, by the vanishing area $A = 0$ of the triangle formed by centers of the disks and the center of the circle representing the meniscus. Using the Cayley-Menger (CM) determinant, the square of the area of the triangle can be cast into the form

$$A^2 = -\frac{1}{16}\begin{vmatrix} 0 & 1 & 1 & 1 \\ 1 & 0 & d^2 & \rho_1^2 \\ 1 & d^2 & 0 & \rho_2^2 \\ 1 & \rho_1^2 & \rho_2^2 & 0 \end{vmatrix} . \tag{3.5}$$

Repeated Laplace expansion of the determinant eqn. (3.5), staring from the first column or row, yields

$$A^2 = \frac{1}{16}\left[2d^2\left(\rho_1^2 + \rho_2^2\right) - d^4 - \left(\rho_1^2 - \rho_2^2\right)^2\right] . \tag{3.6}$$

Using the relation of the radii ρ_i to the contact angle and curvature R (3.1), we observe that the leading power in R of expression (3.6) is two, i.e. the condition $A^2 = 0$ can be cast into a quadratic equation

$$\hat{A}\,R^2 + \hat{B}R + \hat{C} = 0 \tag{3.7}$$

with coefficients

$$\hat{A} = 4\left[d^2 - (r_1\cos\theta_1 - r_2\cos\theta_2)^2\right] , \tag{3.8}$$

$$\hat{B} = 4\left[r_1\cos\theta_1(r_1^2 - r_2^2 - d^2) + r_2\cos\theta_2(r_2^2 - r_1^2 - d^2)\right] \ , \tag{3.9}$$

$$\hat{C} = \left[d^2 - (r_1 - r_2)^2\right]\left[(r_1 + r_2)^2 - d^2\right] \ . \tag{3.10}$$

For any meaningful physical situation of non-overlapping circular disks at a finite distance, the coefficient $\hat{A} > 0$ while the last is always $\hat{C} < 0$. Hence, the quadratic polynomial (3.7) has always two roots in R, one positive R_0^+ and one negative R_0^-. While the positive root can be directly identified with the desired radius of curvature R_{max} related to the Laplace pressure maximum P_{max}, the interpretation of the negative root R_0^- requires further considerations. First, let us recall that the radius of curvature R_{min} corresponding to the Laplace pressure minimum P_{min} is determined from the maximum radius $\bar{R}_{\text{max}}$ for the situation where the contact angles for disk 1 and 2 are replaced by their respective complementary angles $\bar{\theta}_i = \pi - \theta_i$. The form of expression (3.1) for the radii ρ_i is, obviously, invariant when simultaneously changing the sign of R and replacing the contact angles θ_i for $i = 1, 2$ by $\bar{\theta}_i$. The invariance of the expression (3.1) implies that $|R_0^-| = \bar{R}_{\text{max}} = R_{\text{min}}$ and led us to conclude that $P_{\text{min}} = \gamma/R_0^-$ and $P_{\text{max}} = \gamma/R_0^+$, which already respects the signs of the Laplace pressure at it maximum and minimum, respectively.

Touch criterion

In dense disk arrangements, and in a certain range of contact angles, the burst instability may by precluded by other capillary instability that lead to a local advance of the invading liquid. One possible instability is the 'touch' event that occurs when a meniscus that is in the stable range of Laplace pressure $\mathrm{d}P/\mathrm{d}V > 0$ between P_{min} and P_{max} touches the surface of a third disk, cf. also the illustration in Fig. 3.1(b). The criterion for the occurrence of a touch event for a given configuration of three disks $i = 1, 2, 3$ with radius r_i and contact angles θ_i cannot be expressed in a closed form. However, for given radius and position of the center of the circle representing the meniscus, one can first check if the constructed meniscus overlaps with the third disk by simply computing the distance of the two circle centers and comparing to to the sum of their radii. If the sum of radii is larger than the distance of their centers, one needs to further check if the overlap of the circles occurs within the circle segment of the small or the large solution.

Checking for a potential touch event for every meniscus after every increment of the applied pressure involves recalculating the distance of every meniscus from neighboring disks. To save computational costs, one may compute the Laplace pressure that leads to a touch with a third disk once a meniscus with a certain orientation has been established between a pair of neighboring disks. This calculation needs to be performed only one time during the simulation and, thus, saves computational resources.

As we can see in the sketch in Fig. 3.2, the configuration of the meniscus touching the third disk satisfies three conditions: (i-ii) the distance between the center of the circle $\mathcal{C}$ of the meniscus and the centers of disk i with $i \in \{1, 2\}$ equals ρ_i, and (iii) the

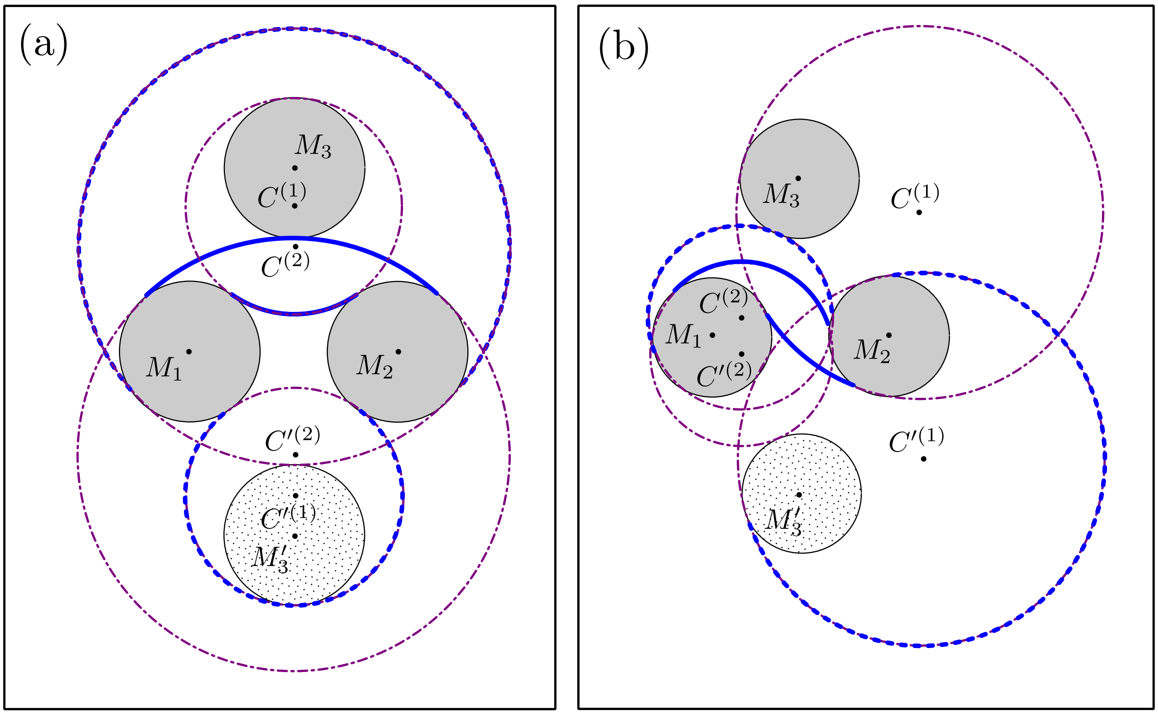

Figure 3.2: Meniscus circles touching the third disk or its reflection obtained from solutions of Eq. (3.11). Unstable (large) solutions are displayed as fat dashed line while stable (small) solutions are shown by fat solid curves. Disk centers labeled by M_i, $i = 1, 2, 3$ while $C^{(1,2)}$ are the centers of the meniscus circles with radius $R_{0,1}$ and $R_{0,1}$. A prime denotes the a reflection. Contact angles are $\theta_1 = \theta_2 = 5°$ in (a) and $\theta_1 = 10°$ and $\theta_2 = 170°$ in (b).

distance between the center of $\mathcal{C}$ and the center of disk 3 is $R + r_3$. These conditions are satisfied if all four vertices of a tetrahedron with side lengths d_{12}, d_{23}, d_{13}, ρ_1, ρ_2 and $R + r_3$ fall into the same plane. Since the volume of a tetrahedron with given side lengths can be expressed as a CM determinant, we can rephrase the condition for the radius R of the meniscus touching disk 3 as

$$V^2 = \frac{1}{288} \begin{vmatrix} 0 & 1 & 1 & 1 & 1 \\ 1 & 0 & \rho_1^2 & \rho_2^2 & (R+r_3)^2 \\ 1 & \rho_1^2 & 0 & d_{12}^2 & d_{13}^2 \\ 1 & \rho_2^2 & d_{12}^2 & 0 & d_{23}^2 \\ 1 & (R+r_3)^2 & d_{13}^2 & d_{23}^2 & 0 \end{vmatrix} = 0 \; . \tag{3.11}$$

Repeated expansion of the determinant eqn. (3.11) yields a quadratic polynomial in the radius R of the meniscus and, thus two solutions. Details on how to arrive at the quadratic polynomial and to select the appropriate solution are provided in Appendix C.3.

If the discriminant is negative, no real solution exists, and, hence, a touch event can be excluded. For a positive discriminant the quadratic equation has two real roots $R_0^{(1,2)}$. Each of the real roots corresponds to the radius of a circle describing a meniscus that touches the third disk. If respective the root is negative, the third disk touches the circle of the meniscus from inside, cf. the examples in Fig. 3.2(a,b). This observation is in line with the previous findings reported in Sec. 3.1.1: Circular arcs describing menisci at negative pressure differences must curve away from the invading fluid.

Unfortunately, the polynomial coefficients do not convey any information on whether the touch occurs on the stable branches $\mathrm{d}P/\mathrm{d}V > 0$ or unstable branches $\mathrm{d}P/\mathrm{d}V < 0$ and at $P > 0$ or $P < 0$, cf. also Fig. 3.1(b). For the case of an unstable meniscus with negative curvature, the meniscus touches the reflection of the third disk at the line passing through M_1 and M_2 and is not relevant. Similarly the touch with the third disk can be for positive curvature, but for a meniscus on the unstable branch. The positive solution $R_{0,1} > 0$ in Fig. 3.2(a) is indeed the radius of a meniscus on the stable branch that touches the third disk. The negative solution with radius $R_{0,2} < 0$, however, corresponds to an unstable meniscus that touches the reflected image of the third disk, cf. Fig. 3.2(a). Hence, for the case depicted in Fig. 3.2(a), only the positive solution of eqn. (3.11) corresponds to a stable meniscus touching the third disk.

A different situation is encountered for the combination of contact angles $\theta_1 = 10°$ and $\theta_2 = 170°$ as shown in the example Fig. 3.2(b). Now, the unstable meniscus with $R_{0,1} > 0$ touches the third disk, while, similar to the previously discussed example in Fig. 3.2(a), again the unstable meniscus with radius $R_{0,2} < 0$ touches the reflected third disk. In other words, in the example shown in Fig. 3.2(b), only unstable menisci are touching the third disk or its reflection, and a burst at $P_{\max}$ or $P_{\min}$ cannot be precluded by a touch.

Even more complex situations can be found by varying the disk radii r_i as well as the disk configuration and contact angles θ_i. A stable or unstable meniscus with positive or negative curvature may touch the third disk or its reflection, respectively. Despite the advantage of computing the pressure difference that leads to a touch event from only distances and contact angles, this method inevitably requires further checks whether the third disk is touched by a meniscus on the stable or on the unstable branch. However, the recalculation of every meniscus shape after a pressure step and checking all menisci for a touch does not suffer from this problem.

Coalescence criterion

The third capillary instability of the Cieplak Robbins model, besides the burst and touch events described in Sec.3.1.1 and Sec.3.1.1, is the 'coalescence' of two menisci [Cieplak and Robbins, 1988, 1990]. This instability leads to the merging of two neighboring menisci once they touch. This can occur either on their free interfaces or at the three phase contact line where the two interfaces intersect on the common disk [Primkulov et al., 2018; Lee et al., 2017]. Both types of coalescence events are illustrated in Fig. 3.3.

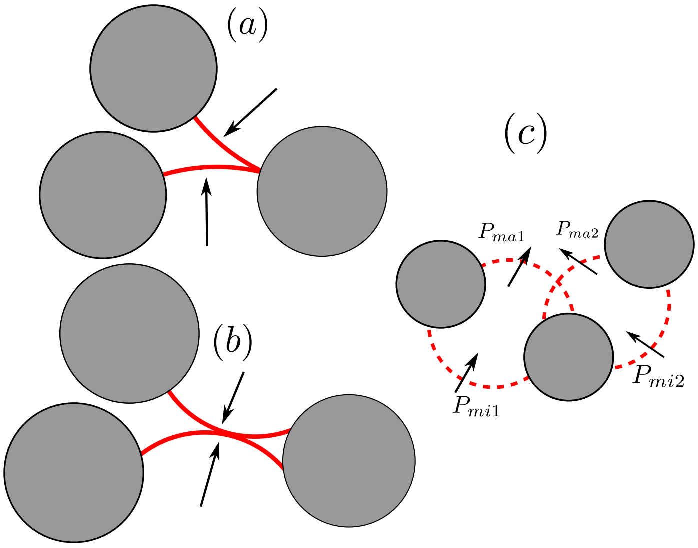

Figure 3.3: Coalescence events triggered two menisci touching (a) on their free interfaces and (b) at the three phase contact line. (c) Illustration for explanation of the numerical implementation of the algorithm. The arrows in the plot indicate the flow direction of the invading liquid.

Similar to the touch instability, checking for the coalescence instabilities requires knowledge of the center positions of the two circles representing the menisci as well as an effective numerical routine to determine whether the intersection occurs inside of one of the two disks.

A semi-analytic approach to solve for the meniscus curvature leading to a coalescence event is presented in C.2. The value of the curvature radius when two neighboring menisci touch must be computed numerically. As shown in Fig.3.3(c), for each pair of disk, the maximum and minimum pressure for a stable meniscus is solved via Eq.C.13. Combining two pressure windows, we obtain a pressure range $[P_1{=}\max(P_{mi1}, P_{mi2}),P_2{=}\min(P_{ma1}, P_{ma2})]$ when two menisci are stable at the same time. We start from testing at pressure P_1 and P_2, whether two menisci are overlapping or not. The overlapping criterion is directly determined by testing whether the intersection points of two circular meniscus circles are on the circular meniscus arcs. When the menisci are overlapping at pressure of P_1, the pressure for overlap event is determined as P_1. Further if two menisci are not overlapping at the high pressure P_1, it indicates that burst event happens before overlap event. Only when the menisci are not overlapping at P_1 and overlapping at P_2, we start to solve the critical curvature by simple binary iteration [Cormen et al., 2009]. We firstly determine when $P_m = \frac{P_1+P_2}{2}$, whether the menisci are overlapping or not. If the menisci overlap with each other, we test the pressure window $[P_1, P_m]$, otherwise we test $[P_m, P_2]$. The iteration continues until the pressure windows is small enough, which is adjustable.

3.1.2 Interface invasion algorithm

The main structure of the algorithm to compute the evolution of the invading interface employed in the present work is similar to the approach of Cieplak and Robbins in Ref. [Cieplak and Robbins, 1988, 1990]. Following the original model outlined in Ref. [Cieplak and Robbins, 1988, 1990], we place the discs on a triangular lattice with lattice unit a. Owing to the triangular arrangement of the disks, it is self-evident to consider the nearly equilateral triangles formed by the centers of three adjacent discs as the fundamental pore bodies of the medium.

Because the radius of every disk is drawn from a discrete set of radii, and not from a continuous distribution as in Ref. [Cieplak and Robbins, 1988, 1990], we need to randomise the center position of the disks. Perfectly regular positions would lead to a cumulation of pore-scale events at a few values of the applied pressure difference such that the proper order of the events cannot be resolved by the algorithm. A randomisation of the arrangement is achieved by displacing each disc center by a random small displacement into a random direction. For simplicity, the magnitude of the random displacement is drawn uniformly from an interval $[0, \delta]$ where $\delta \ll a$.

At the beginning of every simulation run, menisci are created at all inlet throats of the boundary pores. and the applied pressure difference P is set to the smallest burst threshold $P_{\max}$ of all throats in the assembly. In the present study, we consider a rectangular simulation box which is aligned with on lattice direction of the triangular lattice. To minimise the influence of the boundaries, we apply periodic boundary conditions into the direction perpendicular to the initial front of menisci. In the majority of cases, a number of menisci of the initial interface configuration do not conform to the stability criterion of coalescence and touch instability we need to evolve the interface to a stable configuration.

In the first step, all menisci being unstable with respect to the touch instability and generate new menisci bounding the newly invaded pores. In the following step, we check the new interface configuration for pairs of neighboring menisci that are unstable with respect to coalescence, remove the unstable menisci and add new menisci bounding the pores that are invaded as a consequence of invading fluid. The new interface configuration is checked again for menisci that are unstable with respect to a burst event, and the interface is evolved accordingly. Only if all menisci are stable with respect to a touch event, we have reached a stable initial interface configuration where new instabilities are incurred only through an increase of the pressure difference P. If the new interface is unstable with respect to one ore more touch events, the procedure is repeated until the new interface configuration is stable with respect to all three meniscus instabilities.

Ideally, the following pressure increment ΔP is chosen to ensure that no or only a single meniscus instability takes place between P and $P + \Delta P$. For the sake of numerical efficiency, we identify the appropriate pressure increment ΔP for each step using a binary search algorithm [Cormen et al., 2009]. Starting from the current pressure P_n, under which every meniscus is stable, we determine the minimum pressure increment which incurs the instability at smallest pressure. To this end we firstly define $P_>$ as the maximum pressure $\max_i(P_{\max}(i))$ of all i possible bursting thresholds in the disk assembly. This ensures that no meniscus will be stable. We could easily test the pressure with the $\bar{P} = (P_n + P_<)/2$. If there are some unstable menisci, we are sure that for any $P \in [\bar{P}, P_<]$, we always have unstable menisci, and, consequently, update the upper bound $P_> = \bar{P}$. If no unstable menisci are found for $\bar{P}$, we update the lower bound of the pressure $P_< = \bar{P}$. The construction of nested intervals will be repeated until $|(P_> - P_<)/P_>| < \epsilon$ is satisfied. If not stated otherwise, the default value for the ϵ is 10^{-5} is used. As a binary search algorithm scales logarithmically with the number of tested burst thresholds, the present implementation of the Cieplak Robbins model runs much faster compared with the method where the pressure is increased by a fixed pressure increment. By choosing the appropriate threshold ϵ, we are able to control for each time step, if only one or several pore-scale events occur. Finally, the current pressure after the increment is set to $P_{n+1} = P_>$.

3.2 Displacement regimes and pore-scale events

The algorithm outlined in Sec. 3.1.2 allows us to study the evolution of the global fluid displacement patterns, and, at the same time, to collect information about the statistics of the three pore-scale events. Besides the wetting conditions, i.e. the contact angle θ of the invading fluid on the pore walls, the geometry of the pores represents a dominant factor that controls the local advancement of the interfaces at low capillary numbers. The transition between capillary fingering and compact frontal advance observed as the contact angle of the invading fluid is lowered can be understood from the competition between bursts and coalescence events [Jung et al., 2016]. As mentioned in the introduction Sec. 2.5.4, the global shape of the invading interface remains smooth at low contact angles, which can be readily understood from the cooperative nature of the dominating coalescence events. Except for a few remarks in the work of Cieplak and Robbins in 1990, the role of touch events in the formation of displacement patterns has not yet been systematically studied.

The transition from bursts and capillary fingering at high contact angles to coalescence events and stable frontal advance at low contact angles can be observed in experiments using micro-fluidic cells with cylindrical obstacles. Figure 3.4 (a,c) shows examples of the displacement pattern for two fluid combination with a high advancing contact angle of $\theta \approx 125°$ and with a high contact angle $\theta \approx 52°$, respectively. Owing to the low flow rate, viscous forces can be neglected and the displacement operates in the capillarity dominated regime. Interfacial configurations using our displacement algorithm, as displayed in Fig. 3.4(b,d), not only display the same qualitative features, but also the highly similar sequences of local invasion events. As expected, coalescence events dominate over bursts for low contact angle $\theta_a \lesssim 80°$, and a compact invading front is visible in both in the experiments and simulation, cf. Fig. 3.4(c,d).

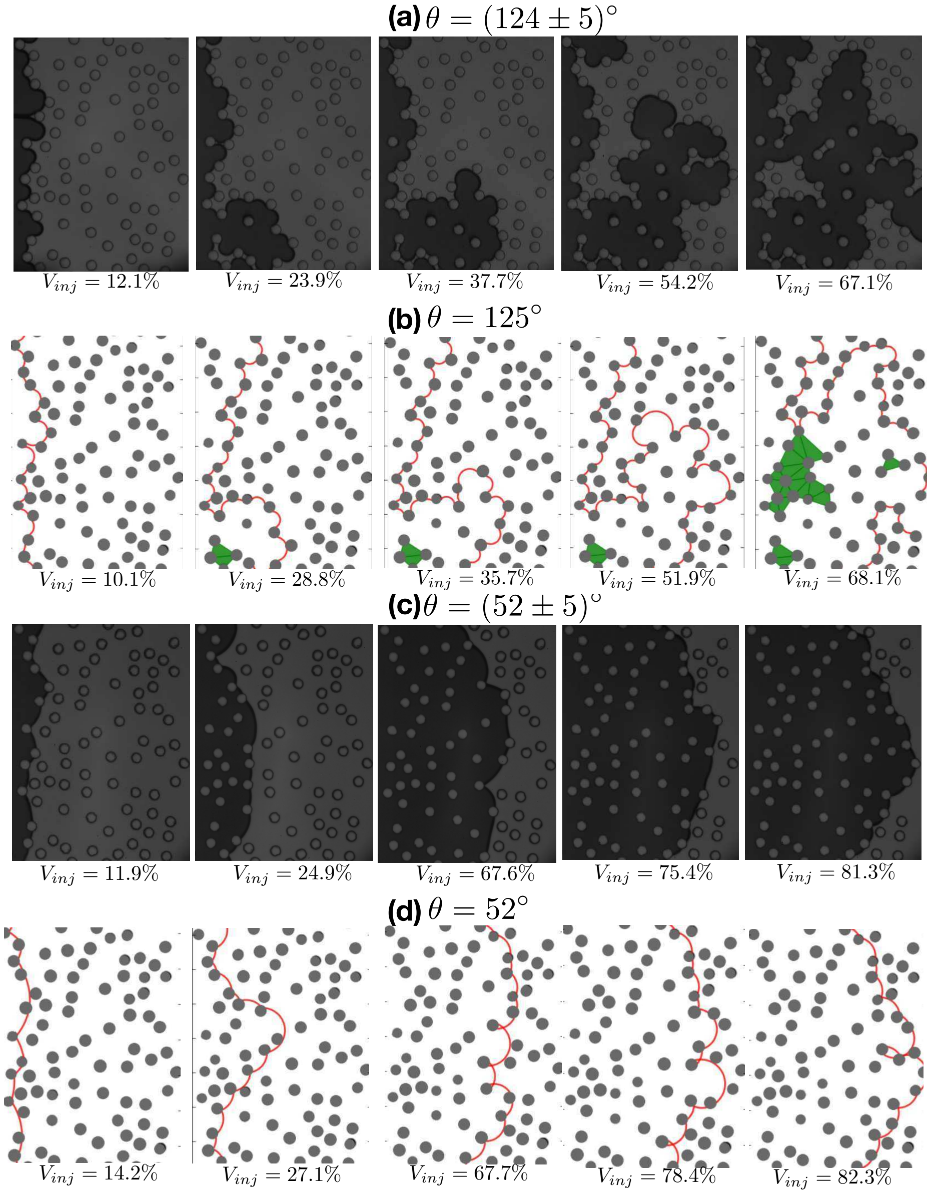

Figure 3.4: Results for different steps of the injected volume V_{inj} during the two-phase fluid displacement. (a,c): Fluid distribution in a microfluidic cell at high ($\theta_{\mathrm{a}} = 125^\circ$) and low ($\theta_{\mathrm{a}} = 54^\circ$) advancing contact angles. Adapted with permission from Jung et al. [Jung et al., 2016], copyright American Physical Society. (b,d): Interface configuration obtained with the present implementation of the CR modelfor comparable contact angles as in the experiments shown in (a) and (c), respectively. The interface between defending and invading phase in (b) and (d)) is shown in red while green triangles highlight the regions of trapped defending fluid.

However, the fingering invasion pattern observed for high advancing contact angle in Fig. 3.4(a,b) is the result of bursts dominating over touch and coalescence events.

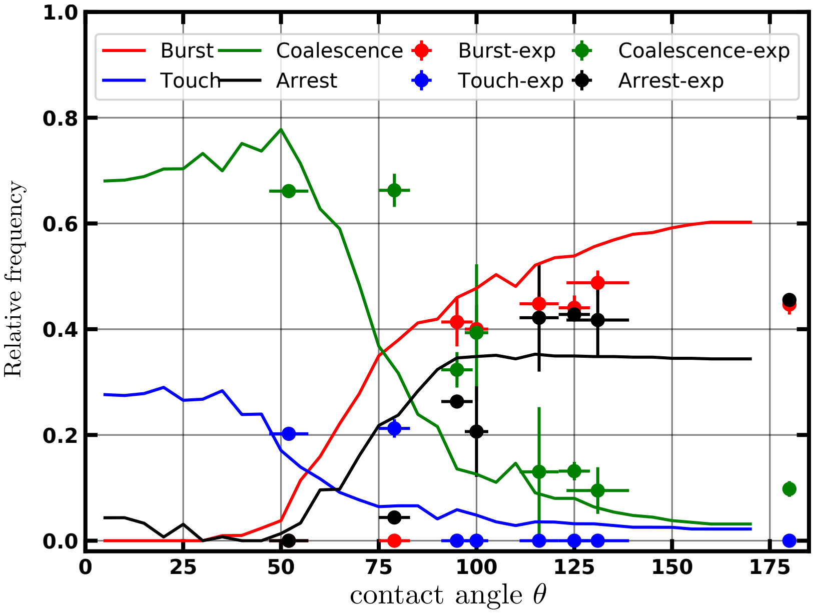

Figure 3.5: Event frequency against different advancing contact angle of the invading liquid. The solid line indicates the results from the simulation, whereas data points represents the experimental results from Jung et al. [Jung et al., 2016].

For the particular density of circular posts chosen in the experiments in Ref. [Jung et al., 2016], we could not find a range of advancing contact angles where touches are the dominating modes of interface advance, cf. also the data shown in Fig. 3.5. It has been found by Cieplak and Robbins in Ref. [Cieplak and Robbins, 1990] that touch events may also dominate over burst and coalescence events in a triangular lattice of disks with porosity $\phi = 0.67$ in a narrow range of contact angles $\theta \approx 60°$. In the following, we will employ our implementation of the CR interface invasion algorithm in combination with analytical considerations to determine the factors that determines the statistics of pore-scale events and, thus, give rise to a touch dominated regime. Moreover, we will answer the question what happens to the global displacement pattern if we add wetting heterogeneity to the disks, what are the dominating pore-scale event, and how does the global invasion pattern change correspondingly.

After validating the simulation with the experiments, we firstly investigate when the touch event dominates over other pore-scale events. Besides the burst and coalescence events, touches are also important in controlling the fluid invasion pattern and have been ignored by such as the work of Motealleh et al. [Motealleh et al., 2010]. A potential influence of touch events on the final displacement patters in disk arrays with low porosity has already been noticed in the work of Cieplak et al. [Cieplak and Robbins, 1990]. We start from the competition between different events in an ideal pore.

3.2.1 Pore-scale event in an ideal pore

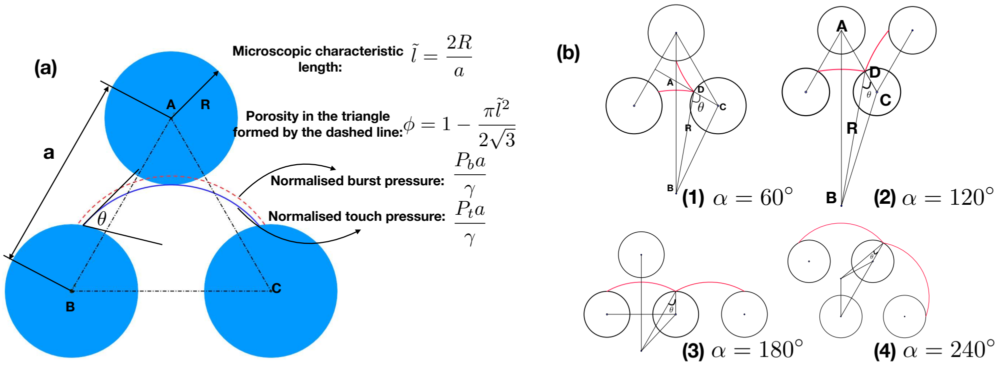

Figure 3.6: (a) The generalized three disks with same radius and same distance between disk centers. The blue meniscus indicates the meniscus when the touch event happens (R_t) and the red dashed line is the burst meniscus (R_b). The triangle formed by the disk centers is the representative element for porosity calculation. (b) Illustration for the positions of overlap event for different interfacial angles. The red circular arcs represent the menisci.

In order to study the competition between three different local instabilities, we will first consider a regular pore formed by three disks of identical radius forming an isosceles triangle. The sketch in Fig. 3.6(a) illustrates the relationship between the porosity ϕ and dimensionless microscopic characteristic length $\tilde{\ell} = \frac{d}{a}$ (a is the spacing, d is the diameter of the disks) within the triangle formed by the three disk center as follows:

$$\phi = 1 - \frac{\pi\tilde{\ell}^2}{2\sqrt{3}} \,. \tag{3.12}$$

A line fraction $\tilde{l} = 1$ corresponds to the densest packs of circular disks with an area fraction (or packing fraction) $\phi = \frac{\pi\sqrt{3}}{6} \approx 0.907$ [Fejes, 1942]. Apart from the burst and touch event, overlap events are classified into four different types based on the interfacial angles as displayed in Fig. 3.6(b). The definition of interfacial angles with $\alpha = n \times 60°$ is according to the work of Cieplak et al. [Cieplak and Robbins, 1990].

3.2.2 Critical capillary pressure for different events

After defining various events in an ideal pore, we continue to calculate the critical capillary pressure for different wetting properties and characteristic lengths. By varying porosity (ϕ) and characteristic length (L), we plot Fig. 3.7. In Fig. 3.7(a), we notice that, there is always a capillary pressure for the burst event for various contact angles. For the rest events in Fig. 3.7(b,c,d,e,f), each curve is not covering the whole range of contact angles. This is in accordance with the analysis in obtaining Eq.C.13, where we show that 2D burst event always exists for any combination of contact angles and

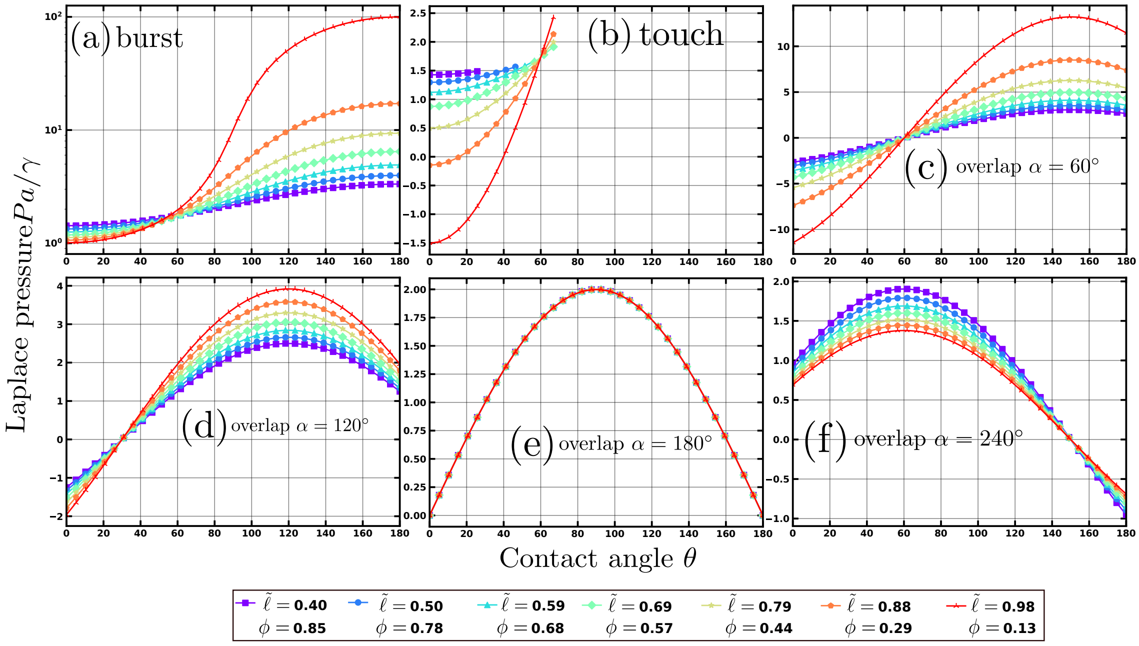

Figure 3.7: Critical dimensionless Laplace pressure against contact angle of the disks. In these plots, ϕ is the porosity of the packing and $\tilde{\ell}$ represents the characteristic length. (a) Burst event (Eq.A.1); (b) Touch event (Eq.A.6); (c,d,e,f) Overlap ($\alpha = 60°, 120°, 180°, 240°$) (Eq.A.12, Eq.A.13, Eq.A.14 and Eq.A.15). When $\theta > 90°$, the coalescence event belongs to Fig.3.3(b).

disk radii. In addition, when the porosity is decreasing, the corresponding pressure for burst event is increasing only when $\theta_a \gtrsim 50$. When $\theta_a \lesssim 50$, the trend is reverse. The similar phenomenon is also shown for touch event and overlap event ($\alpha = 120°$). But the critical contact angle to reverse the trend is different for different events. For touch event in Fig. 3.7(b), the critical angle to allow a touch event is increasing as the porosity is decreased, which indicates that for a dilute packing, it becomes harder to incur a touch event. In addition, touch events can happen with a negative Laplace pressure, which is different from burst event.

3.2.3 Phase diagrams for different pore-scale events in an ideal pore

On top of the critical capillary pressure for individual pore-scale event, we derive phase diagrams to illustrate the competition between different pore-scale events in randomised triangular disk packs of homogeneous wettability. But before we discuss the results of the invasion algorithm according to the CR model, it is instructive to study the competition between different pore-scale events in an uniform triangular lattice. Here, we can make use of the closed form expression for the Laplace pressure at a burst touch or coalescence events. Whenever the Laplace pressure P_b of a burst event is lower than the Laplace pressure of a touch event, P_t, and coalescence event, P_c, a stable meniscus will undergo a burst event during a rise of the pressure difference P between the invading and defending fluid. If P_t is smaller than P_b and P_c, the meniscus undergoes a touch instability while, if P_c is smaller than P_b and P_t, a coalescence instability precludes the burst and touch instability.

Coalescence events can be distinguished based on the relative orientation α of the neighboring menisci involved in the instability. Figure 3.8 (a-c) illustrates all three meniscus configurations leading to potential coalescence events in a triangular regular lattice. The fourth coalescence at $\alpha = 240°$ cannot be observed in an ideal triangular lattice due to steric hindrance.

The meniscus instability with the lowest Laplace pressure for a given solid line fraction $\tilde{\ell}$ of the discs and contact angle θ of the invading fluid is illustrated Fig. 3.8. At high contact angles and low solid line fractions, the burst pressure P_b is smaller than the pressure P_t of a touch event.

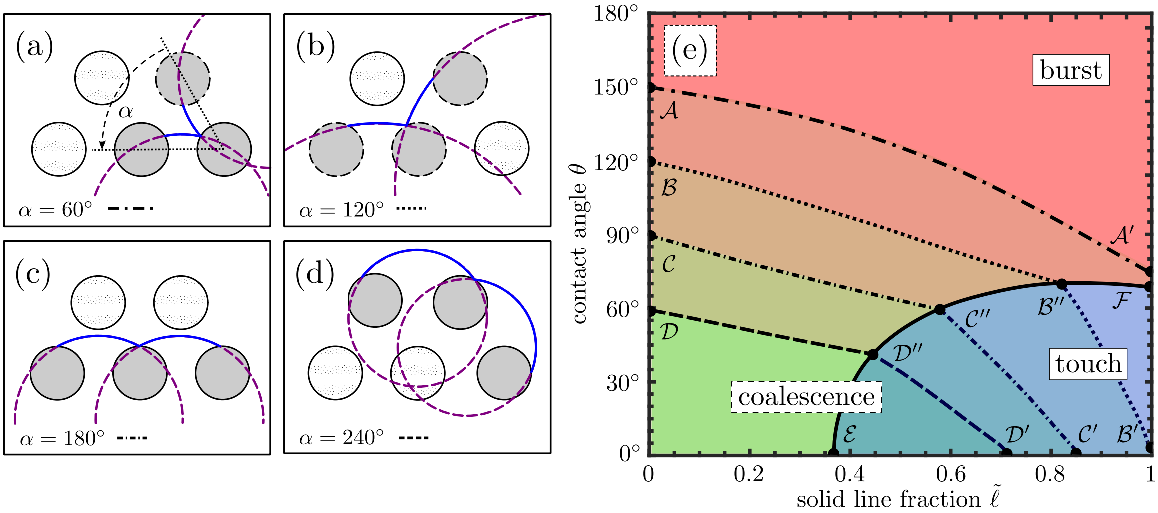

Figure 3.8: Illustration of coalescence events in a regular triangular lattice at different interfacial angles ϕ. (a) $\phi = 60°$, (b) $\phi = 120°$, (c) $\phi = 180°$, (d) $\phi = 240°$. Phase diagrams for different pore-scale events under various contact angles θ and characteristic length $\tilde{\ell}$.

- **Touch and burst:** Burst and touch events are non-cooperative, and it is natural to plot them together for comparison. As in Fig.3.8(b), we plot the phase diagram indicating the competition between burst and touch events. When $\tilde{l}$ is small, the packing is sparse. Burst event always dominates over touch event, which indicates the limitation of current microfluidic experiments [Jung et al., 2016; Holtzman, 2016; Panizza et al., 2018]. In microfluidic experiments, the distance between the pillars could not be too small. For example, in the work of Jung et al. [Jung et al., 2016], the packing density is around 15%. So in Fig.3.8(d), it corresponds to $\tilde{l} = 0.4$.

- **Touch, burst, overlap-60°, 120°, 180° and 240°:** As in Fig.3.8(c), we plot the preceding event for each combination of $\tilde{l}$ and θ based on the normalized pressure $\frac{Pa}{\gamma}$ and generate the corresponding phase diagram. We see that there are only two types of instabilities. For high contact angle, burst events dominate. For low contact angle, overlap events inside the pore dominate. As we increase $\tilde{l}$ (decrease porosity), the contact angle for the transition from overlap dominating invasion mode to burst dominating invasion mode is reduced. That means the cross-talk between neighboring menisci is undermined. But we should point out that, overlap events inside the pore is not as easy to happen as the other events. We need to have at the same time, two menisci inside the pore to trigger the instability. As in the work of Cieplak et al. [Cieplak and Robbins, 1990], overlap-60° is described as the overlap at the most acute angle and this situation is negligible. In addition, in [Holtzman and Segre, 2015], only the overlap-120° and overlap-180° are considered to define the competition between burst events and overlap events. As a result, we exclude this type of overlap-60° and plot Fig.3.8(d).

- **Touch, burst, overlap-120°, 180° and 240°:** As in Fig.3.8(d), we plot the event for each combination of $\tilde{l}$ and θ and generate the corresponding phase diagram. It is easy to see that touch events only dominate when we have relatively large $\tilde{l}$, which is larger than 0.8, and low θ, which is smaller than 70°. It is worth mentioning that in [Jung et al., 2016], the packing density is 15%. So in Fig.3.8(d), it corresponds to $\tilde{l} = 0.4$. If the disks are monodisperse, we are not able to see any touch dominating invasion pattern. As in the current simulation, we only have two types of radii and they are move randomly. The hypothesis is that current way of creating disorder is not going to destroy the major picture in Fig.3.8(d).

- **Touch, burst, overlap- 180° and 240°:** As in Fig.3.8(e), when only overlap-180° is considered, the touch region is larger compared with Fig.3.8(d).

- **Touch, burst and overlap- 240°:** As in Fig.3.8(e), when only overlap-240° is considered. Again the touch region is larger compared with Fig.3.8(e).

Fig.3.8(d) indicates the most representative case for the homogeneous wet disk packing with triangular lattice as shown in Holtzman et al. [Holtzman and Segre, 2015]. And the idea 2D pore has already indicates the existence of touch event dominating regime. In order to further investigate the competition between different events, we perform simulation on a relative large packing.

The ideal 2D pore has already indicates the existence of touch event dominated regime. In order to further investigate the competition between different events, we perform simulations on a relative large packing.

3.2.4 Events statistics in a large packing

Homogeneous wet

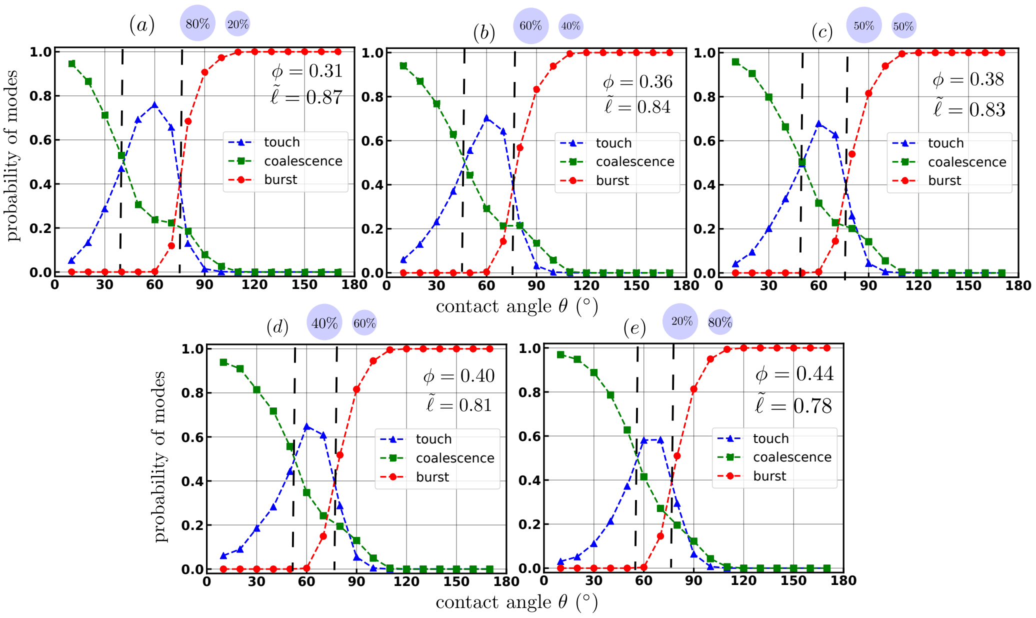

Figure 3.9: Event distribution for homogeneous wet disk packing.

As shown in Fig.3.9, we count the event statistics for a 100×100 packing. By varying the ratio between large and small disks, we see that there is a decrease region for touch event dominating region, where the porosity is increased. The result is in accordance with the trend shown in Fig.3.8. To be more specific, in Fig.3.8, we notice that only when the packing density is higher enough, we could identify a phase where touch event is dominating. This result indicates an invasion process which has been ignored by the majority of the literature [Motealleh et al., 2010; Hu et al., 2019]. For example, the phase diagram in the work of Hu et al. [Hu et al., 2019], described that the cross-over zone between capillary fingering and compact displacement expands as the disorder of the porous media increases and the phase diagram is drawn by considering the competition between the burst and overlap event. But if the packing is dense enough, the cross-over zone will be altered correspondingly. Similar analysis to quantify the competition between burst and overlap events are also available in the work of Holtzman et al. [Holtzman and Segre, 2015], where touch event never plays an important role in controlling the invasion pattern. In this sense, the geometry of the porous region indicates its strong influence on the fluid invasion process.

Heterogeneous wet

Similar simulation process is performed by varying the wetting properties of individual disks based on the packing employed in the homogeneous wet case. As shown in Fig.3.10, when we mix disk with different wettability, touch events and burst events

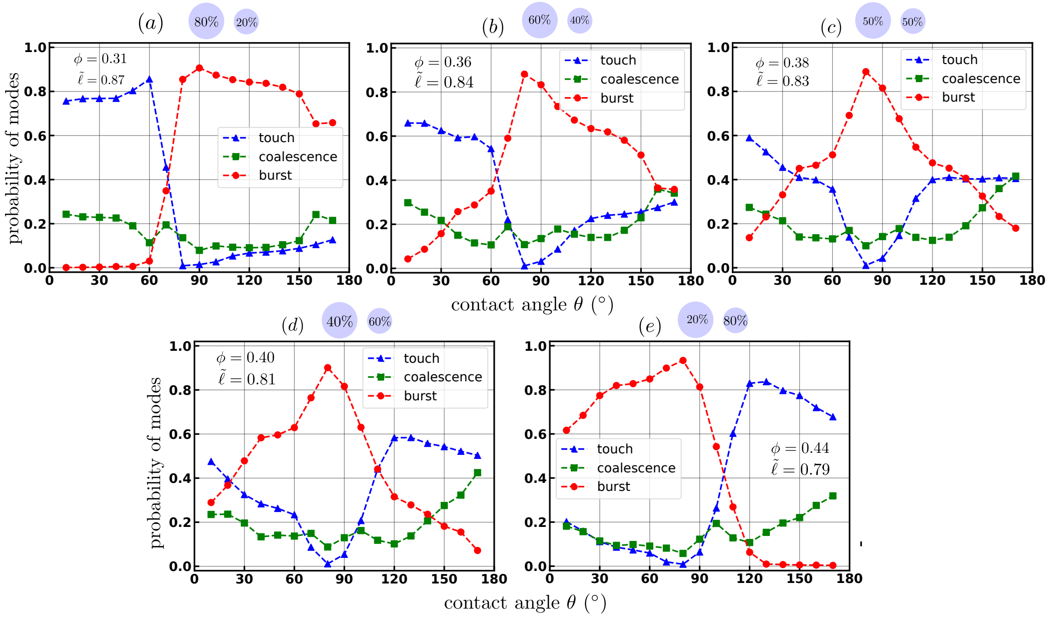

Figure 3.10: Event distribution for heterogeneous wet disk packing. The contact angle (θ) in the X-axis represents the large disk contact angle. The contact angle of the small disks is $\pi - \theta$.

become dominating. This result indicates the potential strong influence of touch events for heterogeneous wet disks packing. As a result, any phase digram drawn without consideration of the touch event becomes meaningless.

The simulation results in 2D inform us the existence of the touch dominated regime when the packing density is relatively high. If we use beads with same radii, the pore space is relative large and the variation of pore size is small. And there is no way to shrink or expand the beads as in two dimensional disks system. One way to approximate the ”shrinking” process in 2d for the 3d packing is to change the shape of the grains in order to achieve a higher packing density. It still takes efforts to investigate the influence of the packing density on the transition of invasion pattern from capillary fingering domain to compact domain in 3D. In the next chapter, we show that the critical angle of around 87° for touch event is taken over by the burst event based on extending the C&R model to 3D, which is in good accordance with the experimental results [Singh et al., 2017b], and it is a good starting point for drawing a similar phase diagram as we do in 2D. It is also obvious, in 3D, a large portion of oil is still connected through liquid bridges, dimers and trimers [Scheel et al., 2008]. However when the liquid is trapped in 2D, they will be trapped permanently. But in 3D, these liquid will continue to be drained out. A natural question comes directly out of the lesson we learn in 2D is that if we have a packing in 3D and the packing density is increased gradually, could we notice similar fingering structure for some contact angle below 90°? Apart from that, when the heterogeneity of the wettability is taken into consideration, identification of the dominating pore-scale invasion mode remains elusive. These questions are not solved by current thesis but they are meaningful to further understand the underlying physics to describe the connection between the pore-scale invasion and the global invasion pattern.

3.2.5 Suppressed capillary fingering by altering porosity

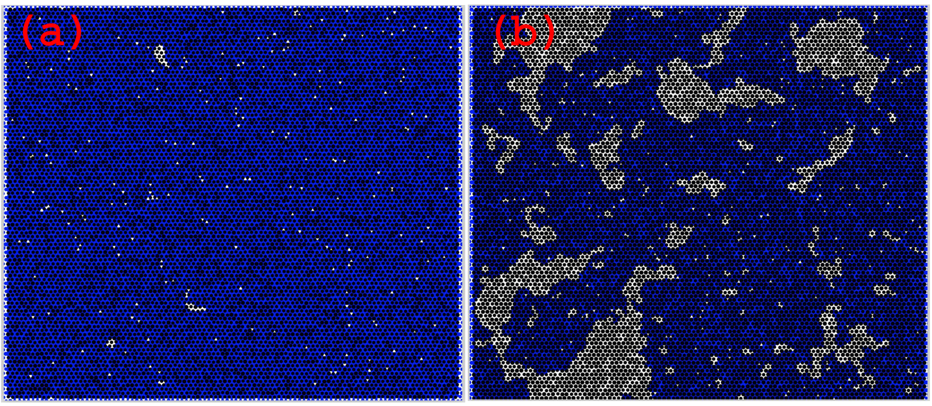

Figure 3.11: (a) 20% large disks, 80 % small disks, (contact angle of 50°, porosity:0.44); (b) 80% large disks, 20% small disks, (contact angle of 50°, porosity:0.31).

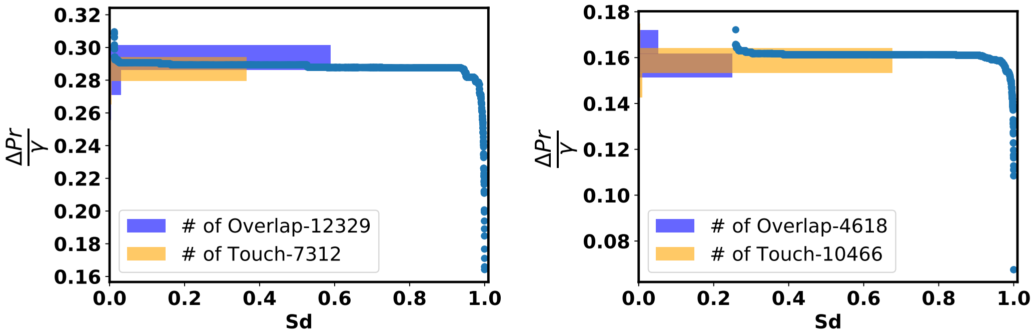

Figure 3.12: left: 20% large disks, 80 % small disks, (contact angle of 50°, porosity: 0.44); right: 80% large disks, 20% small disks, , (contact angle of 50°, porosity: 0.31).

Recent publication in Rabbani et al. and Lu et al. [Rabbani et al., 2018; Lu et al., 2019], on a design of a porous medium in the form of an ordered structure to suppress or trigger viscous fingering or capillary without modifying fluid properties or wettability, inspires us to explore how the touching dominating regime is going to influence the fingering structure in the two-phase invasion process. As CR model mainly considers the influence of capillary pressure, we find that even with disk packing of two different type of radii, it is possible to suppress the capillary fingering just by changing the ratio between large disks and small disks. As in Fig.3.11 and Fig.3.13, we compare the final stage of the imbibition for the advancing contact angle of 50° and 40° and they are visually different. We further plot the event distribution and pressure saturation curve in Fig.3.12 and Fig.3.14. They clearly show that the dominating event changes from overlap event to touch event. To be more specific, when we keep the wetting property of disks unchanged, we are able to trigger the invasion mode with different dominating events by changing the geometry of porous media when the contact angle is relatively low.

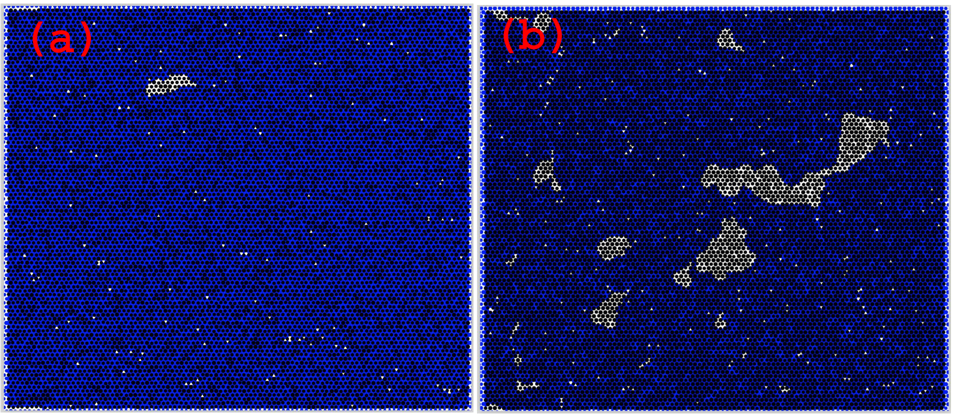

Figure 3.13: (a) 20% large disks, 80 % small disks, (contact angle of 40°, porosity: 0.44); (b) 80% large disks, 20% small disks, (contact angle of 40°, porosity: 0.31).

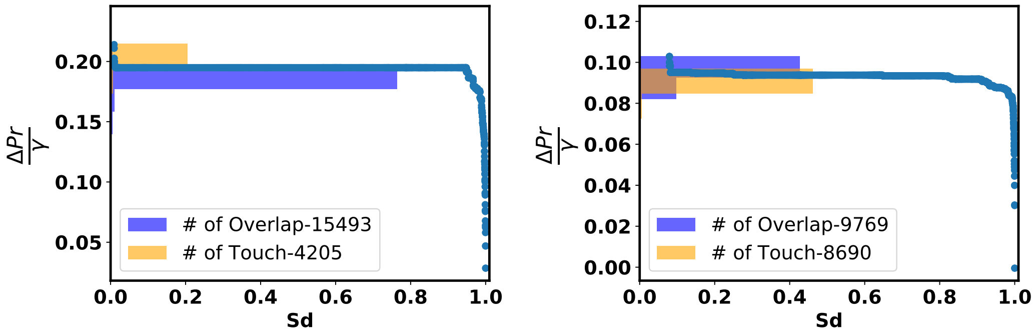

Figure 3.14: left: 20% large disks, 80 % small disks, (contact angle of 40°, porosity: 0.44); right: 80% large disks, 20% small disks, (contact angle of 40°, porosity: 0.31).

3.3 Reduced hysteresis for enhanced wetting heterogeneity

In practical application such as ground water hydrology and oil reservoir engineering, the macroscopic capillary pressure with respect to the saturation of wetting liquid is frequently employed [Bear, 2013]. And the pressure-saturation relationship plays a key role in reservoir engineering because nearly every numerical model in reservoir simulation needs the CPS curve as an input parameter [Dake, 1983]. However, employing saturation of the wetting phase to build a link between the mass fraction of the fluid and capillary pressure naturally ignores the invasion pattern, which oversimplifies the invasion process during two-phase flow and it has been shown that the topology characterized by Euler number indicates a big difference between the drainage and imbibition process [Schlüter et al., 2016]. And the simplification for saturation calculation will inevitable induce hysteresis phenomenon in the pressure-saturation curve. In the work of Moosavi et al. [Moosavi et al., 2018], a series of experiments were conducted to investigate the surprisingly suppressed fluid displacement hysteresis in granular piles with enhanced wetting heterogeneity. Usually, the increased wetting heterogeneity used to enhance the hysteresis [Moosavi et al., 2018]. In this section, we try to give a potential explanation based on the extended Cieplak and Robbins' model and the results contribute a new perspective to the source of the hysteresis in the CPS curve.

3.3.1 Back-forth pressure barrier in a single throat

In this subsection, the pressure difference of a single throat formed by two disks with different wettability is discussed in detail. In order to further analyze how the radii of disks, wettability and gap opening influence the pressure barrier for a single throat, we made some efforts to derive an analytical equation for quantification. Critical burst radius of curvature r_c^* is given by C.13 and critical burst pressure P^* for two-disk system could be given as follows:

$$P^* = \frac{\gamma}{r_c^*} \tag{3.13}$$

We consider a moving meniscus in a single throat like Fig.C.1(a) and suppose that the meniscus is driven by two immiscible liquid. Liquid A takes contact angles of $\theta_1(°)$ and $\theta_2(°)$ with respect to the left disk and the right disk, so liquid B has contact angles of $\pi - \theta_1(°)$ and $\pi - \theta_2(°)$ for each disk. In other words, the disks are heterogeneous wetted (i.e. $\theta_1 \neq \theta_2$) by liquids. We define the normalized pressure difference between advancing burst meniscus and receding burst meniscus as the pressure barrier for a single throat to finish a "drainage-imbibition" cycle, which is detailed as follows:

$$\begin{aligned}
\Delta P_c(\theta_1, \theta_2) &= \Big| P_{cmax} - P_{cmin} \Big| \frac{r_m}{\gamma} = \Big| P^*(\theta_1, \theta_2) + P^*(\pi - \theta_1, \pi - \theta_2) \Big| \frac{r_1 + r_2}{2\gamma} \\
&= \frac{2d(r_1 + r_2)}{(-d^2 + r_1^2 + r_2^2)^2 - 4r_1^2 r_2^2} \sqrt{\alpha_2} \\
&= K_1 \sqrt{\alpha_2}
\end{aligned} \tag{3.14}$$

where, α_2 is the same in Eq.C.17, $K_1 = \frac{2(r_1+r_2)d}{-4r_1^2 r_2^2 + (-d^2 + r_1^2 + r_2^2)^2} > 0$, $K_2 = d^2(d^2 - 2r_1^2 - 2r_2^2) + (r_1^2 - r_2^2)^2 > 0$.

Here we would like to know the state of the point $\Delta P_c(\theta_1 = \frac{\pi}{2}, \theta_2 = \frac{\pi}{2})$:

$$\frac{\partial \Delta P_c}{\partial \theta_1}\Big|_{\theta_1=\frac{\pi}{2},\theta_2=\frac{\pi}{2}} = -K_1 \frac{4r_1^2 r_2^2 \cos\theta_1 \sin\theta_1 - 2r_1 r_2 \cos\theta_2 \sin\theta_1(-d^2 + r_1^2 + r_2^2)}{\sqrt{\alpha_2}} = 0$$

$$\frac{\partial \Delta P_c}{\partial \theta_2}\Big|_{\theta_1=\frac{\pi}{2},\theta_2=\frac{\pi}{2}} = -K_1 \frac{4r_1^2 r_2^2 \cos\theta_2 \sin\theta_2 - 2r_1 r_2 \cos\theta_1 \sin\theta_2(-d^2 + r_1^2 + r_2^2)}{\sqrt{\alpha_2}} = 0$$

$$\left(\frac{\partial^2 \Delta P_c}{\partial^2 \theta_1}\frac{\partial^2 \Delta P_c}{\partial^2 \theta_2} - [\frac{\partial^2 \Delta P_c}{\partial \theta_1 \partial \theta_2}]^2\right)\Big|_{\theta_1=\frac{\pi}{2},\theta_2=\frac{\pi}{2}} = -\frac{4K_1^2 r_1^2 r_2^2[d^2 - (r_1 + r_2)^2]}{K_2^2} < 0$$

(3.15)

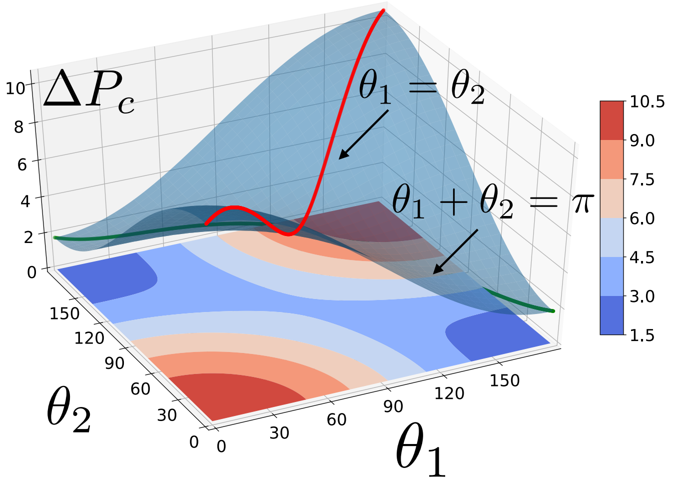

Figure 3.15: ΔP_c as a function of θ_1 and θ_2, s=0.1$(r_1 + r_2)$,$r_1 = r_2$.

Based on Eq.3.15, the point of $(\theta_1 = \frac{\pi}{2}, \theta_2 = \frac{\pi}{2})$ is a saddle point for any combination of geometry and surface property for two disks. We plot the value of the $\Delta P_c(\theta_1, \theta_2)$ against different combination of contact angle as in Fig.3.15. The graph has shown us several useful results. For disk pair with homogeneous wettability, we have $\theta_1 = \theta_2$, so:

$$\frac{\partial \Delta P_c}{\partial \theta} = \sin 2\theta \frac{K_1 8 r_1 r_2 [d^2 - (r_1 - r_2)^2]}{4\sqrt{\alpha_2}}, \quad (\theta = \theta_1 = \theta_2) \tag{3.16}$$

In Fig.3.15, the red curve in the curved surface indicates the pressure difference between the forward and backward invasion for homogeneous wetting disk pair, i.e. $\theta_1 = \theta_2$. Based on Eq.3.16, when the contact angles of the two disks are both 90°, $\Delta P_c(\theta_1, \theta_2)$ reaches its minimum compared with all the other combinations of homogeneous wetting disk pair.

If $\theta_1 + \theta_2 = \pi$, the pressure difference is given as:

$$\frac{\partial \Delta P_c}{\partial \theta_{1,2}} = \sin 2\theta_{1,2} \frac{K_1 8 r_1 r_2 [-d^2 + (r_1 + r_2)^2]}{4\sqrt{\alpha_2}} \tag{3.17}$$

In Fig.3.15, the green curve in the plane is a result of $\Delta P_c(\theta_1, \theta_2)$ for all combinations of $\theta_1 + \theta_2 = \pi$. When we increase the difference between two contact angles of disks while holding the sum of them as a constant, $\Delta P_c(\theta_1, \theta_2)$ is decreasing. According to Eq.3.17, $\Delta P_c(\theta_1 = 90°, \theta_2 = 90°)$ is the maximum.

As it is shown above, the distribution of $\Delta P_c(\theta_1, \theta_2)$ for two circular disks with different combination of contact angle will have the similar shape as in Fig.3.15. $\Delta P_c(\theta_1, \theta_2)$ indicates the maximum pressure barrier the liquid need to overcome when one type of fluid need to displace the other fluid and later it is displaced by the other fluid. If the propagation of the interface in capillarity-dominated regime is only governed by invasion percolation, Fig.3.15 could be employed to predict the hysteresis loop opening. However, as cooperative effects like the overlap event and the non-cooperative touch event also make a contribution to the local menisci instabilities, Fig.3.15 actually provides an upper bound for the hysteresis loop opening. The reason is that touch or overlap events lead to the occupation of pores before the corresponding menisci reach their critical pressure for burst events, so that the global contribution from the cooperative events will continue to reduce the pressure barrier.

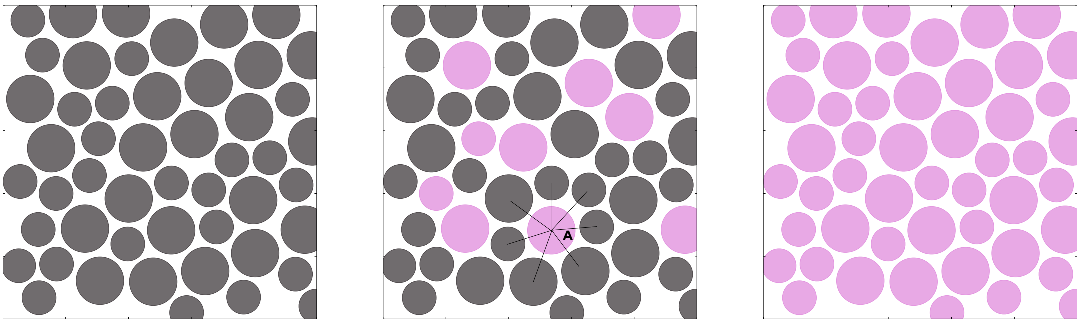

(a) (b) (c)

Figure 3.16: (a) A sketch of 50 disks with the same wettability(θ_1); (b)10 of them randomly chose to be with another wettability(θ_2);(c)A sketch of 50 disks with the same wettability(θ_2). ($\theta_1 + \theta_2 = \pi$)

Now we consider the scenario in Fig.3.16. Supposed that during the fluid invasion process, there is no liquid trappment, which excludes the topological influences [Schlüter et al., 2016]. From (a) to (b), the pressure barrier related to disk A (Fig.3.16b) will be reduced due to the change of wettability of disk A. As we increase the proportion of disks with contact angle of θ_2, more and more throats formed by disks different wettablity will emerge. However, from (b) to (c), we enter into system of disks with same wettability, thus the global ΔP_c will increase again. In Fig.3.16, we do not consider the dynamic capillarity, fluid topological and contact line pinning. But the hysteresis is inevitable due to the change of wettability of the disks. In addition, there exist arguments in the differences between disk packings in 2D and sphere packings in 3D, including the interconnections and the residual to nonwetting phase [Cieplak and Robbins, 1990; Jerauld and Salter, 1990; Sahimi, 2011]. However, the recent research of Singh et al. [Singh et al., 2017b] reveals that there exists a close connection between a numerical model by Cieplak and Robbins and random piles of spherical beads when it comes to the progression of invading interface. The similarity between the simulation results of disk packings and experimental results of sphere packings indicates that some of the mechanisms controlling the wettability characteristics found in disk packings might be also applicable to sphere packings.

3.3.2 Pressure plateau difference in homogeneous and heterogeneous wetting packing

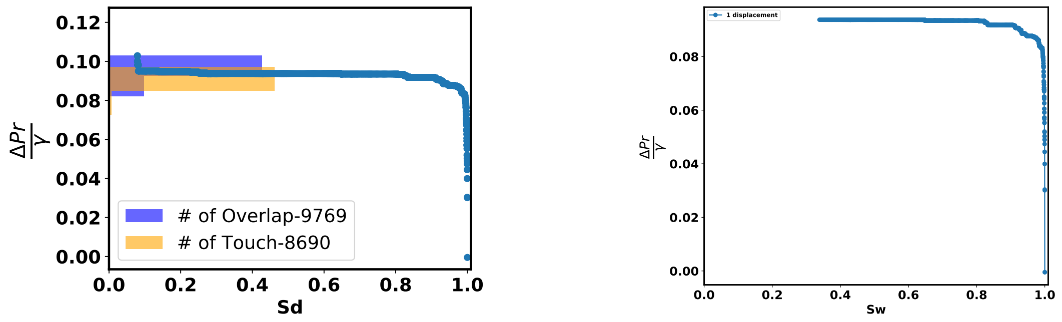

(a) Full range **(b)** Breakthrough

Figure 3.17: 100×100 disk packing with 20 % of small disks. Contact angle of the disks are 40°.

Here we investigate the pressure plateau when the invading liquid percolate the outlet. In Fig.3.17, we show how to determine the pressure plateau from one displacement. In Fig.3.17b, we record the pressure saturation curve for the time of breakthrough, in which the injected fluid first reaches the outlet and represents the percolation threshold of the nonwetting phase [Blunt et al., 1992]. For Fig.3.18a, we see that there is no big difference for the normalized pressure plateau as we change the ratio of large and small disks. In Fig.3.18, we show that by changing the contact angle of two different type of disks, we have a significant change in terms of pressure plateau. As the majority of the disks are large disks and the X-axis represents the contact angle of the large disks, the higher the contact angle of large disks, the higher the plateau for the pressure.

3.4 Quantification of the invasion pattern

In Fig.3.20, the influence of wettability on the evolution of interface can already be identified visually. When the contact angle of the invading liquid is small, in this case it 30°, compact front is developed and for high contact angle, the front ramifies. In the work of Cieplak et al. [Cieplak and Robbins, 1988], finger width is considered as a reliable statistical measure of the growth of interface, which is not dependent on particular realisation of the porous media. As the shape of the liquid is not

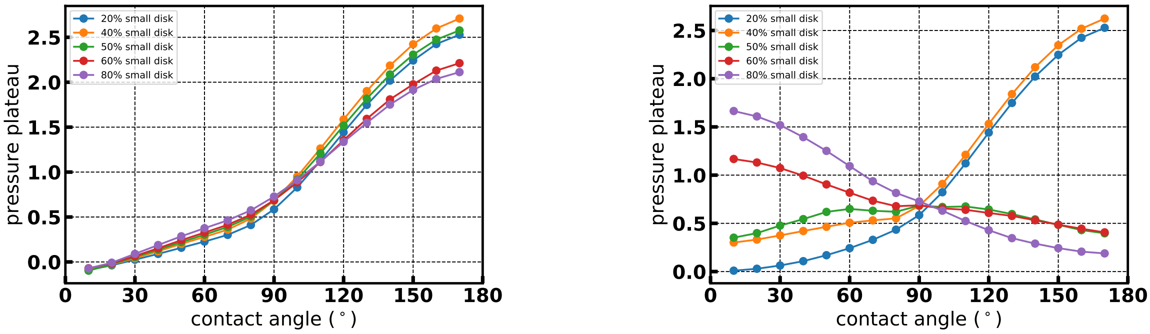

(a) Homogeneous wet **(b)** Heterogeneous wet

Figure 3.18: Pressure plateau for homogeneous and heterogeneous wet disk packing.

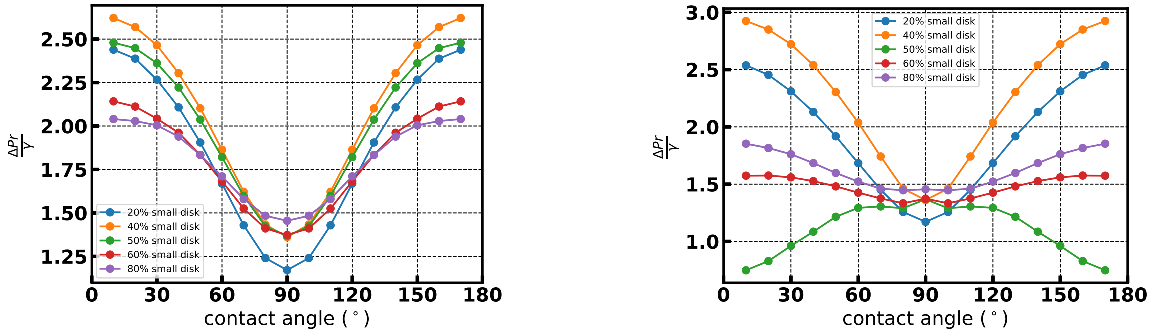

(a) Homogeneous wet **(b)** Heterogeneous wet

Figure 3.19: Pressure plateau difference for homogeneous and heterogeneous wet disk packing.

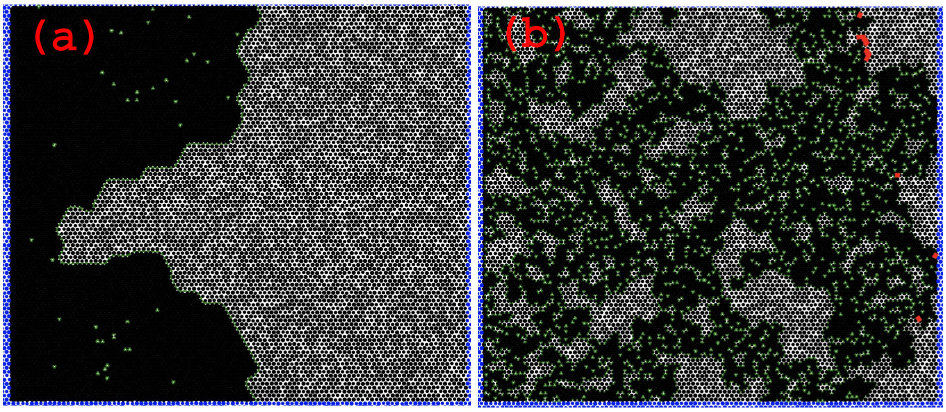

Figure 3.20: (a) 100 × 100 packing with the invading liquid having contact angle 30°; (b) 100 × 100 packing with the invading liquid having contact angle 150°.(The packing here is used in obtaining the results in Fig.3.9)

regular. We directly count the triangles occupied by the invading or defending liquid. To compute the mean finger width we first draw a vertical line passing through the centres of the triangles and record the sequence of triangles that are occupied by either

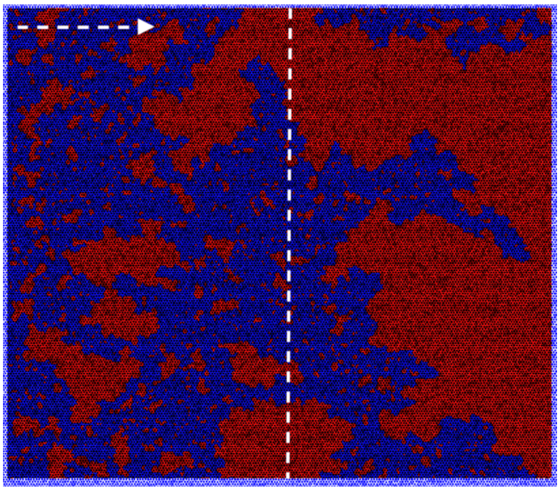

Figure 3.21: 2D-simulation of an immiscible displacement process in a randomized array of (200 x 200) disks. The blue area represents the wetting invading fluid with an advancing contact angle of 70° with respect to the disks. The defending fluid is shown in red, the disk array is shown in black. The white dashed line indicates a vertical cut to measure the finger width. Initially, the disk array is completely filled with the (red) defending fluid. The invading fluid is injected from the left boundary (the white arrow indicates the direction of flow). Periodic boundary condition are applied into vertical direction.

the invading or the defending fluid, c.f. Fig.3.21. For a given sequence we determine the number of disconnected clusters of triangles occupied by the invading fluid while accounting for the periodic boundary conditions perpendicular to the direction of displacement. Finally, we compute the mean finger width as the average size of the connected clusters of the invading fluid over all vertical lines.

In Figure 3.22, we plot the mean finger width as function of the advancing contact angle for homogeneously wet disk arrays with a bi-disperse disk size-distribution with a size ratio of 1.2. For non-wetting invading fluids, the mean finger width attains values on the order of a few pores and is insensitive with respect to the exact value of the contact angle. The finger width appears to be also insensitive to the mixing ratio of large and small disks. For wetting invading fluids, however, we find a mean finger width that differs by up to two orders of magnitude as compared to finger width of invading fluids with large contact angle. In addition to homogeneously wet, bi-disperse disk arrays, we also considered the mean finger width for disks arrays with a heterogeneous wettability, c.f. the plot in Fig.3.22b. By convention, we chose the X-axis to be the contact angle with respect to the large disks. The contact angle of the invading fluid with respect to the small disks is set to the complementary contact angle $\pi - \theta$. The mean finger width of this type of fractional wet disk packing is very similar to the finger width found in homogeneously wettable disk arrays for a high contact angle. Front-like fluid invasion leading to compact domains of the invading fluid is not observed within the range of mixing ratios of large and small disks considered so far.

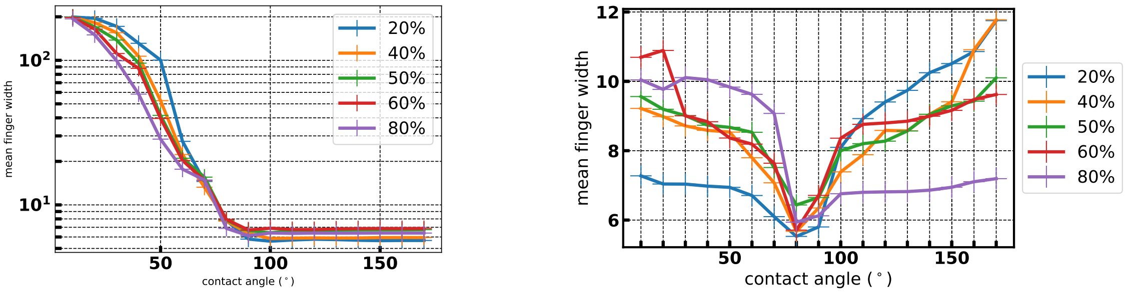

(a) (b)

Figure 3.22: Finger width for the time breakthrough. (a) mean finger width for homogeneous wettable disks; (b) mean finger width for fractional wettable disks. The legend indicates the ratio of large disks. Both of the plots indicate the 100 by 100 hexagonal packing.

In Fig.3.22, we also compute the mean finger width for fractional wet disk packing. The X axis is the contact angle θ of large disk and the corresponding contact angle of the small disks is $\pi - \theta$. As shown in the graph, the mean finger width of the fractional wet disk packing is very similar to finger width for high contact angle in homogeneous wet disk packing. And we do not see any compact domain within current mixing ratio of large and small disks.

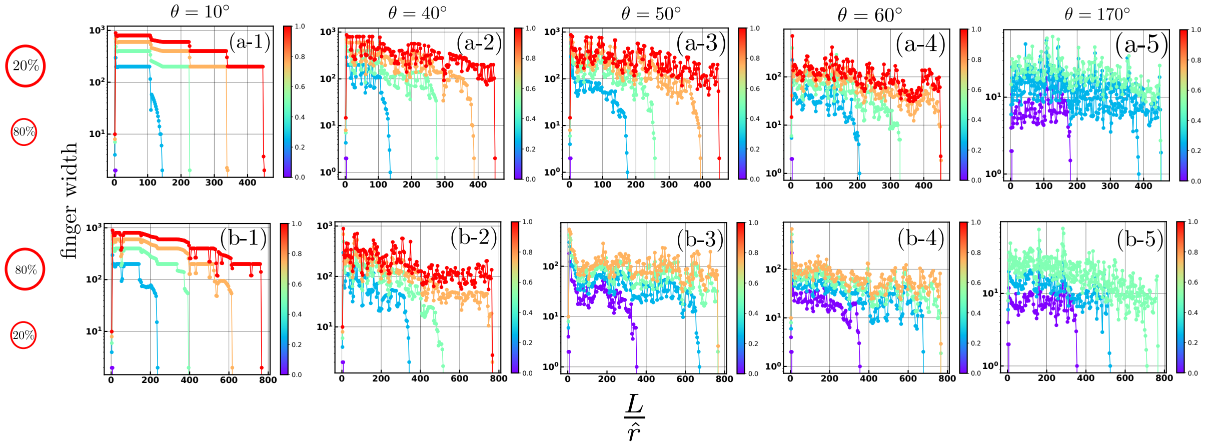

Figure 3.23: Evolution of mean finger width along the invasion direction. (a-1,2,3,4,5) represent packings with 80% small disks and 20% large disks. (b-1,2,3,4,5) indicate packings with 20% small disks and 80% large disks. Colorbar shows the saturation of the invading liquid. The X-axis is the distance from the inlet, which is normalized by the mean radius of the disks ($\hat{r}$).

At the same time, we show the evolution of mean finger width in Fig.3.23. When the contact angle is 10°, there is no strong variation for the finger width along the flow direction compared with the case when $\theta = 40°$. But the magnitude of the finger width is similar between $\theta = 10°$ and $\theta = 40°$. When the contact angle varies from 40° to 50°, we notice that Fig.3.23(b-3) has a clear decrease of finger width compared with Fig.3.23(b-2). Fig.3.23 (b-3) correspond to Fig.3.11 (b). We know that touch events are behind this change of invasion pattern. When contact angle reaches 170°, the finger width is nearly 10, which is slightly different from Fig.3.22a because Fig.3.22a calculated the finger width for the time of liquid breakthrough. The similar approach will be extended to three dimensional space in chapter 4.

3.5 C&R model in ellipse packing

Existing research works [Cieplak and Robbins, 1988; Hu et al., 2019; Primkulov et al., 2018] focus on the circular disks. In order to explore more geometry, we develop a similar C&R model in ellipse packing.

The derivation of threshold curvature radius is in the appendix F. For homogeneous wetting disks, we plot the r-t relationship in Fig.3.24. Here r represents $\frac{\gamma a}{\Delta P}$. And t indicates $\cos n$, where $\cos n$ shows the contact point for the meniscus at the ellipse. Similarly as the burst event in circular packing, there are two branches solution for a specific Laplace pressure (curvature radius). We use the same idea to identify the stable branch due to $\frac{\partial P_c}{\partial \Delta V} > 0$. In addition, there are dashed lines in Fig.3.24, which represent the time when $\partial P_c \sim 0$ and it is calculated with $t = \pm\sqrt{\frac{a^2 \cos^2 \delta}{b^2 + c^2 \cos^2 \delta}}$. After we specify the critical point, we could determine the position of the meniscus given the Laplace pressure($\sim \frac{\gamma}{r}$) by simple iteration.

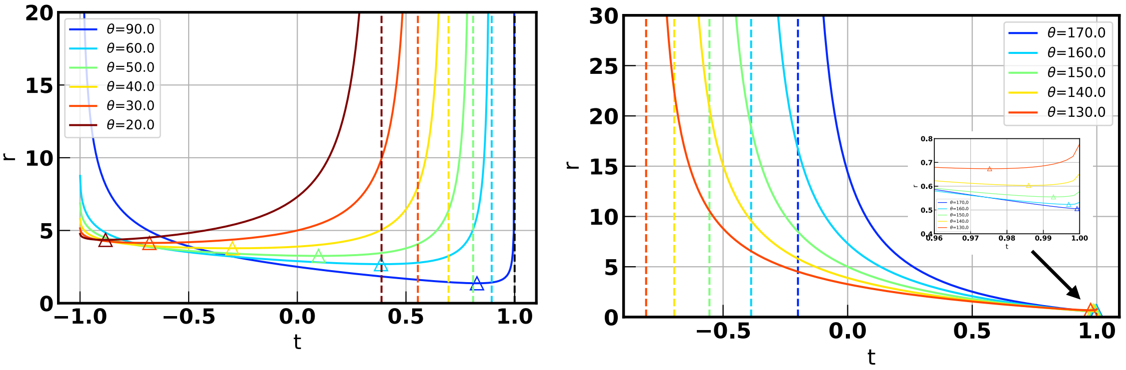

(a) (b)

Figure 3.24: r-t relationship for different contact angles. In this case, a=1, b=$\sqrt{3}$, d=5 (The definition of a,b,d is shown in Fig.F.1b.). The triangle for each line represents the minimum radius and it is indicating the burst event.

We also change the eccentricity of the ellipse as shown in Fig.3.25. In Fig.3.25a, for larger contact angles, increasing the eccentricity will increase the burst pressure when

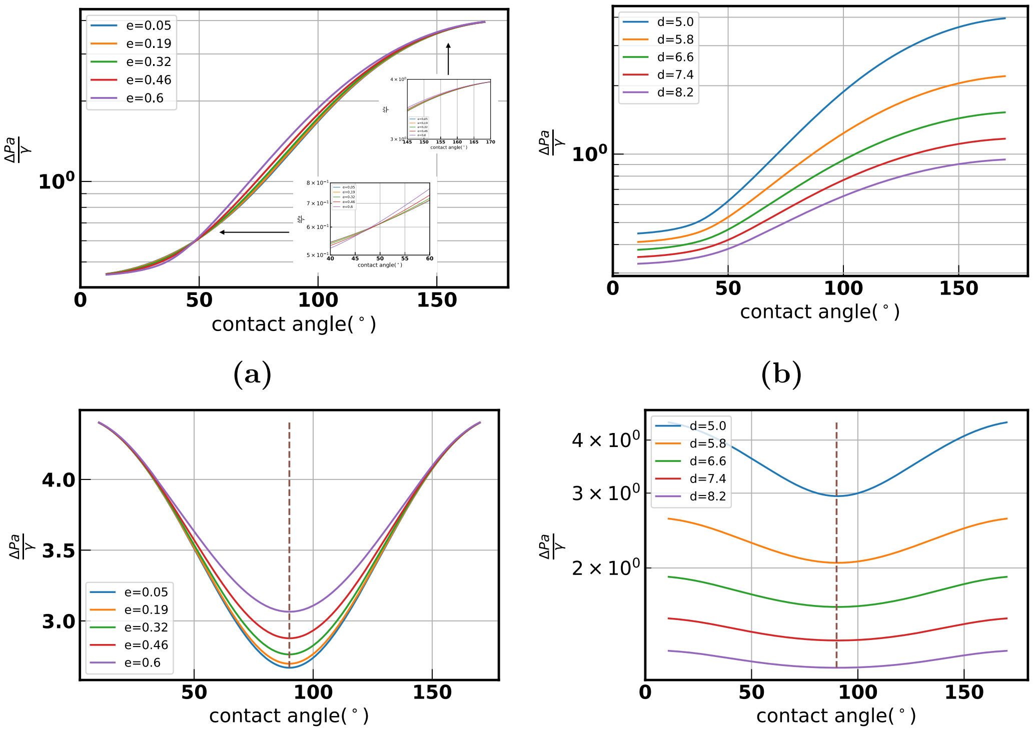

(a) (b)

(c) (d)

Figure 3.25: (a) Plot of dimensionless burst pressure with respect to different contact angles. The pressure is normalized by a. And d=5, a=2. e in the legend represents the eccentricity; (b) d in the legend represents the distance between the center of two ellipses; (c) back-forth pressure difference for different eccentricity; (d) back-forth pressure difference for different gap separation.

contact angle is controlled. When the contact angle is around 180°, the burst event will happen when the diameter of circular meniscus is the gap separation. So that all the curves will meet at the time for $\theta = 180°$. However, for low contact angle (around 46°), the trend is reversed with increasing eccentricity leading to decreased burst pressure. In Fig.3.25b, it is shown that increasing the gap separation between the ellipses, the burst pressure will reduced, which is the same as in the circular packing. We also check the pressure gap to finish a back-forth cycle for a specific contact angle. As shown in Fig.3.25c, increasing the eccentricity of the ellipse will lead to increased pressure difference to finish the back-forth cycle. And for each specific eccentricity, the trend with respect to contact angle is the same as in the circular packing.

Chapter 4

Quantification of influences of wettability on two phase fluid immiscible displacement in spherical bead packs

Wettability is an important factor that controls the fluid interface morphology during slow displacement of immiscible fluids in a permeable medium including storage of CO_2 in saline aquifers, fuel cells, oil industry and the water cycle in the rhizosphere [Sinha et al., 2007; Carminati, 2013; Singh et al., 2016]. A typical classification of the two-phase flow process is based on the wettability of fluids in the invasion processes, where drainage is employed to describe the process when the displacing fluid is the non-wetting fluid and imbibition characterizes the process of the wetting fluid displacing the non-wetting fluid. Fluid displacement as a result of imbibition or drainage leads to substantially different invasion pattern [Lenormand, 1990; Blunt, 2017]. For instance, it is shown that a compact front morphology emerges when the wetting fluid displaces a bead pack saturated with non-wetting liquid and a fingered morphology develops when the invading liquid becomes non-wetting [Singh et al., 2017b]. In order to investigate the influences of different parameters like viscosity ratio between two phases in the porous media and capillary number on the invasion pattern, a phase diagram is frequently employed [Lenormand et al., 1988; Lenormand, 1990; Yortsos et al., 1997, 1998; Medici and Allen, 2009; Mukherjee et al., 2009; Ewing and Berkowitz, 2001; Tsuji et al., 2016; Zacharoudiou et al., 2018] since the seminal work of Lenormand [Lenormand, 1985]. However as commented in the work of Homsy [Homsy, 1987], the phase diagram developed in the work of Lenormand [Lenormand, 1985] is dependent upon the wetting conditions. As a result, a reliable manner to quantify the influence of wetting conditions is meaningful to gain a better understanding with respect to the existing phase diagrams characterizing the invasion pattern.

For instance, for the cases where the contact angle of the invading fluid is 20° and 75°, they are both named as imbibition and qualitatively these two cases should indicate similar invasion pattern. However, in the simulation of two-phase immiscible fluid displacement in 2D disk arrays of Cieplak & Robbins exist a regime for contact angle of the invading liquid below 90° where touch events dominate over other local instabilities such as Haines jumps and overlaps [Cieplak and Robbins, 1990]. Naturally, it raises questions like whether the touch dominating regime exists also for a fluid invasion process in 3D porous media and how to indentify this regime. Quantification of the different displacement behaviors provides an important basis to investigate wettability dependent influences such as local instabilities on the global invasion pattern. In Singh et al., it was shown that wettability dependent interface evolution can be predicted based on a purely qausi-static consideration of local instabilities when capillary forces dominate over viscous forces [Singh et al., 2017b]. Concurrently, with the advent of tools like X-ray tomography, the fluid invasion process can be visualized in three dimensions on the scale of individual pores with rapidly increasing spatial and temporal resolution [Wildenschild and Sheppard, 2013]. This non-destructive technique provides a possibility to record the fluid morphology during the invasion process [Berg et al., 2013; Singh et al., 2017b]. However, to record the invasion process with tomography is delicate as the analysis of images are strongly influenced by the segmentation [Iassonov et al., 2009; Heiko et al., 2013]. For example, the interface areas are often difficult to identify correctly by thresholding and even the porosity obtained from segmented images, i.e. images where e.g. the grey level voxels of the pore space and of the void space are assigned to distinct phases of black or white, indicate a variation of around 13% for Berea sandstone because the segmentation is not unique and the corresponding algorithms require manual control [Sezgin and Sankur, 2004; Heiko et al., 2013]. To achieve a better characterization of the fluid invasion process under the potential influences from segmentation, we developed three methods to quantify the morphology of the invading interface from the acquired X-ray images. Before we present the proposed methods, we employ one classical method to delineate the fluid spreading patterns as a reference.

4.1 Tested data set

The data sets employed to validate the feasibility of various methods are mainly from the experimental work of Singh et al. [Singh et al., 2016]. On top of the work of Singh et al. [Singh et al., 2016], more data are segmented for a better characterization of the invasion process. In these experiments, the porous media is made of dense random piles of spheres and the advancing contact angle of the invading liquid is in well control by surface functionalization and employing different combinations of liquids. For example, when the glass beads are coated with a self-assembled monolayer of octadecyl-trichlorosilane (OTS) molecules, the contact angle of the invading water can achieve $(165 \pm 15)°$ when the defending liquid is dodecane [Lessel et al., 2015; Singh et al., 2017b]. The fluid invasion experiments were implemented within cylindrical polycarbonate cells with 58 mm height and 8 mm inner diameter [Singh et al., 2016]. During the experiments, the aqueous phase is injected into the porous media with a constant volumetric flow rate leading to an average front velocity of $3\mu m/s$ [Singh et al., 2016].

4.2 Fractal dimension

(a) (b) (c)

Figure 4.1: Illustration of box counting method. (a) is the cross section of a bead pack cleaned by Pirahna. The red phase indicates the segmented bead phase and the green phase represents the invading liquid. The black phase shows the defending liquid. The advancing contact angle of the invading liquid is $\theta = (20 \pm 10)^\circ$. In (b) and (c), the colorful boxes are the boxes covering the invading liquid and the plots only show the cross section of the boxes.

The fractal dimension is a classical measure to delineate fluid spreading patterns within 2D domains to characterize the corresponding 2D fluid morphology [Måløy et al., 1985]. The fractal dimension of a compact object equals the dimension of the ambient space. The fractional dimension of an object with a self-similar shape like Koch's flake or Sierpinski's carpet, however, turns out to be a non-integer number [Mandelbrot, 1983]. To obtain the fractal dimension, the "box-counting method" is frequently employed [Grassberger and Procaccia, 2004], where the logarithm of the minimum number of cubes (lines in 1D or squares in 2D) that is necessary to cover the object is first determined for a series of cubes sizes and the plotted against the logarithm of the cube size. A linear relationship is expected for a self-similar object whose slope is the fractal dimension. The fractal dimension is frequently employed to quantify viscous fingering or capillary fingering patterns in both experiments [Zhao et al., 2016] and in numerical simulation [Wilkinson and Willemsen, 1983]. In the following, we make an effort to apply this classical method to study fluid invasion within bead packings at different wetting conditions.

In Fig.4.1, an example is introduced to illustrate the box counting method. The green cluster shown in Fig.4.1 represents the invading fluid. In (b,c) of Fig.4.1, different

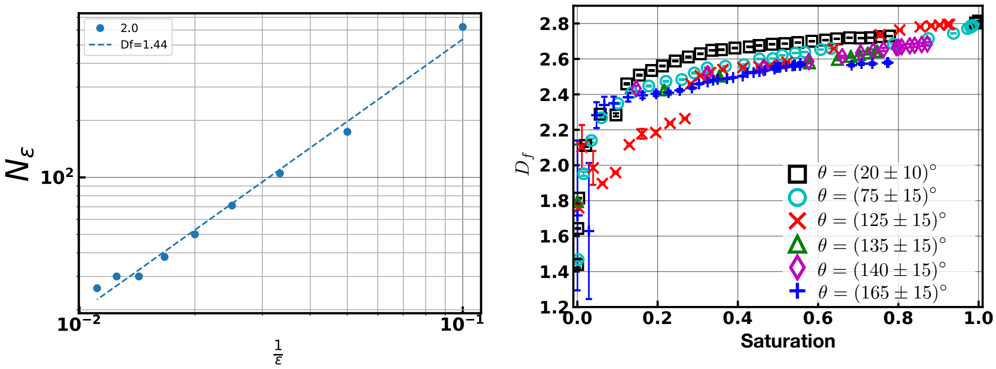

Figure 4.2: (a) The fractal scaling law obtained by the box-counting method applied to the segmented tomography. The data is based on the experiment with Piranha-cleaned glass beads, where the contact angle with respect to the invading liquid is $(20 \pm 10)°$. We choose the first tomography where the saturation of the invading liquid is around 0.0005 and the invading liquid just entered the bottom parts of the bead packs. (b) Plots of fractal dimension (D_f) for the invading liquid against different saturation of the invading liquid . The error bar comes from the sum of the squares of offsets of the points due to linear fitting for obtaining fractal dimension.

box sizes (ϵ) are employed to cover the invading liquid. For each specific box size (ϵ), we count the total number of boxes $N(\epsilon)$ covering the invading phase. Further as illustrated in Fig.4.2(a) after linear fitting the curve in a log-log plot for the reciprocal of various box sizes ($\frac{1}{\epsilon}$) and their corresponding total number of boxes $N(\epsilon)$, we take the slope of the curve as the fractal dimension. Via the same procedure, we calculate all the fractal dimension for all the available segmented data [Singh et al., 2017b] for fronts emerging when liquids of different wettability are displacing another fluid phase from bead packs. Further we plot them together leading to Fig.4.2(b). In Fig.4.2(b), for all the scenarios in terms of wettabilty, the fractal dimension grows from roughly 1.4. Similar analysis with 2D cross section has been shown in the work of Clément et al. [Clement et al., 1987], where the fractal dimension is around 1.5. And it is the time when the invading liquid just touches the bottom of the container. So the shape of the invading fluid cluster could be approximately viewed as a two dimensional object. With the increase of the invading liquid saturation, the fractal dimension also grows correspondingly. And when the liquid wets the media, like Piranha cleaned beads ($\theta = 20 \pm 10°$) and Basalt beads ($\theta = 75 \pm 15°$), the final fractal dimension reaches to approximately 2.8. However, when the contact angle of invading liquid with respect to the media is relatively high, the final fractal dimension is within the range of 2.5 and 2.7, which is in accordance with the simulation work of Wilkinson et al. [Wilkinson and Willemsen, 1983]. With this method, we are not able to find unique features quantifying the differences of influences induced by the wetting conditions of the porous media, which drives us to find alternatives for characterizing invading liquid.

4.3 Proposed methods for quantifying displacement patterns in 3D

The question we are investigating focuses on the how the geometry and wettability of the porous media influence the invasion pattern in two-phase flow in three-dimensional space. Given the data from Singh et al. [Singh et al., 2017b] regarding the change of invasion pattern dependent on the wettability of invading liquid, we are able to test the validity of different quantification methods. In this section, we firstly present three quantities that are suited to characterize the global shape of the invading interfaces. These are mean finger area, the mean Euclidean distance of the connected invading fluid from the connected defending fluid, and the discrete interface area.

4.3.1 Mean finger area

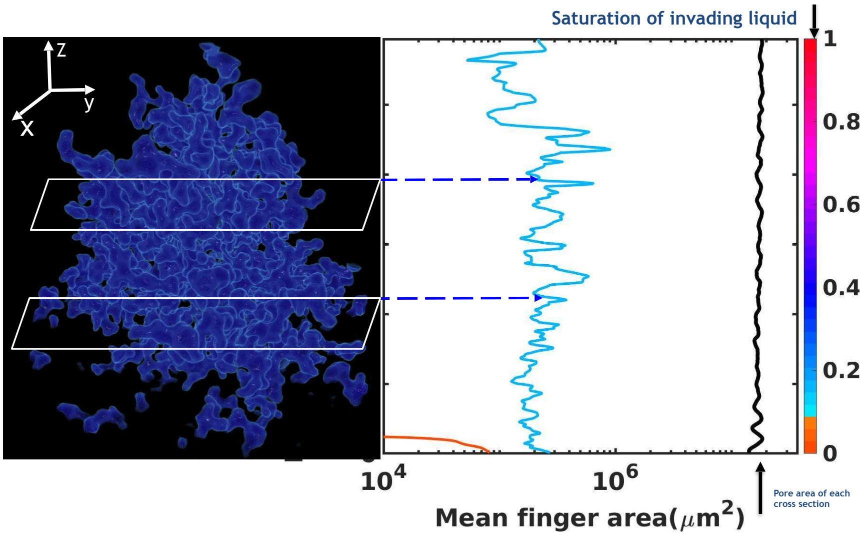

Figure 4.3: Illustration of the mean finger area calculation. Left picture represents the invading liquid cluster in a 3D representation. The right graph represents the mean finger area along the Z-axis for different saturation.

In the following, we will shortly present the reader of the central idea behind mean finger area. In Ref. [Cieplak and Robbins, 1988], the mean finger width was utilized as the most reliable method to quantify the cross-over between compact and ramified patterns of the invading fluid observed at different contact angles. We extend the idea of the mean finger width of the displacement pattern in 2D to quantify the morphology of immiscible two phase flow in three dimensional permeable media and consequently refer to mean finger area in the following. The distribution of lengths of the invaded segments in the 2D model of Cieplak and Robbins are obtained in linear cuts through the fluid pattern [Cieplak and Robbins, 1988]. In full analogy to the 2D case, we consider a sequence of slices through the segmented 3D tomography images perpendicular to the flow direction and compute the distributions of the area of invading fluid domains as shown in Fig.4.3. Following the common definition in percolation theory, the average domain size, $A(m)$, is defined by Eq.4.1 [Aharony and Stauffer, 2003]:

$$A(m) = \sum_{i=1}^{n} w_s s_i = \sum_{i=1}^{n} \left(\frac{n_s s_i^2}{\sum_{j=1}^{n} n_s s_j} \right) \tag{4.1}$$

where, s_i is the area of the i^{th} size of a fluid domain, w_s the probability that a randomly chosen pixel belongs to a invading fluid domain in the of size s_i.

This particular choice of the weighting effectively reduces the influence of the segmentation bias, in particular the influence of individual voxel/pixel "outlier". Also the noise created by small domains and isolated pixels that have been erroneously assigned to the invading fluid is largely reduced using this weighting.

Mean finger area analysis for homogeneous wetting packs

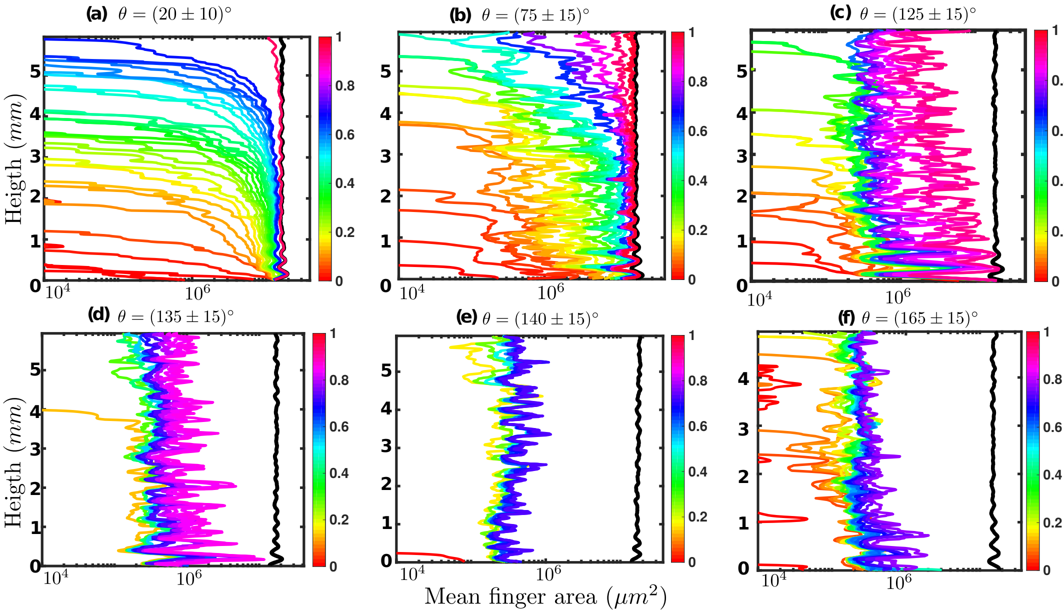

Figure 4.4: Time dependent mean finger analysis of liquids invading spherical bead packs having different wettability as specified in the figure. Zero of the Y-axis represents the bottom of the sample. The colour codes next to the plots indicate the saturation of the invading liquid. Each line in the plot is obtained from the segmented image of a specific tomography corresponding to certain saturation with the injected liquid.

The results of the mean finger area for six data sets with different wettability are plotted in Fig.4.4. The temporal evolution of the mean finger area can be seen by the different color decoding the saturation of the sample with invading phase. From

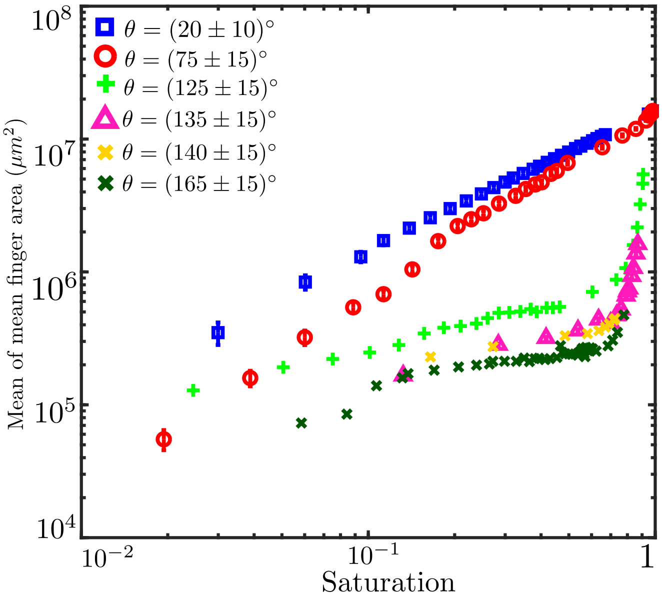

Figure 4.5: Mean of the mean finger area as a function the global saturation of the invading fluid. Shown are data covering a range of advancing contact angles as indicated in the legend.

visual inspection of Fig.4.4 we can recognize a different behavior for contact angles $< 90^\circ$ (panel a) and b)) and for contact angles $> 90^\circ$ (panel c)-f)), that shall be discussed in more detail:

- $\theta < 90^\circ$. When the advancing contact angle of the invading liquid is around 20° as shown in Fig.4.4(a), the distribution of the mean finger area along the flow direction for each specific saturation of the invading liquid displays similar feature, i.e. the bottom parts of the region of interest have larger value of mean finger area followed by a sharp drop at the very top of the invading liquid cluster. In addition, the value of the mean finger area at the bottom parts is already very close to the void area when the saturation of the invading liquid is only around 0.2. This feature indicates a compact domain develops because the liquid behaves as a process of piston-like invasion. When the contact angle increases to around 75°, the overall feature for each specific saturation is similar to the case when θ is around 20°, i.e. larger value at the bottom of the region of interests followed by a sudden drop at the very top of invading liquid cluster. However, we see that for each specific saturation, the mean finger area is not decreasing monotonously along the flow direction as in the case of $\theta \sim 20^\circ$. Instead, the value of the mean finger area is strongly fluctuating but the overall shape of each curve characterizing the mean finger area distribution along the flow direction is similar to the case of $\theta \sim 20^\circ$.

- $\theta > 90^\circ$. When the contact angle is further increased to around 125° as shown in Fig.4.4(c), the invasion pattern indicated by the evolution of mean finger area distribution along the vertical direction is different compared with Fig.4.4(a) and (b). Before the invading liquid penetrates through the view of interest, which is correlated to the time when saturation is around 0.7, the mean finger area always keeps as a nearly constant along the flow direction. In addition, this constant value is several orders smaller than the corresponding pore area. As the invasion continues, there exists a sudden expansion of mean finger area along the view of interest. Similar features are also seen in the case of $\theta \sim 135°$ as shown in Fig.4.4(d). For higher contact angle as shown in Fig.4.4(e) and (f), only constant plateau is identified without a clear sign of mean finger area expansion for the case when $\theta \sim 125°$.

To further compare the features of the invasion pattern for different advancing contact angle, we condense each curve in Fig.4.4 to one number, i.e. taking the mean of the mean finger areas for each line in Fig.4.4 to obtain the data point shown in Fig.4.5. In this Fig.4.5, the mean value of the mean finger width was calculated including the bottom regions, which is influenced by the layering effects of beads.

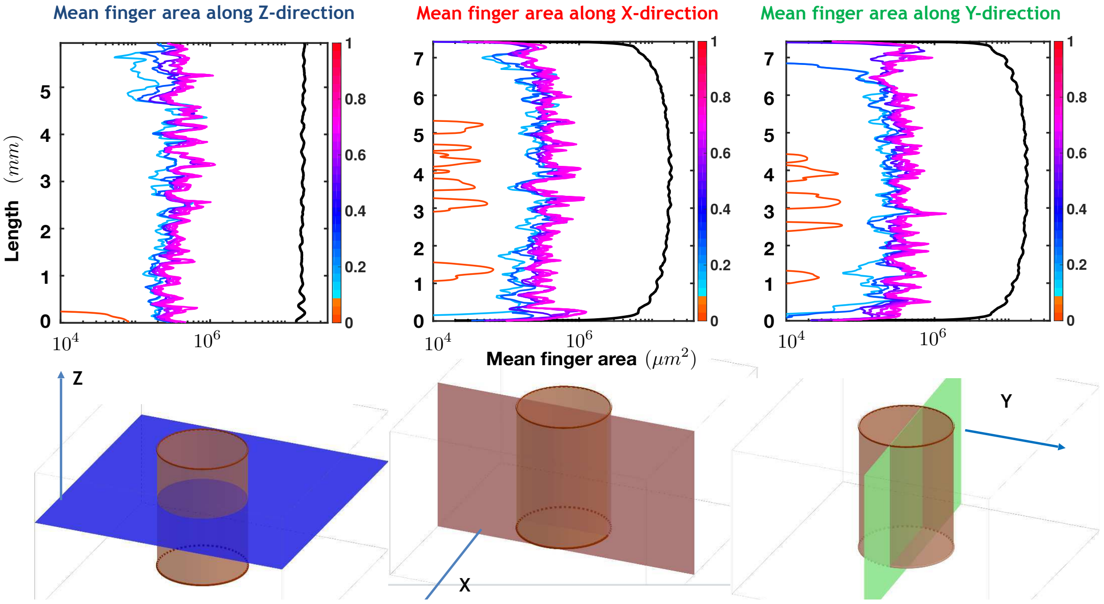

Figure 4.6: Illustration of calculating the mean finger area along different directions. The advancing contact angle is $\theta = (140 \pm 15)°$. The extension of the sample into flow direction is approximately 6 mm in width and the extension perpendicular to the flow direction is around 8 mm. The colorbar indicates the saturation of the invading liquid.

Mean finger area in different direction

After describing the mean finger area method, we further apply the mean finger area profile in different directions to see if the results are robust against chosen directions. It is convenient to choose the planes defined by the Cartesian axis and move along

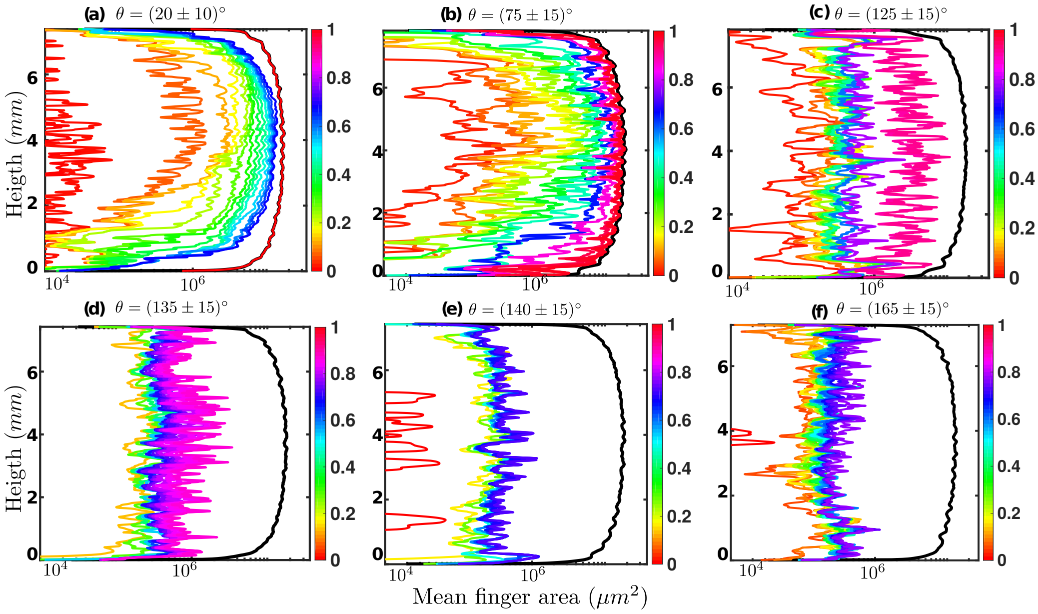

Figure 4.7: Time dependent mean finger analysis of liquids invading spherical bead packs having different wettability as specified in the figure. X axis is chosen for further calculation of mean finger area as indicated in Fig.4.6. Zero of the Y-axis represents one side of the sample. The colour codes next to the plots indicate the saturation of the invading liquid. Each line in the plot is obtained from the segmented image of a specific tomography corresponding to certain saturation with the injected liquid.

the respective perpendicular axis, as shown in Fig.4.6. In Fig.4.6, we could see that along three directions, the mean finger area does not change much between each direction, which further shows the robustness of this method. Further, we show the mean finger area are along X- and Y-direction for various wetting conditions as shown in Fig.4.7 and 4.8. In Fig.4.7 and 4.8, the black curves indicate the void area in the spherical pack for each cross section. Due to the cylindrical geometry of the container, the central parts have the maximum value of void area and the void area decreases towards the edge of the container. For $\theta < 90^\circ$, we notice that the mean finger distribution is in well accordance with the void area indicated by the black curves. For the case when $\theta = (125 \pm 15)^\circ$, the stable constant over the extension is observed followed by an expansion of mean finger area along the extension. The rest cases when $\theta > 90^\circ$, only stable constant is identified. The features observed in Fig.4.7 and 4.8 is in accordance with Fig.4.4, which further validates the robustness of this method.

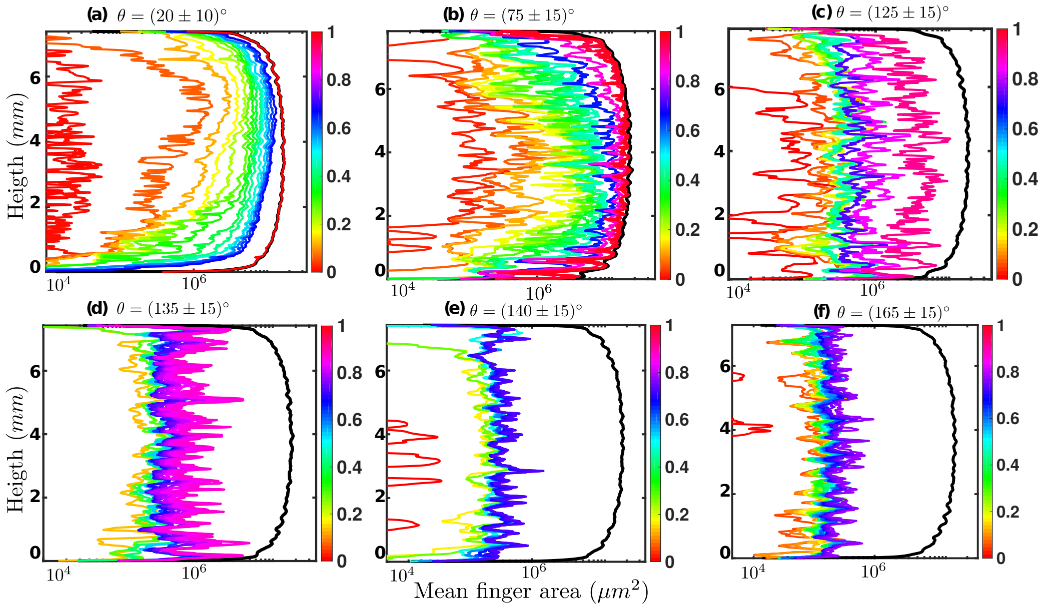

Figure 4.8: Time dependent mean finger analysis of liquids invading spherical bead packs having different wettability as specified in the figure. Y axis is chosen for further calculation of mean finger area as indicated in Fig.4.6. Zero of the Y-axis represents one side of the sample. The colour codes next to the plots indicate the saturation of the invading liquid. Each line in the plot is obtained from the segmented image of a specific tomography corresponding to certain saturation with the injected liquid.

4.3.2 Mean Euclidean distance

The above presented characterisation of the finger is based on their cross-sectional area in a sequence of two dimensional cuts. This implies that the connection of the invading liquid between each 2D cut is not reflected in the definition of the mean finger area. Therefore, we introduced an alternative method to quantify the typical size of the invading fluid fingers that is based on their three dimensional structure. The mean Euclidean distance is defined as the average distance of invading fluid voxels to the closest defending fluid voxel [Danielsson, 1980]. We noticed that for invading liquids with low contact angles, the segmented region within the invading liquid may contain some isolated voxels of defending liquid. By inspection of the original reconstructed tomography image, a large fraction of these voxels can be identified as artefacts created in reconstruction or segmentation. Because these isolated voxels of the defending fluid have strong influence on the Euclidean distance of the invading liquid in their neighbourhood, we ignore these individual voxels. For that, we add artificially a layer of defending fluid on top of each segmented image and only consider the voxels of the defending fluid that have a connecting path within the defending fluid to this top outlet as the reference for determining the Euclidean distance. In

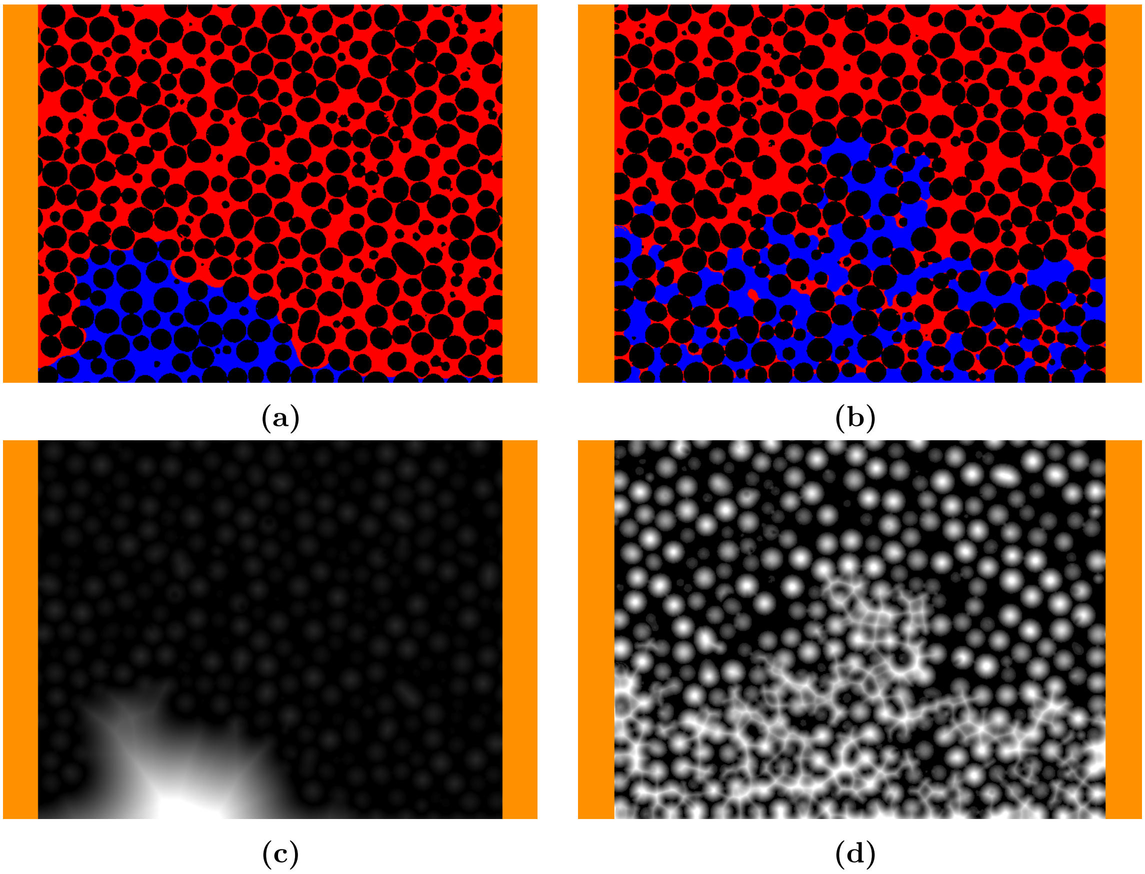

Figure 4.9: Cross sections through segmented tomographic data (a,b) and corresponding Euclidean distance map (c,d) showing invasion patterns of fluids with advancing contact angle of $\theta = (20 \pm 10)^\circ$ (a,c) and $\theta = (125 \pm 15)^\circ$ (b,d) with respect to the invading fluid. (a,b) The invading and defending fluid are shown in blue and red, respectively. The beads are shown in black. The pore space is initially saturated with the defending fluid (oil or air), while the invading fluid (water) is injected from the bottom of the container. (c,d) The intensity of the grey value encodes the value of the Euclidean distance; brighter regions indicate larger Euclidean distances. Note that the space occupied from by the bead matrix is excluded from the calculation of the mean Euclidean distance.

Fig.4.9a and 4.9b, we show examples of vertical cuts for the segmented images for two different contact angles of the invading fluid on the surface of the beads. Corresponding maps of the Euclidean distance of an invading fluid voxel to the closest voxel of the defending fluid are shown in Fig.4.9c and 4.9d. In Figure 4.9c and 4.9d, it can be observed that the invading fluid interface forms a compact front at low contact angles $\theta = (20^\circ \pm 10^\circ)$. At high contact angles $\theta = (125^\circ \pm 15^\circ)$, however, the invading interfaces evolve into a ramified morphology. The grey level in Fig.4.9c and 4.9d gives an impression of the distribution of Euclidean distances in the two cases.

In the following, we investigate more cases for different advancing contact angles.

Mean Euclidean distance for homogeneous wetting packs

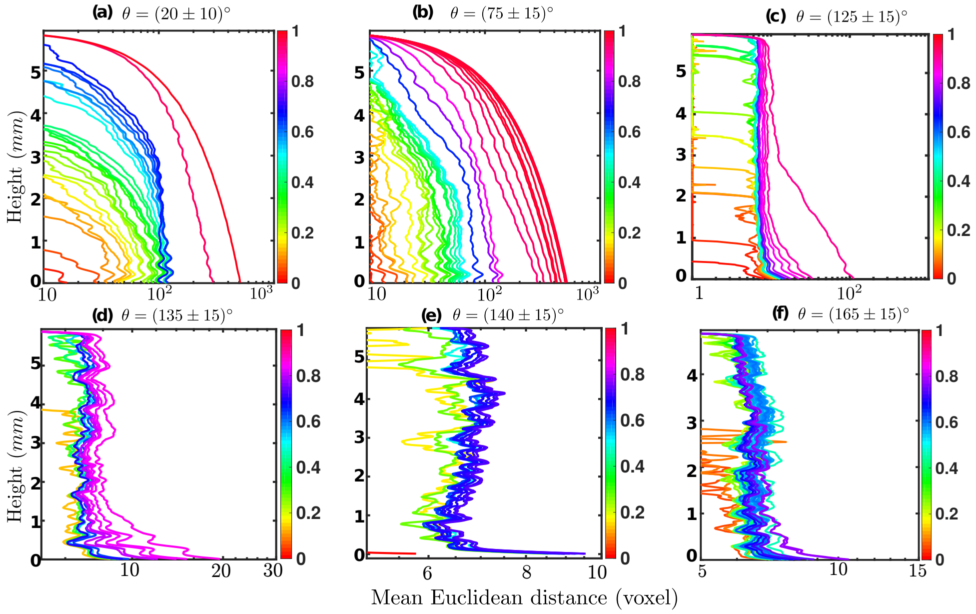

Figure 4.10: Mean Euclidean distance analysis of invading liquid with sphere packings with different wettability. Zero of the Y-axis represents the bottom of the sample. The colour codes next to the plots indicate the saturation of the invading liquid. Each line in the plot is obtained from the segmented image of a specific tomography corresponding to certain saturation with the injected liquid.

In Fig.4.10(a) and (b), we find that for a contact angle smaller than 90°, the overall value along the vertical direction increases for increasing saturation of the invading liquid. Qualitatively, there is no difference between the case of $\theta = (20 \pm 10)°$ and $\theta = (75 \pm 15)°$. This is in contrast to an invading liquid with a contact angle of $(125 \pm 15)°$. In the latter case the value along the vertical direction is not changed much for the early stage of fluid invasion. And when the saturation of the invading liquid exceeds a saturation of about 0.7, we see that a sudden increase in terms of the mean Euclidean distance at the bottom of the sample. For other contact angles higher than $(125 \pm 15)°$, only constant value along the vertical direction is observed without an obvious increase in terms of the mean Euclidean distance at the bottom of the sample. The above mentioned phenomena can also be seen in previously presented mean finger area analysis. However, the layering effect at the bottom does not change the value of the Euclidean distance. The reason for that is that the Euclidean distance method is a three dimensional quantification. Even though that the invading liquid invades larger region in the bottom region, and hence larger area, the ramified interface leads to defending liquid regions connected to the outlet. As a result, we do not see much increase of the Euclidean distance due the

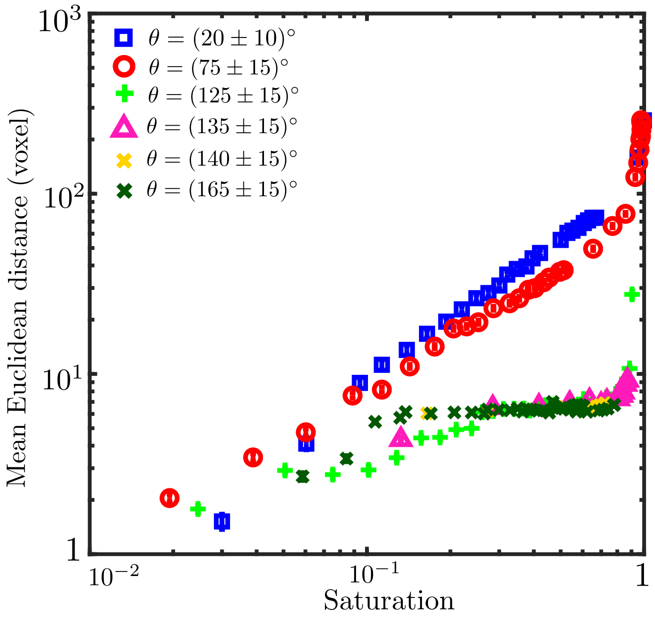

Figure 4.11: Mean of the mean Euclidean distance as a function the global saturation with the invading fluid. Shown are data covering a range of advancing contact angles, as indicated in the label.

layering effect at the bottom. So plotting the mean value for each line of the Euclidian distance analysis in Fig.4.10, as we did that previously for the mean finger analysis, we find that the majority of lines for larger contact angle almost collapse on the same line, which indicates a ramified structure of the invading liquid, cf. Fig.4.11.

4.3.3 Discrete interface

Segmentation of the fluid phases and the porous matrix react very sensitively to changes of the segmentation parameters [Heiko et al., 2013]. As a consequence of this high sensitivity, the area of the fluid-fluid interface typically comes with a large uncertainty and is therefore not suited to distinguish between the different morphologies of invading interfaces. In order to obtain a more robust measure of the interfacial area of an invading fluid, we instead consider the ”discrete interfacial area”. Following the idea that the set of bonds adjacent to unsaturated sites defines the interface of a cluster in percolation theory [Aharony and Stauffer, 2003; Domb et al., 1975], we used the number of menisci in throats formed by three adjacent beads as a measure for the area of fluid-fluid interfaces. In order to find the positions of these menisci, the void space of the bead packing is first decomposed into a network of tetrahedral pores by means of a Delaunay tessellation with respect to the centres of the beads [Si, 2015]. Triangles of adjacent tetrahedra represent the throats of the pore network. To avoid the occurrence of boundary artefacts in the tessellation, we excluded tetrahedra in the boundary region from our analysis, i.e. we restricted our analysis exclusively to pores in the bulk. Figure 4.12a displays an example of the cross section of such a tessellated 3D bead pack.

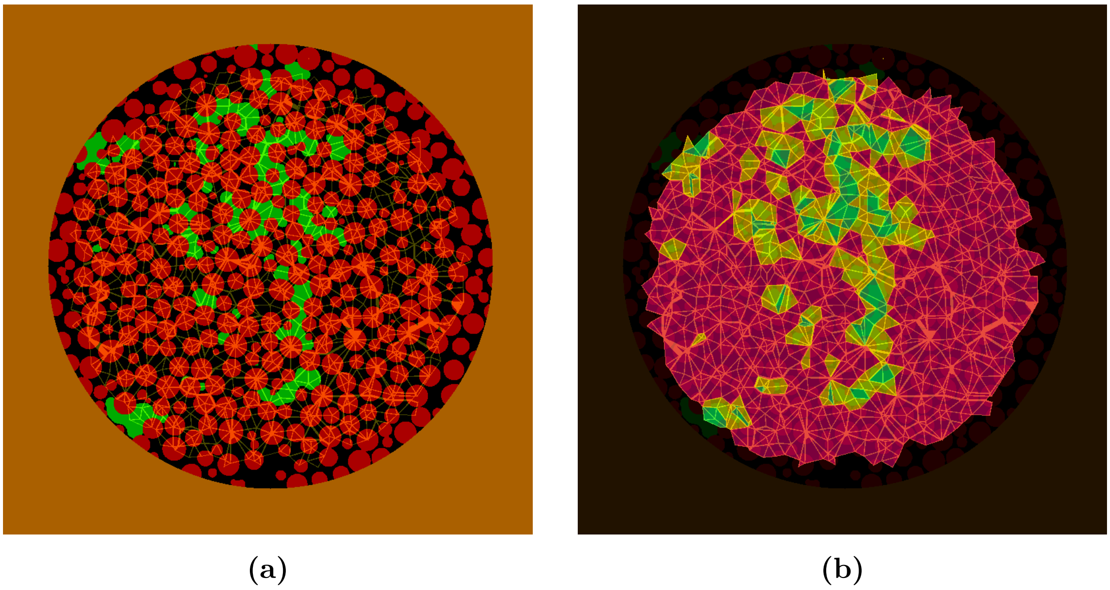
(a) (b)

Figure 4.12: (a) Cross section through a tomography image of a bead pack, where water displaces AK100 silicon oil. The advancing contact angle is θ = (135 ± 15)°. The extension of the sample into flow direction is approximately 6 mm. The green phase is the invading water and the black phase is the defending oil phase. Bright lines are parts of the tetrahedron faces. (b) A cross section of the Delaunay tessellation of the tomography image shown in Fig.4.12a. As the tetrahedrons are in 3 dimensional space, the cross section of them are triangles or convex quadrilaterals. Red color indicates that the tetrahedron (pore) is filled with at least 95% by the defending fluid. Green colour indicates that a tetrahedron is filled with at least 95% with invading fluid while tetrahedra which host the interfaces (menisci) between the invading and defending fluid are displayed in yellow.

For a robust quantification of the area of the evolving fluid-fluid interfaces during invasion we considered a simplified representation of the fluid distribution in the bead pack, cf. Fig.4.12a. In this representation we assign the filling state of each tetrahedron to one of the fluid phases or to the interface. To this end, we first determine the filling degree of every tetrahedral pore based on the ratio of voxels belonging to the invading fluid and the defending phase. To account for the influences from the segmentation, if the filling degree of a pore is less than 0.05, we label the pore as completely occupied by the defending fluid (shown in red in Fig.4.12b). If the filling degree is larger than 0.95, we label the pore as fully saturated with the invading fluid (shown in green in Fig.4.12b). Pores with a filling degree between 0.05 and 0.95 are labelled as pores containing parts of the fluid-fluid interface (shown in yellow in Fig.4.12b). Note that the later pores potentially contain multiple terminal menisci.

After the classification of the pores, we count the number of menisci in each pore that is not assigned to either completely filled with the invading or defending fluid as a discrete measure for the interface area between the invading and defending fluid. To this end, we first loop over all pores that are partially saturated with the invading fluid. For each of these pores, we check the classification of all its four neighbouring pores, cf. Fig.4.12b. If the neighbouring pore is saturated with defending fluid (red colour), the interface connecting the two adjacent pores contains a meniscus. However, if the neighbouring pore is also partially saturated with invading fluid (yellow colour), we determine the fraction of defending fluid voxels at their interface divided with respect to the total number of voxel of the interface. If this fraction is larger than 0.95, we deem the interface to be filled with the defending fluid, and we assume that there are two opposing menisci located between the pore bodies. Otherwise when the fraction is smaller than 0.95, it is assumed that there are no menisci between the two adjacent pore bodies.

Figure 4.13a illustrates two different local scenarios that need to be considered when counting the number of discrete interfaces. Figure 4.13b shows a map of the identical region of interest where the tetrahedral are classified in terms of the filling degree of the invading fluid. The lower left square in both panels indicates the situation when one of the pore bodies is partially saturated with the invading fluid while the pore body of the neighbouring pore is filled with defending fluid. The upper right square indicates the case when both of the neighbouring pores are partially filled with invading fluid while the interface connecting both pores bodies is completely filled with defending fluid.

Discrete interface analysis for homogeneous wetting packs

This method to count the number of menisci was applied to the available segmented data for fluid displacement experiments in bead packs for different wetting conditions with respect to the invading fluid. Figure 4.14 displays the number of such determined discrete menisci against the saturation of the invading fluid. Due to different segmentation parameters and non-ideal packing geometry close to the container walls, the number of boundary tetrahedra that had to be excluded varied slightly from sample to sample. To account for these inevitable variations of the total pore space, and to allow for a proper comparison of the data, the numbers of discrete menisci were normalize by the volume of all bulk pores.

Inspection of Fig.4.14 reveals a clustering of the contact angle dependent data similar as obtained for the previously discussed results of the mean finger area: When the invading fluid is wetting, the number of menisci does not change much during injection. The reason for that is that the invading fluid develops a compact front and before the new menisci are formed, the old menisci are reduced by cooperative pore filling events. However, if the contact angle of the invading fluid is sufficiently large, the number of menisci increases linearly with the progression of the invading fluid. This behaviour

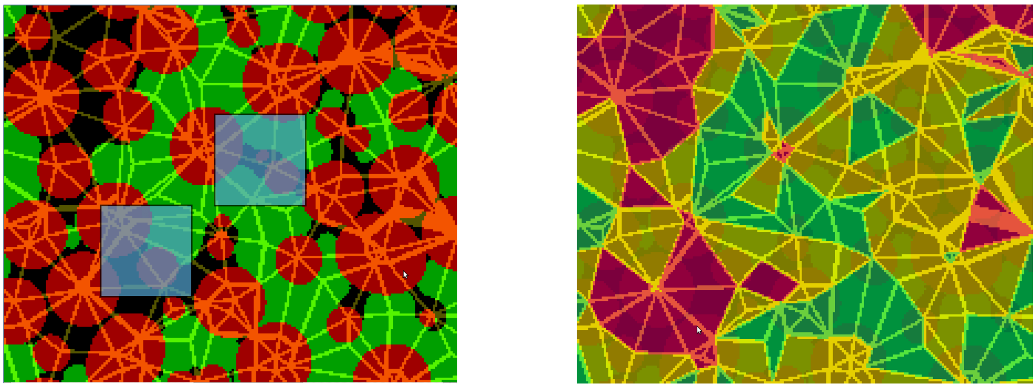

(a) (b)

Figure 4.13: Illustration of two different cases that need to be considered when counting the number of discrete interfaces (menisci). The left bottom square highlights the local situation where one of two adjacent tetrahedra (pores) is partially saturated with the invading fluid while the other tetrahedron is filled with defending fluid, named as filled-empty interfaces in the following text. The upper right square indicates a situation where both of the neighbouring tetrahedra are partially filled with invading fluid and the common interface is filled with defending fluid, name as filled-filled interfaces in the following text.

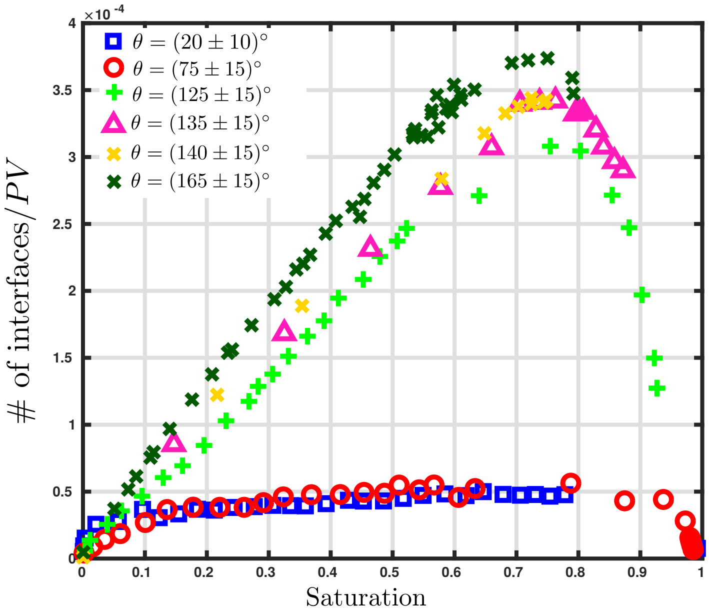

Figure 4.14: Number of menisci in a bead pack normalized by the available pore volume as a function of the global saturation with invading fluid. Shown are data covering a range of advancing contact angles given in the legend.

is indicative for the development of a ramified front, and has been described also for

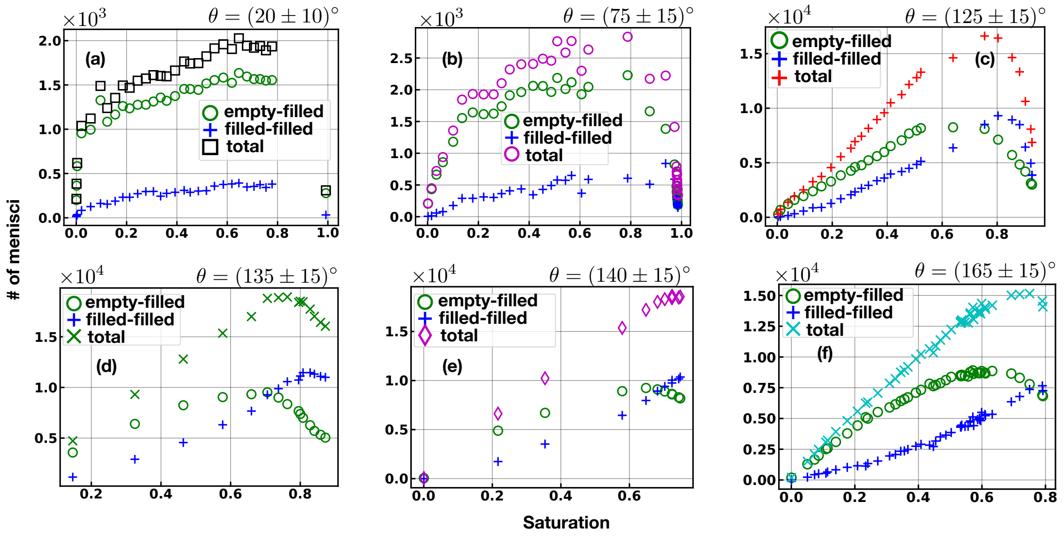

Figure 4.15: Number of different types of menisci for different advancing contact angles.

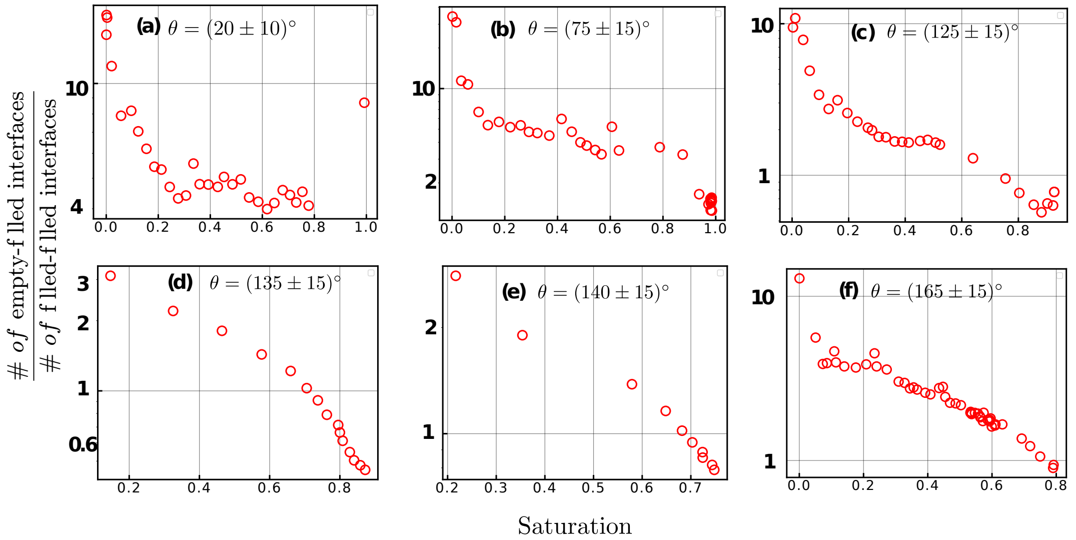

Figure 4.16: Ratio between # of empty-filled interface and # of filled-filled interfaces against saturation of the invading liquid for different advancing contact angles.

the number of dangling bonds in growing clusters close to the percolation threshold [Domb et al., 1975]. It is also worth mentioning that we observe a sudden drop of the number of menisci in samples with larger contact angle at the end of the invasion process. This sharp drop correlates to the situation when the mean finger area starts to expand. A possible explanation for that is that, at this later stage of invasion, the expanding fingers merge and consequently become "fatter". This coarsening of the fingers is accompanied by a fast decrease in the number of menisci.

To further illustrate the reason for the sudden drop of the number of menisci, we plot the quantities and the relationship between two types of menisci as shown in Fig.4.15

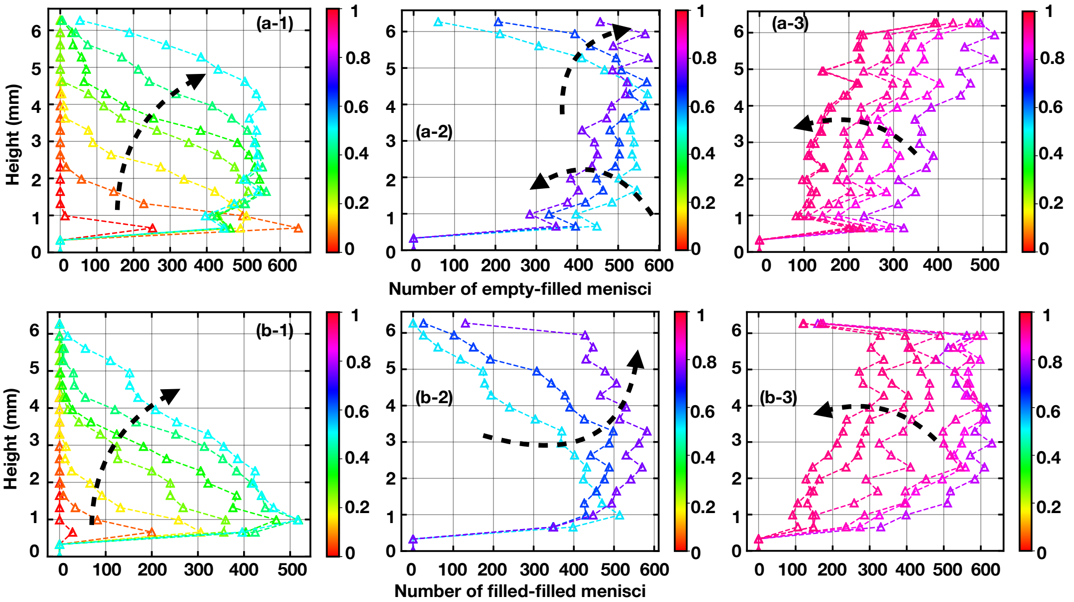

Figure 4.17: Distribution of the number of empty-filled and filled-filled interfaces along the flow direction for different saturation of the invading liquid. 0 in Y axis represents the bottom of the region of interest. Contact angle of the invading liquid is $\theta = (125 \pm 15)^\circ$. Along the flow direction, every 30 voxel layers are grouped to obtain the total number of menisci, which lead to the data point in each plot. The color codes represent the saturation of the invading liquid. The arrows indicate the trend, where the saturation of the invading liquid is increasing. (a-1,2,3) represents the distribution of empty-filled interfaces for various saturation and (b-1,2,3) indicates the corresponding distribution of filled-filled interfaces.

and Fig.4.16. In Fig.4.15(a), we notice that the number of empty-filled menisci dominates over the number of filled-filled mensci all the saturation of invading liquid. This phenomenon indicates that defending liquid trapped within the gap of the spherical beads are rare when the contact angle of the invading liquid is small. In addition, the number of menisci is not growing linearly with the increasing saturation of the invading liquid. Instead, a nearly constant value is specified for the majority of the saturation, which further validates the piston-like invasion pattern identified in the analysis of the mean finger area. The similar phenomenon is shown in Fig.4.15(b). However, for high contact angle of 125°, the number of menisci is firstly growing both linearly with respect to the saturation of the invading liquid as shown in Fig.4.15(c). When the saturation of the invading liquid exceeds a saturation of about 0.5, there is a plateau for the number of empty-filled interfaces but the number of filled-filled interfaces continues to grow. This plateau is explained in Fig.4.17(a-2). In Fig.4.17(a-2), we notice that when the saturation of the invading liquid exceeds around 0.5, the number of empty-filled interfaces is decreasing at the bottom of the region of interest while the number of empty-filled interfaces is increasing at the top of the region of interest. For other high contact angles, the nearly linear growth of two types of the interfaces are similar. However, a clear drop in the number of filled-filled interfaces are not identified as we see in Fig.4.15(c). We further plot the ratio between the empty-filled interfaces and the filled-filled interfaces as shown in Fig.4.16. In Fig.4.16, we notice that when the saturation is small, the number of empty-filled interfaces is always larger than the filled-filled interfaces. The reason is obvious because the liquid just enters the field of interest and there is a rare chance to develop filled-filled interfaces. With the progression of the invading liquid, we notice that for $\theta < 90°$, the ratio reaches a nearly constant value. For the cases when $\theta > 90°$, this ratio is decreasing almost monotonously, implying that more liquids are trapped within the gap formed by the spherical beads.

Based on the results after applying the three methods for the monodisperse bead pack, we know that all of the three methods clearly differentiate the compact invasion pattern and ramified interface invasion pattern but vary in details. Both of mean finger area analysis and mean Euclidean distance analysis are able to show the influences of the layering effects on the interface evolution. But the mean finger area is the easiest way to quantify the interface evolution in terms of computation efforts. In the following application, we mainly focus on the mean finger area analysis as a standard way for interface evolution quantification. In addition, it is clear that all the methods proposed can extract more information and give way better characterization compared with the classic methods like the fractal dimension.

4.4 Heterogeneous wetting bead packs

As shown in the previous section, three methods of analysis present us with different aspects of the invasion pattern. All of these methods are able to clearly distinguish between the different invasion pattern that are linked to the wettability of the invading liquid. Then it is worth trying to apply the same method to investigate the liquid invasion pattern when the bead packing is composed of different wettability. In the following, we test two cases with different mixing ratio of OTS-coated beads $(165 \pm 15)°$ and Basalt beads $(75 \pm 15)°$.

As shown in Fig.4.18, with increasing saturation, the feature shown in the mean finger area and the mean Euclidean distance both indicate the development of fingering structure by showing a plateau. In the heterogeneous wet bead packing, the tessellated tetrahedra are formed by different types of beads. Instead of determining the filling state as shown in the discrete interface method, here we try to analyze the filling frequency for different triangles with increasing saturation of the invading liquid. By further looking at the filling frequency of different triangles in Fig.4.20, we notice that the number of triangles formed by the wetting bead increases much faster than the other types of triangles. This clearly proofs preferred flow paths along throats that are composed of three beads with smaller contact angle, while throats composed of

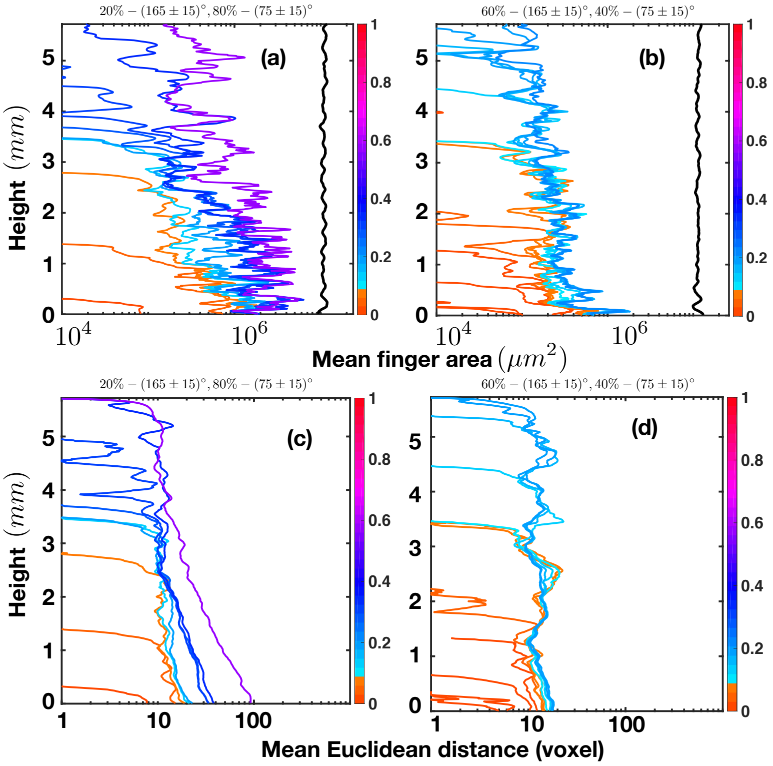

Figure 4.18: Mean finger analysis and mean Euclidean analysis for a packing of 20, 60% OTS-coated beads (165 ± 15)° and 80, 40% Basalt beads (75 ± 15)° (a,c) Distance along the flow direction in the sample against mean finger area; (b,d) Distance along the flow direction against the mean Euclidean distance. The colour codes next to the plots indicate the saturation of the invading liquid.

more non-wettable beads are avoided. Accordingly, we find the lowest frequency for throats composed of three wettable beads.

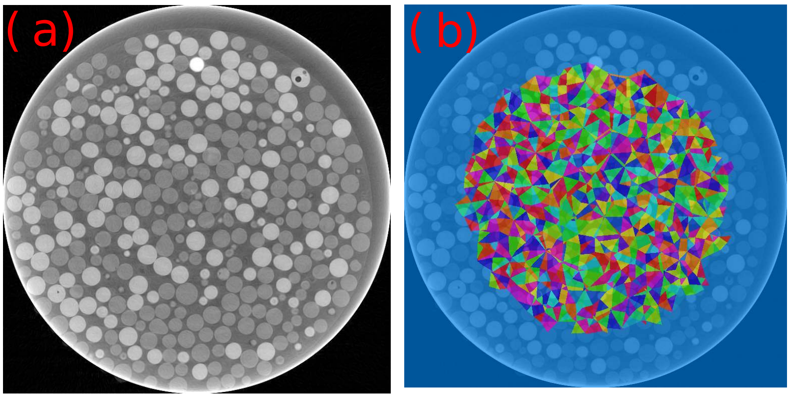

Figure 4.19: Cross section of the tomography for a packing of 60% OTS-coated beads (165 ± 15)° and 40% Basalt beads (75 ± 15)° (a) Cross section of the tomography data;(b) Cross section of the tessellated space.

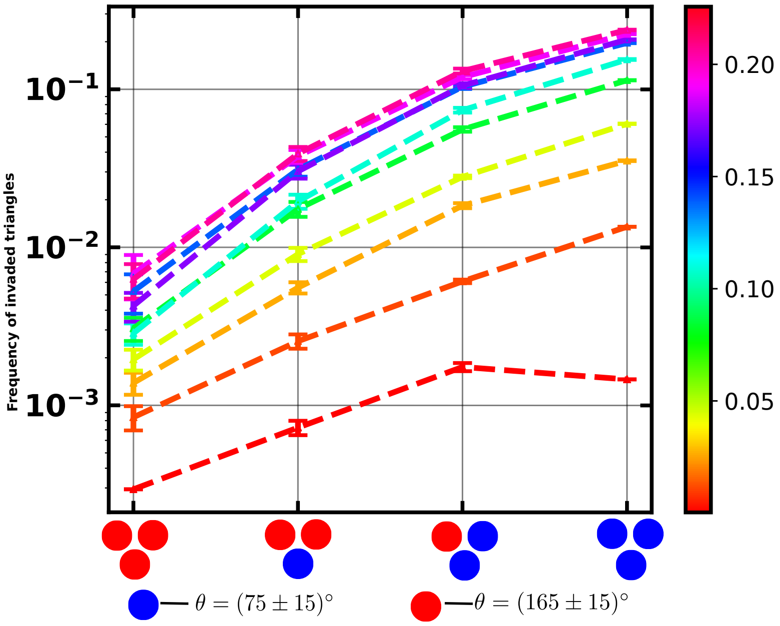

Figure 4.20: Frequency of invaded triangles against different types of triangles. In total, there are four types of triangles. For each tomography, we record the number of filled faces based on the filling degree of the face by the invading liquid. The error bar in the graph comes from varying the threshold of the filling degree from 99.2% to 99.8%. For each triangular face, the filling degree is defined by the number of voxels occupied by the invading liquid divided by the number of voxels occupied by the void region. The filling degree determines whether a triangular face is counted as occupied by the invading liquid.

Chapter 5

Depercolation in the drainage process

In the process of two-phase flow, percolation theory has been frequently employed to delineate the displacement process of one fluid by another when capillary forces are dominating over viscous forces [Wilkinson and Willemsen, 1983; Dias and Wilkinson, 1986; Lenormand, 1985]. For a standard percolation model, it is assumed that the porous media can be described by a network of pores (nodes, sites) connected by throats (ducts, bonds). During an invasion percolation process, there are three conditions to determine whether the defending liquid can be invaded. Firstly the defending liquid should be connected to the injection face. Secondly, there is a continuous path for the defending liquid to the outlets. Otherwise the defending phase is trapped. Thirdly, the invading liquid should overcome a necessary capillary pressure to pass through a throat [Lenormand, 1985; Wilkinson and Willemsen, 1983]. In chapter 3, we have employed this model to investigate how the pore geometry and wetting heterogeneity influence the fluid invasion process in 2D disk packings, where the threshold to pass through a throat is determined analytically based on the local pore geometry and wetting conditions. The primary goal of this chapter is to extend the 2D C&R model in chapter 3 to three dimension. To resolve this question, we need to determine the criteria for the corresponding pore-scale events in three dimensional space including burst and touch events. On top of the existing events in two dimensional space, a pore-scale instability named as "lamella burst" is introduced, which has been shown to be pivotal in explaining the liquid morphology evolution within bead packs [Melnikov et al., 2015; Semprebon et al., 2016]. Finally, the extended C&R model in three dimensional space is employed to investigate the interesting phenomenon shown in chapter 4. In chapter 4, we notice during the invasion process in the bead packs, there is a unique stage at the end of the invasion process which is indicated by all of the three quantification methods (Mean finger area, mean Euclidean distance and the discrete interface). For example, in the discrete interface analysis, we notice that the number of interfaces increases linearly with an increasing saturation of the invading liquid at an early stage of invasion. To a certain stage for larger saturation of invading liquid (≈ 0.8), there is a sudden drop in the number of discrete interfaces. Could we use the pure percolation model to describe this process? To answer these questions, we start the following parts.

5.1 Pore-scale event in 3D

5.1.1 Burst event in 3D

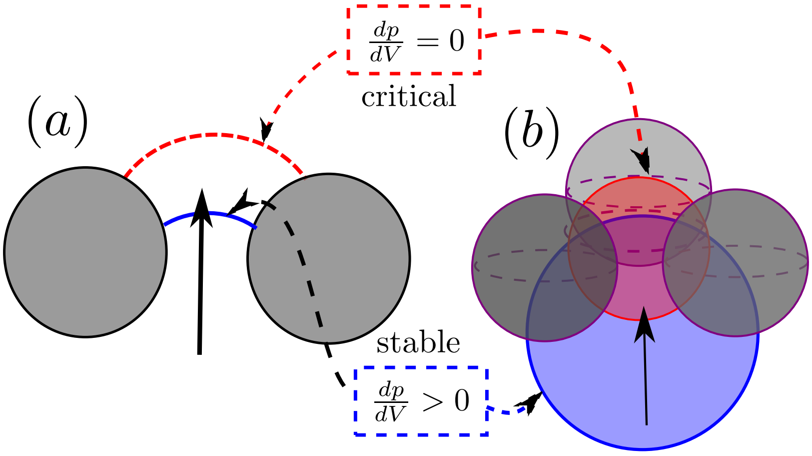

Figure 5.1: An illustration between the connection of 2D burst event (a) and 3D burst event (b). The black arrow indicates the flow direction of the invading liquid. The dashed red circular arc in (a) and red spherical meniscus in (b) indicate the situation for the occurrence of burst event when $\frac{dp}{dV} = 0$ is satisfied. The blue circular arc in (b) and blue spherical meniscus indicate a stable position for menisci when $\frac{dp}{dV} > 0$.

One important question during the drainage process is the way to determine the pore entry pressure, which represents the minimum pressure barrier for the invading liquid to penetrate a neighboring pore. As shown in Fig.5.1(a) for the 2D case in the quasi-static flow process, the drainage can be seen as a gradual build-up of pressure followed by a sudden movement of an interface, which is called Haines jump or burst [Haines, 1930]. When we extend the model in 2D to three dimensional space, it is proposed to employ local spherical approximation for the menisci between the invading and defending liquid. This approximation is within a satisfying agreement with experimental observations [Scheel et al., 2008; Melnikov et al., 2015; Singh et al., 2017b]. The link between 2D and 3D burst event is that the critical position is determined by $\frac{dp}{dV} = 0$. Given the local geometry and wetting conditions, the curvature radius for a burst event in a three-bead system can be directly obtained by solving a quadratic equation with the help of CMD (details in Appendix C.2):

$$R_{meni} = \frac{-\hat{B} + \sqrt{\hat{B}^2 - 4\hat{A}\hat{C}}}{2\hat{A}} \tag{5.1}$$

where R_{meni} is the curvature radius of the meniscus; $\hat{A}, \hat{B}, \hat{C}$ are coefficients based on the radii of three beads and contact angles.

Assuming a spherical shape for the meniscus, the pressure drop ΔP over the meniscus is calculated with Young-Laplace equation:

$$\Delta P = \frac{2\gamma}{R_{meni}} \tag{5.2}$$

The way to determine the position of the meniscus center is described in the appendix H.

Since there are some other well-known methods to predict thte pore entry pressure in packed particulates such as Mayer-Stowe-Princen method [Mayer and Stowe, 1965; Princen, 1970] as well as some numerical approaches in the work of Hilden et al. [Hilden and Trumble, 2003], we would like to compare different approaches to have a better understanding of the pore entry pressure prediction. In the following part, we compare the 3D Haines jump model in Eq.5.1 with Mayer-Stowe-Princen method (MSP) [Mayer and Stowe, 1965; Princen, 1970] with the 3D C&R model as well as the simulation result from Surface Evolver (SE) [Hilden and Trumble, 2003]. The MSP method is briefly described in Appendix G.

Comparison between different methods

In Fig.5.3, we plot the pore entry pressure for three monodisperse beads in close contact and the same geometry where two beads are separated by 0.1 of the radius. We find that when the contact angle is around 90° to 120°, the spherical fit model has a better fit to Hilden's simulation [Hilden and Trumble, 2003] result than the MSP method. The reason is that MSP does not take the converging-diverging pore space into consideration. In addition, when the contact angle of the invading fluid is around 90°, the influence from the liquid bridge on the liquid invasion pressure is small, so that the spherical fit gives us a better result. When the contact angle is larger than 120° ($\cos\theta < -0.5$), the MSP method obtains a better fit. One potential reason for the better fit of MSP is that MSP is based on 2D-geometry, where liquid wedges form between uniform infinite rods as shown in Fig.5.2(a). For a high contact angle, the interface between the invading liquid and defending liquid is long and the invading liquid penetrate through the narrowest gap formed by three beads as shown in Fig.5.2(b). However, when the contact angle reaches 90° ($\cos\theta \to 0$) and the beads are in close contact ($P_{L_{nw}} \to 0$), $r = \frac{A_{eff}}{P_{L_{nw}} + P_{L_{ns}} \cos\theta} = \frac{A_{eff}}{P_{L_{ns}} \times 0} \to \infty$ according to Eq.G.4. This comparison informs us that when the contact angle of invading liquid is relatively high (roughly more than 120°), MSP approximation provides already a good match to the pore entry pressure calculated by the energy minimization method

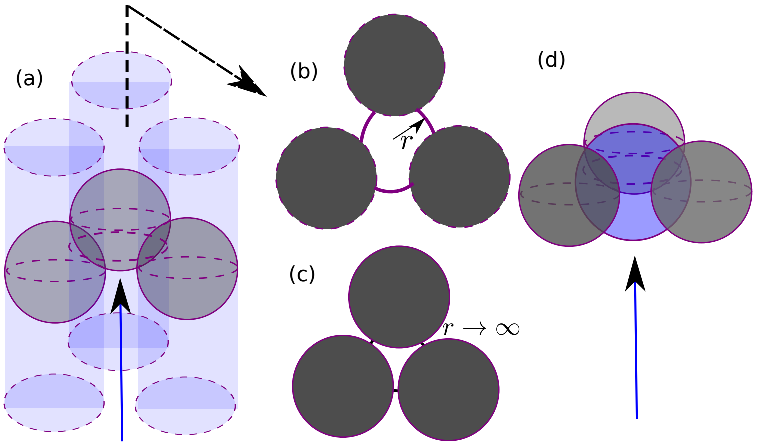

Figure 5.2: Illustration of the differences between MSP method and 3D C&R model. Blue arrows indicate the flow direction for the invading liquid. (a) Three cylinders are employed to form the narrow gap, where each cylinder contains one sphere. (b) The top view of (a). The purple circular arcs are the interfaces between invading and defending liquid. r is the curvature radius. (c) The top view of (a) when spheres are almost close in contact. When contact angle $\theta = 90°$, the interfaces between invading and defending liquid become straight lines. (d) Illustration for the 3D C&R model, where the interface between the invading and defending liquid is assumed to be a spherical cap.

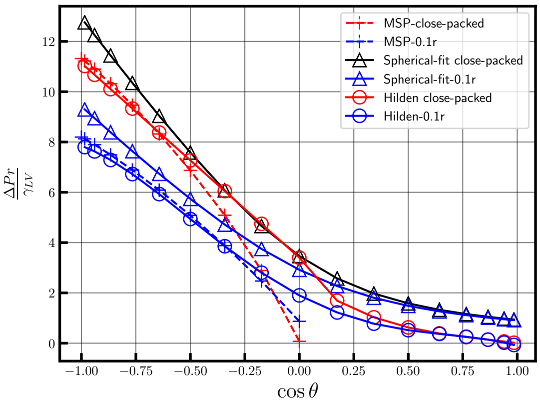

Figure 5.3: Comparison of pore entry pressure between the results in the work of Hilden et al. [Hilden and Trumble, 2003], spherical fit (3D C&R model) and Mayer-Stowe-Princen method.

calculated by Surface Evolver [Brakke, 1992]. However, there is no reliable experiments to validate the accuracy of any of these three calculations. It is difficult to judge which method fits better with the reality. For the work of Hilden et al. [Hilden and Trumble, 2003], they only consider the capillary pressure in planar close-packed spheres and hexagonally packed spheres with constant gap separation. If the radius of the sphere and gap separation is varied in certain range, how these three methods match with each other is still not clear.

Pressure hysteresis for 3D C&R model

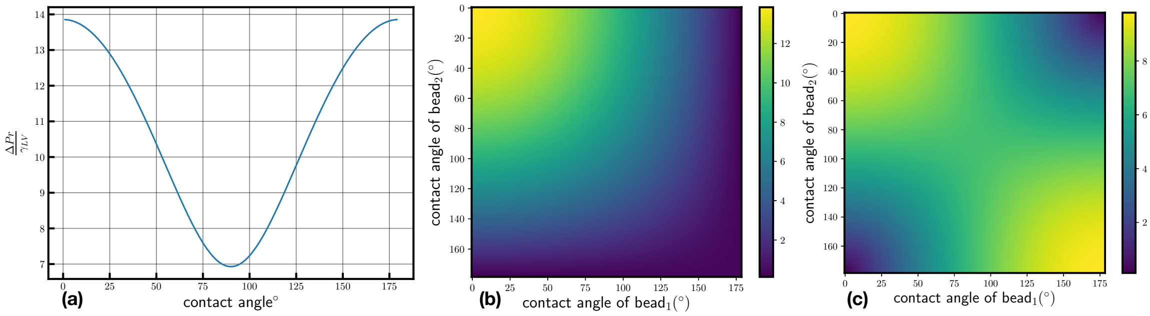

Figure 5.4: Capillary pressure hysteresis for three monodisperse beads with direct contact. (a) Homogeneous wet; (b,c) The color code represents the normalized capillary pressure hystersis for three monodisperse beads with inhomogenous wettability. One bead has a fixed contact angle of 3° (b), repectivley 90° (c). The contact angle of other two beads is varied in the full wettabity range of 0° to 180°.

With the burst equation in 3D, we calculate the difference of the capillary entry pressure for an invading and rejecting fluid meniscus in a 3D pore. In Fig.5.4(a), we plot the capillary pressure hysteresis with respect to different contact angle for homogeneous wet beads. We detect a minimum for contact angle of 90°. If we fix one bead with a small contact angle (3°), we can plot capillary pressure hysteresis with respect to the contact angle of the other two beads in Fig.5.4(b). In the figure it is shown that the capillary pressure hysteresis is reduced for increased contact angle of the other two beads. Due to the symmetry of beads, the trend will be the same if we fix one bead with a larger contact angle. The result of Fig.5.4(b) hints that whenever a highly wetting bead or non-wetting bead exists, the capillary pressure hysteresis will be reduced if we have the other two beads with the opposite wettability, which is experimentally confirmed in the work of Moosavi et al. [Moosavi et al., 2018].

We can also set a bead with a contact angle of 90° and vary the contact angle of the other two beads. As shown in fig.5.4(c). In fig.5.4(c), when both of the beads become wetting or non-wetting, the capillary pressure hysteresis is increased.

Even though the 3d C&R model is not exactly representing the threshold pressure due to the existence of liquid bridge and potential cross talk between two neighboring pores, we could still use it as a predictive tool for qualitative analysis for the capillary pressure hysteresis. This also underlines the dearth of knowledge in terms of the influence of wettability.

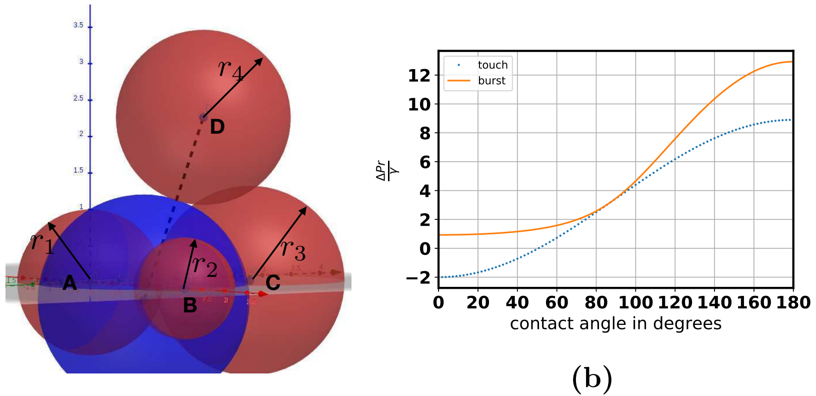

(a)

(b)

Figure 5.5: (a) Illustration of a spherical meniscus in blue touching a fourth bead with center D in 3D. (b) Plot of normalized Laplace pressure against contact angle based on Eq.C.61 and Eq.5.3.

5.1.2 Touch event in 3D

Similarily as shown in Sec.3.1.1 for the touch event in the 2D C&R model, the 'touch' event occurs when a meniscus that is in the stable range of Laplace pressure $\mathrm{d}P/\mathrm{d}V > 0$ between P_{min} and P_{max} touches the surface of a fourth sphere. The criterion for the touch event is also solved with Eq.C.76. For example in figure 5.5a, the blue spherical meniscus resting on sphere A, B, C touches the fourth sphere D. The critical curvature radius is calculated by a quadratic equation based on Cayley Menger determinan, more details are available in appendix C.3. Then we try to resolve the relationship between curvature radius R and θ for the touch event in ideal pore [Singh et al., 2017b]:

$$R = \frac{2r}{1 + \sqrt{6} - (3 + \sqrt{6})\cos\theta} \tag{5.3}$$

Combining Eq.C.61 and Eq.5.3, we could get $\cos\theta = \frac{4\sqrt{6}-9}{15}$, which corresponds to the intersection point in Fig.5.5b and it is around $\theta \sim 87°$. Again, it is in accordance with the calculation in the work of Singh et al. [Singh et al., 2017b]. In Fig.5.5b, we notice that the touch curve cross zero Laplace pressure and it is the time when $1 + \sqrt{6} - (3 + \sqrt{6})\cos\theta = 0$. For that contact angle (around 50.73°), the radius of curvature of the meniscus is infinite and the meniscus forms a flat plane when the meniscus is touching the fourth bead. When the contact angle is below 50.73°, the free meniscus can touch the fourth sphere with negative Laplace pressure. Eq.5.3 can not predict the condition when a touch event is not allowed. When contact angle is larger than 87°, there should be no chance to touch. But Eq.5.3 still gives us a number. So in implementation, we need to employ the burst curvature firstly to test whether there is touch event. If so, we could use Eq.5.3, otherwise just ignore it.

When solving the quadratic equation of Eq.C.76, there is a possibility that there is no solution for Eq.C.76. For that case, there will not be Laplace pressure calculated

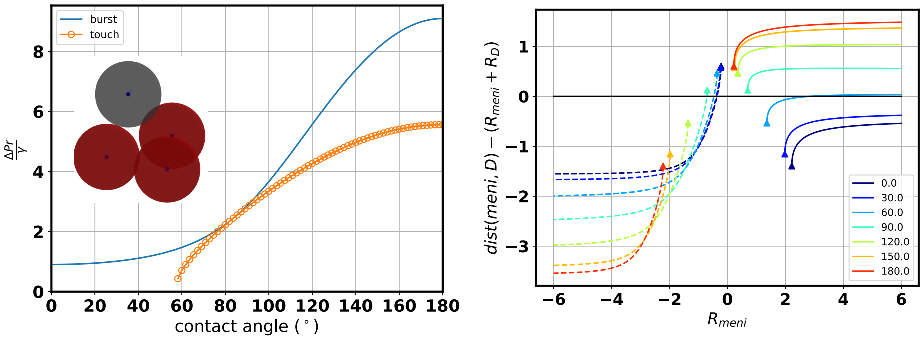

(a)

(b)

Figure 5.6: Dimensionless touch and burst pressure for different contact angles. (a) Coordinates of four beads area (-4.96,-4.01,-11.06), (-6.64,-2.78,-12.03), (-6.02,-4.57,-12.66), (-6.76,-3.66,-10.24)(gray sphere). The gray bead is the one to be touched. Four spheres have radius of an unit and contact angle of 44°. (b) $dist(meni, D)$ represents the distance between the touching sphere and the spherical meniscus center. R_{meni} indicates the radius of the spherical meniscus. The legend indicates the contact angle in degrees.

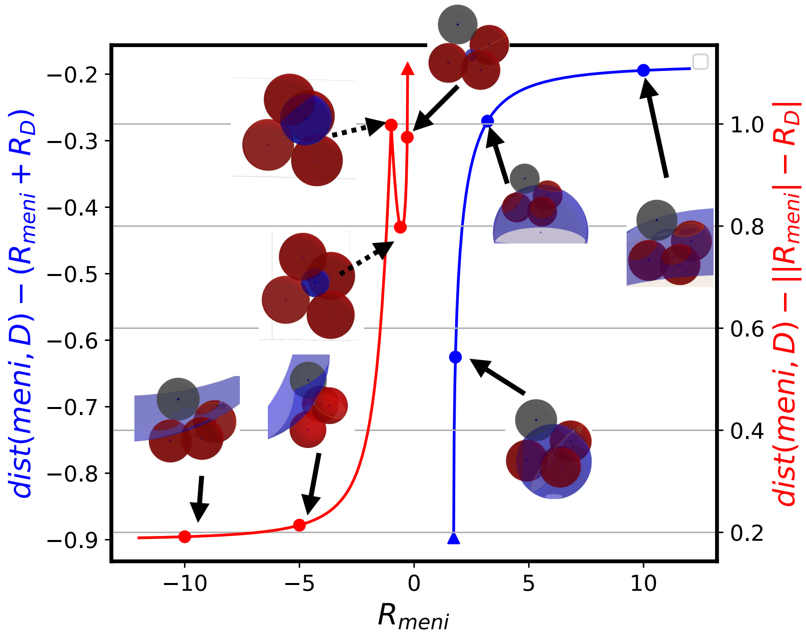

Figure 5.7: The contact is set as 44° and the bead coordinates are the same as in Fig.5.6. The triangles are the points where the burst events happen.

for the touch event. As shown in Fig.5.6, for some contact angle and geometrical configuration, we might not be able to calculate the Laplace pressure when the touch event happens. We take one example in Fig.5.7. Firstly, with the method described in Appendix H, we could determine the position of the meniscus given Laplace pressure and the contact angle. When the Y-axis value of the Fig.5.7 is smaller than 0, it means that the meniscus sphere and the fourth bead are intersecting with each other. We notice that for positive Laplace pressure, the meniscus is always intersecting with the fourth bead. And for negative Laplace pressure, only when $R_{meni} = -0.412$ we have the touch event. However, this touch events corresponds to the contact angle of the fourth sphere is 0°. And the radius could be calculated by modifying the coefficient in Eq.C.76, in which the contact angle of the fourth sphere is 0°. Combining Fig.5.6 and Fig.5.7, we know that even though we could not calculate the Laplace pressure when touch event happens, the touch event still dominate over the burst event.

5.1.3 Lamella burst event

In the process of depercolation, we need to first determine the condition when neighboring meniscus overlap with each other as shown in Fig.5.8, which is described as lamella burst in the work of Semprebon et al. [Semprebon et al., 2016]. The curvature radius of the spherical meniscus is solved analytically and more details are found in Appendix D.

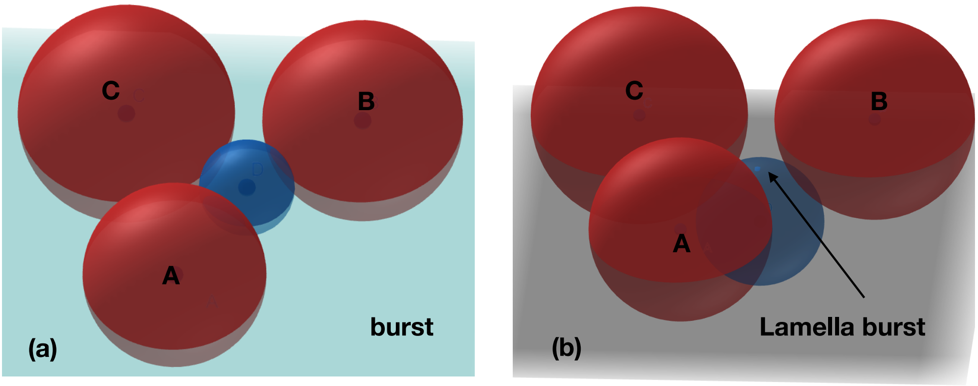

Figure 5.8: Illustration of the burst event and lamella burst event. (a) the center of the spherical meniscus is on the plane formed by the three spheres; (b) the spherical meniscus is touching the plane formed by the three beads. When the neighouring pore is also filled with liquid, due to symmetry of the beads, two menisci will overlap with each other, which is called lamella burst in the work of Semprebon et al. [Semprebon et al., 2016].

5.1.4 Instability of liquid bridge

For a precise computation of the residual oil saturation it is therefore of utmost importance to precisely compute the volume of the remaining capillary bridges between two neighboring beads. Liquid bridges between neighboring spheres play a pivotal role in determining the residual saturation as indicated in Fig.5.9(a). In Fig.5.9(a), we can notice that the total number of menisci is dropping when the remaining oil is displaced out of the porous media. In addition, the number of empty-filled interfaces

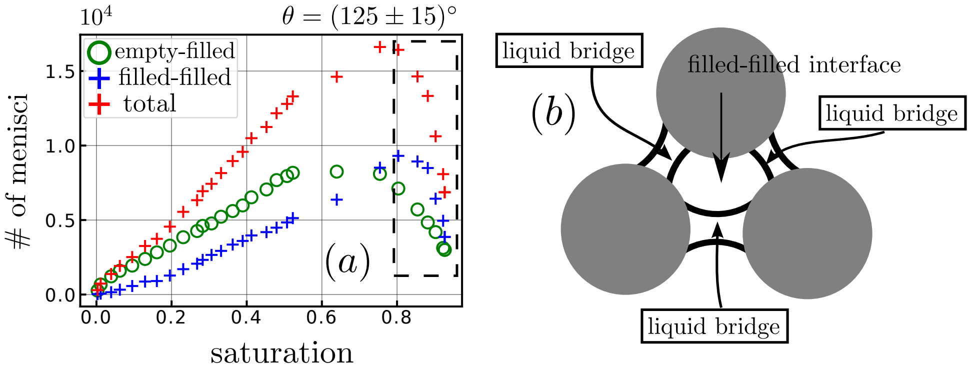

Figure 5.9: (a) Number of different types of menisci for advancing contact angles of 125°, which is a part of the figure 4.16. The region indicated by dashed rectangle is the main focus. (b) Illustration of the configuration filled-filled interface. The gray circles represent the spheres. The stability of the filled-filled interface formed by three spherical beads is closed related to the liquid bridges between every two beads.

and the number of filled-filled interface drop at the same time for the region indicated by dashed line in Fig.5.9(a). The stability of filled-filled interfaces are strongly related to the stability of the liquid bridge. As shown in Fig.5.9(b), before the neighboring filled-filled interfaces come in contact with each other, the boundary of the filled-filled interfaces is partially made of three liqud bridges. As a result, investigating the stability of liquid bridge is important in understanding the physical mechanim controlling the phenomenon we observe in Fig.5.9(a). The problem of liquid bridge or pendular ring shows up when a small amount of fluid forms an axisymmetric interface between two axisymmetric soild. The problem includes addressing the shape of the interface including volume and surface area under a given Laplace pressure. Characterization of the liquid bridge dates back to Delaunay [Delaunay, 1841], who classified the non-trivial surfaces of revolution with constant mean curvature via Young-Laplace equation. And the surfaces are obtained by revolving the axes for the roulettes of conics [Delaunay, 1841; Eells, 1987]. As a scientific topic lasts for more than two centuries, we have seen many contributions such as theoretical studies which approximates a capillary bridge as toroid [Fisher, 1926] and Derjaguin approximation [Willett et al., 2000]. It is worth noting that the toroidal approximation assumes the bridge meridional profile as a part of a circle, which is solved in 2D C&R model. In the following, we firstly review some important results in characterizing liquid bridge. On top of these results, we develop a criterion to determine the stability of liquid bridge, which is further employed in the model.

As shown in the work of Woodrow et al. [Woodrow et al., 1961], when the gravity is negligible and assuming that γ is the surface tension between the liquid-gas phase, $H_1 = \frac{\Delta P}{2\gamma}$ and $y(x)$ is the curve for liquid-gas interface of the liquid bridge in Fig.5.10,

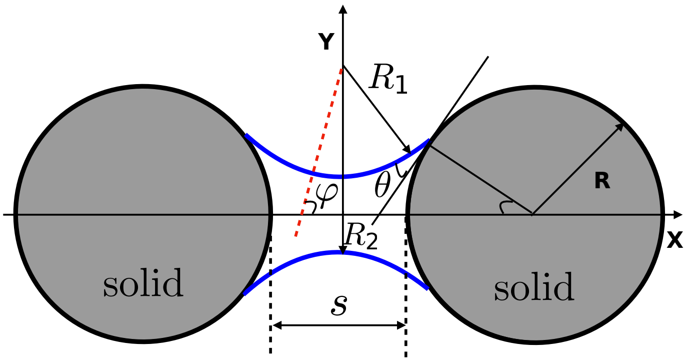

Figure 5.10: Illustration of a liquid bridge. The interfaces are indicated by blue curves.

two principal radius of curvature are:

$$\frac{1}{r_1}=\frac{d(\frac{\pi}{2}-\varphi)}{ds}=\frac{d(\cos\varphi)}{dx}=-\frac{d(\sin\varphi)}{dy},\frac{1}{r_2}=-\frac{\sin\varphi}{y} \tag{5.4}$$

It is worth mentioning that in Eq.5.4, $\frac{1}{r_2}$ is could be calculated via Meusnier's Formula [Do Carmo, 2016]:

$$\kappa_n=\kappa\cos\phi \tag{5.5}$$

where ϕ represents the angle between the pricipal normal and the surface normal. κ and κ_n represents the curvature of the curve and normal curvature.

The surface is obtained by revolving the profile, which gives the curvature of $-\frac{1}{y}$ for the circle perpendicular to the revolving axis. And the principal curvature is calculated by $-\frac{1}{y}\cos(\frac{\pi}{2}-\varphi)=-\frac{\sin\varphi}{y}$.

As a result,

$$\Delta P=\gamma(\frac{1}{r_1}+\frac{1}{r_2})=\gamma(\frac{d(\cos\varphi)}{dx}-\frac{\sin\varphi}{y})=-\gamma\frac{d(y\sin\varphi)}{ydy} \tag{5.6}$$

Eq.5.6 uses the parameterization of φ. Due to $\cos\varphi=\frac{y'}{\sqrt{1+(y')^2}}$ and $\sin\varphi=\frac{1}{\sqrt{1+(y')^2}}$,

$$\Delta P=\gamma(\frac{1}{r_1}+\frac{1}{r_2})=\gamma\left(\frac{y''}{(1+(y')^2)^{\frac{3}{2}}}-\frac{1}{y\sqrt{1+(y')^2}}\right) \tag{5.7}$$

In Eq.5.7, $\Delta P=P_o-P_i$ is the pressure difference between outside of the liquid bridge and inside of the liquid bridge. Multiplying with y' for Eq.5.7,

$$\begin{aligned}&\frac{\Delta P(y^2)'}{2\gamma}+\left(\frac{y}{\sqrt{1+(y')^2}}\right)'=0\\&\frac{\Delta P}{2\gamma}y^2+\frac{y}{\sqrt{1+(y')^2}}=C_1\\&y^2+\frac{y}{H_1\sqrt{1+(y')^2}}=\frac{C_1}{H_1}(H_1\neq 0)\end{aligned} \tag{5.8}$$

where C_1 is constant, $H_1 = \frac{\Delta P}{2\gamma}$.

Eq.5.8 recalls the Delaunay's roulettes [Do Carmo, 2016]. According to the work of Eells [Eells, 1987], when $\frac{C_1}{H_1} > 0$, the meridional profile fits the notary curve and it is the locus of the foci of a hyperbola rolling without slipping on a line. When $\frac{C_1}{H_1} < 0$, the locus will be the undulary, which corresponds to the locus of the foci of an ellipse rolling without slipping on a line. Eq.5.8 is further transformed:

$$y' = \pm\sqrt{\left(\frac{y}{C_1 - H_1 y^2}\right)^2 - 1} \tag{5.9}$$

Eq.5.9 is frequently used to evaluate numerically the profile of the liquid bridge as shown in Lian et al. and Erle et al. [Lian et al., 1993; Erle et al., 1971]. The constant C_1 is linked to the capillary force (F_{cap}) and it is constant over meridional profile of the capillary bridge surface [Erle et al., 1971; Gagneux and Millet, 2014]:

$$\begin{aligned} F_{cap} = 2\pi\gamma C_1 &= 2\pi\gamma\left(\frac{\Delta P}{2\gamma}y^2 + \frac{y}{\sqrt{1+(y')^2}}\right) = \pi\Delta P y^2 + 2\pi\gamma y \sin\varphi \\ &= 2\pi\gamma(H_1 R^2 \sin^2\beta + R\sin\beta\sin(\beta+\theta)) \end{aligned} \tag{5.10}$$

Eq.5.10 leads to the "gorge method" [Lian et al., 1993] to evaluate the capillary force at the neck of the bridge when we set $y = r_n, \varphi = \frac{\pi}{2}$. Based on Eq.5.9, a predictor-corrector integration scheme is employed, where Euler's method is the predictor and trapezoidal rule is the corrector. We use an example to illustrate the numerical integration. In Fig.5.11, we already notice that there will be two solutions of gap separation for the specific mean curvature. The stable branch is reached when separation decreases with the increasing filling angle [Gladkikh, 2005; Lian et al., 1993; Erle et al., 1971]. When $R + 0.5s^* = \frac{h_m}{R} + \cos\beta < 1$ as shown in Fig.5.11 (d), two spheres collide with each other and the corresponding volume will be negative because we remove the spherical cap volume inside the liquid bridge. We can further plot Fig.5.12 to show the double solutions. In Fig.5.12, for each specific gap separation between two spheres, we could always find two half-filling angles for a specific mean curvature. In addition, there will be a point where no combination of mean curvature and half-filling angle will guarantee the condition for the existence of liquid bridge. In Fig.5.12b, we notice that the curve for the "lamella burst" or "snap-in" [Semprebon et al., 2016] intersects with the curve of bridge instability at the point when the separation is around 1.05. Here the separation is equal to $(1.05 - 1) * 2 = 0.1$ in the work of Semprebon et al. [Semprebon et al., 2016]. For larger gap separation, before the pressure reaches the criteria for meniscus burst, the liquid bridge already reaches the unstable state. But when the spheres are getting closer to each other, Haines jump or lamella burst will happen before a single liquid bridge become unstable.

Solving Eq.5.8 for a given volume of liquid bridge or Laplace pressure is numerically expensive, one possible way to address the problem is interpolation based on tabulated values [Melnikov et al., 2015]. For the problem when Laplace pressure is given, we

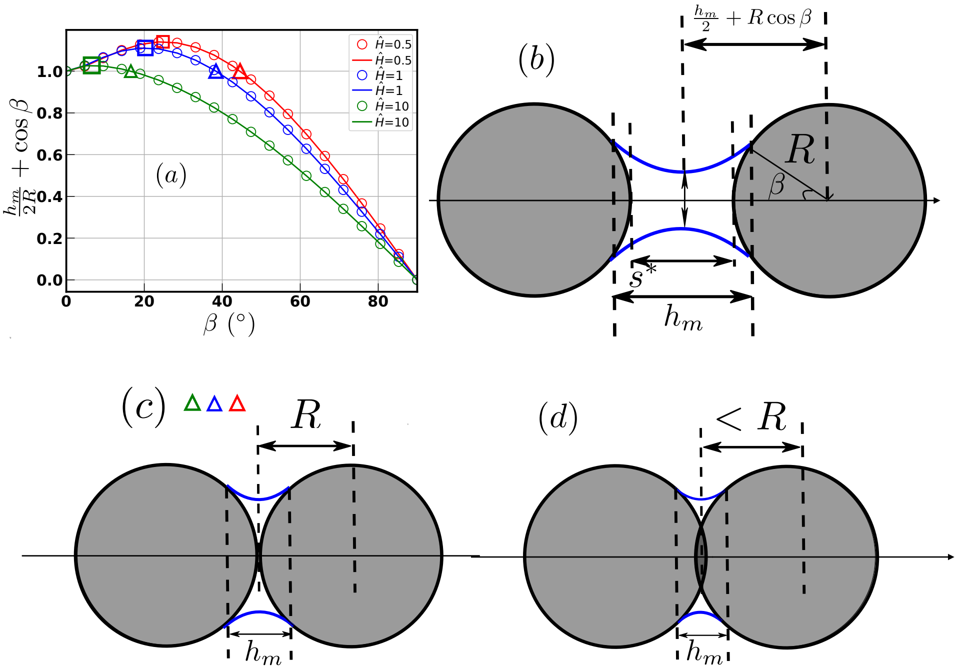

Figure 5.11: (a) Dimensionless distance between the sphere center to the neck against half-filling angle β for spheres with the same radius under different Laplace pressures ($\hat{H} = \frac{\Delta PR}{2\gamma}$). Contact angle is set as 0°. In this plot, circular points represent the analytic result based on Eq.5.12 (gap separation), Eq.5.13 (volume) and the solid lines are the numerical integration as in Lian et al. and Erle et al. [Lian et al., 1993; Erle et al., 1971]. Squares are the maximum value calculated with golden section search [Cormen et al., 2009]. (b) Illustration of the dimensionless distance for (a). (c) Two spheres are in contact with each other, which represents the situation as shown as triangles in (a). (d) Two spheres collide with each other.

developed a routine to determine the half-filling angle (β) for a given Laplace pressure and gap separation and for a constant contact angle of $\theta = 15°$ in a semi-analytical way. The contact angle is chosen for 15° because during the drainage for water displacing oil in OTS-coated glass beads, the contact angle is $\theta = 165° \pm 15°$ $(180° - 15° = 165°)$ [Singh et al., 2017b]. Before that, we perform a series of benchmark test for the validity of the algorithm. We firstly describe the analytical parts.

Two spheres with equal radii

For two spheres with equal radii, the neck radius (y_n) is easily calculated with Eq.5.8 because y' is 0 due to symmetry of the liquid bridge at the neck. Based on the work of Erle et al. [Erle et al., 1971], after normalizing mean curvature (H) with sphere

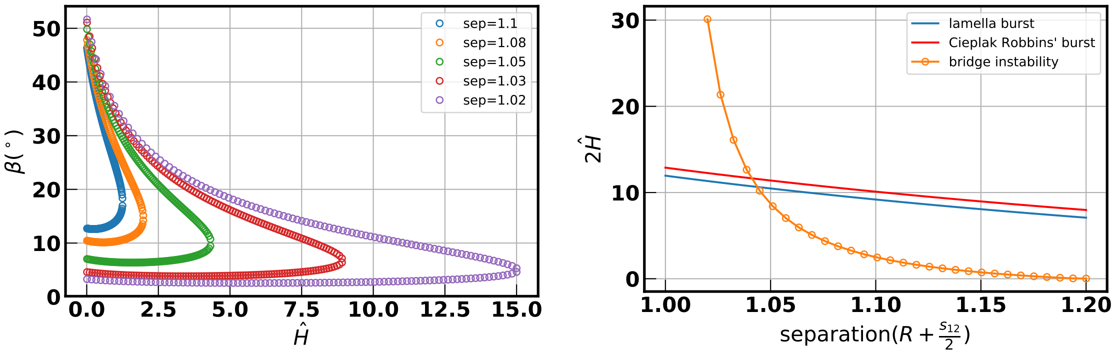

(a) **(b)**

Figure 5.12: Relationship between individual liquid bridge stability and the lamella burst. In this plot, the contact angle is set as 5° in order to compare with the lamella burst event. (a) Plot of half-filling angle (β) against mean curvature ($\hat{H}$) with constant separation (R+0.5s). (b) Maximum $2\hat{H}$ for different gap separation.

radius R, i.e. $\hat{H} = \frac{\Delta PR}{2\gamma}$,

$$r_n = \begin{cases} \frac{-1+\sqrt{1+4\hat{H}\sin\beta(\hat{H}\sin\beta+\sin(\beta+\theta))}}{2\hat{H}}, & \text{if } \hat{H} \neq 0. \\ \sin\beta\sin(\beta+\theta), & \text{if } \hat{H} = 0. \end{cases} \tag{5.11}$$

Because the contact angle of the defending phase is small for the defending phase

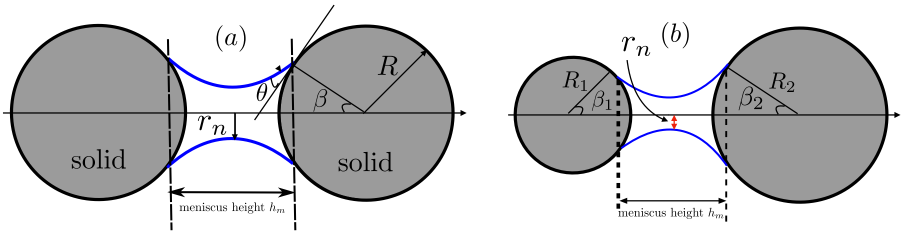

Figure 5.13: Illustration of neck radius (r_n) and meniscus height (h_m) (a) two spheres with equal radii (b) two spheres with different radii. $\beta_{i,j}$ is the opening angle.

and during drainage, the Laplace pressure $H > 0$. So the constant in Eq.5.8 $C_1 = HR^2\sin^2\beta + R\sin\beta\sin(\beta+\theta) > 0$. As a result, we fit the meridional profile with a nodoid. The meniscus height is calculated with the method shown in the literature [Woodrow et al., 1961; Erle et al., 1971]:

$$h_m = \frac{2r_nR}{1-k}(k\sin\Omega + (1-k^2)F(\Omega,k) - E(\Omega,k)) \tag{5.12}$$

In Eq.5.12, $k = \frac{1}{1+2r_n\hat{H}}$, $\Omega = \frac{\pi}{2} - (\theta+\beta)$, $F(\Omega,k), E(\Omega,k)$ are incomplete elliptic integral of the first kind and second kind. The liquid bridge volume is [Erle et al., 1971]:

$$\begin{aligned} V = 2\pi R^3 \Bigg(& (\frac{r_n}{1-k})^3((1-k^2)k\sin\Omega + 4k^3(\sin\Omega - \frac{\sin^3\Omega}{3}) - \\ & (\frac{4}{3})\sqrt{1-k^2\sin^2\Omega}k^2\sin\Omega\cos\Omega - (\frac{1}{3}+\frac{7}{3}k^2)E(\Omega,k) \\ & + (\frac{1}{3}+\frac{2}{3}k^2-k^4)F(\Omega,k)) + \cos\beta - \frac{\cos^3\beta}{3} - \frac{2}{3}\Bigg) \end{aligned} \tag{5.13}$$

We employ the results based on Surface Evolver [Brakke, 1992] as a benchmark for tests. In the simulation of Surface Evolver, the surface energy is set as:

$$U = \gamma(A_{LV} - A_{LS}\cos\theta) \tag{5.14}$$

In Eq.5.14, A_{LV}, A_{LS} represent the surface area between liquid-vapor and liquid-solid. θ is the contact angle.

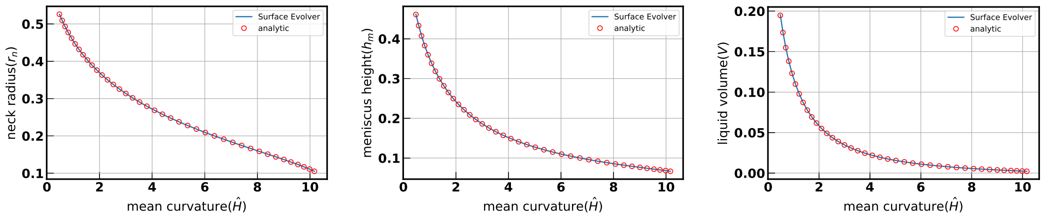

(a) **(b)** **(c)**

Figure 5.14: Comparison between analytic calculation and Surface Evolver results. Two spheres with radius of 1 and gap separation of 0.05. (a) neck radius with Eq.5.11;(b) meniscus height with Eq.5.12.(c) Liquid volume with Eq.5.13

In the Surface Evolver simulation, we start from an initial bridge volume of 0.2 and gradually decrease the volume. For each specific volume, we obtain a stable state, where we record the half-filling angle (β), neck radius (r_n), meniscus height (h_m) and Laplace pressure (ΔP). Given the Laplace pressure and half-filling angle, we employ Eq.5.11, Eq.5.12 and Eq.5.13 to calculate the corresponding analytic results. As shown in Fig.5.14, the neck radius, meniscus height and liquid volume match well between the analytic results and the simulation results based on Surface Evolver.

Two spheres with different radii

For two spheres with different radii, we will obtain two half-filling angles named with β_i, β_j, cf.Fig.5.13(b) and Fig.5.15. Given Eq.5.11, we can calculate the neck radius based on different half-filling angle from two spheres. We divide the liquid bridge into two parts based on the cross section going through the bridge neck as describe in Fig.5.15. For each part of the liquid bridge, we duplicate the same bead and liquid bridge. As a result, the original problem to calculate the volume of liquid bridge

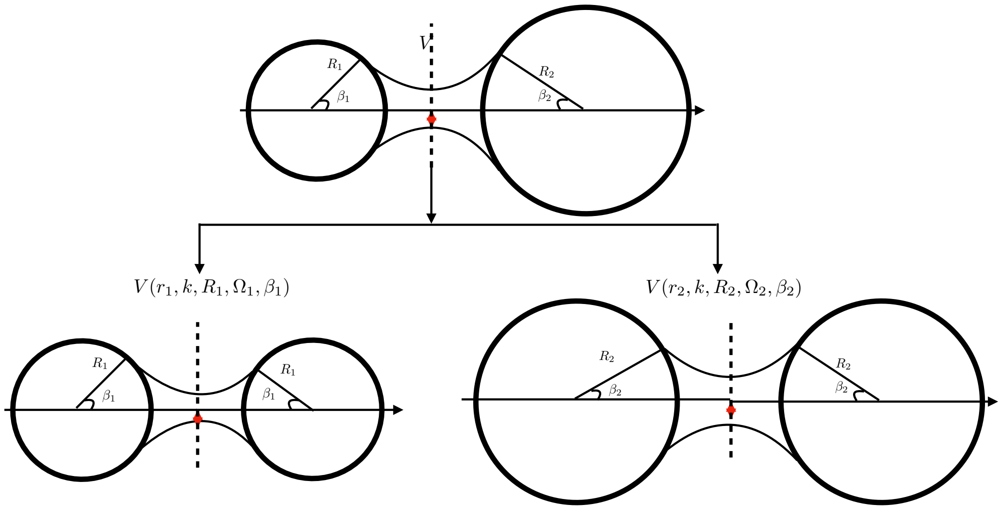

Figure 5.15: Illustration of liquid volume calculation for two spheres with different radii.

calculation is reduced to the problem where the diameter of the spheres is the same. The volume is calculated based on Eq.5.13:

$$V = \frac{1}{2}\Big(V(r_n, k, R_i, \Omega_i, \beta_i) + V(r_n, k, R_j, \Omega_j, \beta_j)\Big) \tag{5.15}$$

Similar as the volume calculation, we could use the average meniscus height to calculate the total meniscus height. We adopt the similar scheme to implement the simulation in Surface Evolver. However, for spheres with different radii, there are two different half-filling angles. As shown in Fig.5.17, the analytic result matches well with the results obtained from Surface Evolver. After validating the analytic equation for liquid bridge volume, neck radius and meniscus height evaluation, we continue to describe the algorithm as follows:

Algorithm to determine $\beta_{i,j}(P(\hat{H}), s, \theta)$

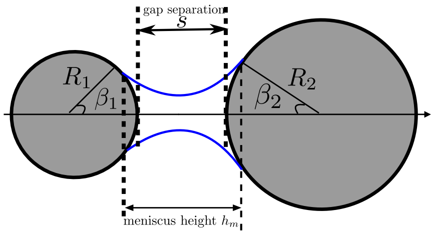

Figure 5.16: Two spheres with different radii.

In order to determine the profile of liquid bridge under a given Laplace pressure (H), the opening angle $\beta_{i,j}$ should be computed. With the relationship of β and H, we can further determine the stability of liquid bridge. We focus on the concave capillary

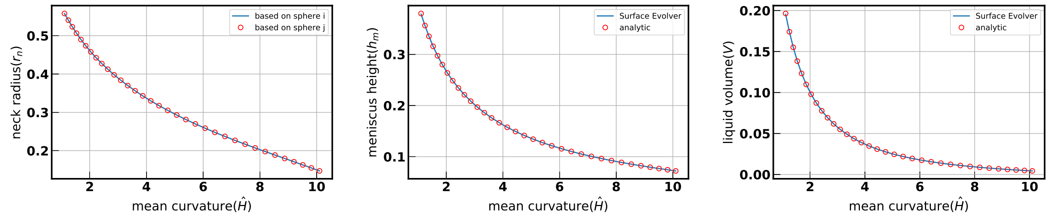

(a) **(b)** **(c)**

Figure 5.17: comparison between analytic calculation and Surface Evolver results. Two spheres(i,j) with radius of 1 and 2, and gap separation(s) of 0.05. (a) neck radius with Eq.5.11;(b) meniscus height with Eq.5.12;(c) Liquid volume with Eq.5.15.

bridge profiles. The analytical results we empolyed in Erle et al. [Erle et al., 1971], i.e. Eq.5.12 and Eq.5.13 are valid when $\theta + \beta_{i,j} \leq \frac{\pi}{2}$.

- For a given β_1, we derived the following equation by considering the boundary condition:

  $$M = H_1 R_1^2 \sin^2 \beta_1 + R_1 \sin \beta_1 \sin(\beta_1 + \theta) = H_1 R_2^2 \sin^2 \beta_2 + R_2 \sin \beta_2 \sin(\beta_2 + \theta) \tag{5.16}$$

  Using the following abbreviation $N = H_1 R_2^2 + R_2 \cos\theta, K = R_2 \sin\theta, t = \sin\beta_2$, Eq.5.16 can be represented as:

  $$\begin{aligned} M &= t^2 N + t\sqrt{1-t^2}K \\ 0 &= t^4(N^2+K^2) - t^2(K^2+2MN) + M^2 \end{aligned} \tag{5.17}$$

  Solving the biquadratic Eq.5.17, we need to consider the determinant $\Delta = K^2(K^2 - 4M^2 + 4MN)$. If $\Delta > 0$, there are two solutions but not both of them are valid. Firstly, the solution should satisfy that the neck radius is positive. Secondly, we need to check $M = t^2N + t\sqrt{1-t^2}K$ is in accordance with Eq.5.17. In addition, $\sin\beta_2 > 0$, we obtain the following expression to compute the half opening angle β_2:

  $$\sin\beta_2 = t = \sqrt{\frac{K^2 + 2MN \pm \sqrt{K^2(K^2 - 4M^2 + 4MN)}}{2(K^2+N^2)}} \tag{5.18}$$

- For each Laplace pressure, we calculate the distance between the center of the two spheres based on Eq.5.12. Again, we employ golden section search to find the maximum value in Y axis. And for a given gap separation, we obtain the corresponding β_1 iteratively.

- Having obtained β_1, β_2, we could directly calculate the gap separation (s), surface area and volume as shown in Eq.5.15. Here we show an example when the ratio of two spheres radii is 3.

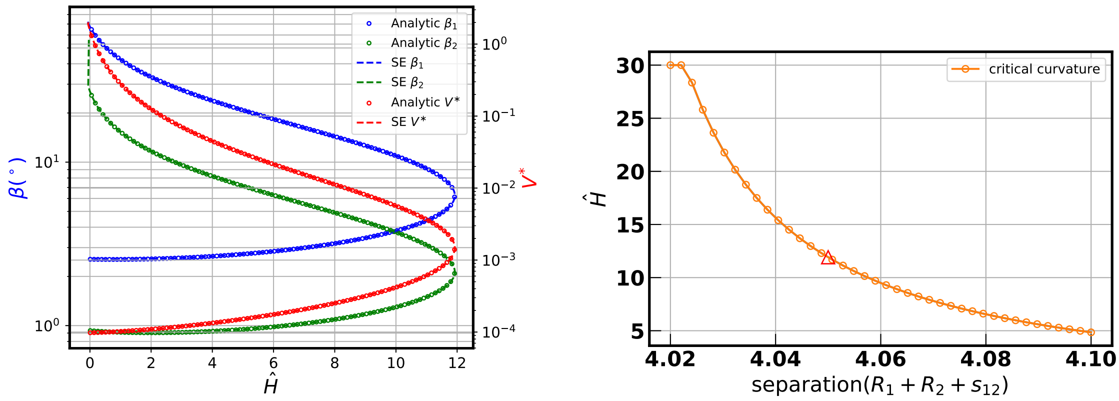

(a) **(b)**

Figure 5.18: In this plot, the contact angle is set as 15° and $\frac{R_2}{R_1} = 3$. (a) Plot of half-filling angle(β_1, β_2) and dimensionless volume (V^*) against mean curvature($\hat{H}$) with constant separation of 4.05. (b) Maximum $\hat{H}$ for different gap separation. The triangle in this plot represents the critical curvature in (a).

5.1.5 Rupture distance

Volume controlled

For a given volume V_{ij}, there exists a critical gap separation S_c, which will lead to the rupture of the liquid bridge. Models as in Lian et al. and Willett et al. [Lian et al., 1993; Willett et al., 2000] are frequently employed to evaluate the rupture distance:

$$S_c^{lian} \simeq (1+\frac{\theta}{2})\sqrt[3]{V^*}, \quad S_c^{Willett} \simeq (1+\frac{\theta}{2})(\sqrt[3]{V^*}+\sqrt[3]{(V^*)^2}/10) \tag{5.19}$$

Pressure controlled

The pressure controlled case represents that the liquid brdige volume is no longer fix. For a given Laplace pressure, there is a distance between two spheres when the liquid bridge is no longer stable. In the work of Gladkikh [Gladkikh, 2005], it is already stated that the pressure-controlled problem differs from the volume-controlled case considered in the literature [Erle et al., 1971]. In order to show the difference between the volume-controlled and pressure-controlled condition, we employ an example combining the analytical method and results based on Surface Evolver simulation. In Fig.5.19, we notice that either for the SE simulation results or the analytic results, there is a maximum Laplace pressure at a fixed gap separation. For a pressure-controlled model, we could still employ the idea based on mechanical unstable condition to identify the stable branch due to $\frac{\partial P_c}{\partial \Delta V} > 0$. As a result, the bridge will break when $\hat{H}$ is around 4. Another way to consider this problem is based on the drainage process. If the liquid bridge is still connected to the outlet, the process of displacing the liquid between the liquid bridge is more realistic to be explained by pressure-controlled model compared with the volume controlled model. If we assume that it is volume-controlled process, a high pressure will be build locally as shown in Fig.5.19. Because the theoretical rupture pressure for the liquid bridge will be $\hat{H} < 0$ based on both of the SE results and Willett's model.

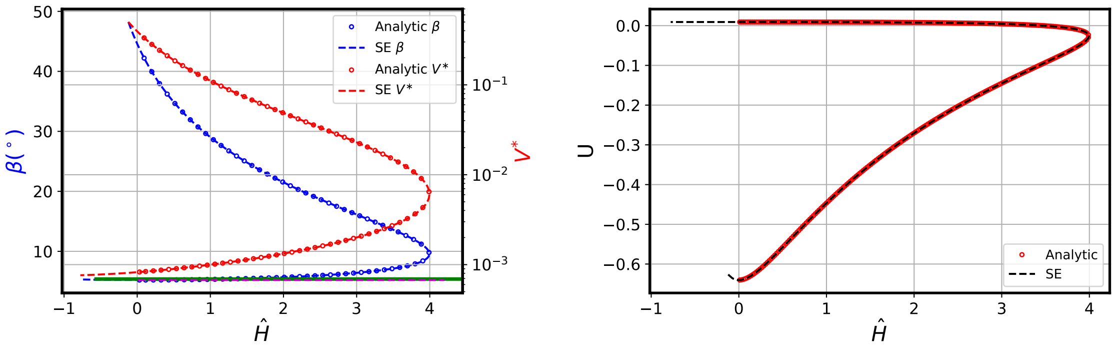

(a) **(b)**

Figure 5.19: Two sphere with equal radii. The gap separation is 0.1. Contact angle is 15°. (a) The green horizontal line represents the volume calculated with Eq.5.19 [Lian et al., 1993]. The magenta dashed line represents the volume calculated with Eq.5.19 [Willett et al., 2000]. (b) Surface energy($U = \frac{A_{LV}-A_{LS}\cos\theta}{R_1^2}$) with respect to $\hat{H}$. The interface area between the defending and invading liquid is calculated with [Erle et al., 1971]. The surface energy is calculated with Eq.5.14.

When $\hat{H} > 0$ for the drainage case, there is a critical gap separation where no stable liquid bridge exists. Based on [Erle et al., 1971] when the Laplace pressure is 0:

$$\frac{h_m}{2} + \cos\beta = -\sin\beta\sin(\beta+\theta)\ln\left(\frac{\sin(\beta+\theta)}{1+\cos(\beta+\theta)}\right) + \cos\beta \tag{5.20}$$

Given spheres with same radii (R_1), the maximum of the gap separation between two spheres is reached:

$$s_{12}^{cri} = 2((\frac{h_m}{2} + \cos\beta)_{max} - 1)R_1 \tag{5.21}$$

Fig.5.21, shows the typical case for the maximum gap separation. In Fig.5.21, by comparing the analytic result and the result from Surface Evolver, we further validate the maximum s_{12} when $\hat{H} > 0$. For spheres with different radii ($R_1 < R_2$), by the neck radius relationship $\sin\beta_1\sin(\beta_1+\theta)R_1 = \sin\beta_2\sin(\beta_2+\theta)R_2$, we could obtain the β_2. Again with β_1, β_2, we are able to derive the maximum gap separation iteratively. And we plot Fig.5.21 as an example with radii ratio of 2.

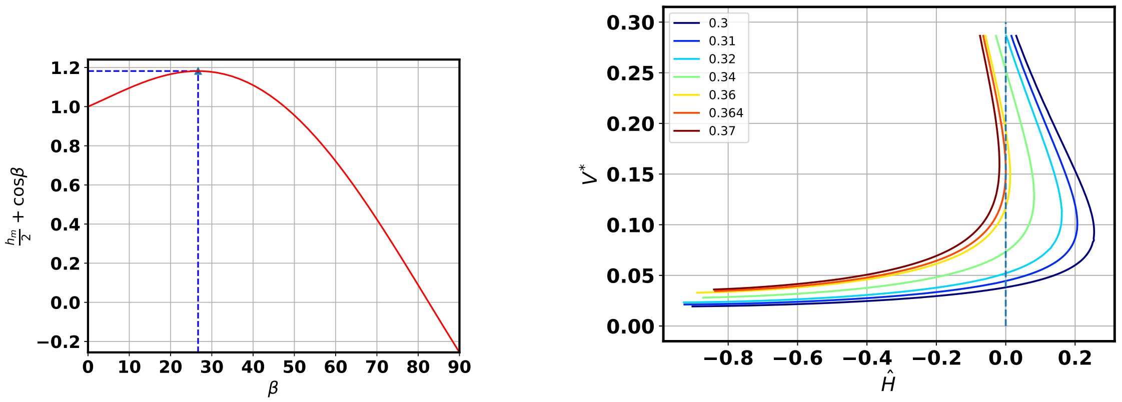

(a) **(b)**

Figure 5.20: determination of maximum gap separation for spheres with equal radii. (a) Catenoid liquid bridge. Contact angle is 15° in this plot. And the maximum $\frac{h_m}{2} + \cos\beta$ is reached at point (26.67°, 1.18)(corresponding $s_{12} \approx 0.36$). (b) Results from Surface Evolver. The legend indicates $\frac{s_{12}}{R_1}$. Contact angle is set as 15° and the $R_1 = R_2$.

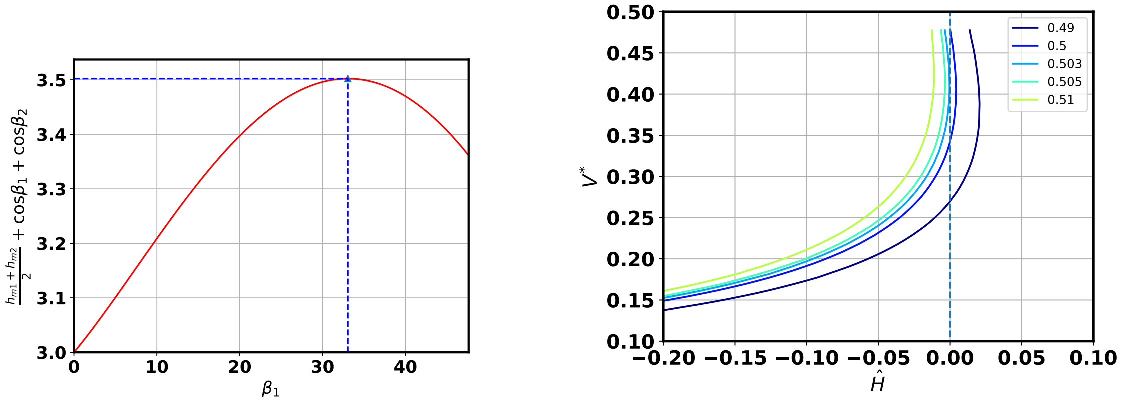

(a) **(b)**

Figure 5.21: determination of maximum gap separation for spheres with unequal radii. (a) Catenoid liquid bridge. Contact angle is 15° in this plot. And the maximum $\frac{h_{m1}+h_{m2}}{2} + \cos\beta_1 + \cos\beta_2$ is reached at point (33.05°, 3.50)(corresponding $s_{12} \approx 0.5$). (b) Results from Surface Evolver. The legend indicates $\frac{s_{12}}{R_1}$. Contact angle is set as 15° and the $2R_1 = R_2$.

5.2 Algorithm in drainage

Similarly as in 2D C&R model, we develop a model based on the local pore-scale invasion events based on the geometrical criteria for instability [Motealleh et al., 2013; Melnikov et al., 2015].

- Criterion 1. Burst events. We assume that the meniscus between the invading and defending liquid is still spherical with constant curvature [Haines, 1930; Melnikov et al., 2015]. As a result, Haines jump in three dimension and the critical curvature is determined by Eq.C.29.

- Criterion 2. Touch events. When the spherical meniscus touches the fourth bead determined analytically by Eq.C.76.
- Criterion 3. Lamella burst event. When two neighboring pores are occupied, there exists a pressure where a collision of two opposing menisci happens [Semprebon et al., 2016].

5.3 Results

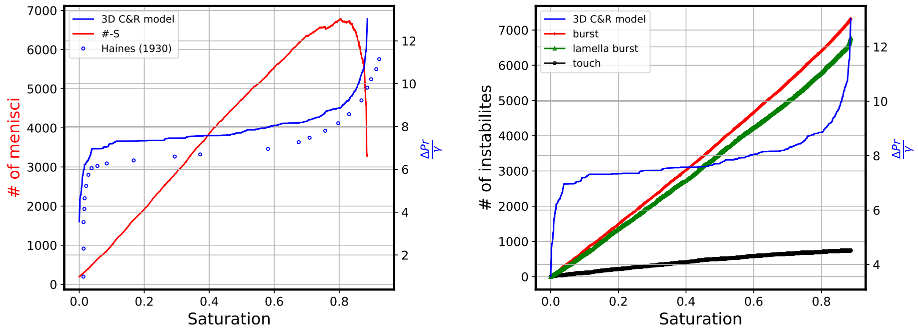

(a) **(b)**

Figure 5.22: (a) P-S and # of menisci-S curves; The legend Haines (1930) indicates the data are extracted from the work of Haines [Haines, 1930]. (b) Different events against saturation of the invading liquid.

In Fig.5.22, we plot the number of menisci against the saturation of the invading liquid. Compared with the results in discrete interface analysis as shown in Fig.4.14, the growing number of menisci also firstly increases linearly with the increasing saturation of the invading liquid. To a certain saturation, there is a sharp decrease of the number of menisci. In Fig.5.22(b), we notice that the touch event is never dominating for all the saturation range. In addition, the number of lamella burst events happen with the similar magnitude with the burst events. During the process when the saturation of invading liquid is exceeding 0.8, burst events are still dominating dominating over other events, which is in accordance with what we observe in Fig.5.9, i.e. the number of empty-filled menisci is decreasing during this stage.

Chapter 6

Strong imbibition

Imbibition is an ubiquitous process for fluid flow in porous media, where a wetting fluid displaces the non-wetting one [Alava et al., 2004]. Previous works [Lenormand, 1990; Reyssat et al., 2008; Gruener et al., 2012; Rabbani et al., 2018; Lu et al., 2019] already investigated how the local pore geometry influences the invasion pattern both in (quasi) 2D and 3D. As summarized in the work of Lenormand et al. [Lenormand, 1990] for the phase diagrams in the imbibition process in quasi-2D microfluidic-system, there are two types of invasion patterns with flat interfaces (small pore-to-throat ratio) and ramified structures (large pore-to-throat ratio) in the capillary domain without film flow. Recently, Zhao et al. and Primkulov et al. [Zhao et al., 2016; Primkulov et al., 2018] conduct experiments and simulation to investigate corner flow for strong imbibition, where the invasion front becomes ramified when the invading liquid gets more wetting. The work of Zhao et al. [Zhao et al., 2016] is conducted in a quasi-2d system, where the circular pillars have a finite size. However, as shown in chapter 4 by three various quantification methods, the invasion mode of the wetting fluid for low contact angle is compact when the porous media is made of smooth glass beads, which is also summarized in the work of Singh et al. [Singh et al., 2019] as the fluid interface during the primary imbibition is always flat with little trapping of the nonwetting fluid. The apparent difference in the invasion pattern in experiments of a quasi 2D model [Zhao et al., 2016] and 3D bead packs [Singh et al., 2016, 2019] for the imbibition process drives us to explore the leading parameters to determine the invasion pattern when the liquid is wetting the porous media. The primary parameter discussed in this chapter is geometry in macro- and micro-scale.

The macroscopic geometry discussed in this chapter refers to the void space formed the porous media. The void space is the space that is remaining from the total volume when excluding the solid grains. For example, in the 2D C&R model in chapter 3, we noticed that by letting the disks getting closer, the statistics of probability of pore-scale events inform us that the change in pore geometry affects the dominating pore-scale invasion mode because touch events dominate over overlap events and burst events. In addition, it was shown in the work of Gruener et al. [Gruener et al., 2012] that pores, which are longer than they are wide, lead to no continuous liquid-vapor interface with coalesced menisci during the imbibition process. For the glass bead packs in the work of Singh et al. [Singh et al., 2016], the macroscopic geometry of the beads guarantees that the potential void space is relatively homogeneous. However, how to quantify the pore geometry and further how to investigate the influences of the macroscopic pore geometry on the fluid invasion process is still lacking in literatures.

The microscopic geometry represents the smaller scale i.e. the surface properties of the beads or other porous media. Previous experiments in the work of Lukyanov et al. [Lukyanov et al., 2012] have already shown that the roughness length scales plays an important role for liquid flow within Ottawa sands. Ottawa sands are rounded grains of pure quartz and have the similar macroscopic geometry with glass beads but the surface properties are different, which provides a good comparison for investigating the leading parameters influencing the imbibition process.

In order to investigate how geometry of porous media influences the fluid displacement pattern, we conducted and analyzed a series of fluid displacement experiments using grains with different geometry and surface properties via computed tomography.

6.1 Experiment setup

6.1.1 Sample holder

Available data from Singh et al. [Singh et al., 2016] explored liquid imbibing water into porous media is made of smooth monodisperse glass beads at a contact angle of $\sim 20°$ using X-ray tomography. To enable good comparison to those data, we employ a similar experimental setup to conduct experiments for natural sands and angular glass granulates. More details about the experimental procedure are available in the work of Singh et al. and Scholl [Singh et al., 2017b; Scholl, 2015]. In the following, we briefly describe our experimental setup. The porous media is made of glass granulates and Ottawa sand grains are placed in a cylindrical sample holder as shown in Fig.6.1. For the purpose of obtaining small contact angle of $(20 \pm 10°)$, Ottawa sand grains and glass granulates are cleaned with piranha etch, a mixture of H_2O_2(50%) and H_2SO_4(50%). Further, the cleaned sand grains and glass granulates are rinsed with hot water. A metal mesh is placed on the bottom part. In the work of Scholl [Scholl, 2015], a water-wet filter paper was used instead of the metal mesh. The metal mesh was used due to the strong imbibition of the invading liquid for the ottawa sand grains, the water-wet filter would immediately imbibe a large amount of liquid and it would be very difficult to achieve a situation where the liquid interfaces are stable to take a tomography. The metal mesh at the top in Fig.6.1 is to make sure that the grains are not moving during the invasion of liquid. At the bottom part of the cylindrical sample holder, an elastic tubing (Masterflex Tygon Fuel &

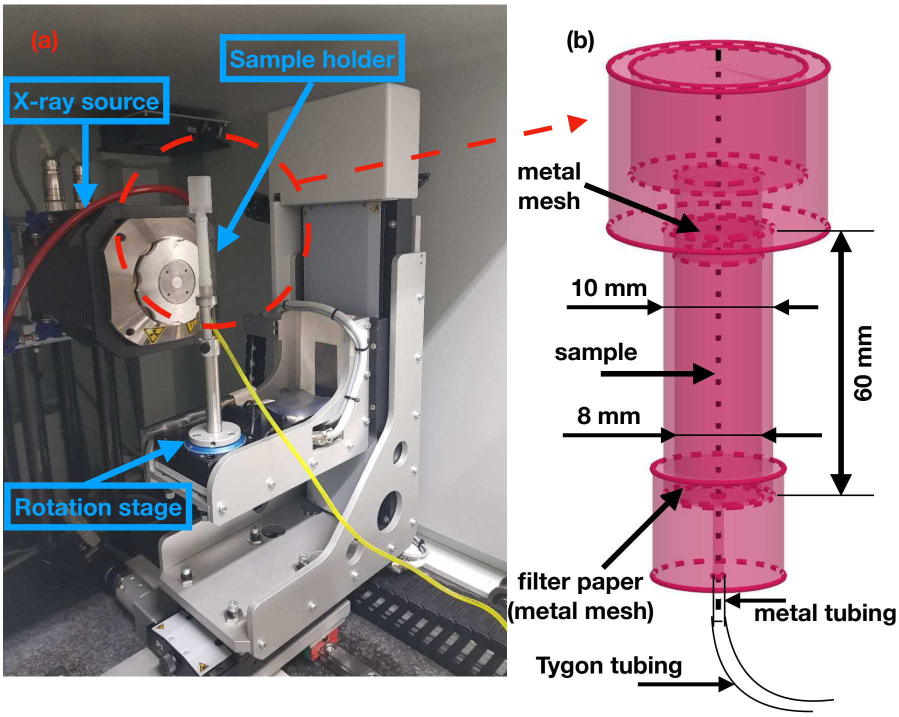

Figure 6.1: (a) photograph of sample placed inside our in-house CT; (b) is an illustration of the part with dashed circle in (a). These parts in (b) are made of polycarbonate.

Lubricant tubing, Novodirect GmbH, Kehl, Germany) is connected via a metal pin. For the volume control imbibition, the Tygon tubing is connected to a Hamilton glass syringe mounted on a homemade computer-controlled syringe pump. For a pressure controlled case, a reservoir with adjustable height is connected with the Tygon tubing.

6.1.2 Lab-based micro-CT

The majority of the presented experiments were conducted in an in-house cone-beam micro-CT (X-tom) assembled by the ProCon company. The 12-bit detector C7942SK-25 produced by Hamamatsu has an area of (120×120 mm^2) with a resolution of (2400×2400 Pixel^2). The minimum exposure time is 500 ms. High resolution microfocus X-ray transmission tube XWT-160-TC performs with a voltage range from 10 KeV to 160 KeV and a current range from 50 μA to 1000 μA. A small number of the presented experiments were conducted with Nanotom in Max Planck Institute for dynamics and self-organisation in Göttingen. Nanotom is a 180-KeV in-house computed tomography produced by GE-Measurement, which has very similar specifications as the X-tom from ProCon. The detector has a resolution of (2304×2304 Pixel^2). The acquired attenuated images are reconstructed to obtain the corresponding tomography via VG Studio 3.2 (Volume Graphics GmbH, Heidelberg, Germany). Segmentation and further image analysis of the reconstructed tomographies are achieved by Avizo software (`https://www.fei.com/software/amira-avizo/`). Details of the protocol for image segmentation and processing can be found in the dissertation of Scholl [Scholl, 2015].

6.2 Volume controlled imbibition-Ottawa sand

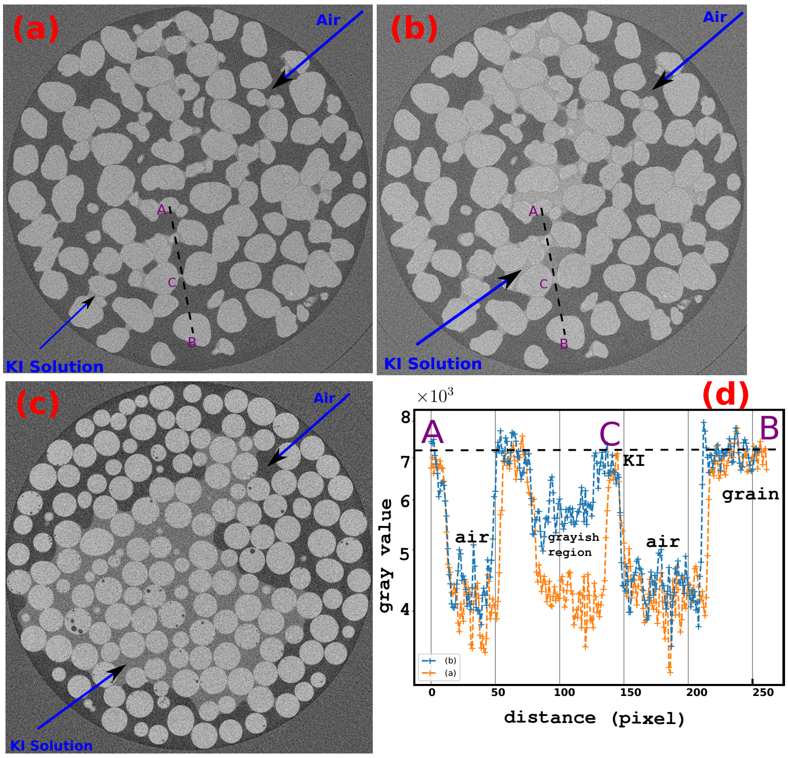

Figure 6.2: Cross sections through tomography images of aqueous KI-solution imbibing into piranha-cleaned Ottawa grains at early stage (a) and later stage (b). The aqueous KI-solution has been volume-controlled added to the cell at rate of 10 μL/min. (c) Same experimental conditions as in (a,b) but with Piranha-cleaned glass beads (diameter:355-425μm) instead of Ottawa quartz grains. (d) A gray value profile along the line ACB indicated in (a,b).

Since the experiments in the work of Singh et al. and Scholl [Singh et al., 2017b, 2016] were conducted with a constant flow rate of the invading liquid, we adopt the same protocol to conduct the experiments. We started experiments with Piranha-cleaned Ottawa quartz grains (sieve fraction: (600-850)µm), where air was displaced by an aqueous KI-solution (density: 1.08g/ml) that provides a sufficient X-ray contrast. Ottawa quartz grains are characterized by a surface roughness in the order of a few µm [Yang et al., 2016]. The advancing contact angle of water/air interface on smooth Piranha-cleaned quartz surface was determined to $\theta = (20 \pm 10)^{\circ}$, which can be assumed to give an approximation of the advancing contact angle of Ottawa sands. The tomography images in Fig.6.2(a) and 6.2(b) show cross-sections of the sample close to the filter paper that paves the bottom of the cell. It is evident that the aqueous KI-solution preferentially invades the narrow gaps around the grain contacts. This is clearly different from the fluid distribution observed in smooth glass bead pack (sieve fraction: (355-425) µm), as displayed in Fig.6.2(c). The invading fluid always develops a compact front. However, due to the fact that there is no chance to capture the stable liquid interface for the imbibition experiments, we change to another setup with pressure-controlled system.

6.3 Pressure controlled imbibition-Ottawa sand

Since the time resolution of in-house CT did not capture the liquid invasion process for the volume controlled imbibition experiments, we change the way to control the liquid advance. The homemade computer-controlled syringe pump is replaced with a reservoir of invading liquid with adjustable height, which guarantees an abundant supply of invading liquid during the imbibition process. As the data acquisition time is about 1 h, this defined also the time interval within that no changes in the liquid distribution should occur. As a result, we need to determine the situation when the invading liquid is in equilibrium in an efficient way: To verify the state of equilibrium, we recorded a sequence of 2D absorption images at different times. And then we directly performed image subtraction between two absorption images, c.f. Fig.6.3. The time delay between image (a) to image (b) in Fig.6.3, around 10 minutes, the wetting invading liquid is still flowing, as revealed by the image subtraction that is displayed as panel (f). From image (d) to image (e), we do not see particular white regions, which indicates that the majority of the liquid is in equilibrium. Even though we are not able to resolve creeping flow within the roughness [Lukyanov et al., 2012] with this method, it provides a fast estimation about the acquisition time needed to take tomography. For example, if we want to take a tomography with 800 projections with an exposure time of one second and no average of the images, it takes around 30 min to record all the projections. In that case, we need to wait until two absorption images taken between 30 min do not have conspicuous change. Based on the results of our current experiments, it takes at least around 12 hours for to reach a sufficient stabilization of the front to capture a full tomography without artifacts.

To quantify the invasion pattern obtained by tomographic images, we firstly plot the mean finger area profile over the vertical direction as shown in Fig.6.4. The glass beads and Ottawa sand grains are both Piranha cleaned, which guarantees that the surface is strongly hydrophilic. Compared with the mean finger area in the imbibition process for smooth glass beads as shown in Fig.4.4, we already notice a very different feature. For Ottawa sand, the mean finger area along the vertical direction is growing homogeneous. When the saturation of the invading liquid reaches around 0.2∼0.3, the bottom region begins to expand. In Fig.6.5, we could clearly specify that the invading liquid wets the contact between the Ottawa sands at the beginning. For Fig.6.5(c), we notice that at the bottom part, there is a continuous liquid cluster formed. This

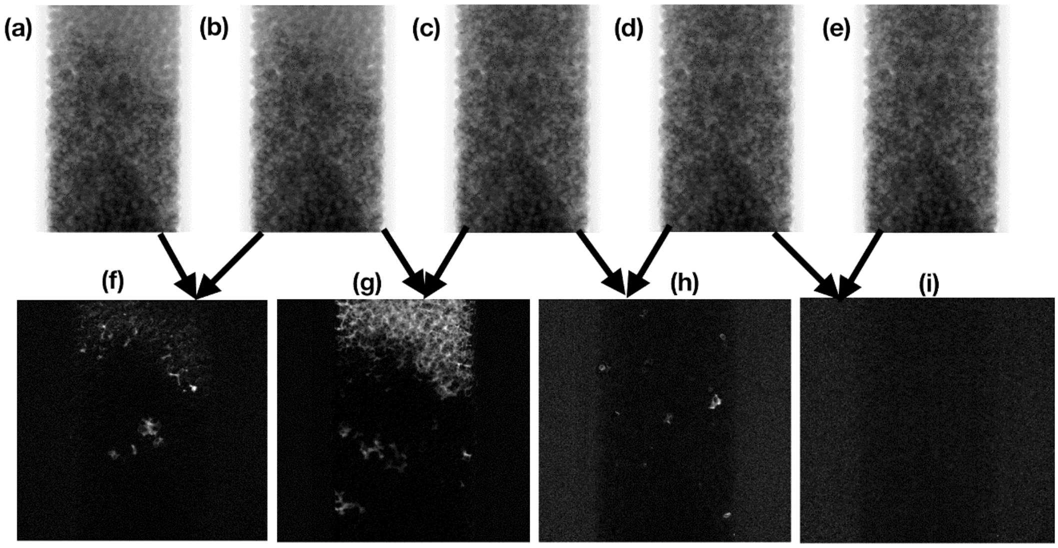

Figure 6.3: Absorption images during one equilibration period in the experiments displacing air with KI-water solution (1.08 g/ml) in piranha-cleaned Ottawa sand. Time intervals between two consecutive images: 12 minutes (a-b), 10 hours 29 minutes (b-c), 5 hours 13 minutes (c-d), 1 hour 14 minutes (d-e). (f,g,h,i) are differential images between two consecutive absorption images as indicated by the arrows. The white regions in image (f) to (i) indicate that there are changes of X-ray attenuation.

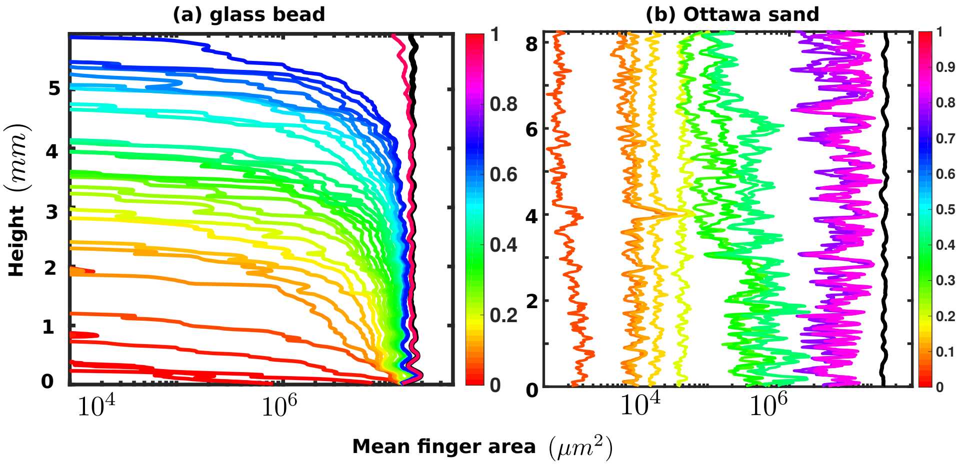

Figure 6.4: (a) Mean finger area distribution for the Piranha-cleaned smooth glass bead, which is also Fig.4.4(a). (b) Ottawa sand grains. Y axis represents the height and 0 indicates the bottom part in the region of interest, which is close to the bottom of the metal grid. The black line indicate the pore area, which is the maximum area for the finger area. Color codes indicate the saturation of the invading liquid.

matches the expansion of mean finger area in Fig.6.5 when the saturation of the invading liquid reaches around 0.2∼0.3. The feature identified in the experiment of

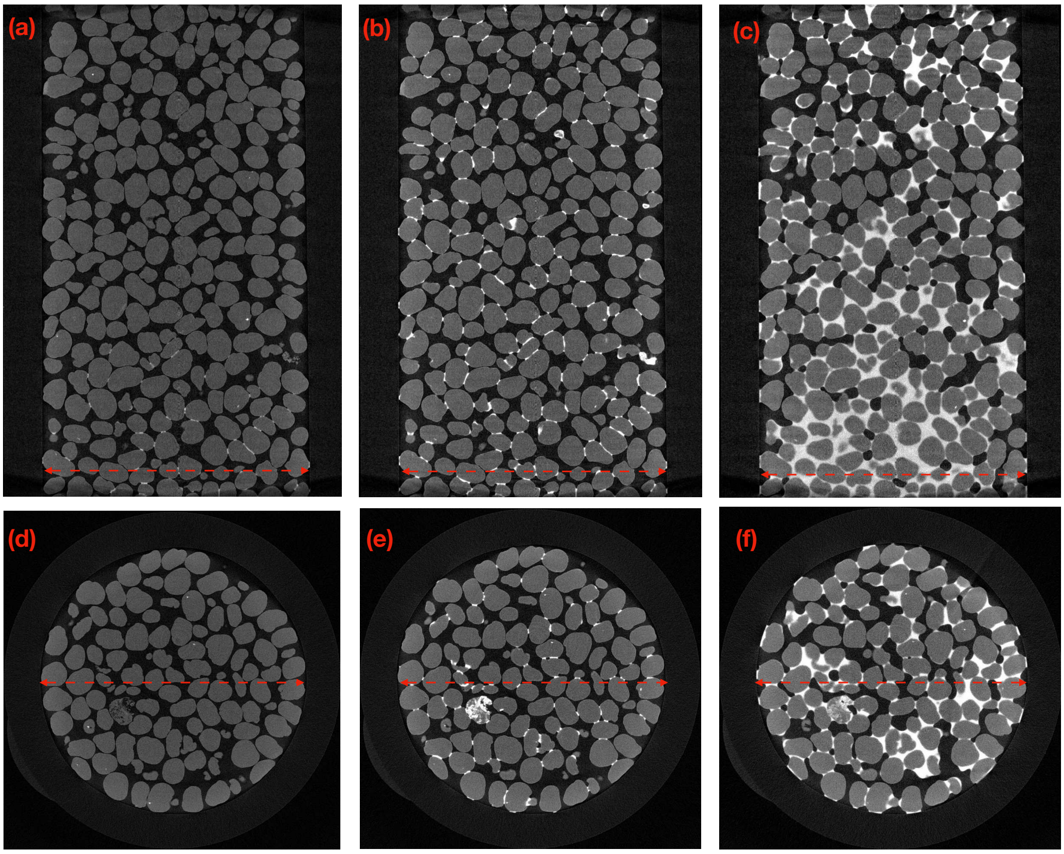

Figure 6.5: Cross section along the vertical direction. (a) nearly dry image (time t=0); (b) Saturation of the invading liquid is 0.11 (t=1180 minutes); (c) Saturation of the invading liquid is 0.34 (t=7560 minutes). (d,e,f) are a cross section of the (a,b,c) at the same height. The inner diameter of the cylinder is 8mm indicated with the red dashed arrow. The bright white phase is the invading liquid.

Ottawa sand is completely different from Fig.4.9a and Fig.4.4 ,i.e. for the invasion of an wetting fluid into a pack of smooth glass beads and its corresponding mean finger area analysis.

In Fig.6.4, we notice that at the beginning of the invasion process, there is a small peak value at the vertical length of ~ 4mm. After inspecting the original raw image, it is obvious that there is a irregular Ottawa grain which is much more porous as shown in Fig.6.5(d). This specific grain accumulates more liquid as shown in Fig.6.5(e). Due to the fact that mean finger area is calculated based on the weight of the area (more details are available in Chapter 4), the sudden occurrence of a relative large amount of liquid causes the peak value in Fig.6.4. In Fig.6.5(f), when the other invading liquid cluster has a similar size to that of the liquid cluster formed around the special grain, the unique peak in terms of mean finger area for the specific layer is gone. This unique peak again shows the advantages of the quantification method in terms of identifying the characteristics of the fluids during the invasion process. And apart from that, we also specify a completely different invasion pattern compared with the imbibition experiments in the smooth glass beads. But the driving mechanism for this invasion pattern is not fully explored. The reason for the fingering structure can be the pore region formed by irregular grains shape, which leads to a different macroscopic pore geometry compared with glass beads. Another influence comes from the surface roughness of Ottawa sands, which is also different from the smooth glass beads. As a result, we continue the following experiments.

6.4 Pressure controlled imbibition-glass granulate

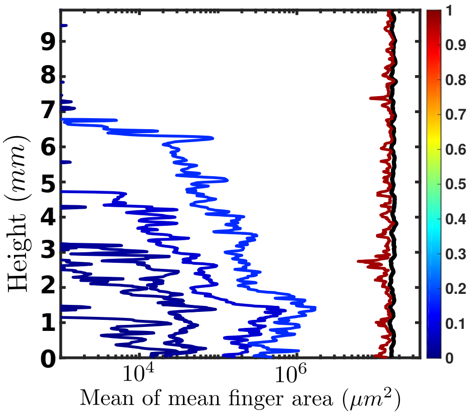

Figure 6.6: Mean finger area distribution for an invading aqueous solution into a pack of piranha-cleaned glass granulates. Y axis represents the height in the region of interest and 0 indicates the bottom part. The black line indicate the pore area, which is the maximum area for the finger area. Color codes indicate the saturation of the invading liquid.

In the previous sub-chapter, we identified that the invasion pattern during the imbibition process in Ottawa sand is different from the imbibition in the smooth glass bead packs. despite that both type of granulates have the same wettability (and very similar packing density). However, both samples differ in their macro-geometry, i.e. their grain shape and in their micro-geometry, i.e. their surface roughness. In order to isolate the influences of macro- and micro-geometry, we conduct experiments with irregular glass granulates. The glass granulates have similar surface properties with the glass beads. However, the grains are irregular, which leads to different pore geometry compared with glass bead packs.

In Fig.6.6, we plot the evolution of mean finger area for the imbibition experiments with Piranha-cleaned glass granulates. Compared with Fig.6.4, we notice that there is no homogeneous growth of mean finger area along the vertical direction for glass granulates. The shape of the glass granulates is more angular and theoretically these packing will generate more contacts between the granulates compared with Ottawa sand packing. Based on the vertical cross sections of tomographies in Fig.6.7, we

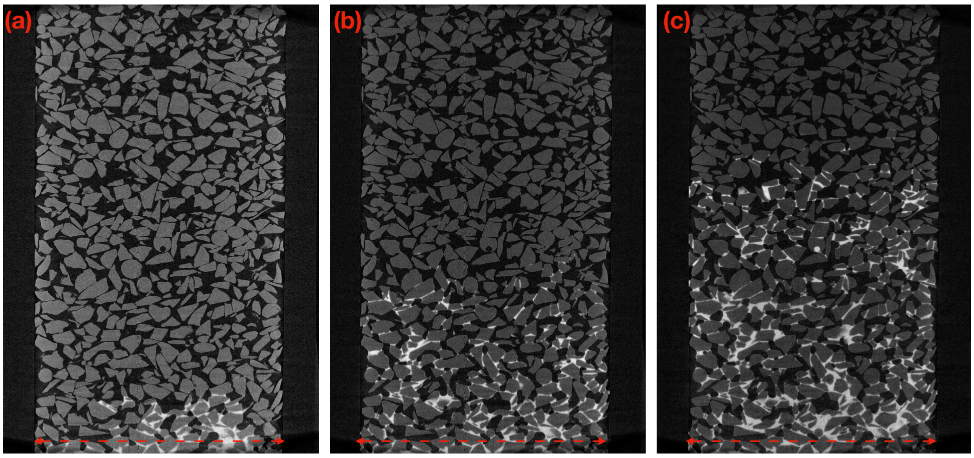

Figure 6.7: Vertical cross-sections of tomographic images of the invasion process of a wetting aqeous solution into a pack of glass granulate. (a,b,c) represent three different invasion stages. The time sequence for (a,b,c): t=0,12941 minutes, 18101 minutes. The inner diameter of the cylinder is 8mm indicated with the red dashed arrow. The bright white phase is the invading liquid.

notice that the invading liquid will preferentially wet the granulate contact points. However, the wetted contact points are not spreading over the entire sample, which is different from what we observe in Fig.6.5. In addition, the invasion pattern is ramified. The ramification of invading liquid does not contradict the compact domain observed in the smooth glass beads. Because the pore-scale invasion mechanism differs between a quasi-static imbibition process and dynamic imbibition process as shown in the work of Zacharoudiou et al. [Zacharoudiou et al., 2017]. For the quasi-static process, snap-off events can occur in the narrowest throats while for the dynamic process, where the invading fluid is injected at constant flow rate, the wetting phase invades the neighboring throat firstly.

6.5 Pressure controlled imbibition-roughened glass bead

In the previous chapter, we excluded the influence of surface roughness of the grains by replacing the glass beads with glass granulates. The results show that the geometry formed by the angular grains does not lead to the same type of invasion of liquid spreading over the region of interests as shown in the experiments with Ottawa sand grains. In order to further investigate the influence of surface roughness on the fluid invasion for the process of imbibition, we conduct experiments with glass beads (diameter of 850-900 m) roughened with different protocols.

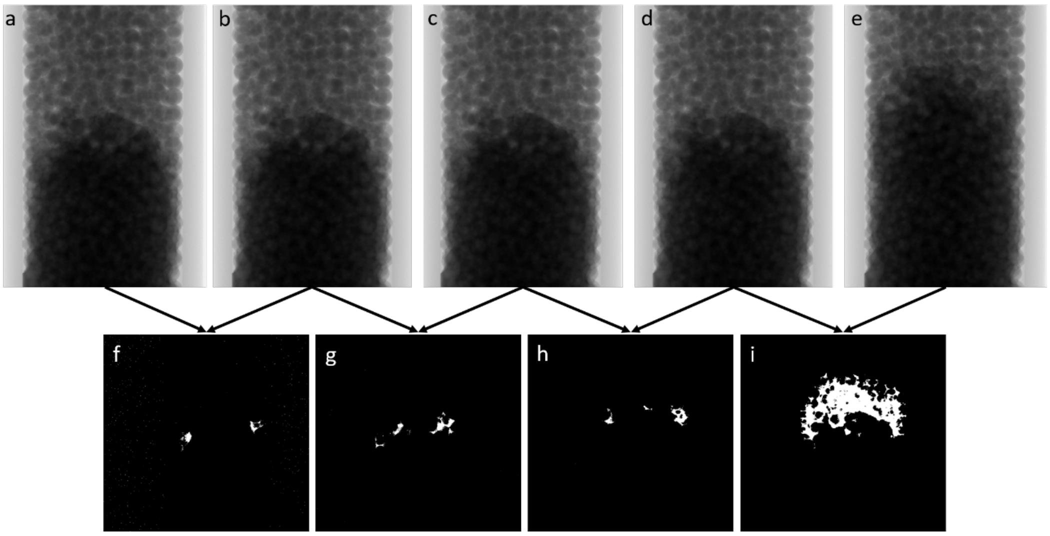

Figure 6.8: Absorption images taken during equilibration in the experiments displacing air with a 30 w% CsCl-water solution in a pack of roughened glass beads. Time intervals between two consecutive images are 40 minutes (a-b), 58 minutes (b-c), 1 hour (c-d), 9 hours (d-e). (f,g,h,i) are difference images between two consecutive absorption images as indicated by the arrows. The white regions in image (f) to (i) indicate that there are changes of X-ray attenuation.

Chemically roughened glass beads (procedure 1)

The initially smooth soda-lime glass beads with a diameter of (850-900) µm where etched with an aqueous 30 w% KOH solution under slightly stirring of 100 rpm for 4 h at 80 °C followed by stirring for another 18 h at room temperature. Charaterization of the surface roughness by white light inteferometry revealed a rms value in the order of several 100 nm to 1 µm for the roughened glass beads compared to a rms value of about 50 nm for untreated glass beads.

We recorded a sequence of absorption images at different time steps, cf. Fig.6.8a-e, to verify the state of equilibrium. To visualize a potential change in the fluid distribution between two consecutive images, we calculated difference images of the respective absorption images, cf. Fig. 6.8f-i. Even 15 h after connecting the bead pack to a liquid reservoir at constant height we do not observe an equilibrium state as the invading fluid is still slowly advancing. Opposite to the ramified displacement pattern for the previously investigated Ottawa sand pack, we observe a smooth, compact displacement pattern for the pack of roughened beads as shown in Fig.6.9. Similar to the displacement pattern for smooth glass beads [Singh et al., 2017b] the defending fluid is complete swept by the invading fluid and no residual saturation is detected.

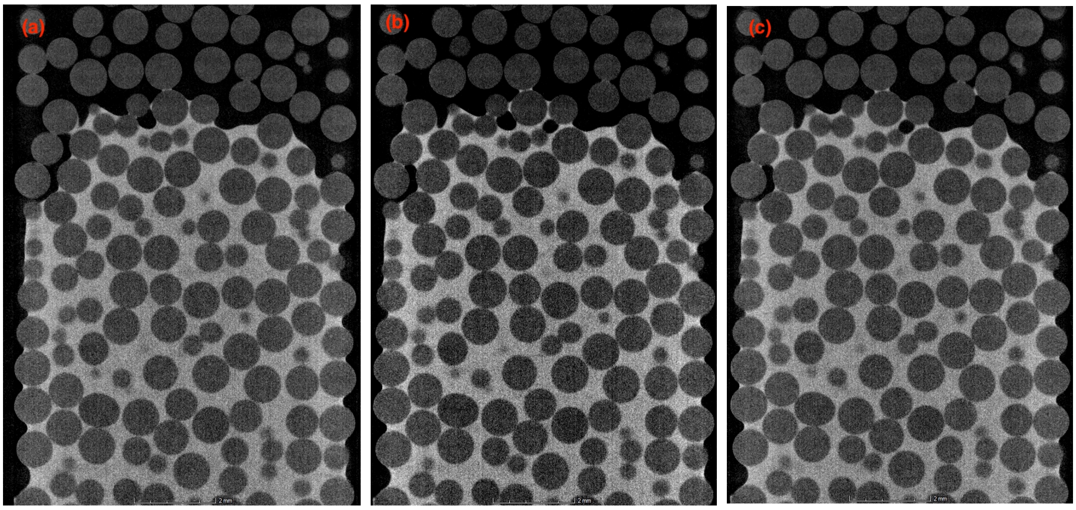

Figure 6.9: Invasion of solution of CsCl (30wt%) into glass beads(etched by 30wt% KOH solution). From (a) to (b) takes around 18 hours. From (b) to (c) takes around 4 hours. The white phase indicates the KOH solution. .

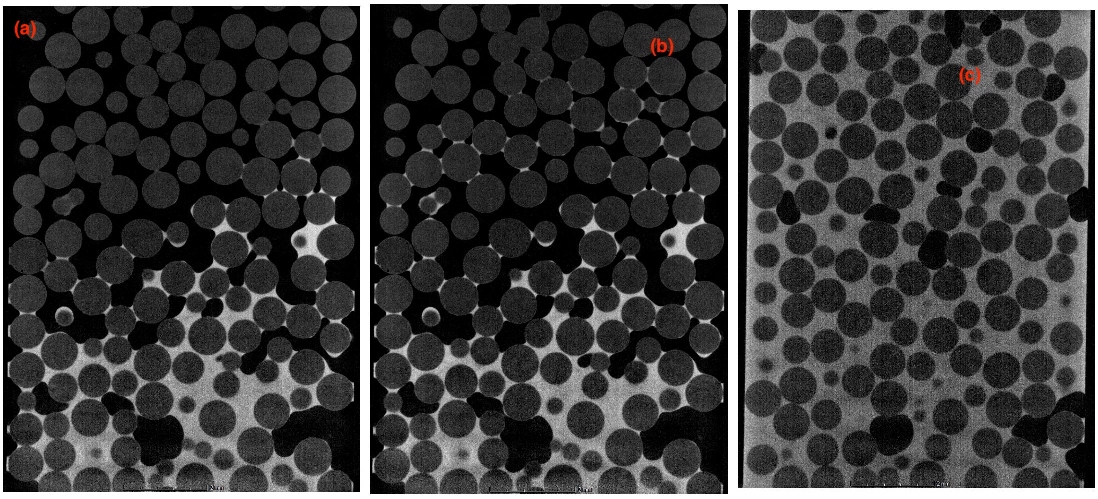

Figure 6.10: Vertical cross sections through tomographies. Invasion of solution of CsCl (30wt%) into glass beads(mechanically roughened and etched by 30wt% KOH solution). From (a) to (b) takes around 18 hours. From (b) to (c) takes around 4 hours. From (a) to (b) takes around 18 hours. From (b) to (c) takes around 58 hours.

Mechanically and chemically roughened glass beads (procedure 2)

To further increase the glass bead roughness, we previously roughened the beads by mechanical mixing the soda-lime beads together with silicon carbide grains at a 1:1 volume ratio for 3 h at a frequency of 60Hz. The beads were subsequently etched in a 30w% KOH solution for about one day during slight stirring at 100 rpm. Independent on the roughening procedure and the achieved roughness, after KOH-etching the glass beads have a very low advancing contact angle $< 20°$ with respect to water. The

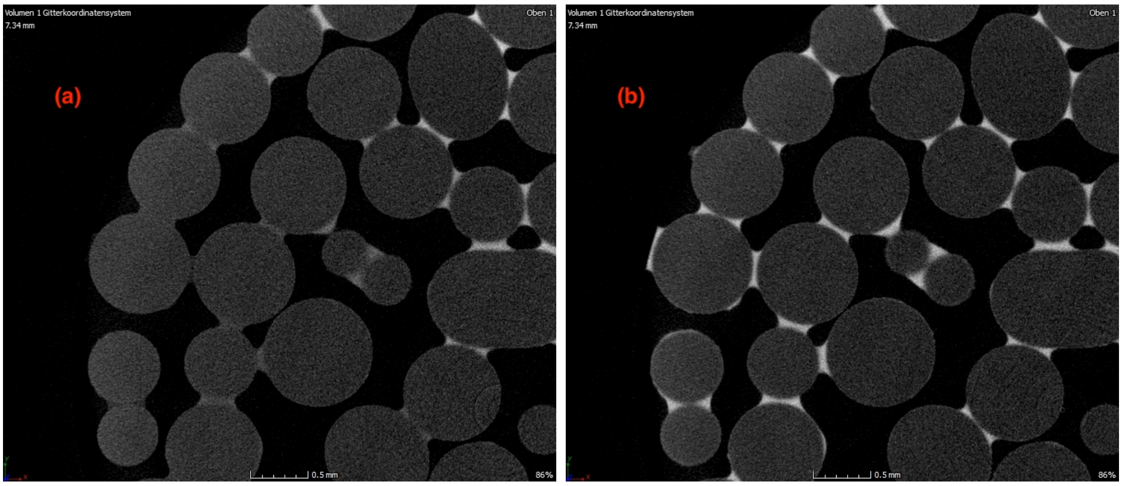

Figure 6.11: (a) is the cross section of the tomography in Fig. 6.10(a). (b) is cross section of the tomography in Fig. 6.10(b). (a) and (b) correspond to the same position of the glass packing with a time interval around 18 hours.

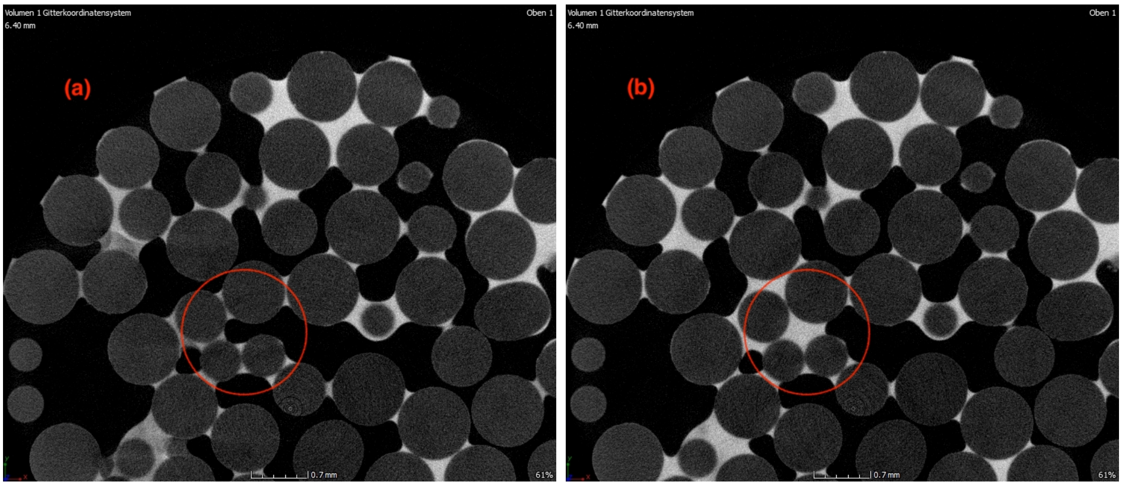

Figure 6.12: (a) is the cross section of the tomography in Fig.6.10. (b) is cross section of the tomography in Fig.6.10. (a) and (b) correspond to the same position of the glass packing with a time interval around 18 hours. The red circle region indicates where the liquid invasion as a result of cooperative pore filling by the neighbouring liquid bridges.

wettability of the roughened glass beads is therefore comparable to the wettability of piranha-cleaned Ottawa sand and piranha-cleaned glass beads and angular glass granulate, respectively. In Fig.6.10, we notice the interface between the invading and defending liquid is ramified, which leads to the air entrapment. In Fig.6.11, we further shows that within 18 hours, the liquid bridges are growing and in Fig.6.12, the growing liquid bridges lead to the cooperative pore filling.

The experiments with the roughened glass beads indicate the strong influence of the microscopic geometry on the imbibition process, which provides a new aspect for characterizing the imbibition process in two phase flow. In order to further quantify the pore geometry, we develop a method that will be described in the following.

6.6 Quantification of macroscopic pore geometry

To quantify the influence of pore geometry of the different imbibition behavior in various glass granulates and Ottawa sand, we firstly apply the maximum inscribed sphere transform (MIS) to the pore space within the bead packs [Silin and Patzek, 2006]. In Fig.6.13a, we notice that within the pore space, there are different bright circles. The gray scale of the pixels indicates the radius of the largest sphere that fits into the pore space and simultaneously covers the pixel. The MIS is conveniently computed with the software package Mango [Middleton et al., 2007]. For the sake of efficiency given the large size of tomography data (one typical segmented tomography data in our current analysis takes more than 2×10^8 voxels), we develop a C++ routine to threshold the pore space based on the MIS value and to subsequently label the connected regions after applying the threshold based on Hoshen-Kopelman algorithm [Hoshen and Kopelman, 1976]. In order to compare the results between different samples, we normalize the threshold radius of the covering spheres with the characteristic length of the system. Following the method proposed in Ref. [Mostaghimi et al., 2010] for segmented tomographic images of porous media with different degrees of consolidation, we define the characteristic length of the pore space as the ratio:

$$L = \frac{3V}{S_a} \tag{6.1}$$

where V denotes the total solid volume and S_a the total surface area of the grains. Note that the value of L for a mono-disperse pack of beads is identical to the bead radius. For the Ottawa quartz grains used in our experiments (diameter: (600-850) μm) we computed a value of L about 360 μm.

A perfectly wetting fluid will preferentially invade those regions of the pore space where the surfaces of two opposing grains are sufficiently close. If the two opposing surfaces of the pore space are exactly parallel or belong to the walls of a cylindrical tube, the MIS provides the exact curvature of an interface that forms a zero contact angle on both surfaces. Hence, the MIS can be employed to identify regions of the pore space that are potentially filled by a perfectly wetting fluid at a given Laplace pressure. These “narrow” regions of the pores space can be characterized by MIS values below a certain global threshold. The threshold is controlled by the Laplace pressure between the two fluids: as we gradually increase the threshold value of the MIS, we will observe a percolation transition of the narrow pore space regions. The example shown in figure 6.14 indicates a threshold MIS value is around 3.1 L to 3.2 L. When the threshold value reaches 3.4 L, there is already very clear connected path from the bottom of the sample to the top of the sample. The color labeled clusters in

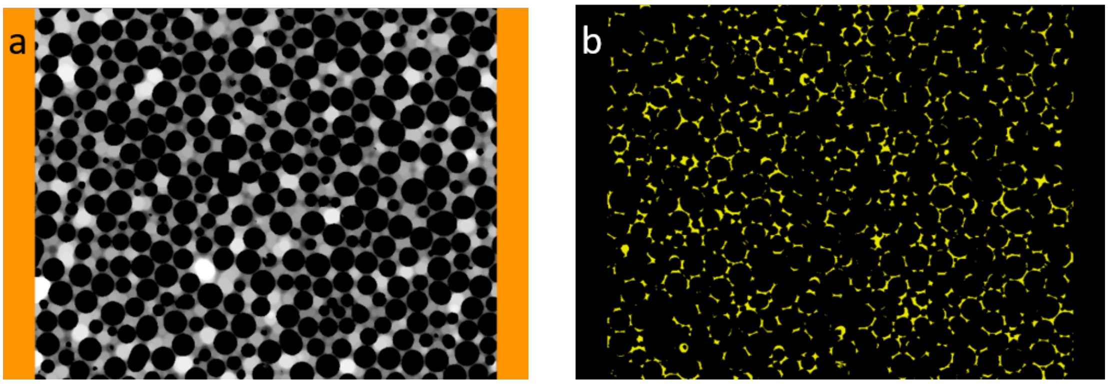

(a) (b)

Figure 6.13: (a) Vertical cross-section of a dry bead pack indicating the value of the maximum inscribed sphere transform (MIS) calculated with the software package Mango. The gray value of a voxel indicates the radius of the largest sphere which fits into the pore space and covers this voxel. (b) All voxels with a MIS value R < 3.5 L are shown in yellow. The voxel resolution in (a) and (b) is $11\mu m\times 11\mu m\times 11\mu m$.

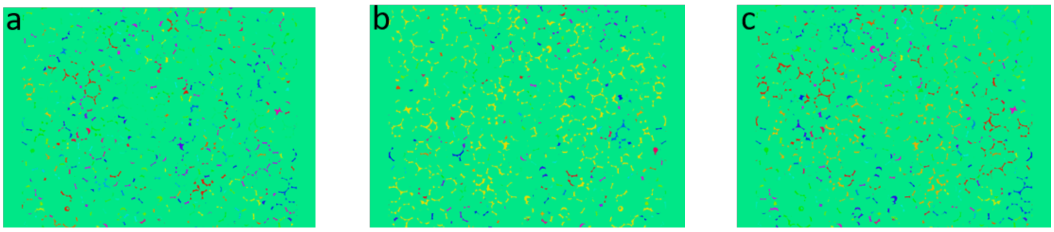

Figure 6.14: Vertical cross-section showing voxels of the pore space whose value of the maximum inscribed sphere radius falls below a certain threshold value. The threshold value is R=3.1 L in (a), R=3.2 L in (b), and R=3.4 L in (c), where L is the pore length scale defined in eqn. 6.1. The voxel resolution for this tomography is $11\mu m \times 11\mu m \times 11\mu m$.

the panels of Fig. 6.15 illustrate the typical cluster size below (a) and above (b) the percolation threshold. In order to determine the percolation threshold quantitatively, we further determine the mean cluster size of the disconnected clusters and plot the value against the dimensionless threshold value of the MIS. Plotting of the average cluster size against the threshold value of the MIS in Fig.6.16a, we notice there is a sudden increase in the normalized average cluster size for the glass bead-pack at the point where large clusters can be observed, cf. also Fig.6.14. So far, we could not observe large variations in the percolation threshold of the narrow pore space regions that could be unambiguously related to differences in the macroscopic grain morphology.

Additionally, to the percolation threshold of the narrow pore space we considered the cumulated number of voxels of the open pore space that exhibit a MIS value below a

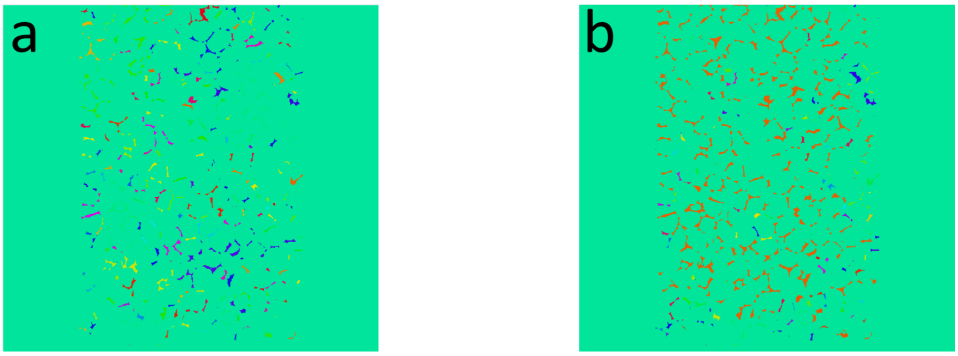

Figure 6.15: Cross sections of different threshold value for the maximum covering sphere map. The threshold value from left to right is 3.0 L (a) and 3.1 L (b). The Voxel resolution is $22.4\mu m \times 22.4\mu m \times 22.4\mu m$.

certain threshold. For the sake of comparability, we normalized the cumulative voxel number with the total number of voxels representing the pore space. In contrast to the percolation threshold illustrated in Fig.6.16a, the data shown in Fig.6.16b exhibit a clear trend. While all cumulative distributions for glass beads almost perfectly collapse onto the same curves, the curves corresponding to the Ottawa quartz grain and Oolith grain sample rise significantly faster than the bead curves at small threshold values. This feature could be seen as an indication for a larger volume fraction of narrow void spaces in the Ottawa and Oolith grain packs, as compared to a lower volume fraction in packs of spherical beads. For the glass granulates shown in Fig.6.16b, the cumulative distribution curve is also similar to the curves with glass beads, which is not as expected for this obviously different packing.

In this section, we compared and discussed local morphological features of the pore space in dense packs of grains based on the statistics of the maximum inscribed sphere transform (MIS). We could demonstrate, in particular, that the pore space formed by non-spherical grains like Ottawa quartz grains and Oolith grains exhibits a larger fraction of narrow pore space. However, we could so far neither prove nor disprove that the global grain geometry is the governing factor that controls finger formation of highly wetting fluids during invasion. As pointed out in Ref. [Lukyanov et al., 2012], surface roughness of Ottawa quartz grains may play a pivotal role in the process of fluid imbibition of perfectly wetting fluid as it allow flow in thin wetting films. As a result, we continue to quantify the microscopic geometry, i.e. surface roughness in the following parts.

6.7 Quantification of microscopic geometry

To characterize the surface roughness of the treated and untreated glass beads as well as of the Ottawa sand we determined the root-mean-square (RMS) value of the surface roughness using with-light interferometry (WLI, 3D Optical Surface Profiler

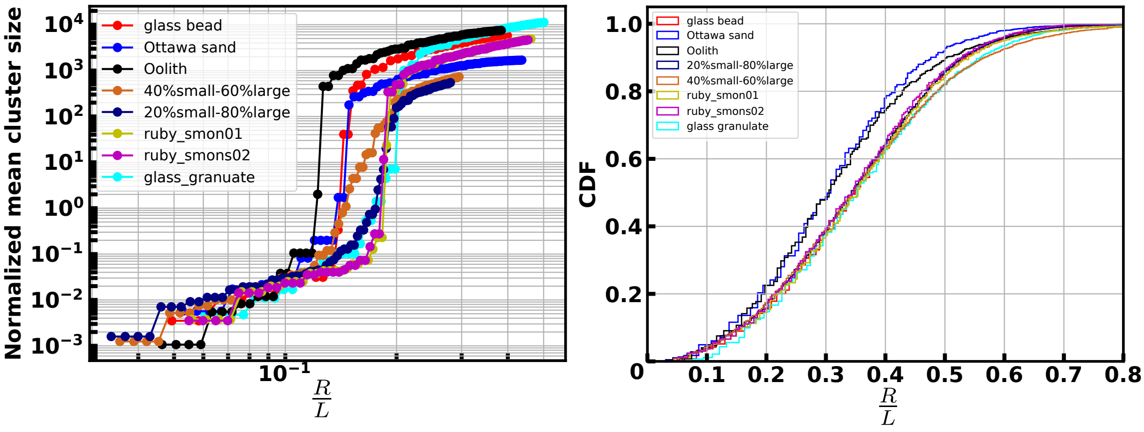

(a) **(b)**

Figure 6.16: (a) Normalized mean cluster size with respect to different threshold values of the MIS. The ordinate is the mean cluster size normalized by the cube of the characteristic length (L). (b) Maximum inscribed sphere radius distribution. The ordinate indicates the cumulative distribution function. The abscissa in both (a) and (b) shows threshold value (R) normalized by the characteristic length (L). The red, blue, and black line indicate data corresponding to dense packs of monodisperse glass beads (diameter: (355-425) µm, characteristic length L≈377 µm), Ottawa quartz grains (characteristic length L≈360 µm), and Oolith grains (characteristic length L≈206 µm), respectively. The dark yellow and dark blue line display data of samples with a mixture of 40% small beads (diameter: (355-425)µm) and 60% large beads (diameter: 710-800 µm), and a mixture of 20% small beads (diameter: 355-425 µm) and 80% large beads (diameter: 710-800 µm), respectively. The legend with ruby indicates the Ruby beads, where only dimensionless quantities are calculated. Glass granulates have a characteristic length of ≈ 241 µm.

ZeGage™, Zygo), cf. Fig.6.17. Due to the random shape of the angular glass granulate, an exact determination of the surface roughness of the granulate was not possible from WLI-data. However, as the breaking edges of the angular granulate are optically smooth we assume them to be at least as smooth as the surface of untreated glass beads.

As shown in panel (2a) and (3a) of Fig. 6.17 large parts of the untreated glass beads are extremely smooth with RMS-value of (0.047 ± 0.003) µm. Objects on the surface resembling “flakes”(i.e. potentially little glass particles either from the manufacturing process or from glass beads scratching against each other) with a height of up to several hundreds of nanometers may lead to high RMS-values of about 0.05 µm or more. These flakes could not be removed by Piranha cleaning. These roughness values

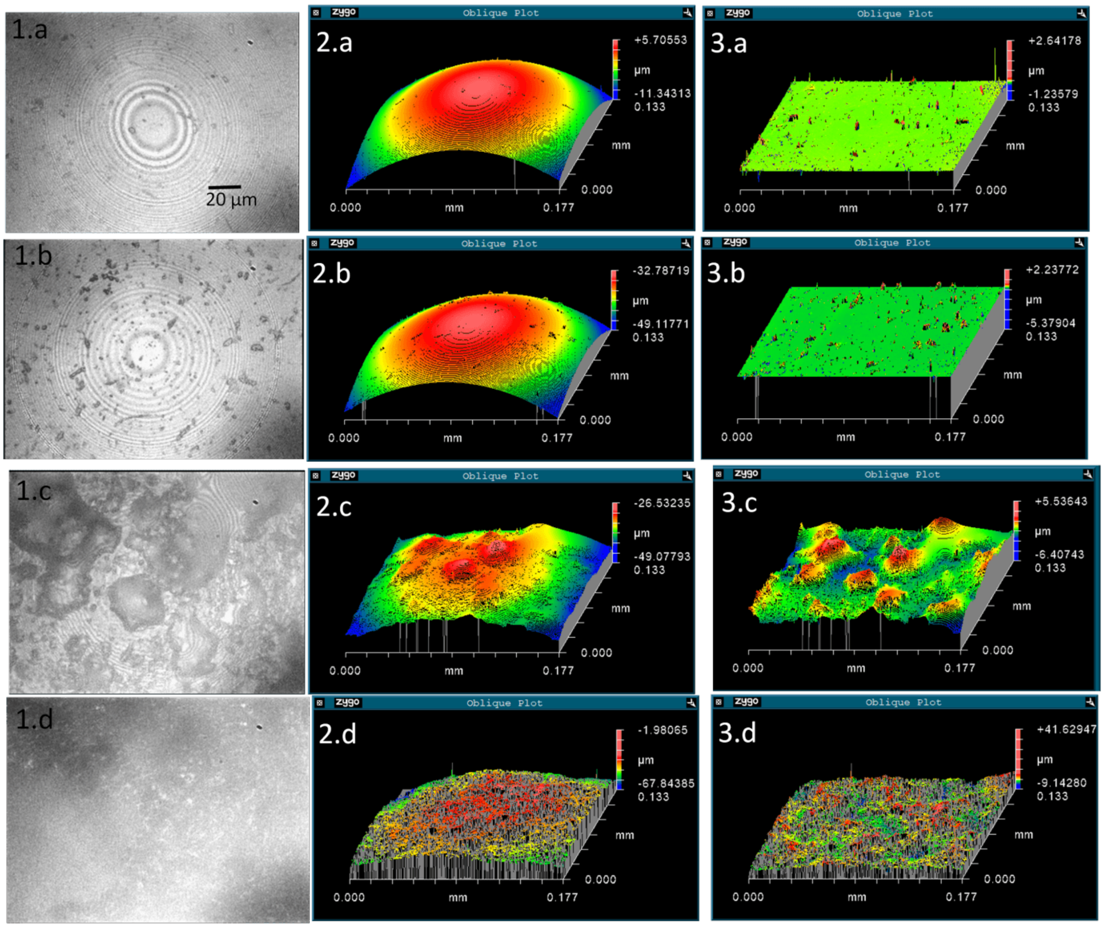

Figure 6.17: The first column displays optical images of ((a) Piranha cleaned glass beads, (b) KOH-etched glass beads, (c) KOH-etched glass beads previously "scratched" with silicon carbide, and (d) Piranha cleaned Ottawa sand grains (mesh size 20-30, approximately (600-850) µm)). All images have a size of about (180 µm x 130 µm). The visible rings in panels (a) - (c) are Newton rings caused by reflection of the spherical glass beads. The second and third column display surface plots obtained from white-light interferometry as raw-data (2) and after subtraction of the underlying bead-curvature using a polynomial-fit of 4th order (3). The measurements of the raw data with the white-light interferometer were performed with the help of Philipp Grützmacher. The analysis was done with the help of Michael Jung.

are confirmed by atomic force microscopy (AFM)-measurements where we obtained an RMS-value of about 0.07 µm if there was a "flake" localized in the scanned area of 5 µm x 5 µm and an RMS-value of about 0.005 µm if we chose an area that is free of "flakes".

For the surface roughness of Ottawa sand grains we obtained RMS values of (1.3 ± 0.3) µm, cf. panel (3d) of figure 6.17. This value is in agreement with the RMS values of 0.4 µm to 3 µm that were determined by Alshibli et al. [Alshibli and Alsaleh, 2004] for Ottawa grains with 550 µm size.

In panels (3b) and (3c) of Fig. 6.17 can be seen, that both tested surface treatments of the glass beads show a remarkable effect on the surface roughness of the glass beads. The RMS-value of KOH-etched glass beads (procedure 1) was determined to (0.3 ± 0.3) µm, whereas the RMS-value of the previously roughened KOH-etched beads (procedure 2) was found to be (1.1 ± 0.8) µm and therefore at the same level as the RMS-value of Ottawa sand.

6.8 Summary

By conducting imbibition experiments with porous media having various macroscopic and microscopic geometry, we investigate how the invasion pattern during the strong imbibition regime is influenced by the geometry. By the analysis of the mean finger area evolution with increasing saturation of invading liquid, we notice that the fluid invasion pattern during the imbibition process in Ottawa sand is completely different from what we observe for the imbibition experiments with the smooth glass beads. In Ottawa sand grains, the liquid wets the contact between grains firstly and the finger area is expanding through the entire sample in the field of view. However, in the experiments of smooth glass beads, the invading liquid developed a compact domain. Further experiments by etching the surface of glass beads to roughen the surface also showed a promotion of fingering structure for the invading liquid, which is an indication that the surface roughness will facilitate the fingering invasion pattern. For the experiments with granulates, the surface properties of the glass is similar to the smooth glass beads but the macroscopic pore geometry is altered. The final invasion pattern is not compact, however we did not observe that the liquid preferentially wets the contact of the grains. The results in total illustrate the important role of surface roughness on the imbibition process.

Chapter 7

Exact calculation of the intersection volume between sphere and arbitrary polyhedron

7.1 Introduction

Calculating the intersection volume between spherical objects and polyhedral bodies is of great importance to many subjects. Examples include the radial distribution function [van Blaaderen and Wiltzius, 1995; Scholz and Pöschel, 2017; Kopera and Retsch, 2018], void volume fraction in fluid-solid interaction problems [Fries et al., 2011; Han and Cundall, 2013; Jones and Williams, 2017; Clarke et al., 2018; Su et al., 2020], droplet on edge-shaped grooves [Khare et al., 2007; Herminghaus et al., 2008] and some computational models of biochemical systems within individual cells [Drawert et al., 2012; Isaacson, 2013; Isaacson and Zhang, 2018]. For example, mesoscopic-microscopic systems are developed to account for porous media flow problems [Noble and Torczynski, 1998; Han and Cundall, 2013]. In these systems, Lattice Boltzmann Method (LBM) is employed to model the fluid flow in pore space at a mesoscopic level and the mechanical behavior of solid particles are modeled at microscopic level by the Discrete Element Method (DEM). To address the interaction between fluids and solid structure, a weight coverage function [Noble and Torczynski, 1998; Owen et al., 2011], which is a function of the volume fraction, will be introduced. To ensure a smooth change of sphere-cell intersection volume as the sphere goes through the LBM cells [Owen et al., 2011; Galindo-Torres, 2013], an efficient and accurate intersection volume computation becomes crucial. Apart from that, the volume fraction is also a key element when modeling coupled granular-fluid systems with a coupled CFD (Computational Fluid Dynamics)-DEM approach [Fries et al., 2011; Kloss et al., 2012; Clarke et al., 2018]. Reference [Clarke et al., 2018] conducts an extensive investigation of the void fraction schemes for CFD-DEM simulations of fluidized beds.

Due to the large quantities (a typical system comprises of $\sim 10^5$ particles [Clarke et al., 2018]) of particles in the system, exact calculation [Strobl et al., 2016] is not applicable in terms of computational performance. The problem of calculating the void fraction is how to find a balance between the computational accuracy and computational efficiency. It is summarized in the work of Kloss et al. [Kloss et al., 2012] that an over simplified approach to calculate the fraction volume can lead to errors due to artificially inhomogeneous volume fraction field.

Also in some lattice particle-based stochastic reaction-diffusion models [Engblom et al., 2009; Isaacson and Zhang, 2018] with the aim to study biochemical reactions within individual cells, the evaluation of the fraction volume is in need. In these models, the cellular molecules are presented as small spheres and the unstructured grid are introduced to simulate chemical processes in complex domain geometries for cellular systems [Isaacson and Peskin, 2006; Erban and Chapman, 2009; Hepburn et al., 2012]. So the interaction volumes between spheres and polyhedra needs to be evaluated in a rapid and accurate way [Isaacson and Zhang, 2018].

In addition, the radial distribution function is very common in analyzing the internal structure of particulate systems including colloid assemblies [Banchio and Nägele, 2008; van Blaaderen and Wiltzius, 1995], sphere packings [Mueller, 1992; Kopera and Retsch, 2018] and protein diffusion [Bucciarelli et al., 2016]. In experiments, the particles are always confined to a space of finite volume and ignoring the finite nature of the sample volume lead to significant distortion of the radial distribution function [Kopera and Retsch, 2018]. As a consequence, the accurate intersection volume between shell and box becomes necessary [Kopera and Retsch, 2018; Mueller, 1992].

Given the importance of the intersection volume calculation, a sophisticated method to calculate the intersection volume between spheres and mesh elements has already been introduced by Strobl and Pöschel [Strobl et al., 2016]. This approach is based on the idea to decompose the overlapping volume into multiple basic parts including wedges, cones and caps, each with a volume that can be computed from closed form expressions [Bernardeau and van de Weygaert, 1996; Wu et al., 2009]. However, decomposition of the overlapping volume requires redundant calculation. For example, to calculate the intersection volume when a vertex of the tetrahedron is inside of the sphere, the intersected volume is calculated by removing the volume of caps based on the sphere volume. Further corrections with the volume of wedges and cones needs to be evaluated. This laborious correction routine introduces unnecessary calculation and leads to a decrease in computational accuracy and efficiency. The algorithm outlined in the present work, however, does not rely on the decomposition of a tetrahedron into a number of shape primitives of known volume but starts from each triangular face bounding the overlapping region and calculate their contribution individually. The result turns out to be advantageous in numerical stability and higher accuracy. In addition, we show that this method is applicable to calculate the intersection volume between spheres and general polyhedra of arbitrary topological genus.

7.2 Volume intersection between a sphere and a polyhedron

Starting point of our approach is the three dimensional vector field **A**, for which $\nabla \cdot \mathbf{A} = 1$, $r < R$ and $\nabla \cdot \mathbf{A} = 0$, $r \geq R$. One potential vector field is the electric field generated by an uniformly charged sphere [Griffiths, 2005]:

$$\mathbf{A} = \begin{cases} \frac{r}{3}\widehat{\mathbf{r}}, & \text{if} \quad r < R. \\ \frac{R^3}{3r^2}\widehat{\mathbf{r}}, & \text{if} \quad r \geq R. \end{cases} \tag{7.1}$$

The bold symbols in Eq.7.1 and in the following equations in this work represent the vectors. In Eq.7.1, $\widehat{\mathbf{r}}$ represents the unit vector pointing radially outward from the center of the sphere. R is the radius of the sphere and r is the magnitude of the position vector. For later convenience we set the center of the Cartesian coordinate system into the center of the sphere O.

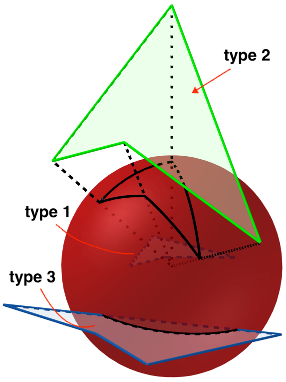

Figure 7.1: Illustration for three different types of polygon. type 1: polygon inside the sphere; type 2: polygon outside the sphere; type 3: polygon intersecting the sphere.

Based on Eq.7.1, we propose two different algorithms as follows. Each method has its own advantages and disadvantages, which will be further discussed after describing these two algorithms.

7.2.1 Algorithm 1

With Eq.7.1, a natural way to calculate the intersection volume is directly achieved by integrating the divergence of the vector field **A** over the whole polyhedron region as shown in Eq.7.2. After applying the Gauss theorem, the original volume integral is equal to the surface integral of the boundary surfaces of the polyhedron.

$$
\begin{aligned}
V_{inter_{sp1}} &= \int_{poly} \nabla \cdot \mathbf{A} dV = \int_{type1} \mathbf{A} \cdot \mathbf{dS} + \int_{type2} \mathbf{A} \cdot \mathbf{dS} + \int_{type3} \mathbf{A} \cdot \mathbf{dS} \\
&= \int_{in} \mathbf{A} \cdot \mathbf{dS} + \int_{out} \mathbf{A} \cdot \mathbf{dS} = \int_{in} \frac{r}{3} \widehat{\mathbf{r}} \cdot \mathbf{dS} + \int_{out} \frac{R^3}{3r^2} \widehat{\mathbf{r}} \cdot \mathbf{dS} \\
&= \int_{in} \frac{r}{3} \widehat{\mathbf{r}} \cdot \mathbf{dS} + \operatorname{sgn}(\widehat{\mathbf{r}} \cdot \mathbf{n_i}) \int_{proj} \frac{R}{3} \widehat{\mathbf{r}} \cdot \mathbf{dS} \\
&= \frac{1}{3} \left(\sum_i A_{fi} \mathbf{n_i} \cdot \mathbf{a_i} + \sum_i A_{si} R \operatorname{sgn}(\widehat{\mathbf{r}} \cdot \mathbf{n_i}) \right) .
\end{aligned}
\tag{7.2}
$$

where, $\mathbf{n_i}$ is the normal vector pointing out of the plane consisting of the closed flat face and $\mathbf{a_i}$ is any point in the i^{th} plane. sgn represents the sign function. A_{fi} represents the area of the closed flat surface, which is bounded by line segments and circular arcs. A_{si} is the area on the sphere surface formed by the circular arc, which are the projected polygon contour on the sphere surface.

In Eq.7.2, we classify all the polygon surfaces into three different types with regard to their relative position to the sphere. For the polygon faces inside the sphere, the surface integral is equal to the area of the polygon face multiplied by a constant. For the faces outside of the sphere, we project the polygon face onto the surface of the sphere by connecting the vertices of the polygon to the center of the sphere as shown by type 2 in Fig.7.1. For the polygon faces which intersect with the sphere as shown by type 3 in Fig.7.1, we further divide them into the parts inside the sphere and outside the sphere. As a consequence, the contribution of this type of polygon to the intersection volume calculation is a combination of type 1 polygon and type 2 polygon. Supposed that the projected region and the original polygon face form a close body with the line segments connecting the original vertexes and projected vertexes and the surface of this body is Σ and volume inside is V. Based on Gauss's theorem, we achieve:

$$
\begin{aligned}
&\int_{out} \frac{R^3}{3r^2} \widehat{\mathbf{r}} \cdot \mathbf{dS} - \int_{proj} \frac{R^3}{3r^2} \widehat{\mathbf{r}} \cdot \mathbf{dS} = \int_{\Sigma} \frac{R^3}{3r^2} \widehat{\mathbf{r}} \cdot \mathbf{dS} = \int_V \nabla \cdot \left(\frac{R^3}{3r^2} \widehat{\mathbf{r}} \right) dV \\
&= \frac{R^3}{3} \int_V \frac{\partial_i r_i}{r^3} + r_i \partial_i (\frac{1}{r^3}) dV = \frac{R^3}{3} \int_V \frac{3}{r^3} - \frac{3 r_i r_i}{r^5} dV = 0 (r \neq 0) .
\end{aligned}
\tag{7.3}
$$

Eq.7.3 helps us to convert the integration over the polygons outside of the sphere into the integration over the projected region, which in the end is a problem to calculate the projected area A_{si} on the sphere. When dealing with the triangles outside of the sphere, A_{si} is calculated as the solid angles and the computational cost can be significantly reduced when the algorithm of Oosterom is applied [Chareyre et al., 2012; Van Oosterom and Strackee, 1983]. For triangles intersecting with the sphere or more general polygons, A_{si} could be calculated with the Gauss-Bonnet theorem [Spivak, 1975]:

$$
\sum_i \theta_i + \sum_i k_{e_i} |l_i| + \frac{A_{si}}{R^2} = 2\pi\chi . \tag{7.4}
$$

where θ_i is the exterior angle when two neighboring circular arcs l_i and l_{i-1} intersect at a point i, k_{e_i} is the geodesic curvature of the edge l_i, $|l_i|$ is the length of the circular arc, A_{si} is the area formed by the circular arcs, and χ is the Euler characteristic of A_{si}.

7.2.2 Calculation of A_f

For all the algorithms proposed in this chapter, the calculation of the flat area A_f is the same. In the following part, we make some efforts to explain the procedure for the evaluation of A_f in detail.

Polygon and circle intersection

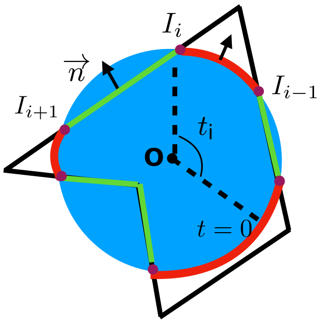

Figure 7.2: Illustration of the polygon and circle intersection. The purple points represent the intersection points between each edge of the polygon and the circle. The red arcs represent the circular arcs which will finally form A_s.

Similarily as in the work of Isaacson et al. [Isaacson and Zhang, 2018], the area of the intersection between a circle and a polygon is given by:

$$\begin{aligned} S_{\text{inter}} &= \int\int_{C\cap P} d\sigma = \frac{1}{2}\int\int_{C\cap P} \nabla\cdot\boldsymbol{r}d\sigma = \frac{1}{2}\int_{\partial(C\cap P)}\boldsymbol{r}\cdot\boldsymbol{n}ds \\ &= \frac{1}{2}\int_{\partial C}\boldsymbol{r}\cdot\boldsymbol{n}ds + \frac{1}{2}\int_{\partial P}\boldsymbol{r}\cdot\boldsymbol{n}ds\ . \end{aligned} \tag{7.5}$$

where, $\boldsymbol{n}$ is the unit outward-pointing normal vector at the point around the boundary. Similarly, we parameterize the circle on the intersection plane. We start from each edge, which intersects the polygon. As shown in Fig.7.2, we go through all the edges, and record all of the n intersection points I_i, $i \in \{1, ..., n+1\}$ and $I_1 = I_{n+1}$. For each intersection point, we define the angle t, which is the angle formed between $t = 0$ and the intersection point. So the angle for each intersection point I_i will be t_i. Firstly, we calculate the contribution of each line segment:

$$S_p = \frac{1}{2}\int_{\partial P}\boldsymbol{r}\cdot\boldsymbol{n}ds \ = \frac{1}{2}\sum|\overrightarrow{I_iI_{i+1}}|(\overrightarrow{OI_i}\cdot\boldsymbol{n})\ . \tag{7.6}$$

The contribution of the circular arcs to the flat area (A_f):

$$S_{cf} = = \frac{1}{2}\int_{\partial C} \boldsymbol{r}\cdot\boldsymbol{n}ds = \frac{1}{2}\int_{\partial C} R^2 dt = \frac{R^2}{2}\sum(t_{i+1}-t_i)\ . \tag{7.7}$$

Averaging over certain quantities

In order to enhance the stability and accuracy of the algorithms, averaging over certain quantities are introduce. For example, we need to take care of the starting point for edge-sphere intersection points calculation. In all of the proposed algorithms to compute the intersection volume between a polyhedron and a sphere in this thesis, even though the polygons are treated individually, these polygons share the same edge with neighbouring polygons. To calculate the intersection point between an edge of a polyhedron and a sphere, the edge is expressed in terms of the two vertexes $\boldsymbol{v_0}$ and $\boldsymbol{v_1}$ forming the edge as $\boldsymbol{v_0} + t\cdot(\boldsymbol{v_1}-\boldsymbol{v_0})$ [Strobl et al., 2016; Galindo-Torres, 2013]. We also calculate the edge sphere intersection point with edge as $\boldsymbol{v_1} + t\cdot(\boldsymbol{v_0}-\boldsymbol{v_1})$. Then the intersection points are averaged by these two results. If we happen to use different starting points in the neighboring triangles, the calculated total exterior angle might cause loss of precision due to the slight shift in the intersection points. In addition, special attention should be paid to when there is a point of the edge is exactly on a sphere. At this case, it happens that if we choose the starting point differently, there will be no intersection points for one direction or the average point is no longer exactly on the sphere. As a result, we need to reset the average intersection point to the vertex on the sphere. Apart from that, quantities like the area of triangle are also averaged to make sure that the order of the vertexes do not make a difference. The process to determine the line-sphere intersection is as followed:

Supposed the sphere, with a radius of r, is positioned at the center at $O = (0, 0, 0)$, the coordinates of the point on the sphere surface is S, so

$$||\overrightarrow{SO}||^2 = r^2\ . \tag{7.8}$$

The point $\hat{S}$ on the line $\overrightarrow{P_1P_2}$ is parameterized as follows with different starting points:

$$\begin{aligned} \overrightarrow{O\hat{S}} &= \overrightarrow{OP_1} + t\overrightarrow{n}, \quad \overrightarrow{n} = \frac{\overrightarrow{P_1P_2}}{|\overrightarrow{P_1P_2}|}, \\ \overrightarrow{O\hat{S}} &= \overrightarrow{OP_2} - t\overrightarrow{n}\ . \end{aligned} \tag{7.9}$$

Because the line and sphere intersect with each other, i.e. $||\overrightarrow{\hat{S}O}|| = ||\overrightarrow{SO}||$ and $\hat{S}$, by combining Eq.7.8 and Eq.7.9, we obtain,

$$\begin{aligned} t &= -\overrightarrow{n}\cdot\overrightarrow{OP_1} \pm \sqrt{||\overrightarrow{n}\cdot\overrightarrow{OP_1}||^2 - ||\overrightarrow{OP_1}||^2}, \\ \hat{t} &= \overrightarrow{n}\cdot\overrightarrow{OP_2} \pm \sqrt{||\overrightarrow{n}\cdot\overrightarrow{OP_2}||^2 - ||\overrightarrow{OP_2}||^2}\ . \end{aligned} \tag{7.10}$$

When using Eq.7.10 and different directions to calculate the intersection points, there is a possibility for slight shift of the intersection points position in the results. In order to guarantee the accuracy of the result, we calculate the intersection points with two different starting points and make an average of the intersection points. In the work of Strobl et al. [Strobl et al., 2016], the intersection points are not calculated to make it independent of the direction of the line segments, so that they have the problem when an intersection is detected for the vertex and two faces with the edge between them not detected. To compensate for that, they [Strobl et al., 2016] introduce a certain threshold and check the consistency of different geometric primitives. However, in that case, the accuracy is also undermined. For the algorithms presented in the current work, the calculation is based on each individual face. And the treatment of the intersection points enhances the stability as well as the accuracy of the final calculation.

7.2.3 Algorithm 2

The algorithm 1 is very efficient and easy to implement when the number of faces for the polyhedron is relative small. However, we notice that the polygon faces which are outside of the sphere do not influence the intersection volume. However, if the polyhedron has plenty of faces outside of the sphere, it will become computationally inefficient to include all the faces of the polyhedron. As a result, we came up with a second algorithm, in which the divergence of the vector field **A** is integrated over the intersection region and obtain Eq.7.11.

$$\begin{aligned} V_{inter_{sp1}} &= \int_{inter} \nabla \cdot \mathbf{A} dV = \int_{in} \mathbf{A} \cdot \mathbf{dS} + \int_{surface} \mathbf{A} \cdot \mathbf{dS} \\ &= \int_{in} \frac{r}{3} \widehat{\mathbf{r}} \cdot \mathbf{dS} + \int_{surface} \frac{R}{3} \widehat{\mathbf{r}} \cdot \mathbf{dS} = \frac{1}{3} \left(\sum_i A_{fi} \mathbf{n_i} \cdot \mathbf{a_i} + \sum_i A_{si} R \right) \ . \end{aligned} \tag{7.11}$$

The difficulty to implement Eq.7.11 lies in the calculation of the curved area on the sphere A_{si}. Actually, the calculation of A_{si} has a long history and it could be directly viewed as a solid angle. Solid angle has a very strong physical background since the time of Gauss [Gauss, 1877]. Maxwell provided three different methods to evaluate the solid angles [Maxwell, 1873]. These three methods have been revived to investigate the construction of knotted fields recently [Binysh and Alexander, 2018]. In the following, we propose also three different methods, which show strong connections to the methods mentioned in the works of Maxwell [Maxwell, 1873]:

Global Euler characteristics (χ)

The area on the sphere surface formed by the circular, A_{si}, that appears in In Eq.7.2, is calculated by focusing on an individual polygon. But with Eq.7.11, before calculating A_{si}, we need to consider χ over the whole spherical surface based on Eq.7.4. To be more specific, all the polygon faces intersecting with the sphere will generate circular arcs on the sphere surface, and we need to record them one by one and then build a graph to address χ as in the works of Quan et al. and Connolly [Quan and Stamm, 2016; Connolly, 1983]. However, in this thesis, we do not follow the approach of Quan and Connolly [Connolly, 1983; Quan and Stamm, 2016] but chose a different approach. For all the implementation of this algorithm in the present work, we only focus on the sphere and tetrahedron intersection. For the calculation of A_{si}, three quantities are required, i.e. total exterior angle ($\sum\limits_i \theta_i$), $\sum\limits_i k_{e_i}|l_i|$ and Euler characteristic (χ) according to Eq.7.4. For total exterior angle and $\sum\limits_i k_{e_i}|l_i|$, we are able to add the contribution from the each triangle separately. χ is calculated after we loop over all the triangles.

- total exterior angle ($\sum\limits_i \theta_i$). Given the tetrahedron, we loop over all the edges and calculate the corresponding θ. In Fig.7.3(a), we can identify three types of edge-sphere intersection. The number of exterior angle is determined by the number of intersection points for each edge. In addition, special attention should be paid to the case as shown in Fig.7.3(b) and (c), the vertex B is exactly on the sphere. In that case, we need to consider the neighbouring edges when an edge is treated. In Fig.7.3(b), the edge AB will contribute to the exterior angle, because the edge BD, BC only intersect with the sphere at B and the rest of the edge are outside of the sphere. And the edge BC and BD will not generate exterior angle. However, in Fig.7.3(c), edge AB does not contribute to the exterior angle. But edge BC, BD will form exterior angle.

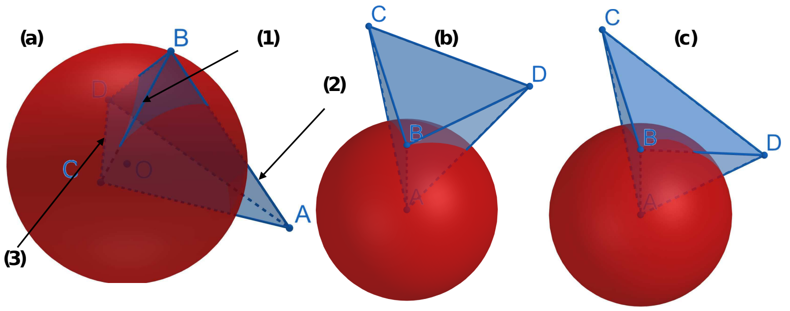

Figure 7.3: Illustration for classification of edges for the exterior angle calculation. (a) three different edges are considered: (1) the edge has one intersection point with the sphere; (2)the edge has two intersection points with the sphere; (3) the edge has no intersection point with the sphere. (b) and (c) illustrate when one vertex is exactly on the sphere, in order to calculate the exterior angle properly, we need to take care of all the edges which connect this vertex.

Because the normal vector of the triangular plane acts as a key role in determining the exterior angle, the normal vector of the triangular plane is calculated with an efficient emulation of quadruple precision (128 bit) [Strobl et al., 2016; Dekker, 1971]. In addition, the summation of exterior angles are also treated with this emulation of quadruple precision.

- $\sum\limits_i k_{e_i}|l_i|$. And all the red arcs in Fig.7.2 are the places where we calculate the geodesic curvature and $k_{e_i} = \mathrm{sgn}(\widehat{\mathbf{r}} \cdot \mathbf{n})\frac{\sqrt{R^2 - r_i^2}}{Rr_i}$.
- Euler characteristic (χ). To address χ, a binary tree is constructed for classification the loops on the surface into several parts [Quan and Stamm, 2016]. The purpose to construct such a tree is to determine the relationship between each loop. When a polyhedron intersects with a sphere, the same approach is also applicable. But when the polyhedron is concave, it will be challenging to determine the relationship between the loop. However, we find that by simple enumeration and classification, we can calculate χ in a much efficient way when we are considering the intersection between a tetrahedron and a sphere. The procedure is as follows:

  We go through all the triangles and build an adjacency matrix between the intersection points. As shown in Fig.7.2, all the red arcs indicate there is a connectivity between two points. Then we count the total number of loops based on the adjacency matrix [Cormen et al., 2009]. We divide the loops into 3 different types based on how many vertexes forming the loop. And the corresponding number of loops are N_0,N_1 and N_2.

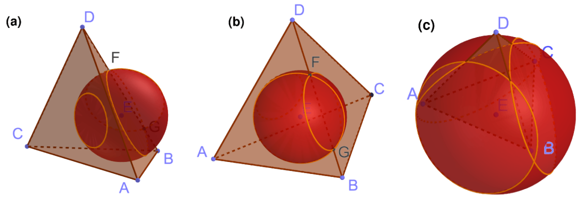

Figure 7.4: (a) a loop on the surface; (b) a loop with intersection for edge; (c) a loop surrounding one vertex.

  - Loop without vertexes (N_0). Fig.7.4(a) shows a loop of circles without crossing the edge of the tetrahedron.
  - Loop with only two vertexes (N_1). Fig.7.4(b) is an example loop with only two vertexes crossing the edge.
  - Loop with 3 or more vertexes (N_2). For example, in Fig.7.4(c) is a loop formed by three vertexes crossing the edge or more.

  By enumerating all the possible cases, we obtain the following way to calculate χ:

$$\chi = \begin{cases} 0, & \text{if } N_0 + N_1 + N_2 == 0. \\ 2 - (N_0 + N_1), & \text{else if } N_2 == 0 \text{ and } N_0 + N_1 != 0. \\ N_2 - N_0, & \text{otherwise.} \end{cases} \tag{7.12}$$

After we verify these three quantities, we are able to calculate the A_{si} based on Eq.7.4 and in the end the intersection volume can be calculated based on Eq.7.11. This process is also applicable when we try to calculate the intersection volume between the sphere and polyhedron. But the way to calculate the total exterior angles should be adjusted correspondingly, especially when the vertex is exactly on the sphere. In addition, we lose the validity of Eq.7.12 and it will take more efforts to obtain χ in an accurate and efficient way.

Reference point method

In the previous method, to obtain the global Euler characteristic is only easy for special cases, which drives us to develop an algorithm in which, the contribution from each circular arc to the volume intersection calculation could be considered individually. Directly inspired by the algorithm 1 in Eq.7.2 in terms of projecting the faces outside of the sphere onto the sphere surface, we provide a new algorithm to calculate A_{si}. As shown as blue curved lines in Fig.7.5a(1), when a polyhedron is intersecting with a sphere, there will be some patchy area generated on the sphere. To achieve the goal without addressing χ globally, we randomly pick a point (shown as blue point in Fig.7.5a(2)) and connect the end points of the circular arcs on the sphere with this chosen point. For each circular arc on the sphere, two curved line

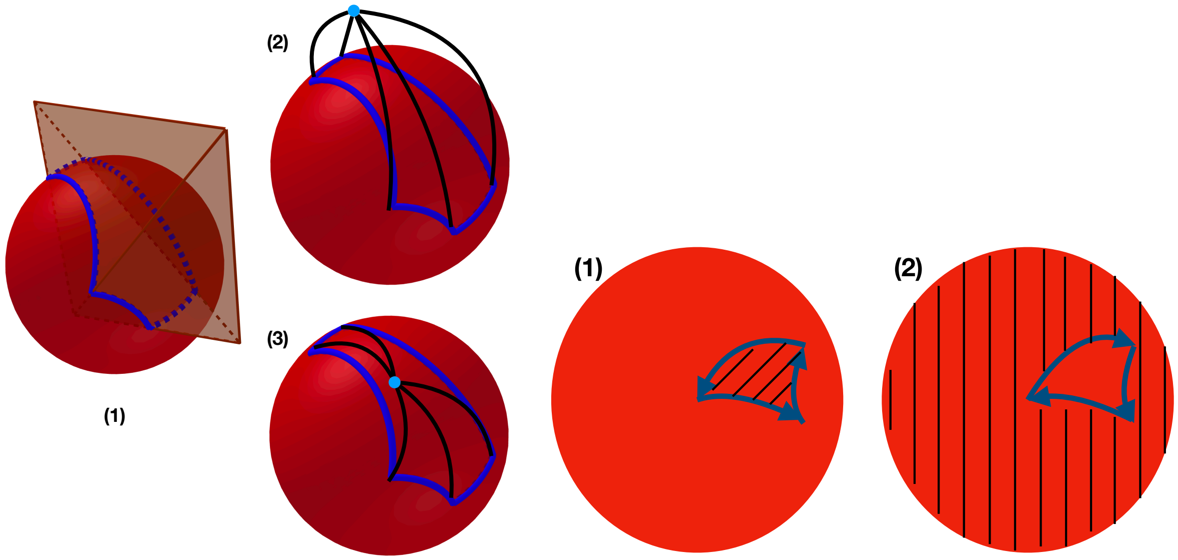

(a) (1) a sphere is intersecting with a tetrahedron. The region formed by the blue circular arcs are A_{si} in Eq.7.2 and Eq.7.11. (2) the reference point is outside of the surface of the sphere while (3) indicates that a reference point on the surface of the sphere.

(b) The shaded area indicates the area calculated if Gauss-Bonnet theorem is applied based on the direction of the circular arcs. (1) one direction for the circular arcs; (2) the reverse direction of the circular arcs in (1).

Figure 7.5: Illustration of the reference point method.

segments are added to form a face. These newly generated faces together with the patchy region on the surface will form a closed body where we integrate over the vector field in Eq.7.1. After applying Gauss theorem [Riley et al., 2006], we obtain Eq.7.13. As the reference point is randomly chosen outside of the sphere, we can as well chose a reference point on the sphere and at the same time, we force the new arcs also on the sphere as shown in Fig.7.5a(3). In that case, all the newly generated faces will be formed by three circular arcs on the sphere.

$$\begin{aligned} \int_{new\_body} \nabla \cdot \mathbf{AdV} &= 0 \ , \\ \int_{A_{si}} \mathbf{A} \cdot \mathbf{dS} + \int_{new\_faces} \mathbf{A} \cdot \mathbf{dS} &= 0 \ , \\ A_{si} &= -\frac{3}{R} \int_{new\_faces} \mathbf{A} \cdot \mathbf{dS} \ . \end{aligned} \tag{7.13}$$

In Eq.7.13, we need to multiply the area formed by three circular arcs with the sign function as shown in Eq.7.2 in algorithm 1. But we find that for a patchy area formed by one closed loop (one example is shown in Fig.7.5b), the summation of the area with reverse direction for the circular arcs will be the surface area of the sphere. Due to the fact that:

$$\begin{aligned} \sum_i \theta_i + \sum_i k_{e_i} |l_i| + \frac{A_{si\_forward}}{R^2} &= 2\pi \ , \\ -\sum_i \theta_i - \sum_i k_{e_i} |l_i| + \frac{A_{si\_backward}}{R^2} &= 2\pi \ , \\ A_{si\_backward} &= -A_{si\_forward} + 4\pi R^2 \ . \end{aligned} \tag{7.14}$$

where, $A_{si\_forward}$ and $A_{si\_backward}$ represent the area calculated for the same closed loop with opposite direction.

Eq.7.13 and Eq.7.14 enable us to directly calculate the patchy area by considering each individual circular arc. In Eq.7.13, the area formed by the circular arcs on the sphere should be multiplied by the sign function, which is determined by the orientation of the circular arcs. But Eq.7.14 reminds us that, if we follow the original direction of the circular arcs and apply Gauss-Bonnet theorem, we naturally obtain the area of A_{si} with sign plus an extra area of the sphere. After applying the Gauss-Bonnet theorem for each individual region formed by three circular arcs, the final summation of the area will be $A_{final} = A_{si} + K \cdot 4\pi R^2$, where $K \geq 0, K \in \mathbb{Z}$. Due to the fact that $A_{si} \leq 4\pi R^2$, we could obtain the A_{si} by taking the modulo of A_{final} over $4\pi R^2$. In the special case that the patchy area is surrounded by several closed loops. In that scenario, the summation will be $\sum(4\pi R^2 - S_i) = K_1 \cdot 4\pi R^2 + 4\pi R^2 - \sum S_i = K_1 \cdot 4\pi R^2 + A_{si}$, which is different from the Fig.7.5a but does not influence the validity of the method. In the works of Richmond [Richmond, 1984], a similar idea to subtract the multiple of 4π is proposed but the connection between each individual circular arc should be given. But the method proposed in the current thesis completely ignores the relationship between the original circular arcs, which makes the calculation more simpler.

Even though each individual region is just formed by three circular arcs in total, we still need to make some efforts to classify how they intersect with each other into different cases as shown in Fig.7.6, because locally we still need to calculate χ.

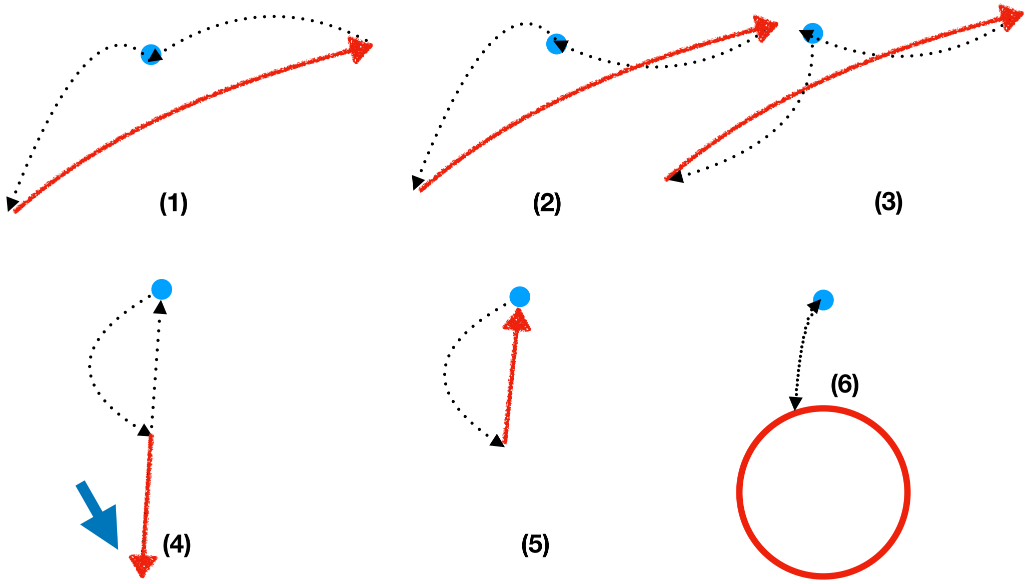

Figure 7.6: Illustration of the cases when three curved circular arcs form a closed loop. The blue point represents the reference point. And the red line represents the original circular arcs formed by the intersection between the polygon face and the sphere. The two black dashed lines indicate the extra lines we add to construct a closed loop. Here we only choose the great circle to avoid calculation of the geodesic curvature. And because the great circle has two branches, we only choose the one with smaller arc length. (1) three circular arcs are connected with only one intersection point between each other $\chi = 1$; (2) one added circular arc is intersecting with the original circular arc $\chi = 2$; (3) two added circular arcs are intersecting with the original circular arcs $\chi = 3$; (4) one added circular arc is overlapping or on the same plane with the original circular arc $\chi = 1$ but the exterior angle pointed by the blue arrow is π or $-\pi$, which should be further considered with the direction of the other added circular arcs; (5) the reference point is overlapping with one of the intersection point $\chi = 1$; (6) the polygon-sphere intersection forms a whole circle $\chi = 1$.

When we derived Eq.7.13, the choice of the reference point was random, which enables us to choose a single point for all the loops on the sphere as followed:

$$\sum A_{si} = \sum - \frac{3}{R} \int_{new\_faces} \mathbf{A} \cdot \mathbf{dS} \ . \tag{7.15}$$

With Eq.7.15, we are able to calculate all the patchy areas on the spherical surface by taking care of each circular arc individually. Through the implementation of a reference point, a relationship between each circular arc is not needed. So there is no requirement to construct a graph [Quan and Stamm, 2016; Connolly, 1983], which dramatically simplified the calculation process.

To implement this algorithm, we pick up a random point on the surface as a reference point as in Fig.7.7.

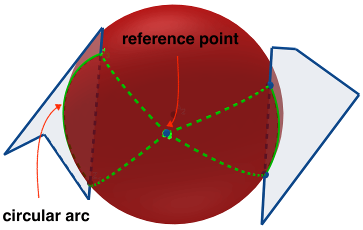

Figure 7.7: Illustration for the method with the reference point method. When a polygon intersects with the sphere, a circular arc will be generated (green solid arcs). We pick a reference point on the sphere and connect the reference point and the intersection points, which give rise to the dashed green arcs. As a result, for each individual arc, there will be a closed loop on the surface of the sphere.

And for each circular arc, we form a closed loop with the two intersection points in the circular arc and the reference point. For each of the closed loop we apply Gauss-Bonnet theorem to calculate the corresponding area. By taking the modulo of the final calculated area over the area of the sphere, we calculate A_{si}. And with Eq.7.11, we obtain the intersection volume.

A more intuitive way to understand the reference point method would be to interpret the area formed by closed loop on the surface with the help of the definition of solid angle. The solid angle is usually defined as the projected area of an orientable surface on a unit sphere. In the following, we take another aspect to interpret the solid angle. In the work of Ricca et al. [Ricca and Nipoti, 2011], it is well summarized that by employing the notion of "magnetic shell", Gauss defined that the potential of a magnetic shell at a given point is the solid angle subtended by the edges at this point multiplied by the magnetic strength [Gauss, 1877]. This is based on the fact that Ampère showed that the magnetic potential is equal to a closed galvanic circuit which forms the edge of the magnetic shell. Supposed that the closed curve C is a current (I) - carrying loop, the field of this loop at the point P is given by the Biot-Savart law [Griffiths, 2005]:

$$\boldsymbol{B} = \frac{\mu_0 I}{4\pi} \int_{\partial s} \frac{d\boldsymbol{l} \times \boldsymbol{r}}{r^3} \ . \tag{7.16}$$

With Einstein summation convention and project the magnetic field $\boldsymbol{B}$ on one direction x_k, where x_k is the component of a Cartesian coordinate system:

$$\begin{aligned} B_k &= x_k \frac{\mu_0 I}{4\pi} \int_{\partial s} \epsilon_{ijk} dl_i \frac{r_j}{r^3} = \frac{\mu_0 I}{4\pi} \int_{\partial s} dl_i \epsilon_{ijk} \frac{r_j}{r^3} x_k \quad \text{[Stokes' theorem]} \\ &= \frac{\mu_0 I}{4\pi} \int_s \epsilon_{lim} \partial_l (\epsilon_{ijk} \frac{r_j}{r^3} x_k) n_m ds = \frac{\mu_0 I}{4\pi} \int_s (\delta_{mj}\delta_{lk} - \delta_{mk}\delta_{lj}) \partial_l (\frac{r_j}{r^3} x_k) n_m ds \\ &= \frac{\mu_0 I}{4\pi} \int_s \partial_k (\frac{r_j}{r^3} x_k) n_j - \partial_j (\frac{r_j}{r^3} x_k) n_k ds = \frac{\mu_0 I}{4\pi} \int_s \partial_k (\frac{r_j}{r^3}) x_k n_j - \partial_j (\frac{r_j}{r^3}) x_k n_k ds \ . \end{aligned} \tag{7.17}$$

When the point P is not on the closed loop C, $\partial_j(\frac{r_j}{r^3}) = 0$ as shown in Eq.7.3. So,

$$B_k = x_k \frac{\mu_0 I}{4\pi} \int_s \partial_k (\frac{r_j}{r^3}) n_j ds \ . \tag{7.18}$$

The solid angle subtended by S for a given point P is [Eyges, 2012]:

$$\Omega = \int_s \frac{\boldsymbol{r} \cdot d\boldsymbol{s}}{r^3} = \int_s (\frac{r_j}{r^3}) n_j ds \ . \tag{7.19}$$

where, $d\boldsymbol{s} = \boldsymbol{n} ds$.

Then the gradient of the solid angle:

$$\nabla \Omega = x_k \partial_k \int_s (\frac{r_j}{r^3}) n_j ds = x_k \int_s \partial_k (\frac{r_j}{r^3}) n_j ds = \frac{4\pi}{\mu_0 I} \boldsymbol{B} \ . \tag{7.20}$$

It is worth noting that from Eq.7.20, we can easily obtain the expression of linking number [Terning and Verhaaren, 2019] and $\nabla \times \nabla \Omega \neq 0$ due to the fact that Ω is not single valued. We used a different approach compared with the work of Eyges [Eyges, 2012] to obtain Eq.7.20 in order to show the valid choice of reference point. And the area formed by the circular arcs can be obtained by $R^2 \Omega$. As a result, the solid angle can be viewed as a magnetic scalar potential [Eyges, 2012] as well as the surface area. And the calculation of the area formed by the circular arcs on the spherical surface is the same as determining the magnetic potential at the center of the sphere with a sequence of closed galvanic circuit on the sphere. For example, we would like to calculate the area bounded by two black circular arcs as shown in Fig.7.8. The orientation of the arcs represents the flow direction of the current, which is determined by the normal direction of the polyhedron plane and the area calculation is equal to the calculation of the potential generated by the circuit formed by black arcs with respect to the center of the sphere. We pick a point, which is not the center of the sphere due to the requirement in Eq.7.18, in the space as a reference point and add two lines with the same trace but the current in opposite directions as the green arrows in Fig.7.8. Due to the fact that these newly added currents are canceling each other in terms of generated potential and they do not change the magnetic potential at the center of the sphere:

$$\boldsymbol{B}^* = \frac{\mu_0 I}{4\pi}\int_{\partial s+\sum l^+ + l^-}\frac{\boldsymbol{dl}\times\boldsymbol{r}}{r^3} = \frac{\mu_0 I}{4\pi}\int_{\partial s}\frac{\boldsymbol{dl}\times\boldsymbol{r}}{r^3} = \boldsymbol{B}\ . \tag{7.21}$$

where l_i^+ and l_i^- represent the newly added i^{th} line with the same trace and opposite current direction. $\boldsymbol{B}^*$ is the magnetic field after adding line l_i^+ and l_i^-.

We could further distribute the added lines to generate two closed loops. The principle to generate these loops is that we always use the original current's direction to complete a loop. For each intersection point between the circular arcs, there are two currents flowing in and out of this point. In that case, we could guarantee that the magnetic potential generated by the current of the newly added lines cancel each other. For more circuits on the sphere, the same procedure is also applied as shown in Eq.7.21. Here, the choice of the reference point is also random except the center of the sphere, so we further explain how to calculate the intersection volume by considering the contribution of each circular arc without addressing the global Euler characteristics. The reason to force the reference point on the sphere and the newly added circular arcs to be part of the great circle is out of computational convenience. In that case, the newly added circular arcs have zero geodesic curvature and the magnetic potential is calculated by Gauss-Bonnet theorem. When Gauss-Bonnet theorem is applied, we do not obtain negative area but the corresponding magnetic potential can be negative. As a result, we need to subtract a multiple of 4π as discussed before.

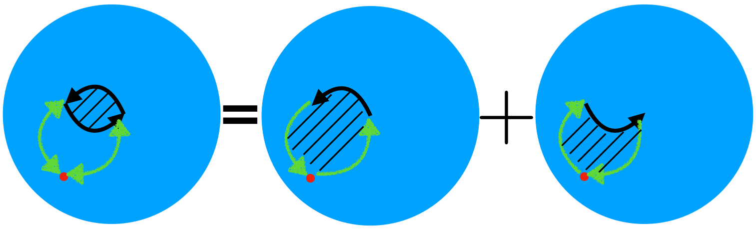

Figure 7.8: Illustration of how to interpret the reference point method with the notion of magnetic potential. The hatched region enclosed by black arcs is the area we should calculate. The arrow of the black arcs indicate the current direction. The area of the hatch region is the same as the magnetic potential at the center of the sphere with respect to the black circuit. And the red point is the reference we choose. The green arcs with arrows in double directions represent that we add two lines with current in opposite direction.

Magnetic field

The method is also named as vector field method in the following. In his treatise on electricity and magnetism [Maxwell, 1873], Maxwell introduced the vector field to calculate the solid angle, which is the projected area on an unit sphere from an orientable surface. We construct a similar vector field as shown in the work of Dirac and Maxwell [Dirac, 1931; Maxwell, 1873], which represents the vector potential of the radial field generated by a magnetic monopole.

$$\mathbf{A_m} = \tan\frac{\theta}{2}\hat{\boldsymbol{\varphi}} \ . \tag{7.22}$$

The vector field has one singular point when $\theta = \pi$, where the Dirac String is defined [Dirac, 1931]. Even though nobody has ever seen a magnetic monopole, there is a sound theoretical reason for the existence of magnetic monopole [Preskill, 1984]. However, we only focus on the mathematics behind the magnetic monopole. When a closed loop on the surface does not include this singular point, we have the following relation based on Stokes theorem for the area formed by a simple closed loop:

$$A_s = R\int\int_s \nabla \times \mathbf{A_m} \cdot \mathbf{r}dS \ \ = R\int_{\partial s} \mathbf{A_m} d\mathbf{l} \ . \tag{7.23}$$

After parameterization of a circle on the sphere as shown in the appendix J, we obtain,

$$A_s = R\int_s \tan\frac{\theta}{2}\hat{\boldsymbol{\varphi}} d\hat{\mathbf{l}} = R^2\Big(-2\arctan\left(\frac{\cos\frac{\alpha+\beta}{2}}{\cos\frac{\alpha-\beta}{2}}\cot\frac{t}{2}\right) - t\cos\alpha\Big)\Big|_{t_1}^{t_2} \ . \tag{7.24}$$

Eq.7.24 gives us the possibility to evaluate the area formed by circular arcs on a sphere

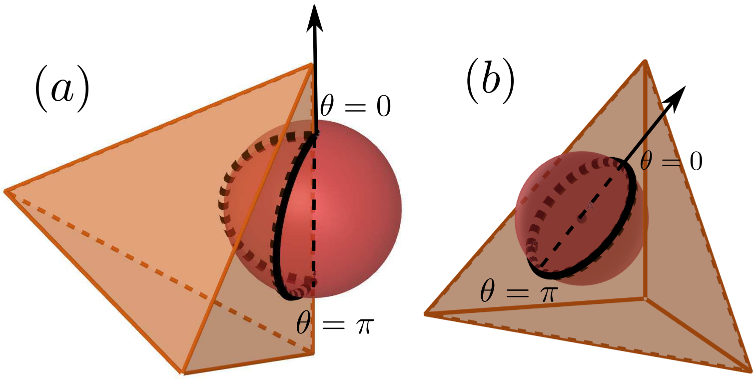

Figure 7.9: (a) one edge of the tetrahedron crosses the south pole. (b) one face of the tetrahedron cross the south pole.

directly by point evaluation. If the curved area on the sphere includes the south polar point, additional $4\pi R^2$ should be added. That also means that, theoretically, Eq.7.24 will give us a negative result if the integrated region includes the singular point. So we could directly determine whether we should add the surface area or not by evaluating the sign of $\sum A_s$. One unique case is that, when the singular point is exactly on the edge as shown in Fig.7.9(a) or the face of a polyhedron as shown in Fig.7.9(b), the contribution from the singular point to the total surface area calculation is only a portion of surface area. This is because only a part of the circle is employed for the integration. More details are available in Appendix J.1.

As a result, in the implementation process, we use one of the other methods, i.e. projection method, as a reference to evaluate the correctness of calculated volume. If the difference between the calculated volume and the reference volume is relatively high (we use the surface area multiplied by a coefficient as a threshold), we rotate the sphere and calculate the intersection volume again. It should be pointed out that we do not directly calculate α and β in Eq.7.24 because $\cos\alpha(\beta)$ and $\sin\alpha(\beta)$ are directly determined by the geometry. Any extra calculation of angles will introduce some round-off errors and undermine the accuracy of the calculation. To resolve the unnecessary rotation, we propose an approach to remove the singular point in the appendix J.1. Due to the fact that we do not implement the algorithm in the current thesis, only the central idea is described.

In addition, Eq.7.24 provides an efficient way to evaluate whether the point is inside or outside of a closed loop. In order to show the advantage of our algorithm, we describe some traditional methods in the literature. For example, in the work of Connolly [Connolly, 1983], the test point is set as the north pole of the stereographic projection. By examining the orientation of the polygon, which is projected from the loop, we can check the point is inside or outside of the loop or cycle. Also in the work of Quan et al. [Quan and Stamm, 2016], a Lemma is given to determine the relationship between different loops, which however can not be extended to a complex contour on the surface of the sphere. With Eq.7.24, we set the test point as the south pole, if the integral Eq.7.24 of the loop turns out to be negative, then the test point is inside the loop. Otherwise, it is outside of the loop. Our current method does not require projection, so that the calculation is much more simplified. This result has a potential application in the point-in-spherical-polygon test, which is usually solved by projecting the spherical polygon into a planar polygon [Li et al., 2017]. Moreover in the work of Bevis et al. [Bevis and Chatelain, 1989], a algorithm is developed to locate a point on a spherical surface relative to a spherical polygon of arbitrary shape. But our method here is not restricted to the spherical polygon and can be applied to arbitrary region formed by circular arcs on the sphere.

7.3 Validation and benchmarking

7.3.1 Validation

To test the accuracy and stability of the algorithm 1 and algorithm 2, we make use of the code [Strobl et al., 2016] as a reference, which will be referred as literature method in the following. The first tested example, where an analytical solution is known, is an intersection volume between a tetrahedron and a sphere. The tetrahedron has four vertexes at (10^5,0,0), (0,10^5,0), (0,10^5,0), (0,0,0). And the sphere has its center at the origin of the coordinate and the radius $R \in (0, \frac{10^5\sqrt{3}}{3}]$. The theoretical intersection volume between the sphere and the tetrahedron is $\frac{\pi R^3}{6}$. And for each radius of the sphere, we calculate the relative change of volume compared with the theoretical volume as shown in Fig.7.10. When we gradually increase the radius of the sphere, $\frac{|\Delta V|}{V_{analytic}}$ in Fig.7.10, i.e. the relative deviation from the analytical solution, for all methods fluctuates. We notice that the results calculated based on the literature method [Strobl et al., 2016] have larger relative deviation from the analytical results compared with the results based on the methods proposed in this work. In addition, the literature method is sensitive to the ratio of the sphere size and the tetrahedron size. Especially when $\hat{R} < 0.1$, there is a sharp increase of relative difference with decreasing $\hat{R}$. This difference originates from the fact that the literature method requires the division of the intersection volume into basic parts but, whereas our method calculates the value directly based on the boundary information of the intersection region.

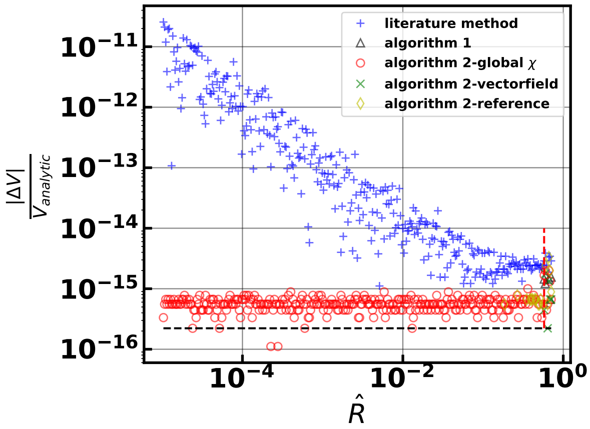

Figure 7.10: Comparison between five different methods to calculate the intersection volume between a sphere and a tetrahedron. The dashed black line indicates the machine epsilon for double-precision floating-number. $\hat{R}$ represent the normalized sphere radius by the length of the tetrahedron edge along the axis. $|\Delta V|$ indicates $V_{calculated} - V_{analytic}$, which is the absolute difference between the calculated intersection volume and the theoretical intersection volume. In the legend, literature method represents the result calculated by the work of Strobl et al. [Strobl et al., 2016].

The second validation test we implement is the same test as in the work of Strobl et al. [Strobl et al., 2016]. We calculate the intersection volume between a sphere and a mesh consisting of equally sized regular cuboids with an edge length of unity. Then we add the intersection volume up and compare it with the original volume of the sphere. We test 10^5 random sampling points using 40 logarithmically spaced intervals for radius between 0.05 and 20. As shown in Fig.7.11, the overall deviation is one order better compared with the work of Strobl et al. [Strobl et al., 2016]. From the previous example, we already notice that one reason for the improved accuracy. In addition, our methods also make an average over quantities like intersection points and area, so that the overlapping faces inside the cuboid are able to cancel with each other in the final summation. In Fig.7.11, we also notice that the general relative difference for the results based on algorithm 1, which are indicated in green, is higher than the results based on algorithm 2 indicated by colors of blue, magenta and black. The reason is that for the algorithm 1, we need to take care of every triangle for the tetrahedron. But algorithm 2 only covers the contribution from the triangle inside or intersecting the sphere. To be more specific, algorithm 2 does not count the contribution for the type 2 triangles as can be seen in Fig.7.1. The extra triangles considered in algorithm 1 will introduce extra calculation of exterior angles, which in the end will increase the round-off error in the final results. When we look at the

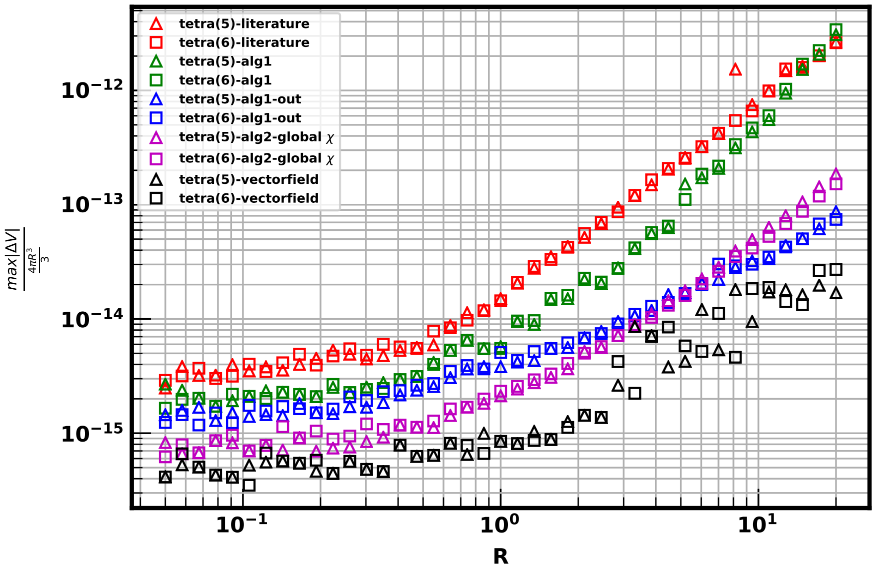

Figure 7.11: The maximum relative difference in the total overlapping volume between a cuboid mesh composed of 5 or 6 tetrahedra and a sphere. In the legend, alg1 (2) represents implementation with the algorithm 1(2). '-out' represents that when the triangle is outside of the sphere, we use a different approach [Van Oosterom and Strackee, 1983] to calculate the solid angle.

results of the literature methods shown in red in Fig.7.11, the relative difference increases monotonically with increasing radius of the sphere for $R > 1$. However, when the radius of the sphere is 8.14181063073808531, we notice that there is a jumping point for the results calculated by the literature method [Strobl et al., 2016]. We further identify the signle point (2.97371894263335768e-01, 2.97371894263335768e-01, 6.45279046742336382e-02) from all the 200000 points. In order to investigate whether this point might cause a potential failure of the algorithm described by the literature method, we try to increase and decrease the radius with machine epsilon based on the jumping point radius and the resuls are shown in Fig.7.12. The results in Fig.7.12 indicate that even though there is a jump, the results calculated by Strobl et al. [Strobl et al., 2016] do not lead to errors. The reason for the existence of these ”outlayers” is not further explored in current thesis.

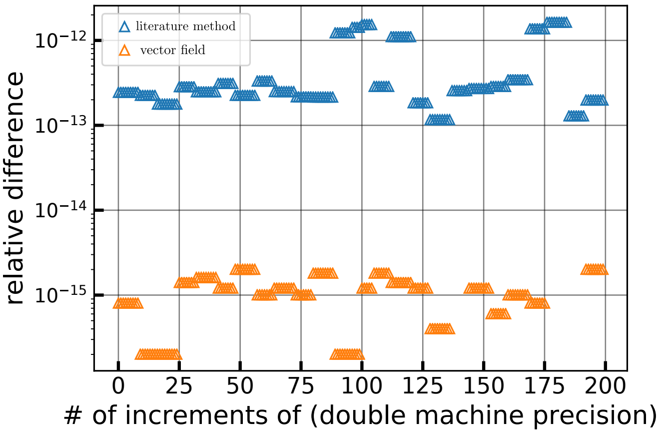

Figure 7.12: An individual case based on the jumping point when the tetrahedron is divided into 5 tetrahedra for the literature method as shown in Fig.7.11. The coordinate of the center of the sphere is (2.97371894263335768e-01, 2.97371894263335768e-01, 6.45279046742336382e-02) and the radius of the sphere R=8.14181063073808531+(x-100)×ϵ. ϵ represents machine epsilon, which is equal to 2.2204460492503131e-16 in this implementation. x represents abscissa. As a result, x=100 represents radius of the sphere, which leads to the jumping point in Fig.7.11. Y axis shows the relative difference with respect to the theoretical volume, i.e. $\frac{\Delta V_{sphere}}{V_{sphere}}$. We shrink and expand the sphere with increments in machine epsilon. ’vector field’ represents the vector field method developed in this thesis.

Due to the fluctuation in Fig.7.11, we further try to quantify the potential uncertainty with generalized extreme value distribution, which is a stochastic method to characterize ”extreme events” and has been frequently used to model the distribution of flood peaks [Morrison and Smith, 2002], prediction of gas production [Patzek et al., 2019] and critical market events [Markose and Alentorn, 2011]. Firstly, generalized extreme value (GEV) family of distributions can be combined into a single family of models having the following distribution functions of the form [Coles et al., 2001]:

$$G(x) = \exp\{-[1+\xi(\frac{x-\mu}{\sigma})]_{+}^{\frac{-1}{\xi}}\} \ . \tag{7.25}$$

where x_+=max$(x, 0)$; μ and σ are location and scale parameters; ξ is a shape parameter determining the rate of tail decay.

- $\xi > 0$ - heavy-tailed case, Fréchet
- $\xi = 0$ - light-tailed case, Gumbel
- $\xi < 0$ - bounded-tailed case, Weibull

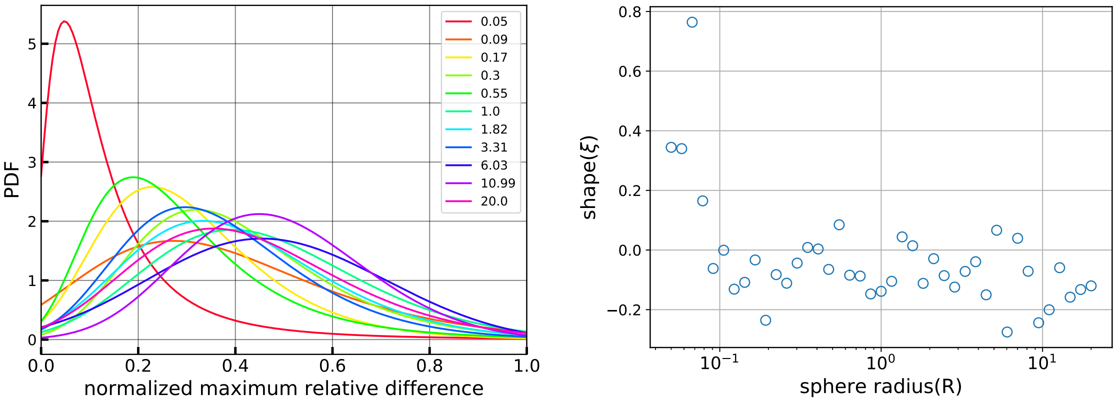

(a) **(b)**

Figure 7.13: The cuboid is decomposed into 6 tetrahedra and the corresponding intersection volume is calculated via literature method. The radius of the sphere is varied from 0.05 to 20 as shown in Fig.7.11. (a) is a plot of the PDF (probability distribution function) for each specific radius of sphere; (b) is shape factor with respect to different radii.

There are two fundamental approaches: block maximum method and the peaks-over-threshold method [Ferreira et al., 2015]. In this thesis, we only focus on the block maximum method. For each specific radius, we divide the relative difference obtained by 10^5 random position of spheres into 100 blocks with equal size.

We plot Fig.7.13 when the radius of sphere R=20 as an example to illustrate this method. As shown in Fig.7.13, when the radius of the sphere is small, we still have the fat tail ($\xi > 0$). When the radius is large enough, the tail is thin or truncated ($\xi < 0$). But there are still some fat tails, which might cause the jump we see in Fig.7.11. Further we choose a specific radius $R = 20$ and quantify the uncertainty with generalized extreme value distribution. As shown in Fig.7.14, for the same radius of sphere, literature method is much less fluctuated with $\xi = -0.12$ as shown in Fig.7.14 (b) while the algorithm 2 based on vector field in Fig.7.14 (a) has a larger $\xi = 0.22$. This observation also matches what we find in Fig.7.11, where the relative difference does not increase monotonously with increasing sphere radius. However, we should notice that the vector field has maximum relative difference two orders smaller than the literature method. In this sense, the proposed method is much more accurate compared with literature method.

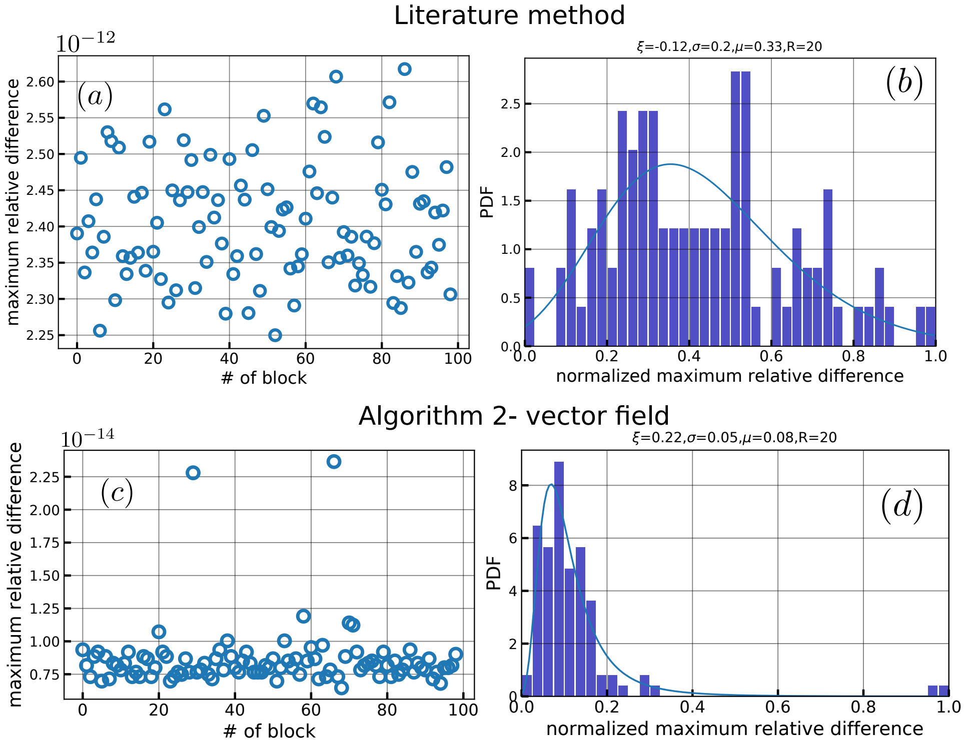

Figure 7.14: The radius of the sphere R=20. The cuboid is decomposed into 6 tetrahedra and the corresponding intersection volume is calculated via literature method in (a,b) and algorithm 2 with the vector field method in (c,d). (a,c) is a plot of the maximum relative difference for each block including one thousand evaluation; (b,d) is the fitted distribution for the relative difference of volume.

7.3.2 Benchmark

The computational performance of the proposed algorithms is also evaluated here. All the benchmark runs are performed on a typical computer with an Intel (R) Core i7-4770 CPU with a base frequency of 3.4 GHz. The code is compiled using the GNU C++ complier 4.8.4. We repeat the benchmarking example as in the work of Strobl et al. [Strobl et al., 2016]. So we vary the radius of sphere within $[0.1, 1.0]$, whose center is placed in the central unit hexahedron and the overlapping volume with all the elements are calculated. For each radius, we record the time for the evaluation of the total overlap volume for 10000 samples and make an average over that.

In Fig.7.15, we find that when we increase the number of tetrahedra, the averaged runtime increases correspondingly for all of the three algorithms. Algorithm 1 shows s similar performance compared with the literature result, while Algorithm 2 shows a better performance in comparison with the literature method. The reason for that is that for algorithm 1, we need to process all the faces while algorithm 2 does not, which we already discuss in the validation section. To enable a fair comparison of the performance that depends on the computer specifications and the choice of the compiler, we choose the same computer and compiler to run all the tests as shown in Fig.7.15. In that case, it is fair to show that our algorithm 2 is able to have a better performance. In addition, algorithm 1 with the applied algorithm of Oosterom [Van Oosterom and Strackee, 1983] is also comparable with algorithm 2, however the work of Oosterom is only applicable for calculating the solid angle of a triangle when the triangle is not intersecting with the sphere.

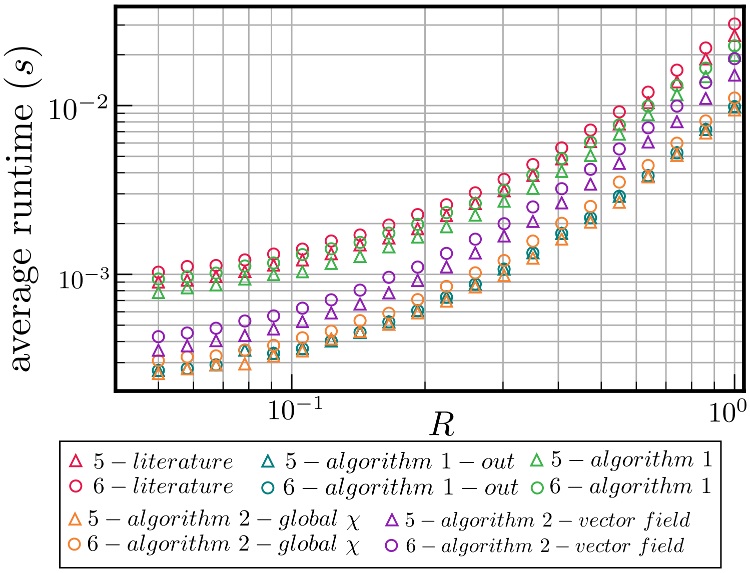

Figure 7.15: Averaged wall-clock times comparison between new algorithms and the literature method in the work of Strobl et al. [Strobl et al., 2016]. The average runtime is measured during calculation of a sphere with radius R and a regular mesh of 5 or 6 tetrahedra. "5-" or "6-" in the legend indicates that the cuboid is decomposed into 5 or 6 tetrahedra. "out-" for algorithm 1 represents that the algorithm of Oosterom is applied [Van Oosterom and Strackee, 1983].

7.4 Application

In order to demonstrate that the algorithms presented in this work are not restricted to tetrahedron-sphere volume intersection, we additionally calculate the intersection volume between a cylinder and a sphere, which is solved analytically in the work of Lamarche et al. [Lamarche and Leroy, 1990]. For this example, we only implement algorithm 1 due to the convenience of implementation. Even though the cylinder is not a polyhedron, we use triangular mesh to approximate the surface of the cylinder and then calculate the intersection volume between them.

For the test, we generate a cylinder with Surface Evolver [Brakke, 1992] and put a sphere with varying radius originally out of the cylinder with radius of 1 and height of 4. The distance between the sphere center and the cylinder center is 2. We gradually increase the radius of the sphere and calculate the intersection volume between the sphere and the cylinder. As shown in Fig.7.16(a), before the radius of the sphere reaches 1, the ideal intersection volume should be 0. But we see that our method gives ”virtual intersection volume”. This is also an indication of the source for difference between theoretical result and numerical implementation. Resulting from finite precision, the round-off error is inevitable. If the radius of the sphere is larger than 1, we see a good match between the analytic result and both of our methods. As we continue to grow the radius of the sphere, we find that there is a sudden increase in terms of the relative difference with respect to the analytic value at $R = \sqrt{5}$. The reason is also obvious. In the work of Lamarche et al. [Lamarche and Leroy, 1990], they calculate the intersection volume between a sphere and an infinite long cylinder. But in our case, the cylinder has a height of 4. As a result, when the radius of the sphere reaches $\sqrt{5}$, the intersection volume we calculate should be smaller than the analytic value. In addition, when the radius of the sphere reaches $\sqrt{13}$, the sphere will cover the cylinder, so that the intersection value should be the cylinder volume. Fig.7.16(a) also shows that the increased number of triangles will enhance the accuracy for intersection volume calculation as the cylinder surface is more accurately approximated by more triangular surfaces approximating.

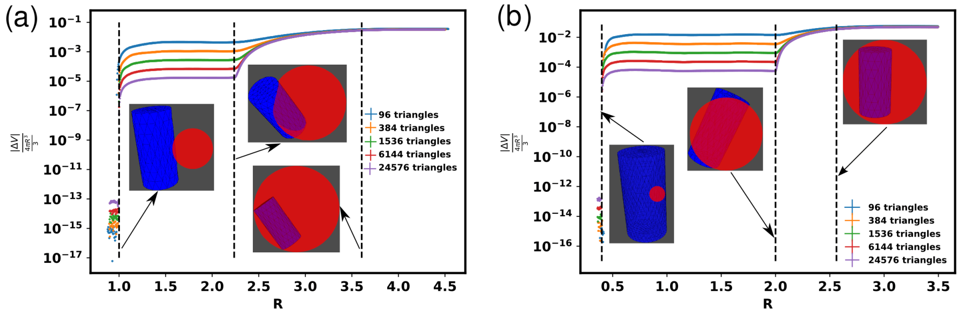

Figure 7.16: Plot of the relative difference between numerical and analytical results with respect to the sphere volume against the radius of the sphere, when calculating the intersection volume between a sphere and a cylinder (radius of 1 and height of 4). (a) The sphere is outside of the cylinder, and the distance between the sphere center and cylinder center is 2. The dark dashed vertical lines represent $R = 1, \sqrt{5}, \sqrt{13}$. (b) The sphere is originally inside of the cylinder, the distance between the sphere center and cylinder center is 0.6. The dark dashed vertical lines represent $R = 0.4, 2, \frac{2\sqrt{41}}{5}$.

We construct another growing sphere case, in which the sphere is originally inside the cylinder as in Fig.7.16(b). Before the radius of the sphere reaches 0.4, the intersection volume should be the volume of the sphere. But we also see that this method is not going to give the exact volume of the sphere. The reason is similar to the case discussed in the context of Fig.7.16(a). However, our aim here is to show the potential application of the algorithm, but not to optimize the mesh generation. It is worth mentioning that this method is also able to determine whether a sphere is inside or outside of a polyhedron. A similar idea has already been shown in the work of Lane et al. [Lane et al., 1984].

7.5 Summary

We provide two algorithms to calculate the intersection volume between a sphere and a tetrahedron. The first algorithm needs to consider all the faces of a polyhedron for intersection volume calculation. The second algorithm focus on the faces of a polyhedron, which are either inside of intersecting with the sphere. For the second algorithm, we further develop three different algorithms to calculate the area (A_s) formed by the circular arcs on a sphere. By decomposing the calculation of intersection volume between a sphere and a tetrahedron into the contribution from a specific triangles, without specification of any shape like wedges or caps [Bernardeau and van de Weygaert, 1996; Wu et al., 2009; Strobl et al., 2016], we are able to achieve an improved accuracy and better computational performance compared with current published results [Strobl et al., 2016]. This algorithm is employed in chapter 5 for calculating the intersection volume between spherical meniscus and the tetrahedron pore. In addition, the algorithms presented in this thesis can be extended to calculate the intersection volume between the sphere and any closed polyhedron with orientable surface.

Appendices

A Critical curvature radius for different events

- **Burst events**

  The critical curvature for two disks with normalized mean diameter (also known as dimensionless microscopic characteristic length) is defined as follows [Holtzman and Segre, 2015]:

$$R_b = -r\cos\theta + \frac{\sqrt{d^2 - 4r^2\sin^2\theta}}{2} = \frac{d}{2}(\sqrt{1-\tilde{l}^2\sin^2\theta} + \tilde{l}\cos\theta)\ . \tag{A.1}$$

- **Touch events**

  With Eq.C.63, we let $r_1 = r_2 = r_3 = r, \theta_1 = \theta_2 = \theta, d_1 = d_2 = d_3 = d$:

$$\begin{aligned}
\hat{C}_{t2} &= -\begin{vmatrix} -2d^2 & -d^2 & d^2 \\ -d^2 & -2d^2 & d^2 \\ d^2 & d^2 & -2r^2 \end{vmatrix} = -2d^4(d^2-6r^2), \\
\hat{A}_{t2} &= -\begin{vmatrix} -2 & -2r\cos\theta - 2r & -2r\cos\theta - 2r \\ -2r\cos\theta - 2r & -2d^2 & -d^2 \\ -2r\cos\theta - 2r & -d^2 & -2d^2 \end{vmatrix} \\
&= 2d^2[3d^2 - 4r^2(1+\cos\theta)^2], \\
\hat{B}_{t2} &= 2\begin{vmatrix} -2r\cos\theta - 2r & -2r\cos\theta - 2r & 2r \\ -2d^2 & -d^2 & d^2 \\ -d^2 & -2d^2 & d^2 \end{vmatrix} = 4d^4 r(1-2\cos\theta)\ .
\end{aligned} \tag{A.2}$$

$$\begin{aligned}
R_t &= \frac{d^2 r(-1+2\cos\theta) \pm \sqrt{3}[d^3 - 2dr^2(1+\cos\theta)]}{3d^2 - 4r^2(1+\cos\theta)^2} \\
&= \frac{d}{2}\frac{(2\cos\theta - 1)\tilde{\ell} \pm \sqrt{3}[2 - \tilde{\ell}^2(1+\cos\theta)]}{3 - \tilde{\ell}^2(1+\cos\theta)^2}\ .
\end{aligned} \tag{A.3}$$

  One solution:

$$R_{t1} = \frac{d}{2}\frac{[(1+\cos\theta)\tilde{\ell} + \sqrt{3}](-\sqrt{3}\tilde{\ell} + 2)}{[\sqrt{3} - \tilde{\ell}(1+\cos\theta)][\sqrt{3} + \tilde{\ell}(1+\cos\theta)]} = \frac{d}{2}\frac{(-\sqrt{3}\tilde{\ell} + 2)}{\sqrt{3} - \tilde{\ell}(1+\cos\theta)}\ . \tag{A.4}$$

  Second solution:

$$R_{t2} = \frac{d}{2}\frac{[(1+\cos\theta)\tilde{\ell} - \sqrt{3}](\sqrt{3}\tilde{\ell} + 2)}{[\sqrt{3} - \tilde{\ell}(1+\cos\theta)][\sqrt{3} + \tilde{\ell}(1+\cos\theta)]} = \frac{d}{2}\frac{(-\sqrt{3}\tilde{\ell} - 2)}{\sqrt{3} + \tilde{\ell}(1+\cos\theta)} < 0\ . \tag{A.5}$$

  Excluding the spurious solution, we obtain:

$$R_t = \frac{d}{2}\frac{(-\sqrt{3}\tilde{\ell} + 2)}{\sqrt{3} - \tilde{\ell}(1+\cos\theta)}\ . \tag{A.6}$$

  It is easy to know that the for the existence of the touch meniscus is that the burst is able to touch the third disk before burst:

$$R_b \le \frac{d}{2}(\sqrt{3} - \tilde{\ell})\ . \tag{A.7}$$

- **Overlap events-uniform**

  On top of Eq.C.67, $D_1 = D_2 = D$ due to symmetry of the disk configuration. In addition, with $r_1 = r_2 = r_3 = r, d_{12} = d_{23} = d, d_{13} = 2\sin\frac{\alpha}{2}d$, we obtain:

$$\begin{vmatrix} 0 & 1 & 1 & 1 & 1 \\ 1 & 0 & D^2 & r^2 & D^2 \\ 1 & D^2 & 0 & d^2 & 4\sin^2\frac{\alpha}{2}d^2 \\ 1 & r^2 & d^2 & 0 & d^2 \\ 1 & D^2 & 4\sin^2\frac{\alpha}{2}d^2 & d^2 & 0 \end{vmatrix} = 0 \; . \tag{A.8}$$

As a result,

$$D^2 = d^2 + r^2 - 2dr\cos\frac{\alpha}{2} \; . \tag{A.9}$$

With Eq.C.68

$$\begin{vmatrix} -2 & -2r\cos\theta & -2r\cos\theta & 0 & 1 \\ -2r\cos\theta & -2D^2 & d^2 - r^2 - D^2 & D^2 - r^2 & 0 \\ -2r\cos\theta & d^2 - D^2 - r^2 & -2r^2 & 0 & 0 \\ 0 & D^2 - r^2 & 0 & 0 & R \\ 1 & 0 & 0 & R & 0 \end{vmatrix} = 0 \; . \tag{A.10}$$

Solving Eq.A.10 and replace D^2 with Eq.A.9:

$$\begin{aligned} R_o &= \frac{-d\cos\theta\cos\frac{\alpha}{2} + 2r\cos\theta\cos^2\frac{\alpha}{2} \pm (d - 2r\cos\frac{\alpha}{2})\sin\theta\sin\frac{\alpha}{2}}{\cos\alpha + \cos 2\theta} \\ &= d\frac{(-1 + \tilde{\ell}\cos\frac{\alpha}{2})\cos\theta\cos\frac{\alpha}{2} \pm (1 - \tilde{\ell}\cos\frac{\alpha}{2})\sin\theta\sin\frac{\alpha}{2}}{\cos\alpha + \cos 2\theta} \\ &= d\frac{(-1 + \tilde{\ell}\cos\frac{\alpha}{2})\cos(\theta \pm \frac{\alpha}{2})}{\cos\alpha + \cos 2\theta} \; . \end{aligned} \tag{A.11}$$

When $\cos\alpha + \cos 2\theta = 0$, $R_o = \infty$. In addition, there are two roots and should be further determined. As shown in deriving critical curvature radius for touch event, we need to address the double solutions where one of them is spurious solution.

Overlap events-60°

$$\begin{aligned} R_o &= d\frac{(-1 + \tilde{\ell}\cos\frac{\alpha}{2})\cos(\theta - \frac{\alpha}{2})}{\cos\alpha + \cos 2\theta} \\ &= d\frac{(-1 + \tilde{\ell}\cos 30^\circ)\cos(\theta - 30^\circ)}{\cos 60^\circ + \cos 2\theta} \\ &= d\frac{(-1 + \frac{\sqrt{3}}{2}\tilde{\ell})(\sqrt{3}\cos\theta + \sin\theta)}{4\cos^2\theta - 1} \; . \end{aligned} \tag{A.12}$$

As in Fig.3.6(b-1), i.e. overlap inside the pore. Here 60° represents the angle formed by the lines go through the disk center.

Overlap events-120°

$$\begin{aligned} R_o = d\frac{(-1 + \tilde{\ell}\cos\frac{\alpha}{2})\cos(\theta - \frac{\alpha}{2})}{\cos\alpha + \cos 2\theta} &= d\frac{(-1 + \tilde{\ell}\cos 60^\circ)\cos(\theta - 60^\circ)}{\cos 120^\circ + \cos 2\theta} \\ = d\frac{(-1 + \frac{1}{2}\tilde{\ell})(\cos\theta + \sqrt{3}\sin\theta)}{4\cos^2\theta - 3} \; . \end{aligned} \tag{A.13}$$

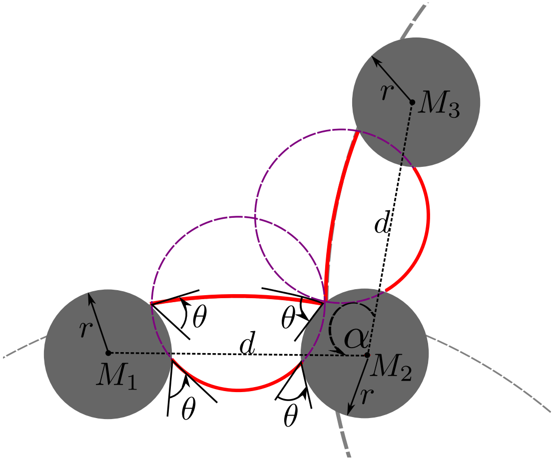

Figure A.1: An illustration of double solutions determined by CMD. The red circular arcs indicate the menisci. We find that two circles indicated by purple dashed line intersect at a point. This point is supposed to be the place where two menisci overlap. As a result, it is a spurious solution. Disks with radius of r form an interface angle α. The distance between the center of disks is d. θ represents the contact angle.

overlap events-180°

As in Fig.3.6(b-3), overlap with neighboring pore with interfacial contact angle of 180°. The curvature for this event is very clear:

$$R_{o3} = d\frac{(-1+\tilde{\ell}\cos\frac{180^\circ}{2})\cos(\theta-\frac{180^\circ}{2})}{\cos 180^\circ + \cos 2\theta} = \frac{d}{2\sin\theta}\ . \tag{A.14}$$

overlap events-240°

As shown in Fig.3.6(b-4), overlap with neighboring pore with interfacial contact angle of 240°. The radius of curvature for this event is very clear:

$$R_{o4} = d\frac{(-1+\tilde{\ell}\cos\frac{240^\circ}{2})\cos(\theta-\frac{240^\circ}{2})}{\cos 240^\circ + \cos 2\theta} = \frac{(d+r)(\cos\theta - \sin\theta\sqrt{3})}{4\cos^2\theta - 3}\ . \tag{A.15}$$

- **Overlap events-disorder**

  Due to the good property of symmetry, we are able to solve the curvature radius when two disks have different radii. Silimar to Eq.A.16:

$$D^2 = d^2 + r_2^2 - 2dr_2\cos\frac{\alpha}{2} \tag{A.16}$$

$$\begin{aligned}
\hat{C}_{o2} &= -\begin{vmatrix} -2D^2 & d^2-r_2^2-D^2 & D^2-r_1^2 \\ d^2-r_2^2-D^2 & -2r_2^2 & 0 \\ D^2-r_1^2 & 0 & 0 \end{vmatrix} = -2r_2^2(D^2-r_1^2)^2, \\
\hat{A}_{o2} &= -\begin{vmatrix} -2 & -2r_1\cos\theta & -2r_2\cos\theta \\ -2r_1\cos\theta & -2D^2 & d^2-r_2^2-D^2 \\ -2r_2\cos\theta & d^2-D^2-r_2^2 & -2r_2^2 \end{vmatrix}, \\
\hat{B}_{o2} &= 2\begin{vmatrix} -2r_1\cos\theta & -2r_2\cos\theta & 0 \\ -2D^2 & d^2-r_2^2-D^2 & D^2-r_1^2 \\ d^2-r_2^2-D^2 & -2r_2^2 & 0 \end{vmatrix} \\
&= 4(D^2-r_1^2)r_2[-d^2+D^2+r_2(-2r_1+r_2)]\cos\theta\ .
\end{aligned} \tag{A.17}$$

The critical curvature radius for the overlap event is:

$$R_o = \frac{-\hat{B}_{o2}+\sqrt{\hat{B}_{o2}^{\,2}-4\hat{A}_{o2}\hat{C}_{o2}}}{2\hat{A}_{o2}}\ . \tag{A.18}$$

B Determination of the meniscus position in 2D

Consider a meniscus passing through a narrow gap formed by two disks like Fig.B.1, where the disk radius is r_1, r_2 and the contact angle of the invading fluid with respect to the defending fluid is θ_1, θ_2. And r_p is the radius of the curvature due to $\frac{1}{r_p} = \frac{\Delta P}{\gamma}$ for a given Laplace pressure ΔP. As shown in the work of Holtzman et al. [Holtzman and Segre, 2015], in this 2D model, $\frac{1}{r_p} = \frac{1}{R_{in}} + \frac{1}{R_{out}} \approx \frac{1}{R_{in}}$ because the out-of-plane curvature ($\frac{1}{R_{out}}$) is way more smaller than the in-plane curvature ($\frac{1}{R_{in}}$). When the out-of-plane curvature is not negligible in some experiments [Zhao et al., 2016; Panizza et al., 2018], $\frac{1}{R_{out}} = \frac{2\cos\theta}{h}$ is considered (θ being the contact angle), which is not considered in current model. The position of the meniscus can be determined as follows.

For all the cases, by simple transformation we bring the center coordinates for both disks on the X axis. And in $\triangle ABC$,$\triangle BDE$ and $\triangle ABD$:

$$\begin{aligned}
\overline{AB} &= \sqrt{r_1^2+r_p^2-2r_1r_p\cos\theta_1}, \quad \overline{BD} = \sqrt{r_2^2+r_p^2-2r_2r_p\cos\theta_2} \\
\cos <\vec{AB},\vec{AD}> &= \frac{\overline{AB}^2+\overline{AD}^2-\overline{BD}^2}{2\overline{AB}\ \overline{AD}}\ .
\end{aligned} \tag{B.1}$$

So,

$$\begin{aligned}
x_B = x_A + \overline{AB}\cos <\vec{AB},\vec{AD}> &= x_A + \frac{\overline{AB}^2+\overline{AD}^2-\overline{BD}^2}{2\ \overline{AD}} \\
&= x_A + \frac{r_1^2-r_2^2+d^2-2r_p(r_1\cos\theta_1-r_2\cos\theta_2)}{2d}\ .
\end{aligned} \tag{B.2}$$

Then,

$$y_B = \pm\sqrt{\overline{AB}^2-(x_B-x_A)^2}\ . \tag{B.3}$$

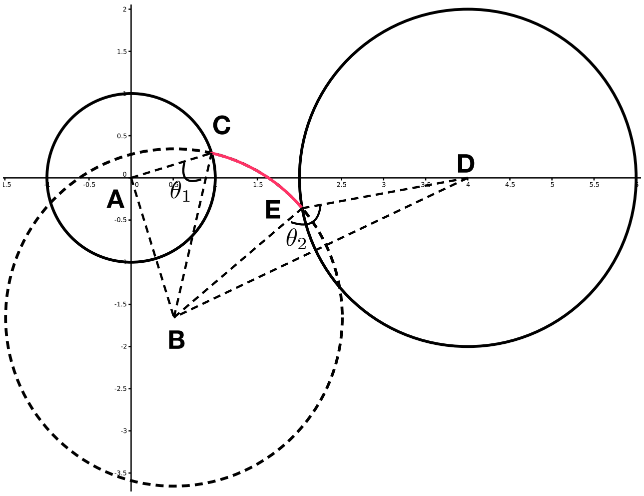

Figure B.1: Determination of the meniscus position. The red arc indicates the meniscus. In this case, $\theta_1 = 60°, \theta_2 = 150°$.

With Eq.B.2 and Eq.B.3, we are able to determine the position of the meniscus given the Laplace pressure ΔP.

C C&R's model

C.1 Haines jump in 2D

A burst event also known as a Haines jump is characterized by a sudden jump of the fluid interface when the applied capillary pressure exceeds a maximum Laplace pressure permitting a stable meniscus. In 2D, since the work of Cieplak and Robbins [Cieplak and Robbins, 1990], a model consisting of arrays of disks are frequently employed [Chapuis et al., 2008; Primkulov et al., 2018; Hu et al., 2019] to study how the pore-scale events lead to a global invasion pattern because a Haines jump for a meniscus as well as the movement of a meniscus in the quasistatic limit under applied capillary pressure is well resolved mathematically. In the following, we firstly describe the Haines jump model for a meniscus passing through the narrow gap formed by two disks. As shown in Fig.C.1(b), when the meniscus is moving forth from the state indicated by the red point ($P_c = P_{min}$) and blue point ($P_c = P_{max}$), it is stable due to $\frac{\partial P_c}{\partial \Delta V} > 0$. When $P_c < P_{min}$ or $P_c > P_{max}$, the meniscus exceeds its range of stability and a Haines jump will occur. To obtain the critical curvature radius for the burst events or Haines jumps, several key literature are summarized as follows. In the work of Ceiplak and Robbins [Cieplak and Robbins, 1990], a biquadratic equation is solved to obtain the angle between the two contact points as seen from the arc center. When there is no solution for the proposed equation, the meniscus is deemed as not stable leading to a Haines jump. However, there is no closed form expression for the Haines jump as a function of contact angle and geometry. The first closed form expression to calculate the critical curvature radius is achieved by Holtzman et al.

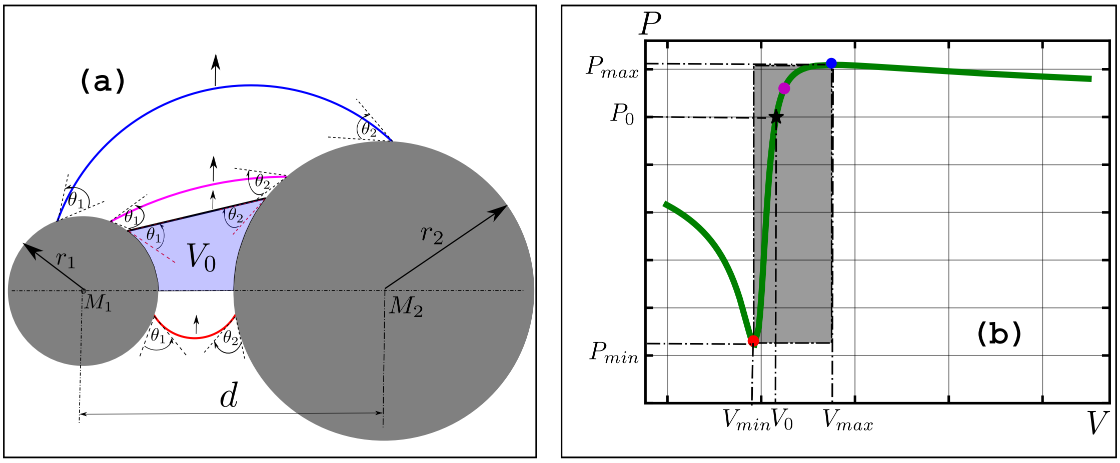

Figure C.1: (a) Sketch of a meniscus passing through a throat formed by two disks with $\theta_1 = 50°, \theta_2 = 40°$. The arrows indicate the moving direction of the meniscus. (b) Sketch of the relationship between capillary pressure P and volume V. Here V indicates the area formed by the current meniscus and the boundary of disks together with a reference boundary M_1M_2. For example, V_0 in (b) indicates the area swept by the meniscus shown as the blue region in (a) when the applied pressure is 0. The indicated blue/red point in (b) at P_{max}/P_{min} represents the advancing front indicated by blue/red arrow in (a).

[Holtzman and Segre, 2015]. However, the work of Holtzman et al. [Holtzman and Segre, 2015] restricted on two disks with homogeneous wettability and no explicit expression to calculate the critical curvature for touch event was presented. Since the work of Holtzman et al. [Holtzman and Segre, 2015], there are some literature [Primkulov et al., 2018; Hu et al., 2019] showing that the curvature radius of burst event and touch event are both solved by a quadratic equation. However, in the work of Primkulov et al. [Primkulov et al., 2018], no exact form of the critical radius for both burst event and touch event was presented because it was described as laborious algebra to obtain expanded form of the solution for the quadratic equation. In the work of Hu et al. [Hu et al., 2019], explicit expressions for the critical curvature radius were obtained for a burst event but only when the disks have the same surface property, which do not differ from the ones given in the work of Holtzman et al. [Holtzman and Segre, 2015]. The explicit expression to describe the curvature radius for touch event is only solved when the three disk centers form a equilateral triangle [Hu et al., 2019]. At the same time, Motealleh et al. [Motealleh et al., 2010, 2013] only described the criteria to determine the critical position for burst event in 2D as well as in 3D. But in 3D, the analytic expression to determine the burst curvature radius has not been derived. In the following, we present a novel method which not only gives the critical curvature radius for the burst and touch event for arbitrary surface properties and disk positions in 2D, but also can be extended to determine the critical curvature radius in three or higher dimension.

Cayley-Menger determinant

The mathematical tool we employ is named as Cayley-Menger determinant (CMD) [Menger, 1928], which has been described as an arcane but effective tool in the work of Kostinski et al. [Kostinski et al., 2014]. Basically, CMD is a formula for the volume evaluation of a simplex in any number of dimensions with L_2 norm to compute the edge length of the simplex. Given $N+1$ points $(p_1, ..., p_{N+1})$ forming the simplex in N dimensions and r_{ij} is the distance between point p_i and p_j, the N-dimensional volume $V_N(p_1, ..., p_{N+1})$ is given [Menger, 1928]:

$$\begin{aligned} V_N^2 &= \frac{(-1)^{N+1}}{2^N (N!)^2} \begin{vmatrix} 0 & 1 & 1 & \dots & 1 \\ 1 & 0 & r_{12}^2 & \dots & r_{1(N+1)}^2 \\ 1 & r_{21}^2 & 0 & \dots & r_{2(N+1)}^2 \\ \vdots & \vdots & \vdots & \ddots & \vdots \\ 1 & r_{(N+1)1}^2 & r_{(N+1)2}^2 & \dots & 0 \end{vmatrix} \\ &= \frac{1}{2^N (N!)^2} \begin{vmatrix} 2r_{12}^2 & r_{12}^2 + r_{13}^2 - r_{23}^2 & \dots & r_{12}^2 + r_{1(N+1)}^2 - r_{2(N+1)}^2 \\ r_{12}^2 + r_{13}^2 - r_{23}^2 & 2r_{13}^2 & \dots & r_{13}^2 + r_{1(N+1)}^2 - r_{3(N+1)}^2 \\ \vdots & \vdots & \ddots & \vdots \\ r_{12}^2 + r_{1(N+1)}^2 - r_{2(N+1)}^2 & r_{13}^2 + r_{1(N+1)}^2 - r_{3(N+1)}^2 & \dots & 2r_{1(N+1)}^2 \end{vmatrix} . \end{aligned} \tag{C.1}$$

In two dimensions, Eq.C.1 is equivalent to the famous Heron's formula for the triangle area calculation.

To establish the link between CMD and the model to determine the critical curvature radius for burst event in disk packing, we employ an example as shown in Fig.C.2. In Fig.C.2, the existence of a meniscus resting on two disks guarantees the existence of a circle with center O_1. Further, the existence of the point O_1 make

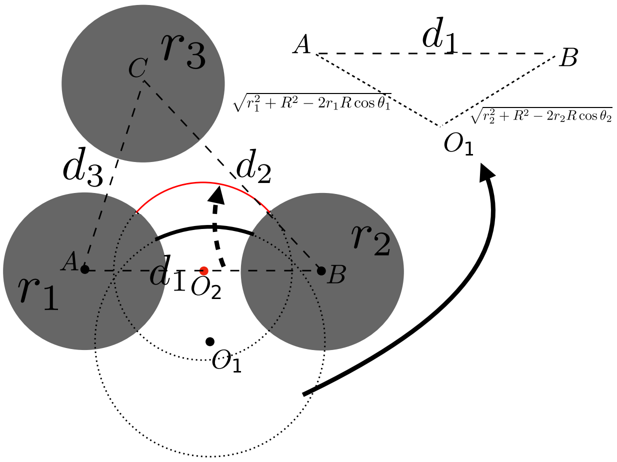

Figure C.2: Illustration of meniscus moving through the gap formed by two disks. O_1 and O_2 are centers for two circular menisci. The dashed arrow indicates the moving direction of circular meniscus. The red circular arc indicates the situation when burst event happens. The contact angles of the disk A and B with respect to the invading fluid are θ_1 and θ_2. R is the radius of the circular meniscus.

sure that the triangle ABO_1 exists. Since we know the sides of the triangle ABO_1 ($AO_1 = \sqrt{r_1^2 + R^2 - 2r_1R\cos\theta_1}$ and $BO_1 = \sqrt{r_2^2 + R^2 - 2r_2R\cos\theta_2}$ when the curvature radius of the meniscus is R), we can use the CM determinant to express the area of this triangle and obtain an equation to solve the smallest radius R of the arc by investigating the sign of the CMD.

According to CMD, the squared area of the triangle AO_1B is expressed as:

$$V_2^2 = -\frac{1}{16}\begin{vmatrix} 0 & R^2 + r_1^2 - 2Rr_1\cos\theta_1 & R^2 + r_2^2 - 2Rr_2\cos\theta_2 & 1 \\ R^2 + r_1^2 - 2Rr_1\cos\theta_1 & 0 & d^2 & 1 \\ R^2 + r_2^2 - 2Rr_2\cos\theta_2 & d^2 & 0 & 1 \\ 1 & 1 & 1 & 0 \end{vmatrix} . \tag{C.2}$$

We suppose that $a_{i,j}$ is the entry for the i^{th} row and j^{th} column of the matrix in Eq.C.2. With the basic property of determinant [Strang, 2016], we are able to simplify Eq.C.2. For the row operation:$a_{1k} - R^2a_{4k} \to a_{1k}$; $a_{ik} - r_{i-1}^2a_{4k} \to a_{ik}, i = 2, 3$. For the column operation:$a_{k1} - R^2a_{k4} \to a_{k1}$; $a_{ki} - r_{i-1}^2a_{k4} \to a_{ki}, i = 2, 3$. As a consequence:

$$V_2^2 = -\frac{1}{16}\begin{vmatrix} -2R^2 & -2Rr_1\cos\theta_1 & -2Rr_2\cos\theta_2 & 1 \\ -2Rr_1\cos\theta_1 & -2r_1^2 & d^2 - r_1^2 - r_2^2 & 1 \\ -2Rr_2\cos\theta_2 & d^2 - r_1^2 - r_2^2 & -2r_2^2 & 1 \\ 1 & 1 & 1 & 0 \end{vmatrix} , \tag{C.3}$$

With $a_{4k} \to Ra_{4k}$, $a_{k1} \to a_{k1}/R$ and $a_{k4} \to Ra_{k4}$, $a_{1k} \to a_{1k}/R$:

$$V_2^2 = -\frac{1}{16}\begin{vmatrix} -2 & -2r_1\cos\theta_1 & -2r_2\cos\theta_2 & 1 \\ -2r_1\cos\theta_1 & -2r_1^2 & d^2 - r_1^2 - r_2^2 & R \\ -2r_2\cos\theta_2 & d^2 - r_1^2 - r_2^2 & -2r_2^2 & R \\ 1 & R & R & 0 \end{vmatrix} , \tag{C.4}$$

With $a_{2k} - a_{3k} \to a_{2k}$, $a_{k2} - a_{k3} \to a_{k2}$:

$$V_2^2 = -\frac{1}{16}\begin{vmatrix} -2 & -2r_1\cos\theta_1 + 2r_2\cos\theta_2 & -2r_2\cos\theta_2 & 1 \\ -2r_1\cos\theta_1 + 2r_2\cos\theta_2 & -2d^2 & d^2 - r_1^2 + r_2^2 & 0 \\ -2r_2\cos\theta_2 & d^2 - r_1^2 + r_2^2 & -2r_2^2 & R \\ 1 & 0 & R & 0 \end{vmatrix} . \tag{C.5}$$

Define the Levi Civita symbol as the sign of the permuation i_n of indices (the bijective function $n \mapsto i_n$) [Riley et al., 2006]:

$$\det(A) = \epsilon_{i_1 \cdots i_n} a_{1i_1} .. a_{ni_n} . \tag{C.6}$$

Expanding Eq.C.5, to obtain the coefficient of R^2:

$$-\frac{1}{16}\epsilon_{ij43}a_{1i}a_{2j}a_{34}a_{43} = \frac{1}{16}\epsilon_{ij34}a_{1i}a_{2j}R^2 . \tag{C.7}$$

In addition, when the disks are not overlapping with each other:

$$\frac{1}{16}\epsilon_{ij34}a_{1i}a_{2j} = \frac{1}{16}(4d^2 - 4(r_1\cos\theta_1 - r_2\cos\theta_2)^2) > 0 . \tag{C.8}$$

For the coefficient of R:

$$
\begin{aligned}
-\frac{1}{16}\epsilon_{ij41}a_{1i}a_{2j}a_{34}a_{41} \times 2 &= \frac{2}{16}\epsilon_{1ij4}a_{1i}a_{2j}R \\
&= \frac{1}{16}\left[4r_1\cos\theta_1(r_1^2 - r_2^2 - d^2) + 4r_2\cos\theta_2(r_2^2 - r_1^2 - d^2)\right] \ ,
\end{aligned}
\tag{C.9}
$$

For the constant without R:

$$
\begin{aligned}
&-\frac{1}{16}\epsilon_{4ij1}a_{14}a_{2i}a_{3j}a_{41} = \frac{1}{16}\epsilon_{1ij4}a_{2i}a_{3j} \\
&= \frac{1}{16}[d^2 - (r_1 - r_2)^2][(r_1 + r_2)^2 - d^2] < 0 \ .
\end{aligned}
\tag{C.10}
$$

As a result, we express the squared area of the triangle as a quadratic equation:

$$
V_2^2 = \frac{1}{16}(\hat{A}_2R^2 + \hat{B}_2R + \hat{C}_2) \ . \tag{C.11}
$$

where,

$\hat{A}_2 = \epsilon_{ij3}a_{1i}a_{2j}, \hat{B}_2 = 2\epsilon_{1ij}a_{1i}a_{2j}, \hat{C}_2 = \epsilon_{1ij}a_{2i}a_{3j}$

a_{ij} is the i^{th} row and j^{th} column in the matrix of Eq.C.12

$$
\begin{vmatrix}
-2 & -2r_1\cos\theta_1 + 2r_2\cos\theta_2 & -2r_2\cos\theta_2 \\
-2r_1\cos\theta_1 + 2r_2\cos\theta_2 & -2d^2 & d^2 - r_1^2 + r_2^2 \\
-2r_2\cos\theta_2 & d^2 - r_1^2 + r_2^2 & -2r_2^2
\end{vmatrix} \ . \tag{C.12}
$$

With Eq.C.11, a clear geometrical interpretation of a Haines jump event within two disks is given. As shown in Fig.C.3, we plot the square of the area of the triangle (V_2^2) against the curvature radius (R). There are two roots $x_1 > 0$ and $x_2 < 0$ because $\hat{C}_2 < 0$ and $\hat{A}_2 > 0$ (based on Eq.C.8 and C.10). When $x \in (x_2, x_1)$, A^2 is negative. This negative square of area does not lead to a geometrically meaningful situation. As a result, x_1 is the minimum positive curvature radius. When burst event happens, the area V_2 turns 0. As a result, for a burst event, the center of the circular meniscus is on the line connecting centers of two disks as shown in Fig.C.2. So this critical curvature radius is expressed:

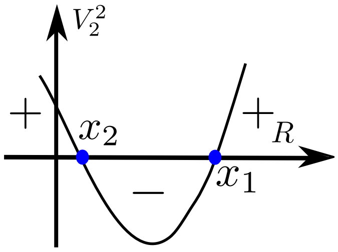

Figure C.3: An illustration of the quadratic equation obtained by CMD. The Y-axis represents the squared area of the triangle V_2 and the X-axis represents the curvature radius.

$$
R_{b2} = \frac{-\hat{B}_2 + \sqrt{\hat{B}_2^{\ 2} - 4\hat{A}_2\hat{C}_2}}{2\hat{A}_2} \ . \tag{C.13}
$$

Eq.C.13 covers the models in all of the existing literature [Cieplak and Robbins, 1990; Motealleh et al., 2010; Primkulov et al., 2018; Hu et al., 2019] which derived various forms of the critical curvature radius for a burst event for various restrictions on surface property and positions of the disks. Apart from that, it also shows that for any combination of contact angle, there is always a solution for the burst curvature radius because the discriminant of the quadratic equation $\Delta_3 = \hat{B_2}^2 - 4\hat{A}_2\hat{C}_2 > 0$ and $\hat{A}_2 > 0$. In addition, the discriminant of Eq.C.11 Δ_3 is calculated as follows, which is helpful for understanding a 3D Haines jump later:

$$\Delta_3 = 8d^2 \begin{vmatrix} -2 & -2r_1\cos\theta_1 & -2r_2\cos\theta_2 \\ -2r_1\cos\theta_1 & -2r_1^2 & d^2 - r_1^2 - r_2^2 \\ -2r_2\cos\theta_2 & d^2 - r_1^2 - r_2^2 & -2r_2^2 \end{vmatrix} . \tag{C.14}$$

The discriminant Δ_3 is closely related to the submatrix in Eq.C.4. We find the same feature for the three dimensional model. We formulate a new form of Eq.C.14 in order to show the geometric interpretation of Eq.C.14:

$$\begin{aligned}\Delta_3 &= -8d^2 \begin{vmatrix} 2\times 1^2 & 1^2 + r_1^2 - (1^2 + r_1^2 - 2r_1\cos\theta_1) & 1^2 + r_2^2 - (1^2 + r_2^2 - 2r_1\cos\theta_2) \\ 1^2 + r_1^2 - (1^2 + r_1^2 - 2r_1\cos\theta_1) & 2r_1^2 & r_1^2 + r_2^2 - d^2 \\ 1^2 + r_2^2 - (1^2 + r_2^2 - 2r_1\cos\theta_2) & r_1^2 + r_2^2 - d^2 & 2r_2^2 \end{vmatrix} \\ &= -8d^2 \begin{vmatrix} 0 & 1 & 1 & 1 & 1 \\ 1 & 0 & 1 & 1 + r_1^2 - 2r_1\cos\theta_1 & 1 + r_2^2 - 2r_2\cos\theta_2 \\ 1 & 1 & 0 & r_1^2 & r_2^2 \\ 1 & 1 + r_1^2 - 2r_1\cos\theta_1 & r_1^2 & 0 & d^2 \\ 1 & 1 + r_2^2 - 2r_2\cos\theta_2 & r_2^2 & d^2 & 0 \end{vmatrix} \\ &= -2304d^2V_3^2 .\end{aligned}$$

(C.15)

According to CMD, V_3 in Eq.C.15 represents the volume of a tetrahedron as shown in Fig.C.4(a). It is easy to know the maximum of d is reached when the vertexes of the tetrahedron are on the same plane as shown in Fig.C.4(b). In Fig.C.4(b), the maximum of d is shown as $d_{max}^2 = r_1^2 + r_2^2 - 2r_1r_2\cos(\theta_1 + \theta_2) \le (r_1 + r_2)^2$ and the minimum of d is $d_{min}^2 = r_1^2 + r_2^2 - 2r_1r_2\cos(\theta_1 - \theta_2) > (r_1 - r_2)^2$. For the non-overlapping disks, $d^2 > (r_1 + r_2)^2 > d_{max}^2$. In addition, expanding V_3^2 in Eq.C.15 leads to a quadratic equation of $V_3^2(d^2) = A_q(d^4) + B_qd^2 + C_q$ as shown in Fig.C.5.

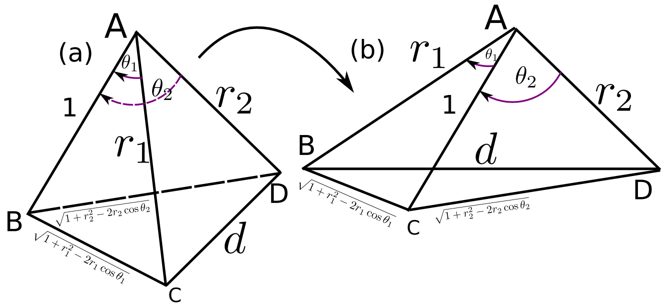

Figure C.4: (a) An illustration of tetrahedron for the volume (V_3) calculation in Eq.C.15; (b) An illustration when the maximum of d is reached.

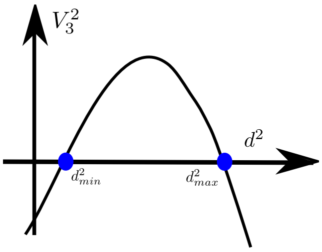

Figure C.5: (a) An illustration of tetrahedron for the volume (V_3) calculation in Eq.C.15; (b) An illustration when the maximum of d is reached.

The coefficient are calculated as follows:

$$
\begin{aligned}
A_q &= -\begin{vmatrix} 0 & 1 & 1 \\ 1 & 0 & 1 \\ 1 & 1 & 0 \end{vmatrix} = -2, \\
B_q &= -2\begin{vmatrix} 0 & 1 & 1 & 1 \\ 1 & 0 & 1 & 1+r_1^2-2r_1\cos\theta_1 \\ 1 & 1 & 0 & r_1^2 \\ 1 & 1+r_2^2-2r_2\cos\theta_2 & r_2^2 & 0 \end{vmatrix}, \\
C_q &= \begin{vmatrix} 0 & 1 & 1 & 1 & 1 \\ 1 & 0 & 1 & 1+r_1^2-2r_1\cos\theta_1 & 1+r_2^2-2r_2\cos\theta_2 \\ 1 & 1 & 0 & r_1^2 & r_2^2 \\ 1 & 1+r_1^2-2r_1\cos\theta_1 & r_1^2 & 0 & 0 \\ 1 & 1+r_2^2-2r_2\cos\theta_2 & r_2^2 & 0 & 0 \end{vmatrix}.
\end{aligned}
\tag{C.16}
$$

So $V_3^2 \geq 0$ when $d \in [d_{min}, d_{max}]$. As a consequence, when $d > (r_1 + r_2)$, $V_3^2 < 0$ and $\Delta_3 = -8d^2V_3 > 0$. A similar approach has been shown for estimating the length of an edge of a tetrahedron given the rest five edges in the work of Havel [Havel, 1998]. When we swap the invading and defending fluid ($\tilde{\theta} = \pi - \theta$), the coefficient of the quadratic equation will be $\hat{As}_2 = \hat{A}_2$, $\hat{Bs}_2 = -\hat{B}_2$ and $\hat{Cs}_2 = \hat{C}_2$. As a consequence, the burst curvature radius is $\frac{-\hat{Bs}_2 + \sqrt{\hat{Bs}_2^{\,2} - 4\hat{As}_2\hat{Cs}_2}}{2\hat{As}_2} = \frac{\hat{B}_2 + \sqrt{\hat{B}_2^{\,2} - 4\hat{A}_2\hat{C}_2}}{2\hat{A}_2} = -x_2$. As a result, the other root also has a physical meaning and that represents the burst curvature radius when we swap the invading and defending phase. In a nutshell, the curvature radius determined by x_1 and x_2 corresponds to two critical positions as shown in Fig.C.1.

We further expand Eq.C.13, which is easy to be compared with the literature results [Holtzman and Segre, 2015; Hu et al., 2019]:

$$R_{b2} = \frac{\alpha_1 + d\sqrt{\alpha_2}}{2\alpha_3}$$

where,

$$
\begin{aligned}
&\alpha_1 = (d^2 - r_1^2 + r_2^2)r_1\cos\theta_1 + (d^2 + r_1^2 - r_2^2)r_2\cos\theta_2, \alpha_3 = d^2 - (r_1\cos\theta_1 - r_2\cos\theta_2)^2 \\
&\alpha_2 = d^2(d^2 - 2r_1^2 - 2r_2^2) + (r_1^2 - r_2^2)^2 + 4r_1^2r_2^2(\cos^2\theta_1 + \cos^2\theta_2) \\
&\quad + 4r_1r_2\cos\theta_1\cos\theta_2(d^2 - r_1^2 - r_2^2).
\end{aligned}
$$

(C.17)

C.2 Haines jump in 3D

The method proposed in the previous section can be directly employed to address the critical curvature radius for a Haines jump in 3D. In the following, we show the process to obtain the critical curvature radius when a spherical meniscus is passing through the region formed by three spherical beads, which turns out to be merely solving a quadratic equation.

Supposed that we have three spherical beads with radius as r_i $(i = 1, 2, 3)$ and corresponding contact angle of invading liquid is θ_i $(i = 1, 2, 3)$ as shown in Fig.C.6a. The distance between the center of each bead is d_{ij} $(i, j = 1, 2, 3)$. As shown in Fig.C.6b, the distance between the center of the spherical bead and the spherical meniscus center is:

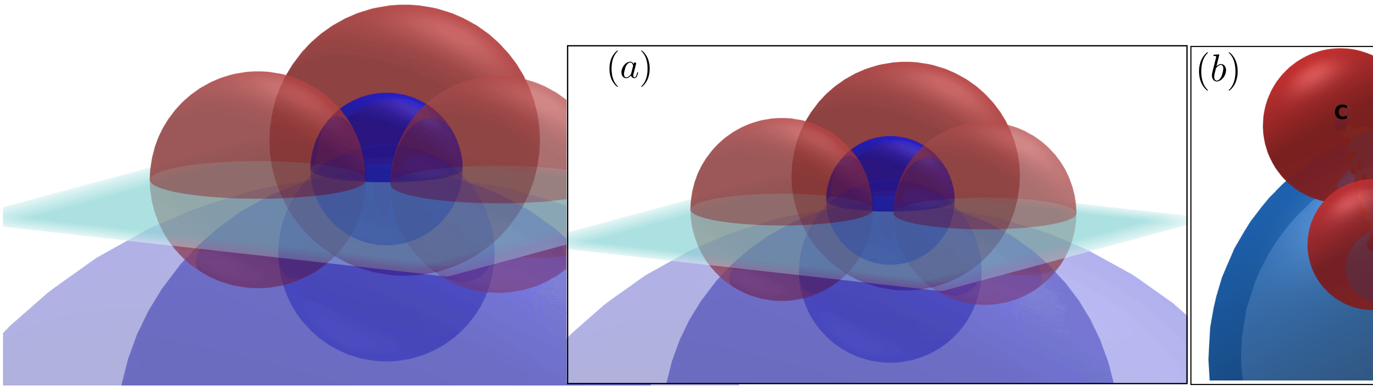

(a) **(b)**

Figure C.6: Illustration to determine the critical curvature for the 3D burst event. (a) The red spheres indicate the grains and the blue spheres indicate the spherical interface between the invading and defending phase. As the pressure difference between the two phase increases, the radius of the sphere is reduced. And at the same time, the position of the sphere center of the spherical meniscus is adjusted with respect to boundary condition of contact angles; (b) Illustration to calculate the critical curvature for the burst event. Points A,B,C,M will form a tetrahedron and M is the center of the meniscus sphere.

$$\begin{aligned}
&\overline{AM} = \sqrt{R^2 + r_1^2 - 2Rr_1\cos\theta_1}, \overline{BM} = \sqrt{R^2 + r_2^2 - 2Rr_2\cos\theta_2} \\
&\overline{CM} = \sqrt{R^2 + r_3^2 - 2Rr_3\cos\theta_3}\ .
\end{aligned} \tag{C.18}$$

The four points (A,B,C,M) as shown in Fig.C.6b form a tetrahedron and the corresponding volume is calculated with CMD, i.e. Eq.C.1:

$$V_3^2 = \frac{(-1)^4}{2^3(3!)^2} \begin{vmatrix} 0 & \overline{AM}^2 & \overline{BM}^2 & \overline{CM}^2 & 1 \\ \overline{AM}^2 & 0 & d_{12}^2 & d_{13}^2 & 1 \\ \overline{BM}^2 & d_{12}^2 & 0 & d_{23}^2 & 1 \\ \overline{CM}^2 & d_{13}^2 & d_{23}^2 & 0 & 1 \\ 1 & 1 & 1 & 1 & 0 \end{vmatrix} . \tag{C.19}$$

As a result:

$$V_3^2 = \frac{1}{288} \begin{vmatrix} 0 & R^2 + r_1^2 - 2Rr_1\cos\theta_1 & R^2 + r_2^2 - 2Rr_2\cos\theta_2 & R^2 + r_3^2 - 2Rr_3\cos\theta_3 & 1 \\ R^2 + r_1^2 - 2Rr_1\cos\theta_1 & 0 & d_{12}^2 & d_{13}^2 & 1 \\ R^2 + r_2^2 - 2Rr_2\cos\theta_2 & d_{12}^2 & 0 & d_{23}^2 & 1 \\ R^2 + r_3^2 - 2Rr_3\cos\theta_3 & d_{13}^2 & d_{23}^2 & 0 & 1 \\ 1 & 1 & 1 & 1 & 0 \end{vmatrix} ,$$

(C.20)

To calculate the determinant of a 5 × 5 matrix A in Eq.C.20, where $a_{i,j}$ is the entry for the i^{th} row and j^{th} column of A, we perform linear transformation with the basic properties of determinant, i.e. subtracting a multiple of one row or one column from another leaving the same determiant [Strang, 2016]. For the row operation:$a_{1k} - R^2 a_{5k} \rightarrow a_{1k}$; $a_{ik} - r_{i-1}^2 a_{5k} \rightarrow a_{ik}, i = 2, 3, 4$. For the column operation:$a_{k1} - R^2 a_{k5} \rightarrow a_{k1}$; $a_{ki} - r_{i-1}^2 a_{k5} \rightarrow a_{ki}, i = 2, 3, 4$. As a consequence:

$$V_3^2 = \frac{1}{288} \begin{vmatrix} -2R^2 & -2Rr_1\cos\theta_1 & -2Rr_2\cos\theta_2 & -2Rr_3\cos\theta_3 & 1 \\ -2Rr_1\cos\theta_1 & -2r_1^2 & d_{12}^2 - r_2^2 - r_1^2 & d_{13}^2 - r_3^2 - r_1^2 & 1 \\ -2Rr_2\cos\theta_2 & d_{12}^2 - r_1^2 - r_2^2 & -2r_2^2 & d_{23}^2 - r_3^2 - r_2^2 & 1 \\ -2Rr_3\cos\theta_3 & d_{13}^2 - r_1^2 - r_3^2 & d_{23}^2 - r_2^2 - r_3^2 & -2r_3^2 & 1 \\ 1 & 1 & 1 & 1 & 0 \end{vmatrix} , \tag{C.21}$$

With $a_{5k} \rightarrow Ra_{5k}$, $a_{k1} \rightarrow a_{k1}/R$ and $a_{k5} \rightarrow Ra_{k5}$, $a_{1k} \rightarrow a_{1k}/R$:

$$V_3^2 = \frac{1}{288} \begin{vmatrix} -2 & -2r_1\cos\theta_1 & -2r_2\cos\theta_2 & -2r_3\cos\theta_3 & 1 \\ -2r_1\cos\theta_1 & -2r_1^2 & d_{12}^2 - r_2^2 - r_1^2 & d_{13}^2 - r_3^2 - r_1^2 & R \\ -2r_2\cos\theta_2 & d_{12}^2 - r_1^2 - r_2^2 & -2r_2^2 & d_{23}^2 - r_3^2 - r_2^2 & R \\ -2r_3\cos\theta_3 & d_{13}^2 - r_1^2 - r_3^2 & d_{23}^2 - r_2^2 - r_3^2 & -2r_3^2 & R \\ 1 & R & R & R & 0 \end{vmatrix} , \tag{C.22}$$

With $a_{ik} - a_{4k} \rightarrow a_{ik}, i = 2, 3$,$a_{ki} - a_{k4} \rightarrow a_{ki}, i = 2, 3$:

$$V_3^2 = \frac{1}{288} \begin{vmatrix} -2 & -2(r_1\cos\theta_1 - r_3\cos\theta_3) & -2(r_2\cos\theta_2 - r_3\cos\theta_3) & -2r_3\cos\theta_3 & 1 \\ -2(r_1\cos\theta_1 - r_3\cos\theta_3) & -2d_{13}^2 & d_{12}^2 - d_{23}^2 - d_{13}^2 & d_{13}^2 + r_3^2 - r_1^2 & 0 \\ -2(r_2\cos\theta_2 - r_3\cos\theta_3) & d_{12}^2 - d_{13}^2 - d_{23}^2 & -2d_{23}^2 & d_{23}^2 + r_3^2 - r_2^2 & 0 \\ -2r_3\cos\theta_3 & d_{13}^2 - r_1^2 + r_3^2 & d_{23}^2 - r_2^2 + r_3^2 & -2r_3^2 & R \\ 1 & 0 & 0 & R & 0 \end{vmatrix} .$$

(C.23)

With Eq.C.6, Eq.C.23 can be written directly as a function of R. To obtain the constant part without R, we need to choose a_{15}, a_{51} to avoid R:

$$\begin{aligned}
&\epsilon_{5ijk1}a_{15}a_{2i}a_{3j}a_{4k}a_{51} = -\epsilon_{1ijk5}a_{2i}a_{3j}a_{4k} \\
&= - \begin{vmatrix} -2d_{13}^2 & d_{12}^2 - d_{23}^2 - d_{13}^2 & d_{13}^2 + r_3^2 - r_1^2 \\ d_{12}^2 - d_{13}^2 - d_{23}^2 & -2d_{23}^2 & d_{23}^2 + r_3^2 - r_2^2 \\ d_{13}^2 - r_1^2 + r_3^2 & d_{23}^2 - r_2^2 + r_3^2 & -2r_3^2 \end{vmatrix} \\
&= - 2\Big[- 4r_1^2r_2^2r_3^2 + r_1^2(d_{23}^2 - r_2^2 - r_3^2)^2 + r_3^2(d_{12}^2 - r_2^2 - r_1^2)^2 + r_2^2(d_{13}^2 - r_1^2 - r_3^2)^2 \\
&\quad + (d_{12}^2 - r_2^2 - r_1^2)(d_{13}^2 - r_1^2 - r_3^2)(d_{23}^2 - r_2^2 - r_3^2)\Big] \\
&\quad \leq -2\Big[4r_1^2r_2^2r_3^2 + r_1^2(d_{23}^2 - r_2^2 - r_3^2)^2 + r_3^2(d_{12}^2 - r_2^2 - r_1^2)^2 + r_2^2(d_{13}^2 - r_1^2 - r_3^2)^2\Big] < 0 \ .
\end{aligned}$$

(C.24)

To obtain the coefficient of R by considering the symmetry of the matrix, we have:

$$\begin{aligned}
&2\epsilon_{ijk51}a_{1i}a_{2j}a_{3k}a_{45}a_{51} \\
=&2R\begin{vmatrix} -2(r_1\cos\theta_1 - r_3\cos\theta_3) & -2(r_2\cos\theta_2 - r_3\cos\theta_3) & -2r_3\cos\theta_3 \\ -2d_{13}^2 & d_{12}^2 - d_{23}^2 - d_{13}^2 & d_{13}^2 + r_3^2 - r_1^2 \\ d_{12}^2 - d_{13}^2 - d_{23}^2 & -2d_{23}^2 & d_{23}^2 + r_3^2 - r_2^2 \end{vmatrix} \ .
\end{aligned} \tag{C.25}$$

To obtain the coefficient of R^2, we have:

$$\begin{aligned}
&\epsilon_{ijk54}a_{1i}a_{2j}a_{3k}a_{45}a_{54} = -R^2\epsilon_{ijk45}a_{1i}a_{2j}a_{3k} \\
&= -R^2\begin{vmatrix} -2 & -2(r_1\cos\theta_1 - r_3\cos\theta_3) & -2(r_2\cos\theta_2 - r_3\cos\theta_3) \\ -2(r_1\cos\theta_1 - r_3\cos\theta_3) & -2d_{13}^2 & d_{12}^2 - d_{23}^2 - d_{13}^2 \\ -2(r_2\cos\theta_2 - r_3\cos\theta_3) & d_{12}^2 - d_{13}^2 - d_{23}^2 & -2d_{23}^2 \end{vmatrix} \\
&= 2R^2\Big[(-d_{12} + d_{13} + d_{23})(d_{12} - d_{13} + d_{23})(d_{12} + d_{13} - d_{23})(d_{12} + d_{13} + d_{23}) \\
&- 2(r_1\cos\theta_1 - r_2\cos\theta_2)^2(-d_{12}^2 + d_{13}^2 + d_{23}^2) - 2(r_1\cos\theta_1 - r_3\cos\theta_3)^2(d_{12}^2 - d_{13}^2 + d_{23}^2) \\
&- 2(r_2\cos\theta_2 - r_3\cos\theta_3)^2(d_{12}^2 + d_{13}^2 - d_{23}^2)\Big] \ .
\end{aligned}$$

(C.26)

As a result, we express the squared volume of the tetrahedron as a quadratic equation:

$$V_3^2 = \frac{1}{288}(\hat{A}_3R^2 + \hat{B}_3R + \hat{C}_3) \ . \tag{C.27}$$

where,

$$\hat{A}_3 = -\epsilon_{ijk4}a_{1i}a_{2j}a_{3k}, \hat{B}_3 = 2\epsilon_{1ijk}a_{1i}a_{2j}a_{3k}, \hat{C}_3 = -\epsilon_{1ijk}a_{2i}a_{3j}a_{4k},$$

a_{ij} is the i^{th} row and j^{th} column in the matrix of Eq.C.28

$$\begin{vmatrix} -2 & -2(r_1\cos\theta_1 - r_3\cos\theta_3) & -2(r_2\cos\theta_2 - r_3\cos\theta_3) & -2r_3\cos\theta_3 \\ -2(r_1\cos\theta_1 - r_3\cos\theta_3) & -2d_{13}^2 & d_{12}^2 - d_{23}^2 - d_{13}^2 & d_{13}^2 + r_3^2 - r_1^2 \\ -2(r_2\cos\theta_2 - r_3\cos\theta_3) & d_{12}^2 - d_{13}^2 - d_{23}^2 & -2d_{23}^2 & d_{23}^2 + r_3^2 - r_2^2 \\ -2r_3\cos\theta_3 & d_{13}^2 - r_1^2 + r_3^2 & d_{23}^2 - r_2^2 + r_3^2 & -2r_3^2 \end{vmatrix} \ . \tag{C.28}$$

When $\hat{A}_3 > 0$, we can directly obtain the curvature for the burst event in a three-bead system by solving a quadratic equation:

$$R_{b3} = \frac{-\hat{B}_3 + \sqrt{\hat{B}_3^{\,2} - 4\hat{A}_3\hat{C}_3}}{2\hat{A}_3} \ . \tag{C.29}$$

It is worth noting that $\hat{A}_3$ in Eq.C.29 is not always larger than 0 as in 2D case. To further explore the range of the coefficient $\hat{A}_3$, we perform some analysis based on triangle inequality. According to Pedoe's inequality [Pedoe, 1942]:

$$\begin{aligned}&2(r_1\cos\theta_1 - r_2\cos\theta_2)^2(-d_{12}^2 + d_{13}^2 + d_{23}^2) + 2(r_1\cos\theta_1 - r_3\cos\theta_3)^2(d_{12}^2 - d_{13}^2 + d_{23}^2)\\ &+ 2(r_2\cos\theta_2 - r_3\cos\theta_3)^2(d_{12}^2 + d_{13}^2 - d_{23}^2) \geq 32\Delta'\Delta \ .\end{aligned} \tag{C.30}$$

Without loss of generality in Eq.C.30, we suppose $r_1\cos\theta_1 \geq r_2\cos\theta_2 \geq r_3\cos\theta_3$. Then Δ' is the area of triangle with edges of $L_1 = r_1\cos\theta_1 - r_2\cos\theta_2$, $L_2 = r_2\cos\theta_2 - r_3\cos\theta_3$, $L_3 = r_1\cos\theta_1 - r_3\cos\theta_3$. So $L_1 + L_2 = L_3$. As a result, $\Delta' = 0$ because three edges (L_1,L_2 and L_3) are on the same line. Δ is the area of the triangle with edges of d_{12}, d_{13} and d_{23}. Combining Eq.C.26 and C.30, we know that $\hat{A} \leq 32\Delta^2$. When the beads are nearly mono-disperse and homogeneous wet ($r_1 \simeq r_2 \simeq r_3$, $\theta_1 \simeq \theta_2 \simeq \theta_3$):

$$\hat{A}_3 \simeq 2(-d_{12} + d_{13} + d_{23})(d_{12} - d_{13} + d_{23})(d_{12} + d_{13} - d_{23})(d_{12} + d_{13} + d_{23}) > 0 \ . \tag{C.31}$$

Eq.C.31 reminds us that for mono-disperse and homogeneous wet beads, there is no difference between the way to calculate the critical curvature radius in 2D and 3D because the sign of the coefficients are the same ($\hat{A_{2,3}} > 0$,$\hat{C_{2,3}} < 0$). Eq.C.29 is obtained directly by the geometry and surface properties of the three beads, which assumes that the liquid-gas interface between the invading and defending liquid is of spherical shape with constant curvature. However, in three dimension, the cross talk between neighboring pores might be strong, which is also influenced by the surface properties of the beads. Similar ideas to calculate the critical curvature radius for burst event in 3D are employed with one focusing on homogeneous wetting beads [Melnikov et al., 2015] and the other one focusing on the fractional wetting beads [Motealleh et al., 2013]. But they did not give an explicit expression for the calculation of critical curvature. In addition, Melinkov et al. and Gladkikh [Melnikov et al., 2015; Gladkikh, 2005] used the spherical approximation to find the center of the spherical meniscus but assumed that there is only one contact point between the spherical meniscus and bead. Strictly speaking, this assumption is valid when the contact angle of the invading fluid is close to 180°.

Similar as shown in deriving the critical curvature radius in the two dimensional model, the discriminant of Eq.C.27 is written as:

$$\Delta_4 = -64S_\triangle^2 \begin{vmatrix} -2 & -2r_1\cos\theta_1 & -2r_2\cos\theta_2 & -2r_3\cos\theta_3 \\ -2r_1\cos\theta_1 & -2r_1^2 & d_{12}^2 - r_2^2 - r_1^2 & d_{13}^2 - r_3^2 - r_1^2 \\ -2r_2\cos\theta_2 & d_{12}^2 - r_1^2 - r_2^2 & -2r_2^2 & d_{23}^2 - r_3^2 - r_2^2 \\ -2r_3\cos\theta_3 & d_{13}^2 - r_1^2 - r_3^2 & d_{23}^2 - r_2^2 - r_3^2 & -2r_3^2 \end{vmatrix} \ . \tag{C.32}$$

where, $S_{\triangle}$ is the area formed by a triangle with edges of d_{12}, d_{13}, d_{23} and $S_{\triangle} > 0$. By reformulating Eq.C.32:

$$\begin{aligned}\Delta_4 &= -64S_{\triangle}^2 \begin{vmatrix} 2\times 1^2 & 1^2+r_1^2-(1^2+r_1^2-2r_1\cos\theta_1) & 1^2+r_2^2-(1^2+r_2^2-2r_2\cos\theta_2) & 1^2+r_3^2-(1^2+r_3^2-2r_3\cos\theta_3) \\ 1^2+r_1^2-(1^2+r_1^2-2r_1\cos\theta_1) & 2r_1^2 & r_2^1+r_2^2-d_{12}^2 & r_1^2-r_3^2+d_{13}^2 \\ 1^2+r_2^2-(1^2+r_2^2-2r_2\cos\theta_2) & r_1^2+r_2^2-d_{12}^2 & 2r_2^2 & r_3^2+r_2^2-d_{23}^2 \\ 1^2+r_3^2-(1^2+r_3^2-2r_3\cos\theta_3) & r_1^2+r_3^2-d_{13}^2 & r_2^2+r_3^2-d_{23}^2 & 2r_3^2 \end{vmatrix} \\ &= 64S_{\triangle}^2 \begin{vmatrix} 0 & 1 & 1 & 1 & 1 & 1 \\ 1 & 0 & 1 & 1+r_1^2-2r_1\cos\theta_1 & 1+r_3^2-2r_3\cos\theta_3 & 1+r_2^2-2r_2\cos\theta_2 \\ 1 & 1 & 0 & r_1^2 & r_3^2 & r_2^2 \\ 1 & 1+r_1^2-2r_1\cos\theta_1 & r_1^2 & 0 & d_{13}^2 & d_{12}^2 \\ 1 & 1+r_3^2-2r_3\cos\theta_3 & r_3^2 & d_{13}^2 & 0 & d_{23}^2 \\ 1 & 1+r_2^2-2r_2\cos\theta_2 & r_2^2 & d_{12}^2 & d_{23}^2 & 0 \end{vmatrix} \\ &= -589824 S_{\triangle}^2 V_4^2 \ .\end{aligned}$$

(C.33)

As shown in Fig.C.7,we construct a pentachoron based on Eq.C.33. When the spheres are not in contact with each other, i.e. $r_1 + r_2 < d_{12}, r_1 + r_3 < d_{13}, r_2 + r_3 < d_{23}$, the calculated squared volume (V_4^2) is always negative. A proof is shown in the following.

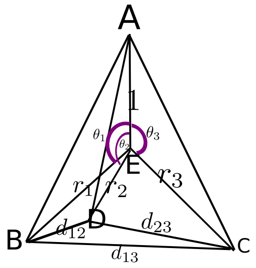

Figure C.7: Illustration of a pentachoron for Eq.C.33.

Proof of $\Delta_4 \geq 0$

$S_{\triangle}^2 > 0$ because the triangle formed by d_{13}, d_{23}, d_{12} is not degenerate in Eq.C.33. As a result, we need to prove $V_4^2 \leq 0$. We start with the relationship between CMD and its corresponding eigenvalues. We define Ω_N as shown in Eq.C.34, which is the main part of Eq.C.1.

$$\Omega_N = \begin{vmatrix} 0 & 1 & 1 & ... & 1 \\ 1 & 0 & d_{12}^2 & ... & d_{1(N+1)}^2 \\ 1 & d_{21}^2 & 0 & ... & d_{2(N+1)}^2 \\ \vdots & \vdots & \vdots & \ddots & \vdots \\ 1 & d_{(N+1)1}^2 & d_{(N+1)2}^2 & ... & 0 \end{vmatrix} . \tag{C.34}$$

where, d_{ij} is the distance between point i and point j.
Given one edge or a 1-simplex:

$$\Omega_1 = \begin{vmatrix} 0 & 1 & 1 \\ 1 & 0 & d_{12}^2 \\ 1 & d_{12}^2 & 0 \end{vmatrix} . \tag{C.35}$$

It is well-kown that a Hermitian matrix has real eigenvalues [Riley et al., 2006] and let the eigenvalues of Ω_1 be $\lambda_1 \leq \lambda_2 \leq \lambda_3$:

$$\Omega_1 = \lambda_1\lambda_2\lambda_3 = 2d_{12}^2 > 0, \quad \sum_{i=1}^{3} \lambda_i = 0 \ . \tag{C.36}$$

According to Eq.C.36, the sign of λ_i is $(-,-,+)$. We continue to explore the sign of eigenvalues of Ω_2 for a triangle or a 2-simplex:

$$\Omega_2 = \begin{vmatrix} 0 & 1 & 1 & 1 \\ 1 & 0 & d_{12}^2 & d_{13}^2 \\ 1 & d_{12}^2 & 0 & d_{23}^2 \\ 1 & d_{31}^2 & d_{32}^2 & 0 \end{vmatrix} = \tilde{\lambda}_1\tilde{\lambda}_2\tilde{\lambda}_3\tilde{\lambda}_4 \ . \tag{C.37}$$

Ω_1 can be viewed as a principal submatrix of Ω_2, so the range of $\tilde{\lambda}_i$ by Cauchy's interlace theorem [Hwang, 2004] is determined as follows:

$$\tilde{\lambda}_1 \leq \underset{(-)}{\lambda_1} \leq \tilde{\lambda}_2 \leq \underset{(-)}{\lambda_2} \leq \tilde{\lambda}_3 \leq \underset{(+)}{\lambda_3} \leq \tilde{\lambda}_4 \ . \tag{C.38}$$

As a result, we determine the sign of the characteristic roots $\tilde{\lambda}_i$ $(-,-,?,+)$. The marker ? indicates that it is not certain whether $\tilde{\lambda}_3$ is positive or negative. If the triangle exists and satisfies the triangle inequality, we know $\Omega_2 < 0$ according to the work of Menger [Menger, 1928]. As a result, the sign of characteristic roots will be $(-,-,-,+)$. Otherwise, when the triangle inequality is violated:

$$\begin{aligned} \Omega_2 &= \tilde{\lambda}_1\tilde{\lambda}_2\tilde{\lambda}_3\tilde{\lambda}_4 \\ &= -\frac{1}{16}(-d_{12}+d_{13}+d_{23})(d_{12}-d_{13}+d_{23})(d_{12}+d_{13}-d_{23})(d_{12}+d_{13}+d_{23}) > 0 \ . \end{aligned} \tag{C.39}$$

As a result, $\tilde{\lambda}_i$ $(-,-,+,+)$. In the above process, we find that the sign of characteristic roots of the principal submatrix is helpful to evaluate the sign of CMD. Given a tetrahedron or a 3-simplex:

$$\Omega_3 = \begin{vmatrix} 0 & 1 & 1 & 1 & 1 \\ 1 & 0 & d_{12}^2 & d_{13}^2 & d_{14}^2 \\ 1 & d_{12}^2 & 0 & d_{23}^2 & d_{24}^2 \\ 1 & d_{31}^2 & d_{32}^2 & 0 & d_{34}^2 \\ 1 & d_{41}^2 & d_{42}^2 & d_{43}^2 & 0 \end{vmatrix} = \hat{\lambda}_1\hat{\lambda}_2\hat{\lambda}_3\hat{\lambda}_4\hat{\lambda}_5 \ . \tag{C.40}$$

The tetraherdon described by Eq.C.40 is formed by four triangles, which correspond to four different principal submatrices of Eq.C.40. If there is one triangle is realizable while one triangle is not, we can obtain the sign of characteristic roots for these two principal submatrices:

$$\begin{aligned} &\tilde{\lambda}_{11}\tilde{\lambda}_{12}\tilde{\lambda}_{13}\tilde{\lambda}_{14}(-,-,-,+) \\ &\tilde{\lambda}_{21}\tilde{\lambda}_{22}\tilde{\lambda}_{23}\tilde{\lambda}_{24}(-,-,+,+) \ . \end{aligned} \tag{C.41}$$

We employ Cauchy's interlace theorem and derive two different possibilities of signs of the $\hat{\lambda}_i$ based on Eq.C.41:

$$\begin{aligned} &\hat{\lambda}_1\hat{\lambda}_2\hat{\lambda}_3\hat{\lambda}_4\hat{\lambda}_5(-,-,-,?,+) \\ &\hat{\lambda}_1\hat{\lambda}_2\hat{\lambda}_3\hat{\lambda}_4\hat{\lambda}_5(-,-,?,+,+) \ . \end{aligned} \tag{C.42}$$

As a result, we know that $\hat{\lambda}_1\hat{\lambda}_2\hat{\lambda}_3\hat{\lambda}_4\hat{\lambda}_5(-,-,-,+,+)$ and $\Omega_3 < 0$. When the triangle inequalities for all of the four triangular faces do not strictly obeyed or violated, we can not determine the sign of Ω_3 by the sign of eigenvalues [Crippen et al., 1988]. With this result, we go back to our original question about the sign of CMD. We know that Eq.C.33 is calculating the volume of a pentachoron as shown in Fig.C.4(c). Firstly, we control the distance d_{12}, d_{23}, d_{13} to guarantee that at least one tetrahedron is realizable and at least one tetrahedron is not realizable. For example, we let $d_{23}^2 \in [r_2^2 + r_3^2 - 2r_2r_3\cos(\theta_2 - \theta_3), r_2^2 + r_3^2 - 2r_2r_3\cos(\theta_2 + \theta_3)]$, so the tetrahedron ACDE in Fig.C.7 is realizable and the characteristic roots for the corresponding Ω_4:

$$\hat{\lambda}_{11}\hat{\lambda}_{12}\hat{\lambda}_{13}\hat{\lambda}_{14}\hat{\lambda}_{15}(-,-,+,+,+) \ . \tag{C.43}$$

In addition, we keep $d_{12} > r_1 + r_2$ and $d_{13} > r_1 + r_3$. As a result, for the tetrahedron ABDE or ACBE in Fig.C.7 based on Eq.C.42 (these two tetrahedron also have realizable and unrealizable faces), we have:

$$\hat{\lambda}_{21}\hat{\lambda}_{22}\hat{\lambda}_{23}\hat{\lambda}_{24}\hat{\lambda}_{25}(-,-,-,+,+) \ . \tag{C.44}$$

Again with Cauchy's interlace theorem, we know $\acute{\lambda}_1\acute{\lambda}_2\acute{\lambda}_3\acute{\lambda}_4\acute{\lambda}_5\acute{\lambda}_6(-,-,-,+,+,+)$ for the following matrix:

$$\begin{aligned} \Omega_4 &= \begin{vmatrix} 0 & 1 & 1 & 1 & 1 & 1 \\ 1 & 0 & 1 & 1 + r_1^2 - 2r_1\cos\theta_1 & 1 + r_3^2 - 2r_3\cos\theta_3 & 1 + r_2^2 - 2r_2\cos\theta_2 \\ 1 & 1 & 0 & r_1^2 & r_3^2 & r_2^2 \\ 1 & 1 + r_1^2 - 2r_1\cos\theta_1 & r_1^2 & 0 & d_{13}^2 & d_{12}^2 \\ 1 & 1 + r_3^2 - 2r_3\cos\theta_3 & r_3^2 & d_{13}^2 & 0 & d_{23}^2 \\ 1 & 1 + r_2^2 - 2r_2\cos\theta_2 & r_2^2 & d_{12}^2 & d_{23}^2 & 0 \end{vmatrix} \\ &= \acute{\lambda}_1\acute{\lambda}_2\acute{\lambda}_3\acute{\lambda}_4\acute{\lambda}_5\acute{\lambda}_6 > 0 \ . \end{aligned} \tag{C.45}$$

Eq.C.45 shows that when $d_{23}^2 \in [r_2^2 + r_3^2 - 2r_2r_3\cos(\theta_2 - \theta_3), r_2^2 + r_3^2 - 2r_2r_3\cos(\theta_2 + \theta_3)]$, $\Omega_4 > 0$. However, d_{23}^2 in Eq.C.32 is larger than $r_2^2 + r_3^2 - 2r_2r_3\cos(\theta_2 + \theta_3)$. So we expand Eq.C.45 as a function of d_{23}^2, i.e. $\Omega_4 = A_t(d_{23}^4) + B_t(d_{23}^2) + C_t$. By simple inspection of the matrix Eq.C.45, we obtain:

$$
\begin{aligned}
A_t &= -\begin{vmatrix} 0 & 1 & 1 & 1 \\ 1 & 0 & 1 & 1+r_1^2-2r_1\cos\theta_1 \\ 1 & 1 & 0 & r_1^2 \\ 1 & 1+r_1^2-2r_1\cos\theta_1 & r_1^2 & 0 \end{vmatrix} = 4r_1^2\sin^2\theta_1 \geq 0, \\
B_t &= -2\begin{vmatrix} 0 & 1 & 1 & 1 & 1 \\ 1 & 0 & 1 & 1+r_1^2-2r_1\cos\theta_1 & 1+r_3^2-2r_3\cos\theta_3 \\ 1 & 1 & 0 & r_1^2 & r_3^2 \\ 1 & 1+r_1^2-2r_1\cos\theta_1 & r_1^2 & 0 & d_{13}^2 \\ 1 & 1+r_2^2-2r_2\cos\theta_2 & r_2^2 & d_{12}^2 & 0 \end{vmatrix}, \\
C_t &= \begin{vmatrix} 0 & 1 & 1 & 1 & 1 & 1 \\ 1 & 0 & 1 & 1+r_1^2-2r_1\cos\theta_1 & 1+r_3^2-2r_3\cos\theta_3 & 1+r_2^2-2r_2\cos\theta_2 \\ 1 & 1 & 0 & r_1^2 & r_3^2 & r_2^2 \\ 1 & 1+r_1^2-2r_1\cos\theta_1 & r_1^2 & 0 & d_{13}^2 & d_{12}^2 \\ 1 & 1+r_3^2-2r_3\cos\theta_3 & r_3^2 & d_{13}^2 & 0 & 0 \\ 1 & 1+r_2^2-2r_2\cos\theta_2 & r_2^2 & d_{12}^2 & 0 & 0 \end{vmatrix}.
\end{aligned}
\tag{C.46}
$$

When $\theta_1 = 0, \pi$, it is easy to check $A_t = 0$ because the triangle degenerates to line. B_t is expanded when $\theta_1 = 0$:

$$
\begin{aligned}
B_t &= -4(d_{12}^2 - r_1^2 - r_2^2 - 2r_1r_2\cos\theta_2)(-d_{13}^2 + r_1^2 + r_3^2 + 2r_1r_3\cos\theta_3) \\
&= 4(d_{12}^2 - r_1^2 - r_2^2 - 2r_1r_2\cos\theta_2)(d_{13}^2 - r_1^2 - r_3^2 - 2r_1r_3\cos\theta_3) \\
&> (2r_1r_2 - 2r_1r_2\cos\theta_2)(2r_1r_3 - 2r_1r_3\cos\theta_3) \geq 0 \ .
\end{aligned}
\tag{C.47}
$$

When $\theta_1 = \pi$:

$$
\begin{aligned}
B_t &= -4(d_{12}^2 - r_1^2 - r_2^2 + 2r_1r_2\cos\theta_2)(-d_{13}^2 + r_1^2 + r_3^2 - 2r_1r_3\cos\theta_3) \\
&= 4(d_{12}^2 - r_1^2 - r_2^2 + 2r_1r_2\cos\theta_2)(d_{13}^2 - r_1^2 - r_3^2 + 2r_1r_3\cos\theta_3) \\
&> (2r_1r_2 + 2r_1r_2\cos\theta_2)(2r_1r_3 + 2r_1r_3\cos\theta_3) \geq 0 \ .
\end{aligned}
\tag{C.48}
$$

As a result, we obtain:

$$
\Omega_4 = B_t(d_{23}^2) + C_t(B_t > 0) \ . \tag{C.49}
$$

As shown in Fig.C.8, we know for the region when d_{23}^2 falls into the region between red point and blue point, $\Omega > 0$ based on Eq.C.45. We also know that $B_t > 0$ when $\theta_1 = 0, \pi$. So when $d_{23} > (r_2 + r_3)$, $\Omega > 0$ given $\theta_1 = 0, \pi$. Because the determination of curvature radius for 2D touch event is a special case of Eq.C.32 when we set one contact angle as π, there will be always a solution for the calculation of 2D curvature radius when the disks are not intersecting with each other.

On top of the special case when $\theta = 0, \pi$, we continue to prove the more general case. Let $X = d_{23}^2$:

$$
\begin{aligned}
\frac{d\Omega_4(X)}{dX} &= 2A_tX + B_t \\
&= 8r_1^2\sin^2\theta_1(X - r_2^2 - r_3^2) + 4(d_{12}^2 - r_1^2 - r_2^2)(d_{13}^2 - r_1^2 - r_3^2) \\
&+ 8r_1r_2\cos\theta_1\cos\theta_2(d_{13}^2 - r_1^2 - r_3^2) + 8r_1r_3\cos\theta_1\cos\theta_3(d_{12}^2 - r_1^2 - r_2^2) \\
&+ 16r_1^2r_2r_3\cos\theta_2\cos\theta_3 \\
&\geq 8r_1^2\sin^2\theta_1(X - r_2^2 - r_3^2) + 16r_1^2r_2r_3(1 + \cos\theta_1\cos\theta_2 + \cos\theta_2\cos\theta_3 + \cos\theta_1\cos\theta_3)
\end{aligned}
\tag{C.50}
$$

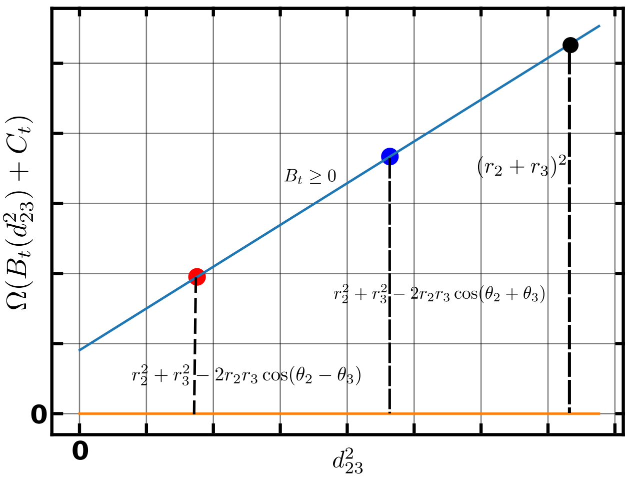

Figure C.8: Illustration for the relationship between Ω_4 and d_{23}^2.

When $X = r_2^2 + r_3^2 - 2r_2r_3\cos(\theta_2-\theta_3)$, Eq.C.50 is further shown as:

$$\frac{d\Omega_4(X)}{dX} \geq 16r_1^2r_2r_3[1+\cos\theta_1\cos\theta_2+\cos\theta_2\cos\theta_3+\cos\theta_1\cos\theta_3-\sin^2\theta_1\cos(\theta_2-\theta_3)] \tag{C.51}$$

In the following, we are going to show $\frac{d\Omega_4(X)}{dX} \geq 0$. Let $t = \cos\theta_1, t \in [-1,1]$, we define $f(t)$ as:

$$\begin{aligned} f(t) &= 1 + t\cos\theta_2 + \cos\theta_2\cos\theta_3 + t\cos\theta_3 - (1-t^2)\cos(\theta_2-\theta_3) \\ &= t^2\cos(\theta_2-\theta_3) + t(\cos\theta_2+\cos\theta_3) + 1 + \cos\theta_2\cos\theta_3 - \cos(\theta_2-\theta_3) \\ &= t^2\cos(\theta_2-\theta_3) + t(\cos\theta_2+\cos\theta_3) + 1 - \sin\theta_2\sin\theta_3 \end{aligned} \tag{C.52}$$

When $t = \pm 1$:

$$\begin{aligned} f(\pm 1) &= \pm(\cos\theta_2+\cos\theta_3) + 1 + \cos\theta_2\cos\theta_3 \\ &= (1\pm\cos\theta_2)(1\pm\cos\theta_3) \geq 0 \end{aligned} \tag{C.53}$$

The discriminant of Eq.C.52:

$$\Delta_t = 2\sin^2(\frac{\theta_2-\theta_3}{2})[1-2\cos(\theta_2-\theta_3)+\cos(\theta_2+\theta_3)] \tag{C.54}$$

Based on the sign of $\cos(\theta_2-\theta_3)$, we have three different cases:

- $\cos(\theta_2-\theta_3) = 0$. $f(t) = t(\cos\theta_2+\cos\theta_3) + 1 + \cos\theta_2\cos\theta_3$. In this case, if $\cos\theta_2+\cos\theta_3 = 0$, $f(t) \geq 0$. If $\cos\theta_2+\cos\theta_3 \neq 0$, $f(t)$ is a straight line. With $f(-1) \geq 0$ and $f(1) \geq 0$, $f(t) \geq 0$ as shown in Fig.C.9(a).
- $\cos(\theta_2-\theta_3) < 0$. Due to $f(-1) \geq 0$ and $f(1) \geq 0$, the parabola has a shape as shown in Fig.C.9(b). As a result, $f(t) \geq 0$.

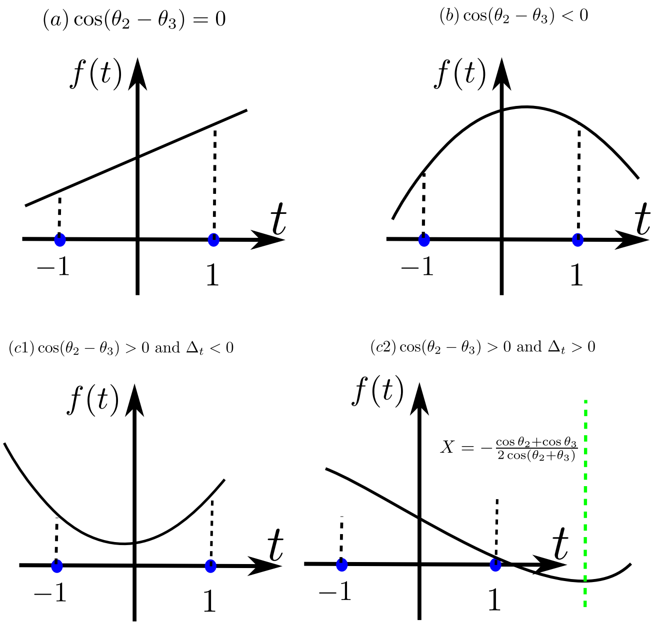
$(a)\cos(\theta_2-\theta_3)=0$ $(b)\cos(\theta_2-\theta_3)<0$

$(c1)\cos(\theta_2-\theta_3)>0$ and $\Delta_t<0$ $(c2)\cos(\theta_2-\theta_3)>0$ and $\Delta_t>0$

Figure C.9: Relationship between $f(t)$ and t.

- $\cos(\theta_2-\theta_3)>0$. We investigate the axis of symmetry, where $X=-\frac{\cos\theta_2+\cos\theta_3}{2\cos(\theta_2-\theta_3)}$. When $\Delta_t<0$, $f(t)\geq 0$ as shown in Fig.C.9(c1). As a result, we only need to consider the case when $\Delta_t>0$. Due to $\theta_2,\theta_3\in[0,\pi]$:

$$\begin{aligned}2\sin\theta_2\sin\theta_3&\geq 0\\ \cos(\theta_2-\theta_3)&\geq\cos(\theta_2+\theta_3)\\ \cos^2\frac{\theta_2-\theta_3}{2}&\geq\cos^2\frac{\theta_2+\theta_3}{2}\\ |\cos\frac{\theta_2-\theta_3}{2}|&\geq|\cos\frac{\theta_2+\theta_3}{2}|\\ |2\cos\frac{\theta_2-\theta_3}{2}\cos\frac{\theta_2+\theta_3}{2}|&\geq|2\cos^2\frac{\theta_2+\theta_3}{2}|\\ |\cos\theta_2+\cos\theta_3|&\geq|1+\cos(\theta_2+\theta_3)|\end{aligned}\tag{C.55}$$

With $\Delta_t>0$ and $\cos(\theta_2-\theta_3)>0$:

$$1+\cos(\theta_2+\theta_3)>2\cos(\theta_2-\theta_3)>0\tag{C.56}$$

Combining C.55 and C.56:

$$|X|=\left|\frac{\cos\theta_2+\cos\theta_3}{2\cos(\theta_2-\theta_3)}\right|\geq\left|\frac{1+\cos(\theta_2+\theta_3)}{2\cos(\theta_2-\theta_3)}\right|>1\tag{C.57}$$

As shown in Fig.C.9(c2), the X coordinate of symmetry axis is larger than 1. With $f(\pm1)\geq 0$, $f(t)\geq 0$. For the case of $X<-1$, we obtain the same result.

When $X=r_2^2+r_3^2-2r_2r_3\cos(\theta_2+\theta_3)$, we know:

$$\begin{aligned}&[r_2^2+r_3^2-2r_2r_3\cos(\theta_2+\theta_3)]-[r_2^2+r_3^2-2r_2r_3\cos(\theta_2-\theta_3)]\\ &=2r_2r_3[\cos(\theta_2-\theta_3)-\cos(\theta_2+\theta_3)]=4r_2r_3\sin\theta_2\sin\theta_3\geq 0\end{aligned}\tag{C.58}$$

Due to $A_t \geq 0$, we know when $X = r_2^2 + r_3^2 - 2r_2r_3\cos(\theta_2 + \theta_3)$:

$$\frac{d\Omega_4(X)}{dX} \geq 0 \tag{C.59}$$

With Eq.C.45 and C.59, the shape of parabola is determined as shown in Fig.C.10. As a result, when $d_{23} > (r_2 + r_3)$, $\Omega_4 \geq 0$.

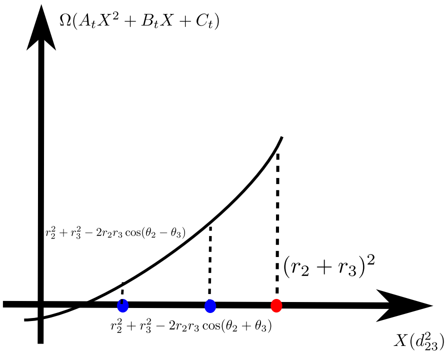

Figure C.10: Relationship between Ω_4 and X.

Validation against the work of Singh et al. [Singh et al., 2017b]

For an ideal pore made of spherical grains with equal size and mutual contact [Singh et al., 2017b], the coefficients of Eq. C.29 are:

$$\begin{aligned}
\hat{C} = -\begin{vmatrix} -8r^2 & -4r^2 & 4r^2 \\ -4r^2 & -8r^2 & 4r^2 \\ 4r^2 & 4r^2 & -2r^2 \end{vmatrix} = -32r^6, \quad \hat{A} &= -\begin{vmatrix} -2 & 0 & 0 \\ 0 & -8r^2 & -4r^2 \\ 0 & -4r^2 & -8r^2 \end{vmatrix} = 96r^4, \\
\hat{B} = 2\begin{vmatrix} 0 & 0 & -2r\cos\theta \\ -8r^2 & -4r^2 & 4r^2 \\ -4r^2 & -8r^2 & 4r^2 \end{vmatrix} = -192r^5\cos\theta \ .
\end{aligned} \tag{C.60}$$

So Eq.C.29 is further simplified as:

$$3R^2 - 6\cos\theta rR - r^2 = 0 \ . \tag{C.61}$$

The touch event happens when $R = (\sqrt{\frac{8}{3}} - 1)r$ [Singh et al., 2017b], so

$$\cos\theta = \frac{3R^2 - r^2}{6Rr} \simeq 0.053 \ . \tag{C.62}$$

Eq.C.62 matches the prediction with the results in Singh et al. [Singh et al., 2017b], which further validates Eq.C.29, which claims no Haines jump in the geometry of a tetrahedral pore with four identical spherical beads with the same wettability where contact angle is smaller than 87 degrees. For touch event with more general configuration of the sphere position, Eq.C.29 is employed to calculate the critical radius R^*.

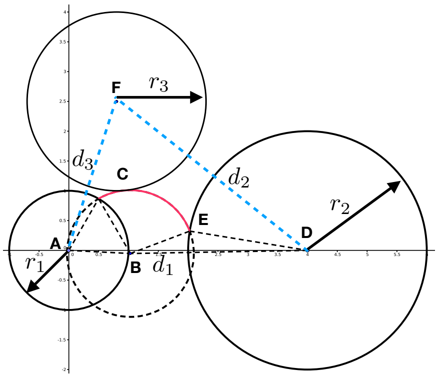

Figure C.11: An illustration of a situation when a meniscus (in pink) resting on two disks touches a third disk. Three disks have radius of r_1, r_2, r_3. The curvature radius of the meniscus and the position of the center of meniscus is determined with Eq.C.63, Eq.B.2 and Eq.B.3. Contact angles of disks with the invading liquid are 60° (disk A) and 150° (disk B).

Touch event in 2D

There is a strong connection between the calculation of critical curvature radius in 3D burst event and 2D touch event. We illustrate the connection via Fig.C.11. As shown in Fig.C.11, supposed that there is a third disk in front of the meniscus with radius r_3, and the distance between the center of the disk is $d_i, i, j = 1, 2, 3$. When touch event happens, we can imagine that there are four spheres. The sphere centers are A,B,D and F. The central sphere with center B happens to be at the burst position because its center is on the plane formed by the three spheres as shown in the derivation of Eq.C.29. When the contact angle of the third sphere (disk) is set to $\theta = \pi$, we immediately obtain the threshold for the touch event based on Eq.C.29:

$$R_{t2} = \frac{-\hat{B_{t2}} \pm \sqrt{\hat{B_{t2}}^2 - 4\hat{A_{t2}}\hat{C_{t2}}}}{2\hat{A_{t2}}} . \tag{C.63}$$

where,

$$\hat{A_{t2}} = -\epsilon_{ijk4} a_{1i} a_{2j} a_{3k}, \hat{B_{t2}} = 2\epsilon_{1ijk} a_{1i} a_{2j} a_{3k}, \hat{C_{t2}} = -\epsilon_{1ijk} a_{2i} a_{3j} a_{4k}$$

a_{ij} is the i^{th} row and j^{th} column in the matrix of Eq.C.64

$$\begin{vmatrix} -2 & -2(r_1 \cos\theta_1 + r_3) & -2(r_2 \cos\theta_2 + r_3) & 2r_3 \\ -2(r_1 \cos\theta_1 + r_3) & -2d_3^2 & d_1^2 - d_2^2 - d_3^2 & d_3^2 + r_3^2 - r_1^2 \\ -2(r_2 \cos\theta_2 + r_3) & d_1^2 - d_3^2 - d_2^2 & -2d_2^2 & d_2^2 + r_3^2 - r_2^2 \\ 2r_3 & d_3^2 - r_1^2 + r_3^2 & d_2^2 - r_2^2 + r_3^2 & -2r_3^2 \end{vmatrix} . \tag{C.64}$$

Eq.C.63 has a concise form and will show its great convenience in implementing the algorithm. In addition, we will apply the same idea to resolve the 3D touch event. Similar equations [Hu et al., 2019] are derived and can be viewed as special case for Eq.C.63 because the equations in the work of Hu et al. did not have variation of contact angles and disk centers are vertexes of a equilateral triangle.

When we let three circle contact with each other and let the meniscus circle tangent to the other three disks, i.e. $d_1 = r_1 + r_2, d_2 = r_2 + r_3, d_3 = r_1 + r_3$, $\cos\theta_i = \pi$ $(i = 1, 2, 3)$, Eq.C.63 is simplified as:

$$\frac{1}{R} = \frac{1}{r_1} + \frac{1}{r_2} + \frac{1}{r_3} \pm 2\sqrt{\frac{1}{r_1 r_2} + \frac{1}{r_1 r_3} + \frac{1}{r_2 r_3}} \, . \tag{C.65}$$

Eq.C.65 is equivalent to the Descartes circle theorem [Soddy, 1936].

Coalescence event in 2D

With the closed form expression to solve the critical curvature radius in 3D Haines jump, in the following we address the overlap event semi-analytically. As shown in Fig.C.12, there are two menisci overlapping (indicated by red circular arcs). When the coalescence event happens, we are able to extract three different groups of points and establish an equation for each group of points. In Fig.C.12, with CMD the degenerated tetrahedron in blue gives rise to:

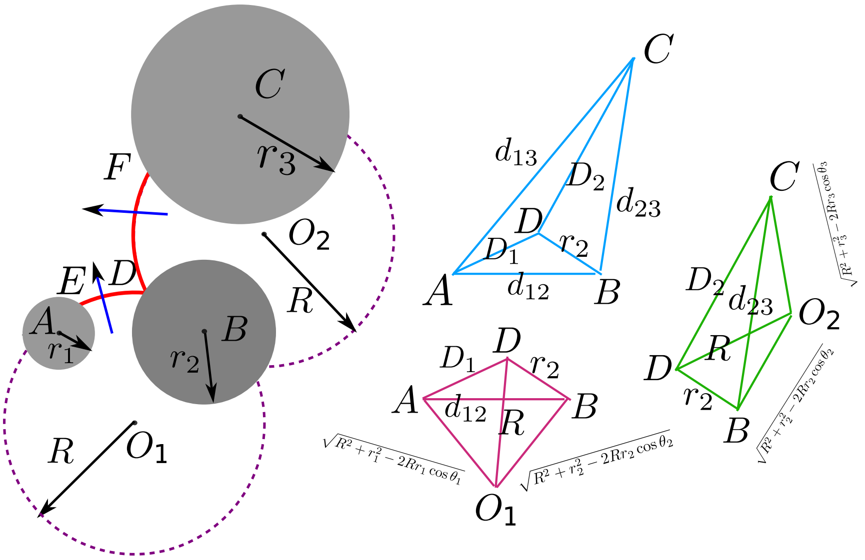

Figure C.12: Three disks with centers of A, B, C and radii of r_1, r_2, r_3. The centers of the menisci are O_1, O_2. Red circular arcs indicate the menisci and blue arrows represent the fluid invading direction. There are three groups of points are chosen as shown in blue, green and magenta.

$$\begin{vmatrix} 0 & 1 & 1 & 1 & 1 \\ 1 & 0 & D_1^2 & r_2^2 & D_2^2 \\ 1 & D_1^2 & 0 & d_{12}^2 & d_{13}^2 \\ 1 & r_2^2 & d_{12}^2 & 0 & d_{23}^2 \\ 1 & D_2^2 & d_{13}^2 & d_{23}^2 & 0 \end{vmatrix} = 0 \, . \tag{C.66}$$

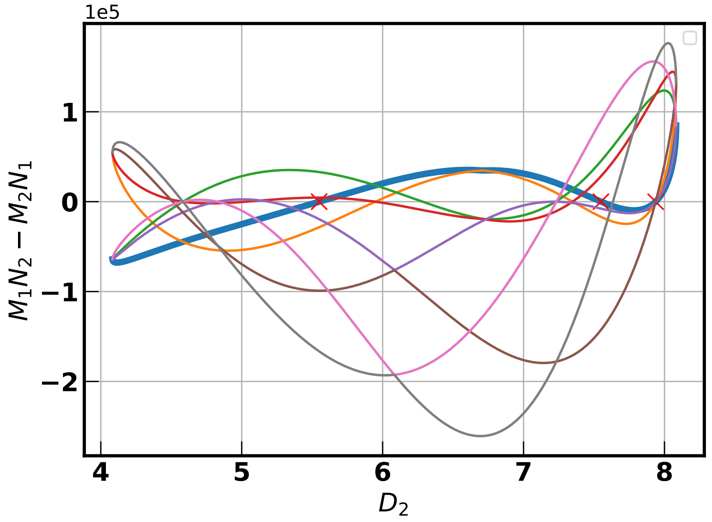

Figure C.13: Based on Fig.C.12, contact angle of three disks are 60°, $r_1, r_2, r_3 = 1, 2, 3$, $d_{12}, d_{13}, d_{23} = 4, \sqrt{61}, \sqrt{37}$. The 8 curves in this plot are based on Eq.C.67,C.69 and C.71. The first red cross represents the solution for Fig.C.12.

As a result:

$$D_1^2 = \frac{D_2^2(d_{12}^2 - d_{13}^2 + d_{23}^2) + r_2^2(-d_{12}^2 + d_{13}^2 + d_{23}^2) + d_{23}^2(d_{12}^2 + d_{13}^2 - d_{23}^2)}{2d_{23}^2} \pm \frac{\sqrt{(d_{12}^4 + (d_{13}^2 - d_{23}^2)^2 - 2d_{12}^2(d_{13}^2 + d_{23}^2))(D_2^4 + (d_{23}^2 - r_2^2)^2 - 2D_2^2(d_{23}^2 + r_2^2))}}{2d_{23}^2} . \tag{C.67}$$

The degenerated tetrahedron in magenta in Fig.C.12 can be solved on top of solving curvature radius for a touch event. We let the third disk shrink to a point ($r_3 = 0$) and force this point to the surface of the disks where an overlap event occurs ($d_{23} = r_2, d_{13} = D_1$). As a result, Eq.C.23 can be directly employed:

$$\begin{vmatrix} -2 & -2r_1\cos\theta_1 & -2r_2\cos\theta_2 & 0 & 1 \\ -2r_1\cos\theta_1 & -2D_1^2 & d_{12}^2 - r_2^2 - D_1^2 & D_1^2 - r_1^2 & 0 \\ -2r_2\cos\theta_2 & d_{12}^2 - D_1^2 - r_2^2 & -2r_2^2 & 0 & 0 \\ 0 & D_1^2 - r_1^2 & 0 & 0 & R \\ 1 & 0 & 0 & R & 0 \end{vmatrix} = 0 . \tag{C.68}$$

So with $t_1 = \cos\theta_1, t_2 = \cos\theta_2, t_3 = \cos\theta_3$,

$$R(D_1) = \frac{r_2(r_1^2 - D_1^2)(2r_1r_2t_1 + t_2(d_{12}^2 - D_1^2 - r_2^2) \pm \sqrt{(D_1^4 + (d_{12}^2 - r_2^2)^2 - 2D_1^2(d_{12}^2 + r_2^2))(t_2^2 - 1)})}{D_1^4 - 2D_1^2(d_{12}^2 + r_2(r_2 + 2r_1t_1t_2 - 2r_2t_2^2)) + d_{12}^4 - 2d_{12}^2r_2(r_2 - 2r_1t_1t_2) + r_2^2(r_2^2 + 4r_1^2t_1^2 - 4r_1r_2t_1t_2)} = \frac{M_1}{N_1} . \tag{C.69}$$

Similarly, for the degenerated tetrahedron in green in Fig.C.12, we need to replace r_1 with r_2, r_2 with r_3, r_3 with 0, d_{12} with d_{23}, d_{13} with r_2, d_{23} with D_2 in Eq.C.23:

$$\begin{vmatrix} -2 & -2r_2\cos\theta_2 & -2r_3\cos\theta_3 & 0 & 1 \\ -2r_2\cos\theta_2 & -2r_2^2 & d_{23}^2 - D_2^2 - r_2^2 & 0 & 0 \\ -2r_2\cos\theta_2 & d_{23}^2 - r_2^2 - D_2^2 & -2D_2^2 & D_2^2 - r_3^2 & 0 \\ 0 & 0 & D_2^2 - r_3^2 & 0 & R \\ 1 & 0 & 0 & R & 0 \end{vmatrix} = 0 . \tag{C.70}$$

So,

$$R(D_2) = \frac{r_2(r_3^2-D_2^2)(2r_2r_3t_3+t_2(d_{23}^2-D_2^2-r_2^2)\pm\sqrt{(D_2^4+(d_{23}^2-r_2^2)^2-2D_2^2(d_{23}^2+r_2^2))(t_2^2-1)})}{D_2^4-2D_2^2(d_{23}^2+r_2(r_2+2r_3t_2t_3-2r_2t_2^2))+d_{23}^4-2d_{23}^2r_2(r_2-2r_3t_2t_3)+r_2^2(r_2^2+4r_3^2t_3^2-4r_2r_3t_2t_3)} = \frac{M_2}{N_2} \ .$$

(C.71)

With Eq.C.69 and Eq.C.71, we can cancel R. Then we replace D_1 with D_2 by Eq.C.67, we obtain an equation with only one variable D_2. After D_2 is solved, R is calculated via Eq.C.71. We implement a case as shown in Fig.C.12 and Fig.C.13. There are 8 different configurations because the Eq.C.67,C.69 and C.71 have two different solutions.

C.3 Touch event in 3D

As shown before in Eq.C.63 in obtaining the critical radius of curvature, 2D touch event corresponds to 3D burst event, and it is natural to extend the idea to resolve 3D touch event. We use CMD to calculate the volume of the simplex in 4D and a 4-simplex is also known as a pentachoron. We assume that the fourth sphere has a contact angle of π. And the radius of the touching sphere is r_4. Then the four dimensional simplex volume is written as:

$$V_4^2 = \tfrac{-1}{9216}\begin{vmatrix} 0 & d(r_1,\theta_1) & d(r_2,\theta_2) & d(r_3,\theta_3) & d(r_4,\theta_4) & 1 \\ d(r_1,\theta_1) & 0 & d_{12}^2 & d_{13}^2 & d_{14}^2 & 1 \\ d(r_2,\theta_2) & d_{12}^2 & 0 & d_{23}^2 & d_{24}^2 & 1 \\ d(r_3,\theta_3) & d_{13}^2 & d_{23}^2 & 0 & d_{34}^2 & 1 \\ d(r_4,\theta_4) & d_{14}^2 & d_{24}^2 & d_{34}^2 & 0 & 1 \\ 1 & 1 & 1 & 1 & 1 & 0 \end{vmatrix} . \tag{C.72}$$

where, $d(r,\theta) = R^2 + r^2 - 2Rr\cos\theta$.

Using the similar simplification routine as shown in obtaining Eq.C.29, we obtain:

$$V_4^2 = \tfrac{-1}{9216}\begin{vmatrix} -2 & -2r_4-2r_1\cos\theta_1 & -2r_4-2r_2\cos\theta_2 & -2r_4-2r_3\cos\theta_3 & 2r_4 & 1 \\ -2r_4-2r_1\cos\theta_1 & -2d_{14}^2 & d_{12}^2-d_{14}^2-d_{24}^2 & d_{13}^2-d_{14}^2-d_{34}^2 & d_{12}^2-r_1^2+r_4^2 & 0 \\ -2r_4-2r_2\cos\theta_2 & d_{12}^2-d_{14}^2-d_{24}^2 & -2d_{24}^2 & d_{23}^2-d_{24}^2-d_{34}^2 & d_{24}^2-r_2^2+r_4^2 & 0 \\ -2r_4-2r_3\cos\theta_3 & d_{12}^2-d_{14}^2-d_{34}^2 & d_{23}^2-d_{24}^2-d_{34}^2 & -2d_{34}^2 & d_{34}^2-r_3^2+r_4^2 & 0 \\ 2r_4 & d_{14}^2-r_1^2+r_4^2 & d_{24}^2-r_2^2+r_4^2 & d_{34}^2-r_3^2+r_4^2 & -2r_4^2 & R \\ 1 & 0 & 0 & 0 & R & 0 \end{vmatrix} .$$

(C.73)

As a result, we express the volume of the pentachoron as a quadratic equation:

$$V_4^2 = \frac{1}{9216}(\hat{A}_4R^2 + \hat{B}_4R + \hat{C}_4) \ . \tag{C.74}$$

where,

$$\hat{A}_4 = \epsilon_{ijkl5}a_{1i}a_{2j}a_{3k}a_{4l}, \hat{B}_4 = 2\epsilon_{1ijkl}a_{1i}a_{2j}a_{3k}a_{4l}, \hat{C}_4 = \epsilon_{1ijkl}a_{2i}a_{3j}a_{4k}a_{5k}$$

a_{ij} is the i^{th} row and j^{th} column in the matrix of Eq.C.75

$$\begin{vmatrix} -2 & -2r_4-2r_1\cos\theta_1 & -2r_4-2r_2\cos\theta_2 & -2r_4-2r_3\cos\theta_3 & 2r_4 \\ -2r_4-2r_1\cos\theta_1 & -2d_{14}^2 & d_{12}^2-d_{14}^2-d_{24}^2 & d_{13}^2-d_{14}^2-d_{34}^2 & d_{14}^2-r_1^2+r_4^2 \\ -2r_4-2r_2\cos\theta_2 & d_{12}^2-d_{14}^2-d_{24}^2 & -2d_{24}^2 & d_{23}^2-d_{24}^2-d_{34}^2 & d_{24}^2-r_2^2+r_4^2 \\ -2r_4-2r_3\cos\theta_3 & d_{13}^2-d_{14}^2-d_{34}^2 & d_{23}^2-d_{24}^2-d_{34}^2 & -2d_{34}^2 & d_{34}^2-r_3^2+r_4^2 \\ 2r_4 & d_{14}^2-r_1^2+r_4^2 & d_{24}^2-r_2^2+r_4^2 & d_{34}^2-r_3^2+r_4^2 & -2r_4^2 \end{vmatrix} . \tag{C.75}$$

According to the work of Hales [Hales, 2012], the volume of a 4-simplex in $\mathbb{R}^3$ is zero. As a result, the critical curvature radius for touch event is obtained:

$$R_{3t} = \frac{-\hat{B}_4 \pm \sqrt{\hat{B}_4^{\,2} - 4\hat{A}_4\hat{C}_4}}{2\hat{A}_4} \ . \tag{C.76}$$

We believe that Eq.C.76 is the first equation to show that the critical curvature radius of 3D touch event can be solved by a simple quadratic equation for various contact angles and random positions of the spheres.

C.4 Generalization of C&R model

In obtaining Eq.C.13, C.29 and C.76, we find a similar procedure to calculate the critical curvature radius for the corresponding burst event in different dimensions, which inspires us to derive an unified equation to describe the curvature radius in various dimensions. In the following, we generalize the C&R model to n dimensional space to achieve this goal. Supposed that we have n spherical beads with radius as r_i $(i = 1, ..., n)$ and corresponding contact angle of invading liquid are θ_i $(i = 1, ..., n)$. And the distance between the center of each bead is d_{ij} $(i, j = 1, ..., n)$. The centers of these spheres with the center of the spherical meniscus forms a n-simplex. The squared volume of the n-simplex is written as:

$$V_n^2 = \frac{(-1)^{n+1}}{2^n(n!)^2}\begin{vmatrix} 0 & d(r_1,\theta_1) & d(r_2,\theta_2) & ... & d(r_n,\theta_n) & 1 \\ d(r_1,\theta_1) & 0 & d_{12}^2 & ... & d_{1n}^2 & 1 \\ d(r_2,\theta_2) & d_{12}^2 & 0 & ... & d_{2n}^2 & 1 \\ \vdots & \vdots & \vdots & \ddots & \vdots & \vdots \\ d(r_n,\theta_n) & d_{1n}^2 & d_{2n}^2 & ... & 0 & 1 \\ 1 & 1 & 1 & ... & 1 & 0 \end{vmatrix}, \tag{C.77}$$

where, $d(r_i, \theta_i) = R^2 + r_i^2 - 2Rr\cos\theta_i$.

For the row operation: $a_{1k} - R^2 a_{(n+2)k} \to a_{1k}$; $a_{ik} - r_{i-1}^2 a_{(n+2)k} \to a_{ik}, i = 2, 3, ..., (n+1)$. For the column operation: $a_{k1} - R^2 a_{k(n+2)} \to a_{k1}$; $a_{ki} - r_{i-1}^2 a_{k(n+2)} \to a_{ki}, i = 2, 3, ..., (n+1)$. As a consequence:

$$V_n^2 = \frac{(-1)^{n+1}}{2^n(n!)^2}\begin{vmatrix} -2R^2 & -2Rr_1\cos\theta_1 & -2Rr_2\cos\theta_2 & ... & -2Rr_n\cos\theta_n & 1 \\ -2Rr_1\cos\theta_1 & -2r_1^2 & d_{12}^2 - r_1^2 - r_2^2 & ... & d_{1n}^2 - r_1^2 - r_n^2 & 1 \\ -2Rr_2\cos\theta_2 & d_{12}^2 - r_1^2 - r_2^2 & -2r_2^2 & ... & d_{2n}^2 - r_2^2 - r_n^2 & 1 \\ \vdots & \vdots & \vdots & \ddots & \vdots & \vdots \\ -2Rr_n\cos\theta_n & d_{1n}^2 - r_1^2 - r_n^2 & d_{2n}^2 - r_2^2 - r_n^2 & ... & -2r_n^2 & 1 \\ 1 & 1 & 1 & ... & 1 & 0 \end{vmatrix}, \tag{C.78}$$

With $a_{5(n+2)} \to Ra_{5(n+2)}$, $a_{k1} \to a_{k1}/R$ and $a_{k(n+2)} \to Ra_{k(n+2)}$, $a_{1k} \to a_{1k}/R$:

$$V_n^2 = \frac{(-1)^{n+1}}{2^n(n!)^2}\begin{vmatrix} -2 & -2r_1\cos\theta_1 & -2r_2\cos\theta_2 & ... & -r_n\cos\theta_n & 1 \\ -2r_1\cos\theta_1 & -2r_1^2 & d_{12}^2 - r_1^2 - r_2^2 & ... & d_{1n}^2 - r_1^2 - r_n^2 & R \\ -2r_2\cos\theta_2 & d_{12}^2 - r_1^2 - r_2^2 & -2r_2^2 & ... & d_{2n}^2 - r_2^2 - r_n^2 & R \\ \vdots & \vdots & \vdots & \ddots & \vdots & \vdots \\ -2r_n\cos\theta_n & d_{1n}^2 - r_1^2 - r_n^2 & d_{2n}^2 - r_2^2 - r_n^2 & ... & -2r_n^2 & R \\ 1 & R & R & ... & R & 0 \end{vmatrix}, \tag{C.79}$$

With $a_{ik} - a_{(n+1)k} \to a_{ik}, i = 2, 3, ..., n, a_{ki} - a_{k(n+1)} \to a_{ki}, i = 2, 3, ..., n$:

$$V_n^2 = \frac{(-1)^{n+1}}{2^n(n!)^2} \begin{vmatrix} -2 & -2r_1\cos\theta_1 + 2r_n\cos\theta_n & -2r_2\cos\theta_2 + 2r_n\cos\theta_n & ... & -2r_{n-1}\cos\theta_2 + 2r_n\cos\theta_{n-1} & -r_n\cos\theta_n & 1 \\ -2r_1\cos\theta_1 + 2r_n\cos\theta_n & -2d_{1n}^2 & d_{12}^2 - d_{1n}^2 - d_{2n}^2 & ... & d_{1(n-1)}^2 - d_{1n}^2 - d_{(n-1)n}^2 & d_{1n}^2 + r_n^2 - r_1^2 & 0 \\ -2r_2\cos\theta_2 + 2r_n\cos\theta_n & d_{12}^2 - d_{1n}^2 - d_{2n}^2 & -2d_{2n}^2 & ... & d_{2(n-1)}^2 - d_{2n}^2 - d_{(n-1)n}^2 & d_{2n}^2 + r_n^2 - r_2^2 & 0 \\ \vdots & \vdots & \vdots & \ddots & \vdots & \vdots & \\ -2r_{n-1}\cos\theta_{n-1} + 2r_n\cos\theta_n & d_{1(n-1)}^2 - d_{1n}^2 - d_{(n-1)n}^2 & d_{2(n-1)}^2 - d_{2n}^2 - d_{(n-1)n}^2 & ... & -2d_{(n-1)n}^2 & d_{(n-1)n}^2 + r_n^2 - r_{n-1}^2 & 0 \\ -2r_n\cos\theta_n & d_{1n}^2 + r_n^2 - r_1^2 & d_{2n}^2 + r_n^2 - r_2^2 & ... & d_{(n-1)n}^2 + r_n^2 - r_{n-1}^2 & -2r_n^2 & R \\ 1 & 0 & 0 & ... & 0 & R & 0 \end{vmatrix} .$$

(C.80)

To obtain the coefficient of R^2:

$$\begin{aligned} &\frac{(-1)^{n+1}}{2^n(n!)^2}\epsilon_{i_1 i_2 ... i_n (n+2)(n+1)} a_{1i_1} a_{2i_2} ... a_{ni_n} a_{(n+1)(n+2)} a_{(n+2)(n+1)} \\ &= \frac{(-1)^n}{2^n(n!)^2}\epsilon_{i_1 i_2 ... (n+1)(n+2)} a_{1i_1} a_{2i_2} ... a_{ni_n} R^2 \ . \end{aligned} \tag{C.81}$$

For the coefficient of R:

$$\begin{aligned} &2 \times \frac{(-1)^{n+1}}{2^n(n!)^2}\epsilon_{i_1 i_2 ... i_n (n+2)1} a_{1i_1} a_{2i_2} ... a_{ni_n} a_{(n+1)(n+2)} a_{(n+2)1} \\ &= 2 \times \frac{1}{2^n(n!)^2}\epsilon_{1 i_1 i_2 ... i_n (n+2)} a_{1i_1} a_{2i_2} ... a_{ni_n} R \ . \end{aligned} \tag{C.82}$$

For the constant without R:

$$\begin{aligned} &\frac{(-1)^{n+1}}{2^n(n!)^2}\epsilon_{(n+2) i_1 i_2 ... i_n 1} a_{1(n+2)} a_{2i_1} a_{3i_2} ... a_{(n+1)i_{n+1}} a_{(n+2)1} \\ &= \frac{(-1)^n}{2^n(n!)^2}\epsilon_{1 i_1 i_2 ... i_{n+1} (n+2)} a_{2i_1} a_{3i_2} ... a_{(n+1)i_n} \ . \end{aligned} \tag{C.83}$$

As a result, we express the squared volume of the n-simplex as a quadratic equation:

$$V_n^2 = \frac{1}{2^n(n!)^2}(\hat{A}_n R^2 + \hat{B}_n R + \hat{C}_n) \ . \tag{C.84}$$

where,

$\hat{A}_n = (-1)^n \epsilon_{i_1 ... i_n (n+1)} a_{1i_1} ... a_{ni_n}, \hat{B}_n = 2\epsilon_{1 i_1 ... i_n} a_{1i_1} ... a_{ni_n}, \hat{C}_n = (-1)^n \epsilon_{1 i_1 ... i_n} a_{2i_1} a_{3i_2} ... a_{(n+1)i_n}$

a_{ij} is the i^{th} row and j^{th} column in the matrix of Eq.C.85, $i_1, ..., i_n \in \mathbb{N} \quad (0 < \mathbb{N} \leq (n+1))$

$$\begin{vmatrix} -2 & 2r_n\cos\theta_n - 2r_1\cos\theta_1 & ... & 2r_n\cos\theta_n - 2r_{n-1}\cos\theta_{n-1} & -2r_n\cos\theta_n \\ 2r_n\cos\theta_n - 2r_1\cos\theta_1 & -2d_{1n}^2 & ... & d_{1(n-1)}^2 - d_{1n}^2 - d_{(n-1)n}^2 & d_{1n}^2 - r_1^2 + r_n^2 \\ 2r_n\cos\theta_n - 2r_2\cos\theta_2 & d_{12}^2 - d_{1n}^2 - d_{2n}^2 & ... & d_{2(n-1)}^2 - d_{2n}^2 - d_{(n-1)n}^2 & d_{2n}^2 - r_2^2 + r_n^2 \\ \vdots & \vdots & \ddots & \vdots & \vdots \\ 2r_n\cos\theta_n - 2r_{n-1}\cos\theta_{n-1} & d_{1(n-1)}^2 - d_{1n}^2 - d_{(n-1)n}^2 & ... & -2d_{(n-1)n}^2 & d_{(n-1)n}^2 - r_{n-1}^2 + r_n^2 \\ -2r_n\cos\theta_n & d_{1n}^2 - r_1^2 + r_n^2 & ... & d_{(n-1)n}^2 - r_{n-1}^2 + r_n^2 & -2r_n^2 \end{vmatrix} .$$

(C.85)

By forcing the n dimensional simplex volume to 0, the curvature radius is expressed:

$$R_n = \frac{-\hat{B}_n \pm \sqrt{\hat{B}_n^{\ 2} - 4\hat{A}_n\hat{C}_n}}{2\hat{A}_n} \ . \tag{C.86}$$

We believe Eq.C.86 is the first equation to generalize C&R model in high dimensional space. When $n = 2, 3, 4$, we are able to achieve the critical curvature radius for 2D burst event (Eq.C.13, $n = 2$), 2D touch event (Eq.C.63, $n = 3$), 3D burst event (Eq.C.29, $n = 3$) and 3D touch event (Eq.C.76, $n = 4$). For the case when $n > 4$, the physical meaning is not yet known and in need of further investigation.

It is worth noting that Yang et al. [Yang and Zhang, 1989] shows that for a simplex with N points, the volume calculated by CMD will turn zero if $N \geq n + 2$, where n is the dimension of the hyperplane E^n. For example, 4-simplex has 5 points and if the 4-simplex is in $\mathbb{R}^3$ ($N = n + 2$), the volume is 0, which is in accordance with the remark in the book of Hales [Hales, 2012].

We further investigate the properties of the coefficients in Eq.C.86 in order to have a better understanding of this model. Expanding $\hat{A}_n$, we find that:

$$\hat{A}_n = 2^n((n-1)!)^2 V_{n-1}^2 - 2^{n-1} \sum_{i=1}^{n} \sum_{j=1}^{n} a_{ij}^2 B_{ij} \ . \tag{C.87}$$

Where V_{n-1} is the volume of the $(n-1)$ dimension simplex by excluding the vertex of the center of the spherical meniscus; $a_{ij} = |r_i \cos\theta_i - r_j \cos\theta_j|$ and B_{ij} is the cofactor of $\frac{1}{2} d_{ij}^2$ for matrix of B. The definition of B is as in the work of Lu et al. [Lu et al., 1983]:

$$B = \begin{vmatrix} 0 & 1 & \dots & 1 \\ 1 & & & \\ \vdots & & -\frac{1}{2} d_{ij}^2 & \\ 1 & & & \end{vmatrix} \ . \tag{C.88}$$

When $n = 2$:

$$B = \begin{vmatrix} 0 & 1 & 1 \\ 1 & 0 & -\frac{1}{2} d_{12}^2 \\ 1 & -\frac{1}{2} d_{12}^2 & 0 \end{vmatrix}, \quad B_{12} = B_{21} = -\begin{vmatrix} 0 & 1 \\ 1 & -\frac{1}{2} d_{12}^2 \end{vmatrix} = 1 \ .$$

As a result:

$$\hat{A}_2 = 4V_1^2 - 4(r_1 \cos\theta_1 - r_2 \cos\theta_2)^2 B_{12} = 4d^2 - 4(r_1 \cos\theta_1 - r_2 \cos\theta_2)^2 \ . \tag{C.89}$$

When $n = 3$:

$$B = \begin{vmatrix} 0 & 1 & 1 & 1 \\ 1 & 0 & -\frac{1}{2} d_{12}^2 & -\frac{1}{2} d_{13}^2 \\ 1 & -\frac{1}{2} d_{12}^2 & 0 & -\frac{1}{2} d_{23}^2 \\ 1 & -\frac{1}{2} d_{13}^2 & -\frac{1}{2} d_{23}^2 & 0 \end{vmatrix}, \quad B_{12} = -\begin{vmatrix} 0 & 1 & 1 \\ 1 & -\frac{1}{2} d_{12}^2 & -\frac{1}{2} d_{23}^2 \\ 1 & -\frac{1}{2} d_{13}^2 & 0 \end{vmatrix} = \tfrac{1}{2}(d_{13}^2 + d_{23}^2 - d_{12}^2)$$

$$B_{13} = \begin{vmatrix} 0 & 1 & 1 \\ 1 & -\frac{1}{2} d_{12}^2 & 0 \\ 1 & -\frac{1}{2} d_{13}^2 & -\frac{1}{2} d_{23}^2 \end{vmatrix} = \tfrac{1}{2}(d_{12}^2 + d_{23}^2 - d_{13}^2) \quad B_{23} = -\begin{vmatrix} 0 & 1 & 1 \\ 1 & 0 & -\frac{1}{2} d_{12}^2 \\ 1 & -\frac{1}{2} d_{13}^2 & -\frac{1}{2} d_{23}^2 \end{vmatrix} = \tfrac{1}{2}(d_{13}^2 + d_{12}^2 - d_{23}^2) \ .$$

As a result:

$$\begin{aligned} \hat{A}_3 = 32V_2^2 &- 4(r_1 \cos\theta_1 - r_2 \cos\theta_2)^2(-d_{12}^2 + d_{13}^2 + d_{23}^2) \\ &- 4(r_1 \cos\theta_1 - r_3 \cos\theta_3)^2(d_{12}^2 - d_{13}^2 + d_{23}^2) \\ &- 4(r_2 \cos\theta_2 - r_3 \cos\theta_3)^2(d_{12}^2 + d_{13}^2 - d_{23}^2) \ . \end{aligned} \tag{C.90}$$

Eq.C.89 and C.90 fit the expression in Eq.C.8 and Eq.C.26, which indicates that the validity of Eq.C.87. In the following part, we provide a simple proof of Eq.C.87. Firstly, by simple inspection, for items without $r_i\cos\theta_i - r_j\cos\theta_j$:

$$\begin{aligned}
&(-2)(-1)^n\begin{vmatrix} -2d_{1n}^2 & \ldots & d_{1(n-1)}^2 - d_{1n}^2 - d_{(n-1)n}^2 \\ d_{12}^2 - d_{1n}^2 - d_{2n}^2 & \ldots & d_{2(n-1)}^2 - d_{2n}^2 - d_{(n-1)n}^2 \\ \vdots & \ddots & \vdots \\ d_{1(n-1)}^2 - d_{1n}^2 - d_{(n-1)n}^2 & \ldots & -2d_{(n-1)n}^2 \end{vmatrix} \\
&= 2\begin{vmatrix} 2d_{1n}^2 & \ldots & -d_{1(n-1)}^2 + d_{1n}^2 + d_{(n-1)n}^2 \\ -d_{12}^2 + d_{1n}^2 + d_{2n}^2 & \ldots & -d_{2(n-1)}^2 + d_{2n}^2 + d_{(n-1)n}^2 \\ \vdots & \ddots & \vdots \\ -d_{1(n-1)}^2 + d_{1n}^2 + d_{(n-1)n}^2 & \ldots & 2d_{(n-1)n}^2 \end{vmatrix} = 2^n V_{n-1}^2((n-1)!)^2 \ .
\end{aligned} \tag{C.91}$$

By replacing the i^{th} row of elements in Eq.C.88 with the corresponding cofactors and considering the relationship between cofactor and determinant:

$$\sum_{j=1}^{n} B_{ij} = B_{i0}\cdot 0 + B_{i1}\cdot 1 + \ldots + B_{in}\cdot 1 = \begin{vmatrix} 0 & 1 & \ldots & 1 \\ 1 & & & \\ \vdots & & -\frac{1}{2}d_{ij}^2 & \\ 0 & 1 & \ldots & 1 \\ \vdots & & -\frac{1}{2}d_{ij}^2 & \\ 1 & & & \end{vmatrix} = 0 \ . \tag{C.92}$$

As a result, $B_{ii} = -\sum_{j=1,j\neq i}^{n} B_{ij}$. In addition:

$$\begin{aligned}
B = \begin{vmatrix} 0 & 1 & \ldots & 1 \\ 1 & & & \\ \vdots & & -\frac{1}{2}d_{ij}^2 & \\ 1 & & & \end{vmatrix} &= \begin{vmatrix} 0 & 0 & \ldots & 0 & 1 \\ 0 & d_{1n}^2 & \ldots & \frac{-d_{1(n-1)}^2 + d_{1n}^2 + d_{(n-1)n}^2}{2} & -\frac{1}{2}d_{1n}^2 \\ 0 & \frac{-d_{12}^2 + d_{1n}^2 + d_{2n}^2}{2} & \ldots & \frac{-d_{2(n-1)}^2 + d_{2n}^2 + d_{(n-1)n}^2}{2} & -\frac{1}{2}d_{2n}^2 \\ \vdots & \vdots & \ddots & \vdots & \vdots \\ 0 & \frac{-d_{1(n-1)}^2 + d_{1n}^2 + d_{(n-1)n}^2}{2} & \ldots & d_{(n-1)n}^2 & -\frac{1}{2}d_{(n-1)n}^2 \\ 1 & -\frac{1}{2}d_{1n}^2 & \ldots & -\frac{1}{2}d_{(n-1)n}^2 & 0 \end{vmatrix} \\
&= \frac{1}{2^{n-1}}\begin{vmatrix} 0 & 0 & \ldots & 0 & 1 \\ 0 & 2d_{1n}^2 & \ldots & -d_{1(n-1)}^2 + d_{1n}^2 + d_{(n-1)n}^2 & 0 \\ 0 & -d_{12}^2 + d_{1n}^2 + d_{2n}^2 & \ldots & -d_{2(n-1)}^2 + d_{2n}^2 + d_{(n-1)n}^2 & 0 \\ \vdots & \vdots & \ddots & \vdots & \vdots \\ 0 & -d_{1(n-1)}^2 + d_{1n}^2 + d_{(n-1)n}^2 & \ldots & 2d_{(n-1)n}^2 & 0 \\ 1 & 0 & \ldots & 0 & 0 \end{vmatrix} \\
&= \frac{(-1)^n}{2^{n-1}}\begin{vmatrix} -2d_{1n}^2 & \ldots & d_{1(n-1)}^2 - d_{1n}^2 - d_{(n-1)n}^2 \\ d_{12}^2 - d_{1n}^2 - d_{2n}^2 & \ldots & d_{2(n-1)}^2 - d_{2n}^2 - d_{(n-1)n}^2 \\ \vdots & \ddots & \vdots \\ d_{1(n-1)}^2 - d_{1n}^2 - d_{(n-1)n}^2 & \ldots & -2d_{(n-1)n}^2 \end{vmatrix} \ .
\end{aligned} \tag{C.93}$$

For items related to $(r_i\cos\theta_i - r_n\cos\theta_n)(r_j\cos\theta_j - r_n\cos\theta_n)$ in $\hat{A}_n$, by comparing

Eq.C.93 and Eq.C.85:

$$
\begin{aligned}
&(-1)^{2n}2^{n-1}\sum_{i=1}^{n-1}\sum_{j=1}^{n-1}(r_i\cos\theta_i - r_n\cos\theta_n)(r_j\cos\theta_j - r_n\cos\theta_n)B_{ij}\\
=&2^{n-1}\left(\sum_{i=1}^{n-1}(r_i\cos\theta_i - r_n\cos\theta_n)^2B_{ii} + \sum_{i=1}^{n-1}\sum_{j=1,j\neq i}^{n-1}(r_i\cos\theta_i - r_n\cos\theta_n)(r_j\cos\theta_j - r_n\cos\theta_n)B_{ij}\right)\\
=&2^{n-1}\left(\sum_{i=1}^{n-1}\sum_{j=1,j\neq i}^{n-1}(r_i\cos\theta_i - r_n\cos\theta_n)^2(-B_{ij})\right.\\
&\left.+\sum_{i=1}^{n-1}\sum_{j=1,j\neq i}^{n-1}(r_i\cos\theta_i - r_n\cos\theta_n)(r_j\cos\theta_j - r_n\cos\theta_n)B_{ij}\right)\\
=&-2^{n-1}\left(\sum_{i=1}^{n}\sum_{j=1,j\neq i}^{n}[(r_i\cos\theta_i - r_n\cos\theta_n) - (r_j\cos\theta_j - r_n\cos\theta_n)]^2B_{ij}\right)\\
=&-2^{n-1}\sum_{i=1}^{n}\sum_{j=1}^{n}a_{ij}^2B_{ij}\ .
\end{aligned}
$$

(C.94)

The reason to expand the coefficient in this form is to employ the following inequality [Lu et al., 1983], which generalizes the Neuberg-Pedoe inequality to high-dimensional Euclidean spaces:

$$\sum_{i=1}^{n+1}\sum_{j=1}^{n+1}a_{ij}^2B_{ij} \geq 2n(n!)^2V(A)^{\frac{2}{n}}V(B)^{2-\frac{2}{n}}\ . \tag{C.95}$$

In Eq.C.95, $V(A)$ and $V(B)$ are the volume of the simplexes A and B. With Eq.C.95, we know $\hat{A} \leq 2^n((n-1)!)^2V_{n-1}^2$. Eq.C.95 only gives the lower bound of the expression. For the upper bound, it is in need for further work and we are not elaborating on that in the current thesis. Expanding $\hat{C}_n$, we have:

$$
(-1)^n\begin{vmatrix}
-2d_{1n}^2 & d_{12}^2 - d_{1n}^2 - d_{2n}^2 & \cdots & d_{1(n-1)}^2 - d_{1n}^2 - d_{(n-1)n}^2 & d_{12}^2 - r_1^2 + r_n^2\\
d_{12}^2 - d_{1n}^2 - d_{2n}^2 & -2d_{2n}^2 & \cdots & d_{2(n-1)}^2 - d_{2n}^2 - d_{(n-1)n}^2 & d_{2n}^2 - r_2^2 + r_n^2\\
\vdots & \vdots & \ddots & \vdots & \vdots\\
d_{1(n-1)}^2 - d_{1n}^2 - d_{(n-1)n}^2 & d_{2(n-1)}^2 - d_{2n}^2 - d_{(n-1)n}^2 & \cdots & -2d_{(n-1)n}^2 & d_{(n-1)n}^2 - r_{n-1}^2 + r_n^2\\
d_{1n}^2 - r_1^2 + r_n^2 & d_{2n}^2 - r_2^2 + r_n^2 & \cdots & d_{(n-1)n}^2 - r_{n-1}^2 + r_n^2 & -2r_n^2
\end{vmatrix}\ .
$$

(C.96)

With row operation of $a_{ik} \rightarrow -a_{ik}, i = 1, 2, ..., n-1$ and column operation of $a_{kn} \rightarrow -a_{kn}$:

$$
\begin{vmatrix}
2d_{1n}^2 & d_{1n}^2 + d_{2n}^2 - d_{12}^2 & \cdots & d_{(n-1)n}^2 + d_{1n}^2 - d_{1(n-1)}^2 & d_{12}^2 + r_n^2 - r_1^2\\
d_{1n}^2 + d_{2n}^2 - d_{12}^2 & 2d_{2n}^2 & \cdots & d_{(n-1)n}^2 + d_{2n}^2 - d_{2(n-1)}^2 & d_{2n}^2 + r_n^2 - r_2^2\\
\vdots & \vdots & \ddots & \vdots & \vdots\\
d_{1n}^2 + d_{(n-1)n}^2 - d_{1(n-1)}^2 & d_{2n}^2 + d_{(n-1)n}^2 - d_{2(n-1)}^2 & \cdots & 2d_{(n-1)n}^2 & d_{(n-1)n}^2 + r_n^2 - r_{n-1}^2\\
d_{1n}^2 + r_n^2 - r_1^2 & d_{2n}^2 + r_n^2 - r_2^2 & \cdots & d_{(n-1)n}^2 + r_n^2 - r_{n-1}^2 & 2r_n^2
\end{vmatrix}\ .
$$

(C.97)

Comparing Eq.C.97 and Eq.C.1, we know that $\hat{C}_n$ has a clear geometrical definition, i.e. the volume of a simplex. This simplex assumes a new vertex, which will form extra edges $r_1, r_2..., r_n$ by connecting the new point with the vertexes of the original simplex.

D Lamella burst event

Lamella burst event

If a spherical meniscus is assumed, then we firstly recalculate the volume of the tetrahedron in Eq.C.20 with Heron's formular [Zwillinger, 2002]:

$$V_1 = \frac{1}{3}Sh$$
$$S = \frac{1}{4}\sqrt{(d_{12}+d_{13}+d_{23})(-d_{12}+d_{13}+d_{23})(d_{12}-d_{13}+d_{23})(d_{12}+d_{13}-d_{23})}\ . \tag{D.1}$$

where S is the area of the triangle formed by the center of the three beads. h is the distance from the meniscus center to the plane formed by the centers of three beads. As a result,

$$V_1^2 = \frac{(d_{12}+d_{23}+d_{13})(-d_{12}+d_{23}+d_{13})(d_{12}-d_{23}+d_{13})(d_{12}+d_{23}-d_{13})}{144}h^2\ . \tag{D.2}$$

When the neighbouring menisci overlap with each other, the spherical meniscus will touch the plane formed by three beads. In that case, the height of the tetrahedron in Eq.D.2 will be $h = R$. With Eq.C.20 and Eq.D.2 ($V^2 = V_1^2$) and the symmetry of the sphere, we obtain the curvature for the lamella burst event:

$$A_{lb}R^2 + B_{lb}R + C_{lb} = 0\ . \tag{D.3}$$

where,

$$A_{lb} = -\epsilon_{ijk4}a_{1i}a_{2j}a_{3k}$$
$$-\,2(d_{12}+d_{23}+d_{13})(-d_{12}+d_{23}+d_{13})(d_{12}-d_{23}+d_{13})(d_{12}+d_{23}-d_{13})$$
$$B_{lb} = 2\epsilon_{1ijk}a_{1i}a_{2j}a_{3k}, C_{lb} = -\epsilon_{1ijk}a_{2i}a_{3j}a_{4k}\ .$$

a_{ij} is the i^{th} row and j^{th} column in the matrix of Eq.C.28

With Eq.C.26 and Eq.C.30, it is easy to check:

$$\begin{aligned} A_{lb} =& -4(r_1\cos\theta_1 - r_2\cos\theta_2)^2(-d_{12}^2+d_{13}^2+d_{23}^2) - 4(r_1\cos\theta_1 - r_3\cos\theta_3)^2(d_{12}^2-d_{13}^2+d_{23}^2) \\ & -4(r_2\cos\theta_2 - r_3\cos\theta_3)^2(d_{12}^2+d_{13}^2-d_{23}^2) \le 0\ . \end{aligned} \tag{D.4}$$

Comparison between the Eq.D.3 and [Semprebon et al., 2016]

Another natural comparison should be made between our analytical model to the results in the work of Semprebon et al. [Semprebon et al., 2016]. We start from a three-bead system, where two pairs of the beads are in mechanical contact, leaving a small separation between the third pair [Semprebon et al., 2016]. Firstly, for the spherical cap with radius of R, the sum of two principal curvatures is:

$$H = \frac{2}{R}\ . \tag{D.5}$$

When the contact angle and sphere diameter is the same, Eq.C.22 can be further simplified as:

$$\begin{vmatrix} -2 & -2r\cos\theta & -2r\cos\theta & -2r\cos\theta & 1 \\ -2r\cos\theta & -2r^2 & d_{12}^2-2r^2 & d_{13}^2-2r^2 & R \\ -2r\cos\theta & d_{12}^2-2r^2 & -2r_2^2 & d_{23}^2-2r^2 & R \\ -2r\cos\theta & d_{13}^2-2r^2 & d_{23}^2-2r^2 & -2r^2 & R \\ 1 & R & R & R & 0 \end{vmatrix} . \tag{D.6}$$

With $a_{ik} - a_{4k} \to a_{ik}, i = 2, 3$,$a_{ki} - a_{ki} \to a_{ki}, i = 2, 3$:

$$\begin{vmatrix} -2 & 0 & 0 & -2r\cos\theta & 1 \\ 0 & -2d_{13}^2 & d_{12}^2-d_{13}^2-d_{23}^2 & d_{13}^2 & 0 \\ 0 & d_{12}^2-d_{13}^2-d_{23}^2 & -2d_{23}^2 & d_{23}^2 & 0 \\ -2r\cos\theta & d_{13}^2 & d_{23}^2 & -2r^2 & R \\ 1 & 0 & 0 & R & 0 \end{vmatrix} . \tag{D.7}$$

Eq.D.7 reminds us that the coefficient of R^2 is:

$$\begin{aligned} \frac{1}{288}\epsilon_{ijk54}a_{1i}a_{2j}a_{3k} &= \tfrac{-1}{288}\begin{vmatrix} -2 & 0 & 0 \\ 0 & -2d_{13}^2 & d_{12}^2-d_{13}^2-d_{23}^2 \\ 0 & d_{12}^2-d_{13}^2-d_{23}^2 & -2d_{23}^2 \end{vmatrix} = \frac{1}{144}(4d_{13}^2d_{23}^2 - (d_{12}^2 - d_{13}^2 - d_{23}^2)^2) \\ &= \frac{(d_{12}+d_{23}+d_{13})(-d_{12}+d_{23}+d_{13})(d_{12}-d_{23}+d_{13})(d_{12}+d_{23}-d_{13})}{144} . \end{aligned} \tag{D.8}$$

Compared with Eq.D.2, we know that $A_{lb} = 0$, so:

$$R = \frac{1}{2r\cos\theta}\left(r^2 - \frac{d_{12}^2d_{13}^2d_{23}^2}{(d_{12}+d_{23}+d_{13})(-d_{12}+d_{23}+d_{13})(d_{12}-d_{23}+d_{13})(d_{12}+d_{23}-d_{13})}\right) . \tag{D.9}$$

In Eq.D.9, when $\theta = \frac{\pi}{2}$, $R \to \infty$. That means whenever the neighboring pores are filled with the invading liquid, lamella burst will always happen if the pressure of the invading liquid is larger than the defending phase. In addition, we notice that in Eq.D.9, there is a triangle inequality. And the area S of the triangle formed by d_{12}, d_{13}, d_{23} [Svrtan and Veljan, 2012]:

$$\begin{gathered} S \leq \frac{\sqrt{3}}{4}(d_{12}d_{23}d_{13})^{\frac{2}{3}}, \\ (d_{12}+d_{23}+d_{13})(-d_{12}+d_{23}+d_{13})(d_{12}-d_{23}+d_{13})(d_{12}+d_{23}-d_{13}) = 16S^2 \end{gathered} \tag{D.10}$$

As a consequence, when $\cos\theta < 0$:

$$R \geq \frac{1}{2r\cos\theta}\left(r^2 - \frac{1}{3}(d_{12}d_{23}d_{13})^{\frac{2}{3}}\right) . \tag{D.11}$$

Eq.D.11 sets a bound for the curvature. That means that for monodisperse beads with the same surface property, there is a critical pressure for which, no isolated trimmer [Scheel et al., 2008] will exist.

In Fig.D.1a, the estimated value H is higher than the literature results [Semprebon et al., 2016], which might be the influence of the cross talk between neighbouring

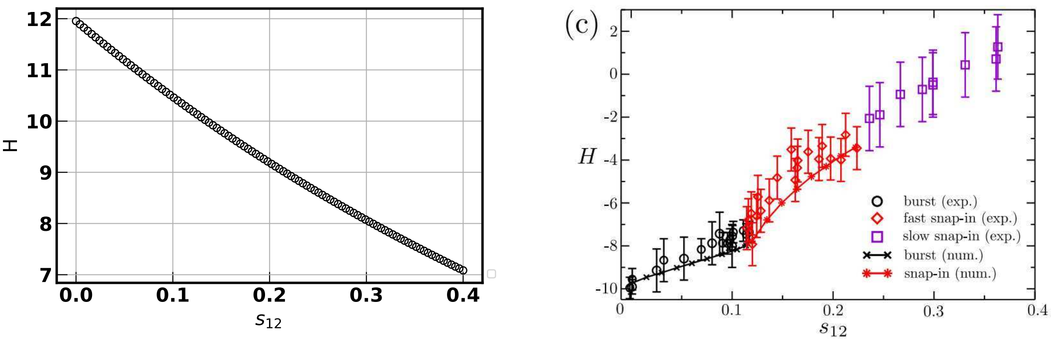

(a) **(b)**

Figure D.1: Lamella burst pressure calculated by geometric approximation and literature. (a) H agains s_{12}. s_{12} is the gap separation normalized by the radius r of the sphere. contact angle is set as $\theta = 175°$. The non-wetting phase is the invading phase, so that the sign is different from Ref. [Semprebon et al., 2016]; (b) Estimated mean curvature H for an evaporating trimer at the point of instability against the gap opening s_{12}. Figures adapted with permission from Semprebon et al. [Semprebon et al., 2016], copyright American Physical Society.

pores or the existence of a liquid bridge. For the case in the work of Semprebon et al. [Semprebon et al., 2016], $d_{23} = d_{13} = 2r, d_{12} = 2r + s$:

$$
\begin{aligned}
R &= \frac{1}{2r\cos\theta}\left(r^2 - \frac{d_{12}^2 d_{13}^2 d_{23}^2}{(d_{12}+d_{23}+d_{13})(-d_{12}+d_{23}+d_{13})(d_{12}-d_{23}+d_{13})(d_{12}+d_{23}-d_{13})}\right) \\
&= \frac{1}{2r\cos\theta}\left(r^2 - \frac{4r^2 4r^2 (2r+s)^2}{(6r+s)(2r+s)(2r+s)(2r-s)}\right) \\
&= \frac{1}{2r\cos\theta}\left(r^2 - \frac{16r^4}{(6r+s)(2r-s)}\right) = \frac{r}{2\cos\theta}\left(1 - \frac{16}{-(\frac{s}{r})^2 - 4\frac{s}{r} + 12}\right).
\end{aligned}
\tag{D.12}
$$

Assume $\frac{s}{r} = \overline{s}$, when the gap is small, $(\frac{s}{r})^2$ is negligible:

$$
R \approx \frac{r}{2\cos\theta}\left(1 + \frac{4}{\overline{s} - 3}\right) \approx \frac{r}{2\cos\theta}\left(\frac{\overline{s}+1}{\overline{s}-3}\right). \tag{D.13}
$$

As a result, with taylor expansion:

$$
H = \frac{2}{R} \approx \frac{4\cos\theta}{r}\left(\frac{\overline{s}-3}{\overline{s}+1}\right) \approx \frac{4\cos\theta}{r}\left(-3 + 4\overline{s}\right). \tag{D.14}
$$

So, the slope will be around $16\cos 175° \approx -15.539$. In Fig.D.1b, we notice that the black region the slope is $\approx 2/0.125 = 16$. The slope between the pure geometric approximation and results from Surface Evolver [Semprebon et al., 2016] is similar. Even though there is a systematic shift around 2 in terms of the mean curvature, the experimental data shown in Fig.D.1b also have error bars ranging around 2. As a result, the spherical cap fit to calculate the lamella burst cuvature provides a relative good and efficient way to determine the lamella burst.

E Zero Laplace pressure

When the meniscus is driven from negative Laplace pressure to positive Laplace pressure, there is a special state where $r_p \to \infty$, which means that the meniscus will be a line segment. So we recalculate the equation for the meniscus in a line segment. As in Fig.E.1a, supposed that the line equation for the meniscus is $ax + by + c = 0$, where x, y are the coordinate for the meniscus. The axises are rotated so that the center of the disks are on the X axis. And the coordinates for the centers of the two disks are $(x_1, 0)$ and $(x_2, 0)$. Due to the constriction of the contact angle, it is easy to obtain the following equation based on the point to line distance:

$$\frac{|ax_1 + c|}{\sqrt{a^2+b^2}} = |r_1 \cos\theta_1|, \quad \frac{|ax_2 + c|}{\sqrt{a^2+b^2}} = |r_2 \cos\theta_2| \ . \tag{E.1}$$

Solving Eq.E.1, we obtain the following expression for the meniscus:

$$\begin{cases} y = r_1 \cos\theta_1, & \text{if} \quad r_1\cos\theta_1 = r_2\cos\theta_2. \\ x + \frac{b}{a}y + \frac{c}{a} = 0 & \text{else.} \end{cases} \tag{E.2}$$

In Eq.E.2,

$$\begin{aligned} (\frac{c}{a}, \frac{b}{a}) = &(\frac{x_1 r_2 \cos\theta_2 - x_2 r_1 \cos\theta_1}{r_1\cos\theta_1 - r_2\cos\theta_2}, \quad \pm\sqrt{(\frac{x_1 - x_2}{r_1\cos\theta_1 - r_2\cos\theta_2})^2 - 1}) \\ &,(-\frac{x_1 r_2 \cos\theta_2 + x_2 r_1 \cos\theta_1}{r_1\cos\theta_1 + r_2\cos\theta_2}, \quad \pm\sqrt{(\frac{x_1 - x_2}{r_1\cos\theta_1 + r_2\cos\theta_2})^2 - 1}) \ . \end{aligned} \tag{E.3}$$

In Eq.E.3, there are four solutions. This is because Eq.E.3 includes solution when θ_1 and θ_2 can also be their corresponding supplementary angles. We firstly solve the line and circle intersection equation:

$$\begin{cases} (x - x_{1,2})^2 + y^2 - r_{1,2}^2 & = 0 \\ x + k_1 y + k_2 & = 0, \quad k_1 = \frac{b}{a}, k_2 = \frac{c}{a} \end{cases} \tag{E.4}$$

There are two intersection points for each line and we choose the one which is closer to the center of the other disk. The X-coordinate for the intersection point between the line and the left disk will be x_{left}. The same for the intersection point for the right disk x_{right}.

$$\begin{aligned} x_{left} &= \frac{x_1 k_1^2 - k_2 + |k_1|\sqrt{k_1^2 r_1^2 - k_2^2 - 2k_2 x_1 + r_1^2 - x_1^2}}{k_1^2 + 1} \\ x_{right} &= \frac{x_2 k_1^2 - k_2 - |k_1|\sqrt{k_1^2 r_2^2 - k_2^2 - 2k_2 x_2 + r_2^2 - x_2^2}}{k_1^2 + 1} \ . \end{aligned} \tag{E.5}$$

After the intersection points for each line in Eq.E.3 are obtained, we can directly calculate the contact angle and choose the correct one. For example, in Fig.E.1b, in order to determine whether T satisfies our requirement of contact angle, we need to calculate the angle when we rotate counterclockwise the $\overrightarrow{AT}$ to the normal vector of the line $\overrightarrow{n}$. For the right hand disk, the vector connecting the intersection point and the center to the disk should be rotated clockwise.

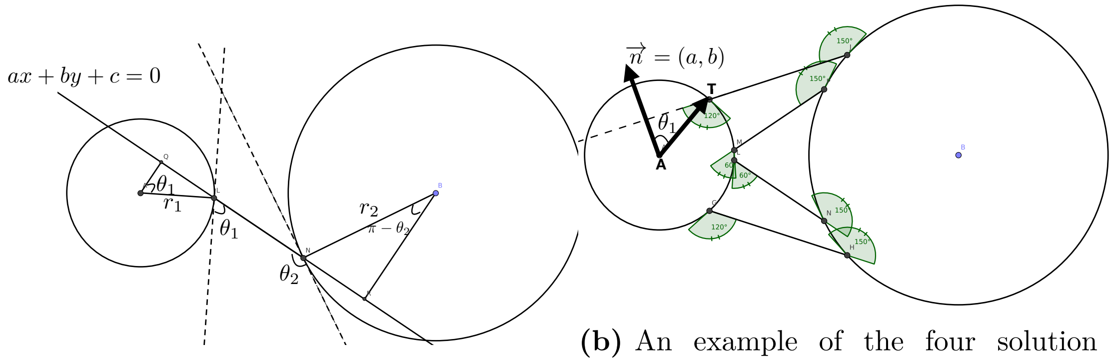

(a) An illustration when a straight line goes through two circles.

(b) An example of the four solution in Eq.E.4. In this case, $x_1 = 0, x_2 = 4, r_1 = 1, r_2 = 2, \theta_1 = 60°, \theta_2 = 150°$.

Figure E.1: The position of meniscus when Laplace pressure is zero.

F Ellipse packing

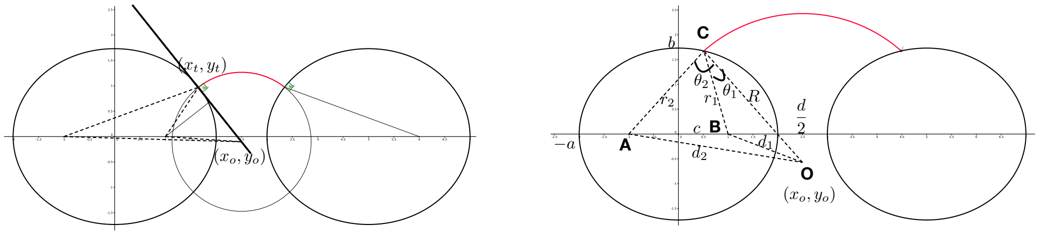

(a) The contact angle is 90°.

(b) More general contact angle.

Figure F.1: Two identical ellipses. The distance between the center of the ellipse d is 5. The red circular arc represents the interface between two phase.

In order to determine the burst criterion for the ellipse packing, we start from an easy case.

Contact angle is 90°

When the contact angle of the invading phase is 90 °, there is a easy way to determine the burst event analytically. For any point on the ellipse in Fig.F.1a, $(x_t, y_t) = (a\cos n, b\sin n)$, there is a tangent line funciton:

$$\frac{xx_t}{a^2} + \frac{yy_t}{b^2} = 1\ . \tag{F.1}$$

If $x_o = \frac{d}{2}$, $y_o = \frac{b}{\sin n} - \frac{bd\cot n}{2a}$, then the square of the distance between the point and the center of the circle when contact angle is 90°:

$$f(n) = (\frac{d}{2} - a\cos n)^2 + (\frac{b}{\sin n} - \frac{bd\cot n}{2a} - b\sin n)^2 = \frac{(d-2a\cos n)^2(a^2+b^2\cot^2 n)}{4a^2}\ . \tag{F.2}$$

When the contact angle is not 90°, we need to rotate the tangent line, which makes it more complicated. When $f(n)$ reaches minimum, we have the burst event. Let $t = \cos n$, $c = \sqrt{a^2 - b^2}$:

$$f'(t) = \frac{-2a^3d + (4a^4 + b^2d^2)t + (4a^3d - 6ab^2d)t^2 - (8a^2c^2)t^3 - (2ac^2d)t^4 + (4a^2c^2)t^5}{2a^2(t^2-1)^2} \; . \tag{F.3}$$

With $f'(t) = 0$, we need to solve a quintic equation:

$$-2a^3d + (4a^4 + b^2d^2)t + (4a^3d - 6ab^2d)t^2 - (8a^2c^2)t^3 - (2ac^2d)t^4 + (4a^2c^2)t^5 = 0 \; . \tag{F.4}$$

For example, $a = 2, c = 1, d = 5$, solving Eq.F.4, we have $t \approx 0.82679$ when $t \in [-1, 1]$, which indicates the minimum radius of circle we can reach, i.e. burst event criterion. And it is the case shown in Fig.F.1a. Another way to check the validity of Eq.F.4 is to make $c = 0$. At that case, it is equivalent to the previous C&R model in circular packing. And it is trivial to check that $r = \frac{\sqrt{d^2-4a^2}}{2}$ for Eq.F.4 and Eq.C.17. We notice that the burst event happens when the center of the meniscus circle is not on the line connecting the centers of the ellipse, which is already different from the circular packing case. For more general Laplace pressure and supposed that the radius of curvature is R, then we need to solve the following quartic equation based on $f(n) = R^2$:

$$0 = -a^2d^2 + 4a^2R^2 + 4a^3dt + (-4a^4 + c^2d^2 - 4a^2R^2)t^2 + (-4a^3d + 4ab^2d)t^3 + (4a^2c^2)t^4 \; . \tag{F.5}$$

Eq.F.5 can be solved analytically [Korn and Korn, 2000].

More general contact angle

Similar as the previous part, we only need to rotate the tangent line to take care of the influence of contact angle. Let us assume that the contact angle is θ and $\delta = \frac{\pi}{2} - \theta$. If the radius of the curvature is r and $f(n)$ is defined in Eq.F.2, then:

$$f(n) + r^2 - [(y_t - y_o) - \sqrt{r^2 - (x_o - x_t)^2}]^2 = 2\sqrt{f(n)}r\cos\delta \; . \tag{F.6}$$

Let $t = \cos n$, $c = \sqrt{a^2 - b^2}$, solving Eq.F.6:

$$r = \frac{(d - 2at)\sqrt{a^2 - c^2t^2}(-a\sqrt{1-t^2}\cos\delta - bt\sin\delta)}{2(b^2t^2 + (c^2t^2 - a^2)\cos^2\delta)} \; . \tag{F.7}$$

In Eq.F.7, if $\delta = 0$:

$$r = \frac{(d - 2at)\sqrt{a^2 - c^2t^2}(-a\sqrt{1-t^2})}{2(b^2t^2 + (c^2t^2 - a^2))} = \frac{(d-2at)}{2a}\frac{\sqrt{a^2 - c^2t^2}}{\sqrt{1-t^2}} = \sqrt{f(n)} \; . \tag{F.8}$$

So Eq.F.7 is consistent with the special case when the contact angle is 90°. We use golden-section search [Cormen et al., 2009] to find the minimum radius of the circle, which matches the point where the burst event happens.

G Mayer-Stowe-Princen method

In order to determine the entry pressure of the pore formed by three beads, we employ the MSP (Mayer-Stowe-Princen) method, which is based on the force balance between wetting and non-wetting interface. The main idea is assuming that the entry pressure is the same as in a cylindrical throat tangent to the solid phase at the narrowest cross section. The first step is to look at the cross section of these three spheres, where the cross section goes through the center of the spheres, because this part is assumed to be the narrowest cross section. And by applying the idea of energy balance, we are able to obtain the pressure to enter the pore. This method is fundamentally a two-dimensional method [Prodanović and Bryant, 2006] and it is closely related to 2D C&R model. Interestingly, Princen already realized that there will be ”one physically meaningless or mechanically unstable branch” when they solve the quadratic equation derived from the force balance [Princen, 1970]. Around 20 years later, the critical position is called burst event in Cieplak & Robbins' model [Cieplak and Robbins, 1990]. Even though in Cieplak & Robbins' model, it is purely based on geometric restriction, the result is exactly the same with the method of force or energy balance. So we directly employ Eq.C.17 in C & R-model for the final calculation of the pore entry pressure. Yuan et al. provided a way to calculate the pore entry pressure when the invading liquid is completely non-wetting ($\theta = 180°$) [Yuan et al., 2016]. But here we would like to apply the method to more general case with different contact angles and gap separations.

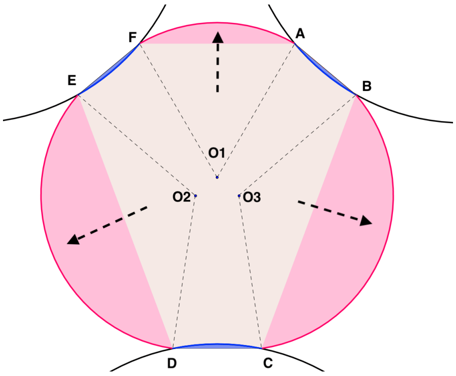

Figure G.1: Cross section of the three sphere. The arrows here indicate the meniscus advancing direction. And the red arcs represent the menisci between two phase, which satisfy the restriction from the contact angle.

A$_{\text{eff}}$ and P$_{\text{eff}}$

Under the capillary pressure P_c, the non-wetting fluid fills the cross-sectional area A_{eff} with the radius of curvature of r. For a reversible displacement of dx for a stable meniscus along a uniform tube, the energy balance gives rise to the following [Mason

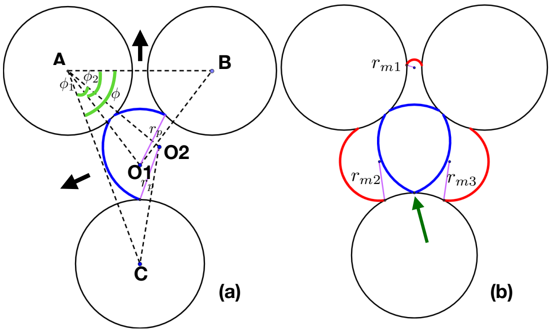

Figure G.2: (a) Illustration to find the maximum radius for the stable meniscus. In this case, the contact angle of the invading fluid with respect to the defending phase is set to be 160°. The arrows indicate the advancing direction for the blue menisci if we increase the pressure of the invading fluid. (b) Three red arcs indicate the time when Haines jump happens, which is calculated based on Eq.C.17. So $r_{min} = max(r_{m1}, r_{m2}, r_{m3})$. The green arrow indicates the time when two of the neighboring blue arcs overlap in one point and we find r_{max}.

and Morrow, 1987]:

$$P_c A_{eff} dx = \sigma P_{L_{nw}} + (\sigma_{SG} - \sigma_{SL}) P_{L_{ns}} dx \; . \tag{G.1}$$

As in Fig.G.1, the red arcs indicate the advancing menisci between the non-wetting phase and the wetting phase. $P_{L_{nw}}$ and $P_{L_{ns}}$ represent the perimeter between non-wetting and wetting phase, non-wetting and solid phase. So $P_{L_{nw}} = \overset{\frown}{AF} + \overset{\frown}{DE} + \overset{\frown}{BC}$ and $P_{L_{ns}} = \overset{\frown}{AB} + \overset{\frown}{CD} + \overset{\frown}{EF}$. With Young-Dupré equation [Young, 1805] ($\sigma_{SG} - \sigma_{SL} = \sigma \cos\theta$),

$$P_c A_{eff} dx = \sigma (P_{L_{nw}} + P_{L_{ns}} \cos\theta) dx \; . \tag{G.2}$$

With,

$$P_{eff} = P_{L_{nw}} + P_{L_{ns}} \cos\theta, \quad P_c = \frac{\sigma}{r} \; . \tag{G.3}$$

We have,

$$r = \frac{A_{eff}}{P_{eff}} \; . \tag{G.4}$$

As in Fig.G.1, the effect area is calculated:

$$\begin{aligned} A_{eff} &= S(\text{polygon}_{ABCDEF}) + S(\text{segment}_{red}) - S(\text{segment}_{blue}) \\ P_{eff} &= \overset{\frown}{AF} + \overset{\frown}{DE} + \overset{\frown}{BC} + (\overset{\frown}{AB} + \overset{\frown}{CD} + \overset{\frown}{EF}) \cos\theta \; . \end{aligned} \tag{G.5}$$

Here we use a more easy way to calculate the area compared with the method described in Yuan et al. [Yuan et al., 2016]. And with the help of eq.C.17, we are able to change the contact angle and gap separation in an easy way.

r_{min},r_{max}

We need to find the r_{min} and r_{max} as the boundary for iteration. For larger r, the neighboring menisci might overlap, which has no physical meaning. For small r, the meniscus might reach the critical value of Haines jump. For that purpose, we consider a more general case as in Fig.G.2 to illustrate how the capillary force and tension force for a pore throat is calculated. In Fig.G.2(a), we calculate the pressure when two blue arcs overlaps with each other. It is easy to write the following equation when two menisci exactly overlap on a specific point.

$$\begin{aligned} \cos\phi &= \frac{AB^2 + AC^2 - BC^2}{2AB \cdot AC}, \cos\phi_1 = \frac{AC^2 + AO_2^2 - CO_2^2}{2AC \cdot AO_2} \\ \cos\phi_2 &= \frac{AB^2 + AO_1^2 - O_1B^2}{2AB \cdot AO_1}, r_p \sin\theta = \sin(\frac{\phi_1 + \phi_2 - \phi}{2})AB \ . \end{aligned} \tag{G.6}$$

In Eq.G.6, $AO_1 = AO_2 = \sqrt{r_p^2 + r_1^2 - 2r_p r_1 \cos\theta}$,then it is easy to obtain r_p when the two menisci just overlap. In order to obtain the maximum radius, we need to consider the relationship between every two neighboring menisci. In Fig.G.2(b), we plot out the final position for blue arcs. As it is shown, the green arrow indicate two neighboring arcs just overlap and we can not increase r_p anymore. r_{min} is easy to get, which is the maximum value for burst radius of the three throats and we plot them in red in Fig.G.2(b). The radius of the meniscus should be within r_{min} and r_{max}. And it should meet the requirements from Eq.G.5 and Eq.G.4. By an iterative algorithm (dichotomy), we are able to calculate the pore entry pressure.

H Determination of the meniscus position in 3D

In the work of Gladkikh and Melnikov et al. [Gladkikh, 2005; Melnikov et al., 2015], the position of the center of the spherical meniscus is determined with similar approach. They firstly defined a point N on the plane formed by the center of three beads (A, B, C), and the center has equidistance from the centers of the three beads. Gladkikh and Melnikov et al. [Gladkikh, 2005; Melnikov et al., 2015] claim that the center of the meniscus O satisfies that ON is perpendicular to the plane A, B, C. However, we know that the distance between the O to the center of the sphere A, B, C is determined by the contact angle θ and the radius of the sphere as shown in Eq.C.18. As a result, the method in the work of Gladkikh and Melnikov et al. [Gladkikh, 2005; Melnikov et al., 2015] will become inappropriate when the bead radius and contact angle of three beads are different from each other. Based on C&R model in three dimension, we propose a more general approach to pinpoint the center of the meniscus.

For the convenience of calculation, we translate point A to the Cartesian coordinate origin, and rotate the plane formed by points A,B,C to the XY-plane and rotate the $\overrightarrow{AB}$ to the positive direction of the X-axis. To achieve that goal, we firstly translate the point A to the origin and obtain three points A′, B′ and C′. We have our first rotation matrix given the normal vector of plane ABC as $\overrightarrow{n} = \overrightarrow{AB} \times \overrightarrow{AC} = (n_x, n_y, n_z)$:

$$R_z(\theta_1) = \begin{bmatrix} \cos\theta_1 & -\sin\theta_1 & 0 \\ \sin\theta_1 & \cos\theta_1 & 0 \\ 0 & 0 & 1 \end{bmatrix}, \theta_1 = \begin{cases} -\mathrm{atan2}(n_y, n_x), & \text{if } n_x, n_y != 0. \\ 0 & \text{otherwise.} \end{cases} \tag{H.1}$$

With Eq.H.1, $\overrightarrow{n_1} = \overrightarrow{n} R_z(\theta_1) = (n_{1x}, 0, n_{1z})$. Then we obtain a second rotation matrix:

$$R_y(\theta_2) = \begin{bmatrix} \cos\theta_2 & 0 & \sin\theta_2 \\ 0 & 1 & 0 \\ -\sin\theta_2 & 0 & \cos\theta_2 \end{bmatrix}, \theta_2 = \begin{cases} -\mathrm{atan2}(n_{1z}, n_{1x}) + \frac{\pi}{2}, & \text{if } n_{1x}, n_{1y} != 0. \\ 0 & \text{otherwise.} \end{cases}$$

(H.2)

Suppose that we have A′(0,0,0) after translation of Point A, then:

$$\overrightarrow{A'B'} = R_y(\theta_2) R_z(\theta_1) \overrightarrow{AB}, \quad \overrightarrow{A'C'} = R_y(\theta_2) R_z(\theta_1) \overrightarrow{AC} \tag{H.3}$$

With Eq.H.3, we transform the point B and C to the XY-plane as B′ and C′. Further, we rotate the A′ and B′ to the X-axis and make sure that $\overrightarrow{A'B'}$ is pointing towards the positive X-axis.

$$\overrightarrow{A'B''} = R_z(\theta_3) \overrightarrow{A'B'}, \quad \overrightarrow{A'C''} = R_z(\theta_3) \overrightarrow{A'C'}, \quad \theta_3 = -\mathrm{atan2}(\overrightarrow{A'B'}_y, \overrightarrow{A'B'}_x) \tag{H.4}$$

To force $\overrightarrow{A'B''}$ in X-axis is very simple. As in Fig.H.1, we can directly use the 2D CR model equation. Because the circle from the intersection of the meniscus sphere and the XY-plane should also satisfy that the circle forms the same contact angle with the two blue circles in Fig.H.1. Based on Eq.B.2, B.3:

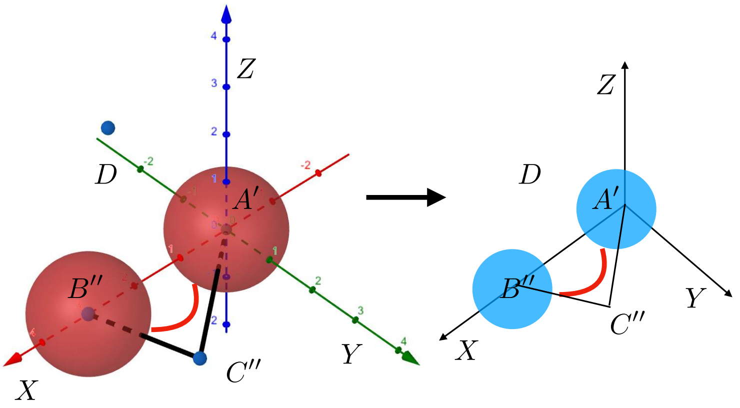

Figure H.1: Illustration to show how to consider the problem in XY-plane.

$$\begin{aligned} x_D &= \frac{r_1^2 - r_2^2 + d_{12}^2 - 2r_1 R\cos\theta_1 + 2r_2 R\cos\theta_2}{2d_{12}} \\ A'D &= \sqrt{r_1^2 + R^2 - 2r_1 R\cos\theta_1}, y_D = \pm\sqrt{A'D^2 - x_D^2}\,. \end{aligned} \tag{H.5}$$

If we suppose the center of the meniscus sphere is $R_o(x_R, y_R, z_R)$, the distance between R_o and $(x_D, 0, 0)$ should be $|y_D|$:

$$x_D = x_R, \quad y_R^2 + z_R^2 = y_D^2 \ . \tag{H.6}$$

And also:

$$\begin{aligned} C''R_o &= \sqrt{r_3^2 + R^2 - 2r_3R\cos\theta_3} \\ C''{R_o}^2 &= (x_{C''} - x_R)^2 + (y_{C''} - y_R)^2 + z_R^2 = (x_{C''} - x_D)^2 + y_{C''}^2 - 2y_{C''}y_R + y_R^2 + z_R^2 \\ &= (x_{C''} - x_D)^2 + y_{C''}^2 - 2y_{C''}y_R + y_D^2 \ . \end{aligned}$$

(H.7)

Combining Eq.H.5, H.6, H.7, we can directly obtain the position of the meniscus:

$$\begin{aligned} x_R &= x_D \\ y_R &= \frac{r_3^2 + R^2 - 2r_3R\cos\theta_3 - (x_D - x_{C''})^2 - y_{C''}^2 - y_D^2}{-2y_{C''}} .z_R &= -\sqrt{y_D^2 - y_R^2} \end{aligned} \tag{H.8}$$

After we obtain $R_o(x_R, y_R, z_R)$ via Eq.H.8, the coordinate of the meniscus center is determined:

$$R_o' = R_z(-\theta_1)R_y(-\theta_2)R_z(-\theta_3)R_o + \overrightarrow{OA} \ . \tag{H.9}$$

I Volume calculation

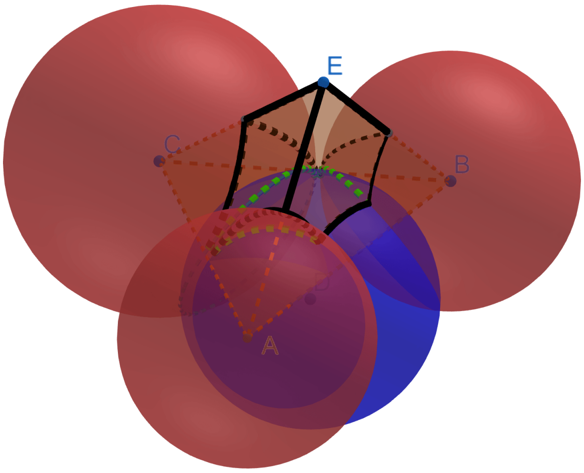

Figure I.1: Illustration of the spherical meniscus intersecting with three red beads.

Similarly as in the work of Motealleh et al. and Melnikov et al. [Melnikov et al., 2015; Motealleh et al., 2013], we divide the space based on Delaunay tessellation. In Fig.I.1, an individual pore is shown as an example. Assumed that the individual pore is separated by the meniscus, the next step is to calculate the volume occupied by the liquid (in blue in Fig.I.1) phase. We firstly calculate the volume formed by the black lines and green lines as shown in Fig.I.1, which is the void space inside the

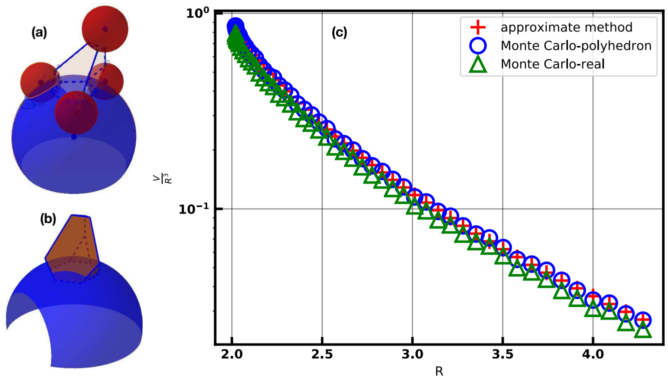

Figure I.2: An example for intersection volume calculation. The position of the spherical meniscus is determined with the method presented in Appendix H. (a) A tetrahedron pore; (b) A polyhedron pore space; (c) Comparison between three methods to evaluate the intersection volume between the invading liquid and the pore space. X-axis is the radius of the spherical meniscus and Y-axis indicates the dimensionless intersection volume normalized by R^3. In (c), the approximate method shows the the intersection volume calculated by the projection method as illustrated in Chapter 7. Monte Carlo-polyhedron indicates the evaluation of intersection volume is achieved by Monte-Carlo method. At the same time, Monte-Carlo-real shows the intersection volume between the spherical meniscus and the tetrahedron pore excluding the solid sphere region.

tetrahedron pore.

We set the coordinate origin at the center of the meniscus sphere. Assumed that $\mathbf{r} = (x, y, z)$ then the contribution for the volume from the region formed by the green circular arcs:

$$V_1 = \frac{1}{3}\int_V \nabla \cdot \mathbf{r} dV = \frac{1}{3}\int_S \mathbf{r} \cdot \mathbf{dS} = \frac{R}{3} S \ . \tag{I.1}$$

The area S formed by green circular arcs is easily calculated as shown in chapter 7. For the black circular arcs on the bead faces, supposed that the center of the bead sphere is $\mathbf{a}$:

$$V_2 = \frac{1}{3}\int_V \nabla \cdot \mathbf{F} dV = \frac{1}{3}\int_S \mathbf{F} \cdot \mathbf{dS} = \frac{1}{3}\int_S \mathbf{a} \cdot \mathbf{dS} + \frac{1}{3}\int_S \mathbf{r}' \cdot \mathbf{dS} \ . \tag{I.2}$$

Again, $\frac{1}{3}\int_S \mathbf{r}' \cdot \mathbf{dS}$ is calculated with the method proposed in chapter 7. For $\frac{1}{3}\int_S \mathbf{a} \cdot \mathbf{dS}$, we employ the parameterization method proposed as shown in Fig.J.1 of chapter 7.

Supposed $\mathbf{A} = (-y, x, 0)$:

$$\begin{aligned} \int_S \nabla \times \mathbf{A} \cdot d\mathbf{S} = 2\int_S \mathbf{k} \cdot d\mathbf{S} = \int_{\partial S} \mathbf{A} \cdot d\mathbf{l} \\ = \int_{\partial S} R^2(\cos\beta \sin\alpha + \cos\alpha \sin\beta \cos t) \sin\alpha dt \\ = R^2(t\cos\beta \sin\alpha + \cos\alpha \sin\beta \sin t)\Big|_{t_1}^{t_2} \ . \end{aligned} \tag{I.3}$$

According to Eq.I.3, a possible way to evaluate $\frac{1}{3}\int_S \mathbf{a} \cdot \mathbf{dS}$ is to rotate the sphere so that $\mathbf{a}$ is transformed to $\mathbf{k}$. Then we can further evaluate the integral based on Eq.I.3. In the implementation, we use the intersection volume between the polyhedron and sphere to approximate the volume occupied by the liquid in the pore. In the following, we test the intersection volume between the invading liquid and the void area formed in a tetrahedron. As shown in Fig.I.2, it is an example when the invading liquid has contact angle of 90°. As the radius gradually increases, we evaluate the intersection volume calculated by three methods. The result indicates that the approximate method already achieve a good match with respect to the real intersection volume. When the pore space is completely filled with invading liquid, the algorithm of Oosterom is applied [Van Oosterom and Strackee, 1983].

J Intersection volume

J.1 Derivation of Eq.7.24 and extension

In this part, we parameterize the circular arc on the sphere with radius of R as shown in Fig.J.1. We first determine the size of the circle and assume that the circle is perpendicular to the Z axis. So the initial coordinate of the circle is $r(t) = (R\sin\alpha\cos t, R\sin\alpha\sin t, R\cos\alpha)$, $t \in [0, 2\pi)$. With the help of the rotation matrix, we obtain the coordinate of the parameterized circle $\hat{r}(\hat{x}(t), \hat{y}(t), \hat{z}(t)) = R_z(\gamma)R_y(\beta)r(t)$:

$$\begin{aligned} \hat{x}(t) &= R(\cos\gamma\cos\beta\sin\alpha\cos t - \sin\gamma\sin\alpha\sin t + \cos\gamma\sin\beta\cos\alpha) \\ \hat{y}(t) &= R(\sin\gamma\cos\beta\sin\alpha\cos t + \cos\gamma\sin\alpha\sin t + \sin\gamma\sin\beta\cos\alpha) \\ \hat{z}(t) &= R(-\sin\beta\sin\alpha\cos t + \cos\beta\cos\alpha) \ . \end{aligned} \tag{J.1}$$

Direct integration

Supposed that the circular arc satifies, $t \in [t_1, t_2]$, then:

$$\begin{aligned}
A_s &= R\int_s \tan\frac{\theta}{2}\hat{\boldsymbol{\varphi}} d\hat{\mathbf{l}} = R\int_{t_1}^{t_2} \frac{\sin\theta}{1+\cos\theta}\frac{R^2}{R\sin\theta}(\cos\beta\sin\alpha + \cos\alpha\sin\beta\cos t)\sin\alpha dt \\
&= R^2\int_{t_1}^{t_2} \frac{1}{1+\cos\theta}(\cos\beta\sin\alpha + \cos\alpha\sin\beta\cos t)\sin\alpha dt \\
&= R^2\int_{t_1}^{t_2} \frac{R}{z+R}(\cos\beta\sin\alpha + \cos\alpha\sin\beta\cos t)\sin\alpha dt \\
&= R^2\int_{t_1}^{t_2} \frac{\cos\beta\sin^2\alpha + \sin\alpha\cos\alpha\sin\beta\cos t}{-\sin\beta\sin\alpha\cos t + \cos\beta\cos\alpha + 1}dt \\
&= R^2\int_{t_1}^{t_2} \frac{\cos\beta\sin^2\alpha}{(-\sin\beta\sin\alpha)\cos t + (\cos\beta\cos\alpha + 1)} + \frac{(\sin\alpha\cos\alpha\sin\beta)\cos t}{(-\sin\beta\sin\alpha)\cos t + (\cos\beta\cos\alpha + 1)}dt \\
&= R^2\Bigg(-2\cos\beta\sin^2\alpha\frac{\tanh^{-1}(\frac{(1+\cos(\alpha-\beta))\tan\frac{t}{2}}{i|\cos\alpha+\cos\beta|})}{i|\cos\alpha+\cos\beta|} + \frac{t\sin\alpha\cos\alpha\sin\beta}{-\sin\beta\sin\alpha} + \\
&\frac{2\cos\alpha(\cos\beta\cos\alpha+1)\tanh^{-1}(\frac{(1+\cos(\alpha-\beta))\tan\frac{t}{2}}{i|\cos\alpha+\cos\beta|})}{-i|\cos\alpha+\cos\beta|}\Bigg)\Bigg|_{t_1}^{t_2} \\
&= R^2\Bigg(-2(\cos\beta+\cos\alpha)\frac{\tanh^{-1}(\frac{(1+\cos(\alpha-\beta))\tan\frac{t}{2}}{i|\cos\alpha+\cos\beta|})}{i|\cos\alpha+\cos\beta|} - t\cos\alpha\Bigg)[\tanh^{-1} z = \frac{1}{i}\tan^{-1}(iz)] \\
&= R^2\Bigg(2\mathrm{sgn}(\cos\beta+\cos\alpha)\tan^{-1}(\frac{|\cos\frac{\alpha-\beta}{2}|\tan\frac{t}{2}}{|\cos\frac{\alpha+\beta}{2}|}) - t\cos\alpha\Bigg)\Bigg|_{t_1}^{t_2} \\
&= R^2\Bigg(2\tan^{-1}(\frac{\cos\frac{\alpha-\beta}{2}\tan\frac{t}{2}}{\cos\frac{\alpha+\beta}{2}}) - t\cos\alpha\Bigg)\Bigg|_{t_1}^{t_2}[\arctan(\frac{1}{x}) = \pm\frac{\pi}{2} - \arctan(x)] \\
&= R^2\Bigg(-2\arctan\left(\frac{\cos\frac{\alpha+\beta}{2}}{\cos\frac{\alpha-\beta}{2}}\cot\frac{t}{2}\right) - t\cos\alpha\Bigg)\Bigg|_{t_1}^{t_2}. \qquad \text{(J.2)}
\end{aligned}$$

Eq.J.2 is much more concise compared with some parameterization such as the work of Hayryan et al. and Vassetti et al. [Hayryan et al., 2005; Vassetti et al., 2020]. In addition, we can further improve the method. We rotate the circle around Z-axis with angle of τ firstly to make sure that the starting point of the integration is 0. With $\hat{r}(\hat{x}(t), \hat{y}(t), \hat{z}(t)) = R_z(\gamma)R_y(\beta)R_z(\tau)r(t)$, $\Delta t = t_2 - t_1$:

$$\begin{aligned}
A_s &= R\int_s \tan\frac{\theta}{2}\hat{\boldsymbol{\varphi}} d\hat{\mathbf{l}} \\
&= R^2\Bigg(-2\arctan\left(\frac{\cos\frac{\alpha+\beta}{2}}{\cos\frac{\alpha-\beta}{2}}\cot\frac{t+\tau}{2}\right) - t\cos\alpha\Bigg)\Bigg|_{0}^{\Delta t} \qquad \text{(J.3)} \\
&= R^2\Bigg(2\tan^{-1}(\frac{(\cos\alpha+\cos\beta)\tan(\frac{\Delta t}{2})}{1+\cos\alpha\cos\beta - \sin\alpha\sin\beta\cos\tau + \sin\alpha\sin\beta\sin\tau\tan\frac{\Delta t}{2}}) - \Delta t\cos\alpha\Bigg).
\end{aligned}$$

We consider a special case when $\alpha = \frac{\pi}{2}$:

$$A_s = R^2\Bigg(2\tan^{-1}(\frac{\cos\beta\tan(\frac{\Delta t}{2})}{1-\cos\tau\sin\beta + \tan(\frac{\Delta t}{2})\sin\beta\sin\tau})\Bigg). \qquad \text{(J.4)}$$

As a result, Eq.J.4 is the same as the Eq.(16) in the work of Asvestas et al. [Asvestas and Englund, 1994], which claimed to have the first formula expressed in terms of an elementary function to evaluate the solid angle formed by a planar figure. In fact, Eq.J.3 is more general compared with Eq.J.4.

In order to find some other vector fields, where the exact solutions for the line integral are easily obtained, we assume that this vector field is a function of $\hat{\boldsymbol{\varphi}}$ because we still want to keep the symmetry of the vector field.

$$\hat{\boldsymbol{A}} = G(r)F(\theta)\hat{\boldsymbol{\varphi}} + (0)\hat{\boldsymbol{r}} + (0)\hat{\boldsymbol{\theta}}$$

$$\nabla \times \hat{\boldsymbol{A}} = \frac{1}{r\sin\theta}(\frac{\partial}{\partial\theta}(A_\varphi \sin\theta) - \frac{\partial A_\theta}{\partial\varphi})\hat{\boldsymbol{r}} + (\frac{1}{r}\frac{\partial(rA_\theta)}{\partial r} - \frac{1}{r}\frac{\partial A_r}{\partial\theta})\hat{\boldsymbol{\varphi}} + (\frac{1}{r\sin\theta}\frac{\partial A_r}{\partial\varphi} - \frac{1}{r}\frac{\partial(rA_\varphi)}{\partial r})\hat{\boldsymbol{\theta}} \ . \tag{J.5}$$

Due to the fact that the surface normal of the sphere, i.e. $\hat{\boldsymbol{r}}$ is orthogonal to $\hat{\boldsymbol{\varphi}}$ and $\hat{\boldsymbol{\theta}}$. Then we need to make sure that:

$$\begin{aligned}(\nabla \times \hat{\boldsymbol{A}})_r &= \frac{1}{\sin\theta}(\frac{\partial}{\partial\theta}(A_\varphi \sin\theta) - \frac{\partial A_\theta}{\partial\varphi}) \\ &= \frac{1}{\sin\theta}(G(r)F^{'}(\theta)\sin\theta + G(r)F(\theta)\cos\theta) = \text{constant} \ .\end{aligned} \tag{J.6}$$

On the surface of the sphere, $G(R)$ is constant. That is to say that we need to solve the following ODE:

$$K = \frac{dF(\theta)}{d\theta} + F(\theta)\cot\theta \ . \tag{J.7}$$

We obtain:

$$\hat{\boldsymbol{A}} = F\hat{\boldsymbol{\varphi}} = \frac{k_1 + k_2\cos\theta}{\sin\theta}\hat{\boldsymbol{\varphi}}(k_2 \neq 0) \ . \tag{J.8}$$

A similar procedure to obtain Eq.J.8 is shown in the work of Webb et al. [Webb et al., 2010]. In Eq.J.8, there are two possibilities to remove the polar points. Because $\sin\theta = 0$, when $\theta = 0, \pi$, we need to take the limit:

$$\lim_{\theta -> \pi} \frac{k_1 + k_2\cos\theta}{\sin\theta} = \frac{k_1 - k_2}{0}, \quad \lim_{\theta -> 0} \frac{k_1 + k_2\cos\theta}{\sin\theta} = \frac{k_1 + k_2}{0} \ . \tag{J.9}$$

In Eq.J.9, we know that only when $k_1 + k_2 = 0$ or $k_1 - k_2 = 0$, we are able to remove the "north" or the "south" singularity point. On top of that, we create two new vector fields, which actually have been discovered long time ago to address the field generated by magnetic monopole [Wu and Yang, 1975]:

$$\hat{\boldsymbol{A_1}} = k_1\frac{1-\cos\theta}{\sin\theta}\hat{\boldsymbol{\varphi}} = k_1\tan\frac{\theta}{2}\hat{\boldsymbol{\varphi}}, \quad \hat{\boldsymbol{A_2}} = k_1\frac{1+\cos\theta}{\sin\theta}\hat{\boldsymbol{\varphi}} = k_1\cot\frac{\theta}{2}\hat{\boldsymbol{\varphi}} \ . \tag{J.10}$$

We notice that $\hat{\boldsymbol{A}} = \frac{k_1 + k_2\cos\theta}{\sin\theta}\hat{\boldsymbol{\varphi}} = k_2\cot\theta\hat{\boldsymbol{\varphi}} + \frac{k_1}{\sin\theta}\hat{\boldsymbol{\varphi}}$ and $\nabla \times (\frac{k_1}{\sin\theta}\hat{\boldsymbol{\varphi}}) = 0$. So pick up three typical vector fields and their corresponding calculated surface area is summarized as follows:

$$A_s = \begin{cases} R^2\Big(-2\arctan\Big(\frac{\cos\frac{\alpha+\beta}{2}}{\cos\frac{\alpha-\beta}{2}}\cot\frac{t}{2}\Big) - t\cos\alpha\Big)\Big|_{t_1}^{t_2}, & \text{if} \quad \mathbf{A} = \tan\frac{\theta}{2}\hat{\boldsymbol{\varphi}}. \quad \text{(J.11a)} \\ R^2\Big(2\arctan\Big(\frac{\sin\frac{\alpha+\beta}{2}}{\sin\frac{\alpha-\beta}{2}}\cot\frac{t}{2}\Big) - t\cos\alpha\Big)\Big|_{t_1}^{t_2}, & \text{if} \quad \mathbf{A} = -\cot\frac{\theta}{2}\hat{\boldsymbol{\varphi}}. \quad \text{(J.11b)} \\ R^2\Bigg(\arctan(\frac{\sin\beta\sin t}{\cos\beta\sin\alpha + \cos\alpha\sin\beta\cos t}) - t\cos\alpha\Bigg)\Bigg|_{t_1}^{t_2}, & \text{if} \quad \mathbf{A} = -\cot\theta\hat{\boldsymbol{\varphi}}. \quad \text{(J.11c)} \end{cases}$$

When $\mathbf{A} = -\cot\frac{\theta}{2}\hat{\boldsymbol{\varphi}}$, the process to calculate the surface area is similar to Eq.J.2. To achieve the surface area calculation when $\mathbf{A} = -\cot\theta\hat{\boldsymbol{\varphi}}$ takes more efforts. Firstly, it is easy to know:

$$\begin{aligned}\frac{R^2}{x^2+y^2} &= \frac{1}{2}\left(\frac{1}{\sin\alpha\sin\beta\cos t+1-\cos\alpha\cos\beta}+\frac{1}{-\sin\alpha\sin\beta\cos t+1+\cos\alpha\cos\beta}\right)\\ \frac{z(-y\mathbf{i}+x\mathbf{j})d\hat{\mathbf{l}}}{R^3} &= (-\sin^2\beta\sin^2\alpha\cos\alpha)\cos^2 t+(\cos\beta\sin\beta\sin\alpha\cos 2\alpha)\cos t+\\ &\quad \cos\alpha\cos^2\beta\sin^2\alpha\end{aligned} \tag{J.12}$$

So,

$$\begin{aligned}A_s &= R\int_s -\cot\theta\hat{\boldsymbol{\varphi}}d\hat{\mathbf{l}} = R\int_s -\frac{z(-y\mathbf{i}+x\mathbf{j})}{x^2+y^2}d\hat{\mathbf{l}}\\ &= \frac{-R^2}{2}\int_s(k_1\cos^2 t+k_2\cos t+k_3)\left(\frac{1}{k_4\cos t+k_5}+\frac{1}{-k_4\cos t+2-k_5}\right)dt\\ &= \frac{-R^2}{2}\frac{T_1-T_2-2k_1t}{k_4^2}+K\ .\\ \text{where, } k_1 &= -\sin^2\beta\sin^2\alpha\cos\alpha, \quad k_2=\cos\beta\sin\beta\sin\alpha\cos(2\alpha)\\ k_3 &= \cos\alpha\cos^2\beta\sin^2\alpha, \quad k_4=\sin\alpha\sin\beta, \quad k_5 = 1-\cos\alpha\cos\beta\\ k_4^2-k_5^2 &= -(\cos\alpha-\cos\beta)^2, \quad k_4^2-(k_5-2)^2=-(\cos\alpha+\cos\beta)^2\\ T_1 &= \frac{2\sin^2\alpha\sin^2\beta(\cos\alpha-\cos\beta)\tanh^{-1}\frac{(1-\cos(\alpha-\beta))\tan(\frac{t}{2})}{i|\cos\alpha-\cos\beta|}}{i|\cos\alpha-\cos\beta|}\\ T_2 &= \frac{-2\sin^2\alpha\sin^2\beta(\cos\beta+\cos\alpha)\tanh^{-1}\frac{(\cos(\alpha-\beta)+1)\tan(\frac{t}{2})}{i|\cos\alpha+\cos\beta|}}{i|\cos\alpha+\cos\beta|}\ .\end{aligned}$$

Then,

$$\begin{aligned}A_s &= -R^2\left(\frac{(\cos\alpha-\cos\beta)\tanh^{-1}\frac{(1-\cos(\alpha-\beta))\tan(\frac{t}{2})}{i|\cos\alpha-\cos\beta|}}{i|\cos\alpha-\cos\beta|}+\right.\\ &\left.\frac{(\cos\beta+\cos\alpha)\tanh^{-1}\frac{(\cos(\alpha-\beta)+1)\tan(\frac{t}{2})}{i|\cos\alpha+\cos\beta|}}{i|\cos\alpha+\cos\beta|}+\cos\alpha t\right)+K \quad [\tanh^{-1}z = i\tan^{-1}(-iz)]\\ &= R^2\left(\operatorname{sgn}(\cos\alpha-\cos\beta)\tan^{-1}\frac{|\sin\frac{\alpha-\beta}{2}|\tan(\frac{t}{2})}{|\sin\frac{\alpha+\beta}{2}|}+\right.\\ &\left.\operatorname{sgn}(\cos\beta+\cos\alpha)\tan^{-1}\frac{|\cos\frac{\alpha-\beta}{2}|\tan(\frac{t}{2})}{|\cos\frac{\alpha+\beta}{2}|}-t\cos\alpha\right)+K\ .\end{aligned} \tag{J.13}$$

Because $\tan^{-1}(-x) = -\tan^{-1}(x)$, so we can put the sign function into $\tan^{-1}(x)$. Firstly,

$$\begin{aligned}U_1 &= \operatorname{sgn}(\cos\alpha-\cos\beta)\frac{|\sin\frac{\alpha-\beta}{2}|}{|\sin\frac{\alpha+\beta}{2}|} = \operatorname{sgn}(\sin\frac{\alpha+\beta}{2}\sin\frac{\beta-\alpha}{2})\frac{|\sin\frac{\alpha-\beta}{2}|}{|\sin\frac{\alpha+\beta}{2}|} = \frac{\sin\frac{\beta-\alpha}{2}}{\sin\frac{\alpha+\beta}{2}}\\ U_2 &= \operatorname{sgn}(\cos\beta+\cos\alpha)\frac{|\cos\frac{\alpha-\beta}{2}|}{|\cos\frac{\alpha+\beta}{2}|} = \operatorname{sgn}(\cos\frac{\beta+\alpha}{2}\cos\frac{\beta-\alpha}{2})\frac{|\cos\frac{\alpha-\beta}{2}|}{|\cos\frac{\alpha+\beta}{2}|} = \frac{\cos\frac{\beta-\alpha}{2}}{\cos\frac{\alpha+\beta}{2}}\\ U_1+U_2 &= \frac{2\sin\beta}{\sin(\alpha+\beta)}, \quad U_1U_2 = \frac{\sin(\beta-\alpha)}{\sin(\alpha+\beta)}\end{aligned} \tag{J.14}$$

$$\begin{aligned} A_s &= R^2\left(\operatorname{sgn}(\cos\beta-\cos\alpha)\tan^{-1}\frac{|\sin\frac{\alpha-\beta}{2}|\tan(\frac{t}{2})}{|\sin\frac{\alpha+\beta}{2}|}+\right.\\ &\left.\operatorname{sgn}(\cos\beta+\cos\alpha)\tan^{-1}\frac{|\cos\frac{\alpha-\beta}{2}|\tan(\frac{t}{2})}{|\cos\frac{\alpha+\beta}{2}|}-t\cos\alpha\right)\Bigg|_{t1}^{t2}\\ &= R^2\left(\tan^{-1}\frac{(U_1+U_2)\tan\frac{t}{2}}{1-U_1U_2\tan^2\frac{t}{2}}-t\cos\alpha\right)\Bigg|_{t1}^{t2}\left[\tan^{-1}x+\tan^{-1}y=\tan^{-1}\frac{x+y}{1-xy}\right]\\ &= R^2\left(\tan^{-1}\frac{2\sin\beta\tan\frac{t}{2}}{\sin(\alpha+\beta)+\sin(\alpha-\beta)\tan^2\frac{t}{2}}-t\cos\alpha\right)\Bigg|_{t1}^{t2}\left[\tan\frac{t}{2}=\frac{\sin t}{1+\cos t}=\pm\sqrt{\frac{1-\cos t}{1+\cos t}}\right] \quad (J.15)\\ &= R^2\left(\tan^{-1}\frac{2\sin\beta\sin t}{\sin(\alpha+\beta)(1+\cos t)+\sin(\alpha-\beta)(1-\cos t)}-t\cos\alpha\right)\Bigg|_{t1}^{t2}\\ &= R^2\left(\arctan\left(\frac{\sin\beta\sin t}{\cos\beta\sin\alpha+\cos\alpha\sin\beta\cos t}\right)-t\cos\alpha\right)\Bigg|_{t1}^{t2}. \end{aligned}$$

In addition, in the process of deriving Eq.J.15 we know that Eq.J.11c is the average between Eq.J.11b and Eq.J.11a because $-\cot\theta = \frac{1}{2}(-\cot\frac{\theta}{2}+\tan\frac{\theta}{2})$. This relationship is more obvious in the following description of geometrical interpretation.
Next step, we deterimine the magintude of singular points in Eq.7.1. When $\mathbf{A} = \tan\frac{\theta}{2}\hat{\boldsymbol{\varphi}}$, we use a circle to converge to a point, within this circle, θ is constant.

$$A_{pole} = \lim_{\theta->\pi} R\int_s \tan\frac{\theta}{2}\hat{\boldsymbol{\varphi}}d\hat{\mathbf{l}} = \lim_{\theta->\pi}(1-\cos\theta)R^2\int_0^{2\pi}d\varphi = 4\pi R^2\ . \quad (J.16)$$

The same magnitude of $4\pi R^2$ goes with $\mathbf{A} = -\cot\frac{\theta}{2}\hat{\boldsymbol{\varphi}}$ at $\theta = 0$. When $\mathbf{A} = -\cot\theta\hat{\boldsymbol{\varphi}}$, the magnitude of the singular points is $2\pi R^2$ and it has two singular points at $\theta = 0, \pi$. Additional singular points bring numerical instability when the edge of the polyhedron is getting close to these points. In this work, we only focus on the case when $\mathbf{A} = \tan\frac{\theta}{2}\hat{\boldsymbol{\varphi}}$ because it only contains one singular point. In addition, it is shown in the work of Wu et al. [Wu and Yang, 1975] that there does not exist a singularity-free vector field. So we need to accept at least one singular point if there is only one vector field.

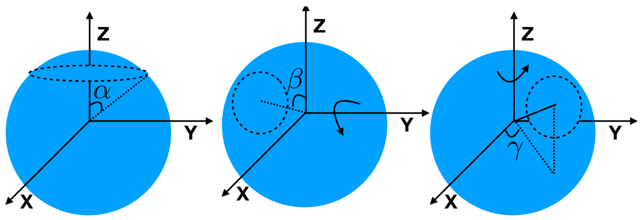

Figure J.1: Parameterisation of the circle on the sphere. We first use α to determine the size of the circle and assume that the circle is perpendicular to the Z axis. Then we rotate it with respect to the Y axis with β. After that we continue to rotate the circle around Z axis with γ.

Geometrical interpretation

Due to the complexity in obtaining the antiderivative of Eq.J.8, here we propose a geometrical way to evaluate the line integral. When the area is not including both the north and south poles ($\theta \neq 0, \pi$):

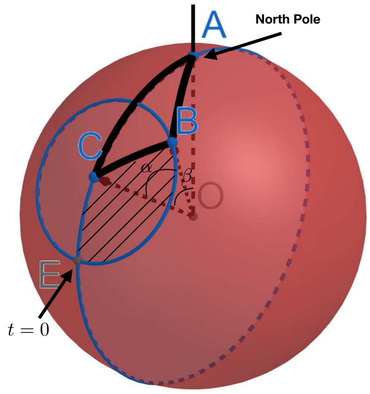

Figure J.2: Illustration of deriving Eq.J.18 with spherical geometry.

$$\int\int_s \nabla \times \frac{k_1 + k_2 \cos\theta}{\sin\theta} \hat{\boldsymbol{\varphi}} \cdot \mathbf{r} dS = -\frac{k_2 A_s}{R} \ . \tag{J.17}$$

We know that the surface area is calculated with line integral:

$$A_s = -\frac{R}{k_2} \int_s \frac{k_1 + k_2 \cos\theta}{\sin\theta} \hat{\boldsymbol{\varphi}} d\hat{\mathbf{l}} \ . \tag{J.18}$$

For example in Fig.J.2, after parameterizing the circular arc, we would like to evaluate the line integral over circular arc $\overset{\frown}{EB}$. We add circular arcs $\overset{\frown}{BA}$,$\overset{\frown}{AE}$ from the north pole, which go through the great circle, due to $\hat{\boldsymbol{\varphi}} \perp d\hat{\mathbf{l}}$:

$$A_{E\overset{\frown}{B}AE} = -\frac{R}{k_2} \int_{\overset{\frown}{EB} + \overset{\frown}{BA} + \overset{\frown}{AE}} f(\theta) \hat{\boldsymbol{\varphi}} d\hat{\mathbf{l}} = -\frac{R}{k_2} \int_{\overset{\frown}{EB}} f(\theta) \hat{\boldsymbol{\varphi}} d\hat{\mathbf{l}} \ . \tag{J.19}$$

That means that the line integral of the circular arc $\overset{\frown}{EB}$ is equal to the area formed by the area (A_1) of a spherical triangle ABC plus the area (A_2) of the shaded region in Fig.J.2. So if we can calculate the area, we are able to directly evaluate the Eq.J.18. The shaded area is calculated as:

$$A_2 = \frac{t}{2\pi} 2\pi R^2 (1 - \cos\alpha) = R^2 t (1 - \cos\alpha) \ . \tag{J.20}$$

In spherical triangle ABC, there is a relation according to Napier's analogies [Todhunter, 1863]:

$$\tan\frac{A+B}{2} = \frac{\cos\frac{a-b}{2}}{\cos\frac{a+b}{2}} \cot\frac{C}{2}, \tan\frac{A-B}{2} = \frac{\sin\frac{a-b}{2}}{\sin\frac{a+b}{2}} \cot\frac{C}{2} \ . \tag{J.21}$$

Because $t = \pi - C$, $\overset{\frown}{BC} = \alpha R$ and $\overset{\frown}{AB} = \beta R$, without loss of generality when $R = 1$ because we are calculating angles, so:

$$
\begin{aligned}
A + B &= 2\arctan(\frac{\cos\frac{\alpha-\beta}{2}}{\cos\frac{\alpha+\beta}{2}}\tan\frac{t}{2}), A - B = 2\arctan(\frac{\sin\frac{\alpha-\beta}{2}}{\sin\frac{\alpha+\beta}{2}}\tan\frac{t}{2}) \\
A &= \arctan(\frac{\cos\frac{\alpha-\beta}{2}}{\cos\frac{\alpha+\beta}{2}}\tan\frac{t}{2}) + \arctan(\frac{\sin\frac{\alpha-\beta}{2}}{\sin\frac{\alpha+\beta}{2}}\tan\frac{t}{2}) \\
&= \arctan(\frac{\sin\alpha\sin t}{\sin\beta\cos\alpha + \sin\alpha\cos\beta\cos t}) \pm \pi \\
B &= \arctan(\frac{\cos\frac{\alpha-\beta}{2}}{\cos\frac{\alpha+\beta}{2}}\tan\frac{t}{2}) - \arctan(\frac{\sin\frac{\alpha-\beta}{2}}{\sin\frac{\alpha+\beta}{2}}\tan\frac{t}{2}) \\
&= \arctan(\frac{\sin\beta\sin t}{\cos\beta\sin\alpha + \cos\alpha\sin\beta\cos t}) \pm \pi \ .
\end{aligned}
\tag{J.22}
$$

In J.22, A and B are also possible to be calculated directly based on the two position of neighboring circular arcs since the position of the circular arcs are known, which in the end will be very similar to the reference point method. However, in the reference method, we can choose a random point in the space and here the choice of the reference point is restricted to the pole on the sphere. With the help of equation for the spherical excess [Todhunter, 1863],

$$
\begin{aligned}
A_1 + A_2 &= R^2(A + B + (\pi - t) - \pi) + R^2 t - R^2 t\cos\alpha = R^2((A + B) - t\cos\alpha) \\
&= R^2(2\arctan(\frac{\cos\frac{a-b}{2}}{\cos\frac{a+b}{2}}\cot\frac{\pi - t}{2}) - t\cos\alpha) \\
&= R^2(2\arctan(\frac{\cos\frac{\alpha-\beta}{2}}{\cos\frac{\alpha+\beta}{2}}\tan\frac{t}{2}) - t\cos\alpha) \pm \frac{\pi}{2}
\end{aligned}
$$

(J.23)

It is worth noting that, in obtaining Eq.J.23, we do not specify the exact form of $f(\theta)\hat{\boldsymbol{\varphi}}$. This indicates that if there is no singular point within the integral region, Eq.J.23 is valid for any other expression of $f(\theta)\hat{\boldsymbol{\varphi}}$.

So if the north pole is not a singular point, then Eq.J.23 describes the antiderivative of the line integral in Eq.J.18. However, if the north pole is a singular point but the integrated region does not include other singular points, we need to determine the magnitude as shown in Eq.J.16:

$$
\begin{aligned}
A_{pn} &= \lim_{\theta->0} -\frac{R}{k_2}\int_s \frac{k_1 + k_2\cos\theta}{\sin\theta}\hat{\boldsymbol{\varphi}}d\hat{\mathbf{l}} = \lim_{\theta->0} -\frac{R}{k_2}\int_0^{2\pi}\frac{k_1 + k_2\cos\theta}{\sin\theta}R\sin\theta d\varphi \\
&= \lim_{\theta->0} -\frac{k_1 + k_2\cos\theta}{k_2}R^2\int_0^{2\pi} d\varphi = (-\frac{k_1}{k_2} - 1)2\pi R^2 \ .
\end{aligned}
\tag{J.24}
$$

Eq.J.24 indicates the total magnitude over the north polar point. But the vertex of the spherical triangle ABC only occupies a part of the total magnitude, which is proportional to the angle A in Eq.J.22. As a result,

$$\begin{aligned} A_s &= -\frac{R}{k_2}\int_s \frac{k_1+k_2\cos\theta}{\sin\theta}\hat{\boldsymbol{\varphi}} d\hat{\mathbf{l}} = A_1 + A_2 + \frac{A_{pn}}{2\pi}A \\ &= R^2(2\arctan(\frac{\cos\frac{\alpha-\beta}{2}}{\cos\frac{\alpha+\beta}{2}}\tan\frac{t}{2}) - t\cos\alpha - \frac{k_1+k_2}{k_2}A)\Big|_{t_1}^{t_2} \\ &= R^2\Big((2-\frac{k_1+k_2}{k_2})\arctan(\frac{\cos\frac{\alpha-\beta}{2}}{\cos\frac{\alpha+\beta}{2}}\tan\frac{t}{2}) - t\cos\alpha - (\frac{k_1+k_2}{k_2})\arctan(\frac{\sin\frac{\alpha-\beta}{2}}{\sin\frac{\alpha+\beta}{2}}\tan\frac{t}{2})\Big)\Big|_{t_1}^{t_2} . \end{aligned}$$
(J.25)

It is easy to check that Eq.J.11 is only special case for Eq.J.25. Changing the form of Eq.J.25:

$$\begin{aligned} A_s &= R^2(\arctan(\frac{\cos\frac{\alpha-\beta}{2}}{\cos\frac{\alpha+\beta}{2}}\tan\frac{t}{2}) - \arctan(\frac{\sin\frac{\alpha-\beta}{2}}{\sin\frac{\alpha+\beta}{2}}\tan\frac{t}{2}) - t\cos\alpha - \frac{k_1}{k_2}A)\Big|_{t_1}^{t_2} \\ &= R^2(-\frac{k_1}{k_2}A + B - t\cos\alpha)\Big|_{t_1}^{t_2} . \end{aligned} \tag{J.26}$$

In Eq.J.26, A, B are in Eq.J.22. In addition, when we change k_1, k_2 ($k_2 \neq 0$), A_s does not change if the closed loop does not include any pole, but the polar magnitude is varying all the time. And it is easy to get the polar magnitude at the south pole:

$$A_{ps} = \lim_{\theta->\pi}\frac{R}{k_2}\int_s \frac{k_1+k_2\cos\theta}{\sin\theta}\hat{\boldsymbol{\varphi}} d\hat{\mathbf{l}} = (\frac{k_1}{k_2}-1)2\pi R^2 . \tag{J.27}$$

As we mention in Eq.7.24, there is a possibility when a edge of the polyhedron is intersecting with the sphere. Then the contribution from the pole is only a part of the total magnitude at the pole. One solution to circumvent that is to rotate the sphere. With Eq.J.26, we investigate whether we are able to determine the contribution from the pole without rotating the sphere. Firstly, supposed that $\frac{k_1}{k_2} = l$, we are able to obtain a set of linear equation based that:

$$-m_1A_{pn} - m_2A_{ps} + \sum A_s = A_r . \tag{J.28}$$

where, A_s is calculated by Eq.J.26 for all circular arcs and A_r is the real surface area enclosed by the circular arcs on the sphere. $\sum A_s = R^2\sum(-lA + B - t\cos\alpha)$ represents the evaluation of Eq.J.26 over all the circular arcs.

We then choose three different $l_i, i = 1,2,3$, and the ratio of the magnitude contribution from the north pole and south pole is $m_1, m_2 \in [0,1]$, $\sum A = C$ and $\sum B - t\cos\alpha = D$, so

$$\begin{aligned} m_1(l_1+1)2\pi R^2 + m_2(-l_1+1)2\pi R^2 - A_r &= R^2(l_1C - D) \\ m_1(l_2+1)2\pi R^2 + m_2(-l_2+1)2\pi R^2 - A_r &= R^2(l_2C - D) \\ m_1(l_3+1)2\pi R^2 + m_2(-l_3+1)2\pi R^2 - A_r &= R^2(l_2C - D) . \end{aligned} \tag{J.29}$$

Solving Eq.J.29, we obtain:

$$\begin{bmatrix} m_1 \\ m_2 \\ A_r \end{bmatrix} = \begin{bmatrix} \frac{C-D}{4\pi} \\ \frac{-C-D}{4\pi} \\ 0 \end{bmatrix} + \begin{bmatrix} \frac{1}{4\pi R^2} \\ \frac{1}{4\pi R^2} \\ 1 \end{bmatrix} c \ . \tag{J.30}$$

where $c \in [0, 4\pi R^2]$.

Eq.J.30 reminds us that even though we are able to vary the magnitude of the pole, but it is not possible to determine the m_1 and m_2 without taking care of how the polyhedron intersects with the pole. In Eq.J.26, Eq.J.24, Eq.J.28 and Eq. J.27, we notice that the choice of $\frac{k_1}{k_2}$ should not influence the result when the circular arcs on the sphere surface are not crossing the polar points. Due to:

$$\sum R^2(-\frac{k_1}{k_2}A + B - t\cos\alpha) + m_1(\frac{k_1}{k_2} + 1)2\pi R^2 + m_2(-\frac{k_1}{k_2} + 1)2\pi R^2 = A_r \ . \tag{J.31}$$

As a result,

$$-\frac{\sum A}{2\pi} + m_1 - m_2 = 0 \ . \tag{J.32}$$

Eq.J.32 is in accordance with Eq.J.30. In Eq.J.32, $\frac{\sum A}{2\pi}$ is very close to the definition of "winding number" of a smooth closed planar curve [Do Carmo, 2016], because $\sum A$ is rotated angle over the north pole as in Fig.J.2:

$$\sum A = \int_s \frac{1}{R\sin\theta}\hat{\boldsymbol{\varphi}} d\hat{\mathbf{l}} = \int_s \frac{1}{R\sin\theta}\hat{\boldsymbol{\varphi}}(dr\hat{\boldsymbol{r}} + Rd\theta\hat{\boldsymbol{\theta}} + R\sin\theta d\varphi\hat{\boldsymbol{\varphi}}) = \sum \Delta\varphi \ . \tag{J.33}$$

In addition,

$$\int_s \frac{\cos\theta}{\sin\theta}\hat{\boldsymbol{\varphi}} d\hat{\mathbf{l}} = \int_s R\cos\theta d\varphi \ . \tag{J.34}$$

By employing Lambert cylindrical equal-area projection [Snyder, 1982], we can have a better geometric interpretation of Eq.J.33 and Eq.J.34. As in Fig.J.3, when we map the simple closed loop to the surrounding cylinder and flatten the side surface of the cylinder, we immediately obtain geometrical meaning of Eq.J.33 and Eq.J.34. Each point $(R\sin\theta\cos\varphi, R\sin\theta\sin\varphi, R\cos\theta)$ on the sphere is mapped to the cylindrical surface point $(R\cos\varphi, R\sin\varphi, R\cos\theta)$. The metric of the spherical surface is $g_{ij} = \begin{pmatrix} R^2 & 0 \\ 0 & R^2\sin^2\theta \end{pmatrix}$ and the metric of the cylindrical surface is $g_{ij} = \begin{pmatrix} R^2\sin^2\theta & 0 \\ 0 & R^2 \end{pmatrix}$. In addition, we know the area is calculated:

$$\int\int_D |\overrightarrow{r_\varphi} \times \overrightarrow{r_\theta}| d\varphi d\theta = \int\int_D \sqrt{det(g_{ij})} d\varphi d\theta \ . \tag{J.35}$$

As a result, the mapping is area-preserving according to Eq.J.35. And Eq.J.34 is merely calculating the area formed by the contour on the cylindrical surface. If the loop cross the north or south pole, there should be an extra segment to complete a close shape as shown in Fig.J.3(b,c). And the length of the segment is equal to $R\Delta\varphi$. With Eq.J.32, if the closed loop is not intersecting with the pole,
$(m_1, m_2) = (0, 1), (1, 0), (0, 0), (1, 1)$.

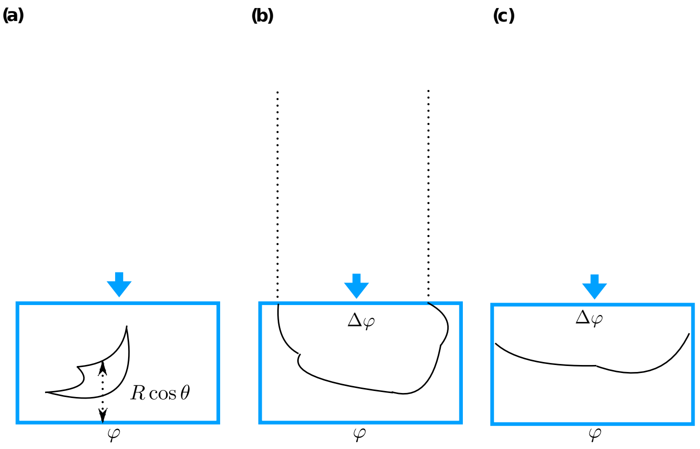

Figure J.3: Illustration of Lambert cylindrical equal-area projection for different cases. (a) the simple closed loop does not cover or cross the north or south pole; (b) the simple closed loop crosses the north pole; (c) the simple closed loop covers the north pole.

- $(m_1, m_2) = (0,1), (1,0)$, $\frac{\sum A}{2\pi} = \mp 1$
- $(m_1, m_2) = (1,1), (0,0)$, $\frac{\sum A}{2\pi} = 0$.

Even though $\frac{\sum A}{2\pi} = 0$, we can not see the direct difference between $(m_1, m_2) = (1,1), (0,0)$. But,

$$\begin{aligned} &\sum R^2(B - t\cos\alpha) = A_r - 4\pi R^2 \leq 0, (m_1, m_2) = (1,1) \\ &\sum R^2(B - t\cos\alpha) = A_r \geq 0, (m_1, m_2) = (0,0)\ . \end{aligned} \tag{J.36}$$

With Eq.J.36, we are still able to evaluate m_1, m_2 with the sign of $\sum R^2(B - t\cos\alpha)$. When the closed loop is intersecting with the north pole or south pole, there is no direct evaluation for m_1, m_2.

According to Eq.J.5, there is another possibility to construct the vector field ($A_\phi = 0$), where the symmetric property of the vector field is not held:

$$\hat{\boldsymbol{A}} = \varphi \sin\theta \hat{\boldsymbol{\theta}}\ . \tag{J.37}$$

As a result,

$$\begin{aligned} A_s &= R\int\int_s \nabla \times \mathbf{A_m} \cdot \mathbf{r} dS = R\int_{\partial s} \varphi \sin\theta \hat{\boldsymbol{\theta}} d\mathbf{l} \\ &= R^2 \int_{\partial s} \varphi \sin\theta d\theta = -R\int_{\partial s} \varphi d(R\cos\theta) = R^2\Big(\sum -\varphi\cos\theta\Big|_{t_1}^{t_2} + \int_s \cos\theta d\varphi\Big)\ . \end{aligned}$$

(J.38)

In Eq.J.38, if the simple closed loop made of the circular arcs is not crossing the poles, $\sum -\varphi\cos\theta\Big|_{t_1}^{t_2} = 0$. And when the contour crosses the poles, φ for the north pole and south pole is not defined. $\sum -\varphi \cos\theta \Big|_{t_1}^{t_2}$ is not continuous at the south and north pole and we need to compensate the corresponding $\sum \Delta\varphi$. Even though Eq.J.37 and Eq.J.8 represent different vector fields, the process to calculate the anti-derivative is not changed. With Fig.J.3, the similarity is more clear because $\int_{\partial s} \varphi d(\cos\theta)$ and $\int_{\partial s} \cos\theta d\varphi$ only change the axis for the integration if we focus on the flattened cylindrical map.

Determination of the zero point

In order to improve the efficiency and accuracy of the computation, we do not explicitly calculate the angle α, β in Eq.J.1. And γ is not in need as shown in Eq.J.25. However, we still need to evaluate the point where $t = 0$ after rotating the circle. Assuming that the coordinate of the point when $t = 0$ is (x_0, y_0, z_0) as shown in Fig.J.4 (a). The center of the sphere is (x_1, y_1, z_1) and the radius is R. The center of the circle after rotation is (x_2, y_2, z_2) with radius of r. We can obtain the following relationship when $R \neq r$:

$$\begin{cases} (x_0 - x_1)^2 + (y_0 - y_1)^2 + (z_0 - z_1)^2 = R^2 \\ (x_0 - x_2)^2 + (y_0 - y_2)^2 + (z_0 - z_2)^2 = r^2 \ . \end{cases} \tag{J.39}$$

Supposed that the circle on the sphere is intersecting with a latitude θ, we obtain by solving Eq.J.39:

$$\begin{gathered} z_0 = z_1 + R\cos\theta, \hat{K} = \frac{1}{2}(R^2 - r^2 - (2z_0 - z_1 - z_2)(z_2 - z_1) + y_2^2 - y_1^2 + x_2^2 - x_1^2) \\ x_0 = \frac{-b_v \pm \sqrt{b_v^2 - 4a_v c_v}}{2a_v} \quad , y_0 = \begin{cases} \frac{\hat{K} - x_0(x_2 - x_1)}{y_2 - y_1} & y_1 \neq y_2 \\ y_1 \pm \sqrt{R^2 - (x_0 - x_1)^2 - (z_0 - z_1)^2} & \text{otherwise} \ . \end{cases} \end{gathered} \tag{J.40}$$

Where, $a_v = (x_1 - x_2)^2 + (y_1 - y_2)^2$, $b_v = 2\hat{K}(x_1 - x_2) - 2(y_1 - y_2)(x_2 y_1 - x_1 y_2)$ and $c_v = (y_1 y_2 - y_1^2 - \hat{K})^2 + ((z_0 - z_1)^2 - R^2 + x_1^2)(y_2 - y_1)^2$.
For the zero point when $t = 0$, it is easy to obtain:

$$\begin{gathered} z_0 = z_1 + R\cos(\alpha + \beta), x_0 = \frac{(x_2 - x_1)\hat{K} + (y_1 - y_2)(x_2 y_1 - x_1 y_2)}{(x_1 - x_2)^2 + (y_1 - y_2)^2} \\ y_0 = \begin{cases} \frac{\hat{K} - x_0(x_2 - x_1)}{y_2 - y_1} & y_1 \neq y_2 \\ y_1 & \text{otherwise} \ . \end{cases} \end{gathered} \tag{J.41}$$

However, when $R = r$ as shown in Fig.J.4 (b), Eq.J.39 is not enough. Assumed that the unit normal vector of the plane where the circle exists is (x_n, y_n, z_n). As a result:

$$\begin{cases} (x_0 - x_1)^2 + (y_0 - y_1)^2 + (z_0 - z_1)^2 = R^2 \\ (x_0 - x_1)x_n + (y_0 - y_1)y_n + (z_0 - z_1)z_n = 0 \ . \end{cases} \tag{J.42}$$

Solving Eq.J.42:

$$z_0 = z_1 + R\cos\theta, \quad \hat{K}_1 = (z_1 - z_0)z_n + x_1 x_n$$

$$x_0 = \frac{-b_w \pm \sqrt{b_w^2 - 4a_w c_w}}{2a_w}, y_0 = \begin{cases} \frac{(z_1-z_0)z_n+(x_1-x_0)x_n}{y_n} + y_1 & y_n \neq 0 \\ y_1 \pm \sqrt{R^2 - (x_0 - x_1)^2 - (z_0 - z_1)^2} & \text{otherwise} \end{cases}.$$

(J.43)

Where, $a_w = x_n^2 + y_n^2$, $b_v = -2x_1 y_n^2 - 2x_n \hat{K}_1$ and $c_v = \hat{K}_1^{\,2} + y_n^2(x_1^2 + (z_0 - z_1)^2 - R^2)$. For the zero point when $t = 0$, it is easy to obtain:

$$z_0 = z_1 + R\cos(\alpha + \beta)$$

$$x_0 = \begin{cases} \frac{x_1 y_n^2 + (z_1-z_0)z_n + x_1 x_n}{x_n^2 + y_n^2} & x_n^2 + y_n^2 \neq 0 \\ x_1 + R & \text{otherwise} \end{cases}, y_0 = \begin{cases} \frac{(z_1-z_0)z_n+(x_1-x_0)x_n}{y_n} + y_1 & y_n \neq 0 \\ y_1 & \text{otherwise} \end{cases}.$$

(J.44)

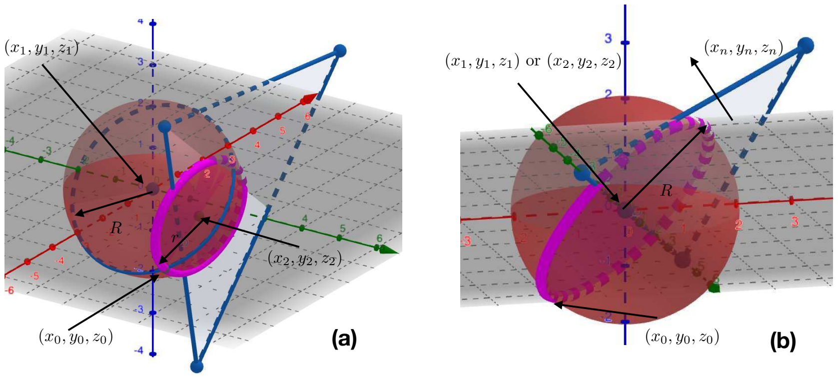

Figure J.4: (a) The plane does not go through the center of the sphere; (b) sphere center and circle center are the same.

Correction for discontinuity

In deriving Eq.J.2, Eq.J.15 and Eq.J.25, we need to take care of the jumping point or spurious discontinuities for some antiderivatives. As described in the work of Jeffery et al. [Jeffrey and Rich, 1994], expressions for the antiderivative of an integrand obtained by Weierstrass substitution sometimes contain discontinuity. As shown in Fig.J.5, when $t \in [0, 2\pi]$, there will be no discontinuities for the antiderivative with single pole as in Eq.J.2. When $t = 0, \pi$, the corresponding $\arctan(\infty)$ is finite for Eq.J.2. So we will always choose $\cot\frac{t}{2}$ instead of $\tan\frac{t}{2}$ for the integration evaluation. However, when there is a dipole, the existence of the jumping point is dependent on α, β. Apart from that, the direction of circular arc also leads to the discontinuity even we adopt $\cot\frac{t}{2}$ because the rotation shown in Fig.J.1 assumes a default normal vector of plane where the circle is contained. In the implementation, we consider four cases as shown in Fig.J.6. In (b,c) of Fig.J.6, extra correction is needed. For example of (c) in Fig.J.6 assuming that the antiderivative is $f(t)|_{t_1}^{t_2}$. The final contribution of this circular arc is $f(2\pi) - f(t_1) + f(t_2) - f(0)$.

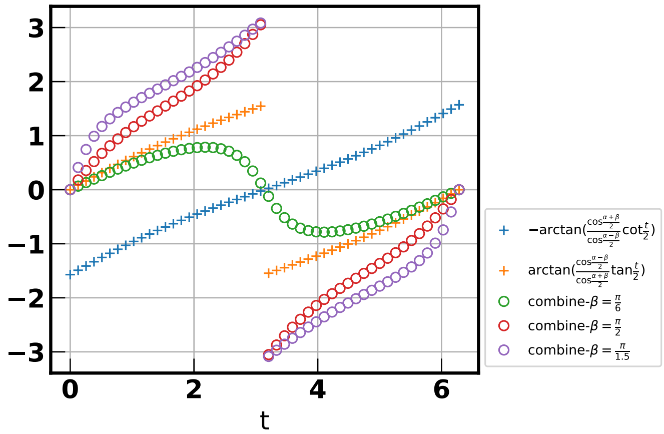

Figure J.5: Evaluation of the key components in the antiderivative in Eq.J.2, Eq.J.15 and Eq.J.25. And here we always start from $t_1 = 0$, and the x axis represents the end point of the integration (t_2). In this figure, all $\alpha = \frac{\pi}{4}$. $\beta = \frac{\pi}{6}$ if it is not specified in the legend. "combine" represents $\arctan(\frac{\sin\beta\sin t}{\cos\beta\sin\alpha+\cos\alpha\sin\beta\cos t})$. In addition, standard atan2 function is empolyed.

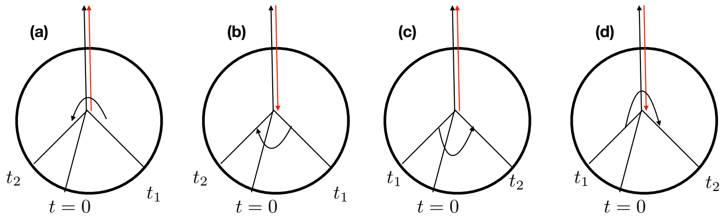

Figure J.6: Red vector indicates the normal vector controlling the orientation of the circular arc. The black vector parallel to the red vector indicates the default normal vector of the plane, which determines the parameterization of $t_{1,2}$. $t = 0$ represents the zero point for the parameterization.

Topological invariant

It becomes important when we try to calculate $\sum A$ in Eq.J.32 because A in Eq.J.22 is the same to the antiderivative when there is a dipole. In order to obtain an expression of antiderivative without jumping points, we modify the antiderivative based on α, β. With $\alpha \in (0, \frac{\pi}{2}]$ and $\beta \in [0, \pi]$, we know that $\frac{\alpha+\beta}{2} \in (0, \frac{3\pi}{4}]$ and $\frac{\alpha-\beta}{2} \in (-\frac{\pi}{2}, \frac{\pi}{4}]$. When $\frac{\alpha+\beta}{2} = \frac{\pi}{2}$, the circle will go through the south pole. And when $\alpha = \beta$, the circle will go through the north pole.

$$\frac{\sum A}{2\pi}=\begin{cases}\dfrac{-\sum \text{atan2}\left(\frac{\cos\frac{\alpha+\beta}{2}}{\cos\frac{\alpha-\beta}{2}}\cot\frac{t}{2},1\right)-\sum \text{atan2}\left(\frac{\sin\frac{\alpha+\beta}{2}}{\sin\frac{\alpha-\beta}{2}}\cot\frac{t}{2},1\right)}{2\pi}, & \text{if} \quad \frac{\alpha+\beta}{2}\neq\frac{\pi}{2},\alpha\neq\beta\\ \dfrac{-\sum \text{atan2}\left(\frac{\sin\frac{\alpha+\beta}{2}}{\sin\frac{\alpha-\beta}{2}}\cot\frac{t}{2},1\right)}{2\pi}, & \text{if} \quad \frac{\alpha+\beta}{2}=\frac{\pi}{2},\alpha\neq\beta\\ -\dfrac{\sum \text{atan2}\left(\frac{\cos\frac{\alpha+\beta}{2}}{\cos\frac{\alpha-\beta}{2}}\cot\frac{t}{2},1\right)}{2\pi}, & \text{if} \quad \frac{\alpha+\beta}{2}\neq\frac{\pi}{2},\alpha=\beta\\ 0. & \text{if} \quad \frac{\alpha+\beta}{2}=\frac{\pi}{2},\alpha=\beta\end{cases}$$

(J.45)

To test the validity of Eq.J.45, we perform a calculation with three beads and a tetrahedron. The center of the bead is fixed and the radius of the bead is increased as shown in Fig.J.7b. For the red sphere, the south pole is included inside the tetrahedron until the sphere touches the bottom face of the tetrahedron ($r = 2$). Before that, $\frac{\sum A}{2\pi} = -1$. For the blue bead, the sphere is outside of the tetrahedron. When the radius is 1, the north pole touches the bottom pole. So $\frac{\sum A}{2\pi} = 1$, which is evaluated with Eq.J.45. The blue sphere will grow until the north pole is out of the tetrahedron again. For the green sphere, as the north pole and south pole will never be inside of the tetrahedron, so $\frac{\sum A}{2\pi} = 0$.

The calculation we perform here shows a strong connection to Berry phase [Berry, 1984] and Chern number [Chern, 1946] due to the analogies between classical Maxwell's equations and quantum mechanical Schrödinger equation [Gangaraj et al., 2017]. We are not going to discuss in details about the connection as we are only interested in the calculation of solid angle in this part.

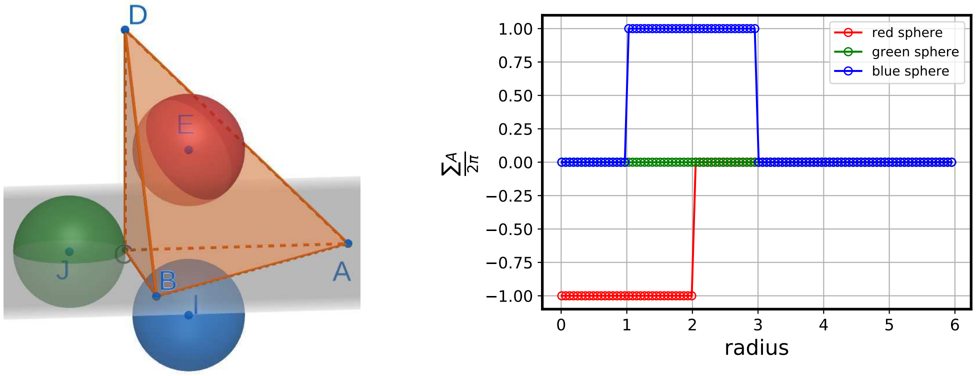

(a) **(b)**

Figure J.7: (a) The coordinates of the red bead E (1,1,2), the blue bead I (1,1,-1) and green bead J (0,-1,0). The coordinates of the vertexes of the tetrahedron are A (0,4,0),B (4,0,0), C (0,0,0) and D (0,0,4). (b) $\frac{\sum A}{2\pi}$ is calculated with Eq.J.45.

Magnetic potential and vector field

With the vector field as derived in Eq.7.24, there is still a singularity point, which is not convenient for numerical implementation and forces unnecessary rotation of the sphere for special scenarios. Here we propose an improved method which combines the idea of the magnetic potential and the vector field. As shown in the work of Wu et al. [Wu and Yang, 1975], we can use two singularity-free regions to cover the whole sphere. Instead of creating overlapping region [Wu and Yang, 1975], we create two patches to remove singular points, where they meet at the equator as shown in Fig.J.8. The corresponding vector field is:

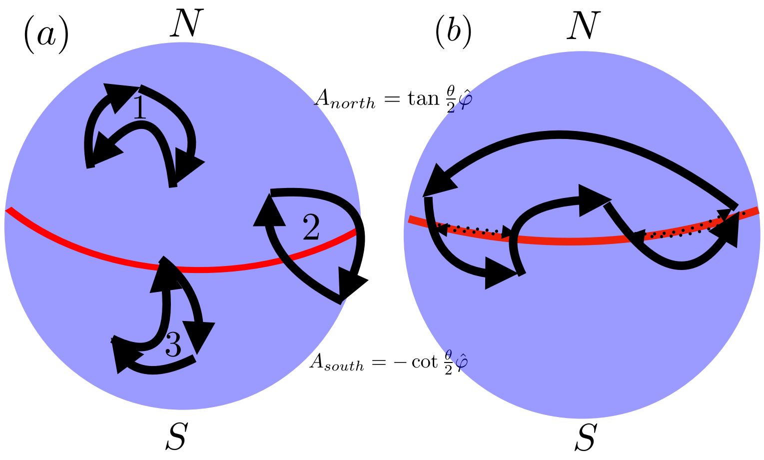

Figure J.8

Figure J.9: (a) Illustration of the three different types of loops. The red line represents the equator of the sphere. 1,3 represent the two loops only lie in the north hemisphere or south hemisphere. And 2 means the loop will intersect with the equator. (b) As shown in this figure, four circular arcs in black form a loop, which intersect with the equator. For the circular arcs and equator intersection points, extra circular arcs are added with reverse direction, which lie on the equator and is indicated with dot line in the figure.

$$\mathbf{A_{mv}} = \begin{cases} \tan\frac{\theta}{2}\hat{\boldsymbol{\varphi}}, & \text{if} \quad \theta \leq \frac{\pi}{2}. \\ -\cot\frac{\theta}{2}\hat{\boldsymbol{\varphi}}, & \text{if} \quad \theta \geq \frac{\pi}{2}. \end{cases} \tag{J.46}$$

For this method, the loops formed by circular arcs are firstly divided into three different types with respect to their relative position to the equator. If the loops are completely lying in the northern hemisphere or southern hemisphere, we directly use Eq.7.24 to evaluate their contribution to the calculation of the surface area. Naturally, if a loop belongs to the northern hemisphere, every circular arc is also lying in the northern hemisphere. The area calculated with these two types of loop will be $S +$

$K4\pi R^2$, where $K \in \mathbb{Z}$. When we apply Stokes theorem, with two reverse direction, we obtain:

$$\begin{aligned} A_{posi} &= R\int\int_s \nabla \times \mathbf{A_{mv}} \cdot \mathbf{r} dS = R\int_{\partial s} \mathbf{A_{mv}} d\mathbf{l} \ , \\ A_{posi} + A_{nega} &= 4\pi R^2 \ . \end{aligned} \tag{J.47}$$

Where, A_{posi} represents the direction, where the area closed by the loop does not include the equator and A_{nega} represents the other part of the area when the surface area of the sphere is excluded from A_{posi}. However, when we directly make use of Eq.7.24 to evaluate the A_{nega}, we obtain:

$$\hat{A_{nega}} = -R\int_{\partial s} \mathbf{A_{mv}} d\mathbf{l} = A_{nega} - 4\pi R^2 \ . \tag{J.48}$$

Eq.J.48 tells us that if we consider the contributions from the loops not crossing the equator, the final summation will be $S + K4\pi R^2$, where $K \in \mathbb{Z}$.

For the case when the circular arcs are intersecting with the equator, we directly add auxiliary curves as shown in Fig.J.8(b). In Fig.J.8(b), after adding extra lines, we notice that we have three closed loops which are either in the northern hemisphere or southern hemisphere, so that we still are able to apply Stokes theorem for each individual loop. To calculate the surface area, there will be two contributions in total:

- Newly added curve.

  The newly added circular arcs on the equator are exactly overlapping with each other. But when we evaluate their contribution to the surface area calculation, we need to specify whether they belong to the north or south hemisphere. For the newly added curves, $\alpha = \frac{\pi}{2}, \beta = 0, \frac{\pi}{2} - \frac{t}{2} \in [-\frac{\pi}{2}, \frac{\pi}{2}]$ and supposed that we need to integrate from t_1 to t_2 in the northern hemisphere, we can simplify Eq.7.9 to read:

$$\begin{aligned} A_{neqa} &= R^2\Bigg(-2\arctan\left(\frac{\cos\frac{\alpha+\beta}{2}}{\cos\frac{\alpha-\beta}{2}}\cot\frac{t}{2}\right) - t\cos\alpha\Bigg)\Bigg|_{t_1}^{t_2} \\ &= R^2(-2\arctan(\cot\frac{t}{2}))|_{t_1}^{t_2} = R^2(t_2 - t_1) \ . \end{aligned} \tag{J.49}$$

  For the reverse direction belonging to the southern hemisphere, it is integrated from t_2 to t_1:

$$\begin{aligned} A_{seqa} &= R^2\Bigg(2\arctan\left(\frac{\sin\frac{\alpha+\beta}{2}}{\sin\frac{\alpha-\beta}{2}}\cot\frac{t}{2}\right) - t\cos\alpha\Bigg)\Bigg|_{t_2}^{t_1} \\ &= R^2(2\arctan(\cot\frac{t}{2}))|_{t_2}^{t_1} = R^2(t_2 - t_1) \ . \end{aligned} \tag{J.50}$$

  With Eq.J.49 and Eq.J.50, it is easy to see that whenever a circular arc is crossing the equator, a new contribution of $\pm 2R^2 t_2$ or $\mp 2R^2 t_1$ should be added to the final area calculation for each intersection point between the individual circular arc and the equator. The sign of $2R^2 t_2$ and $2R^2 t_1$ is determined by the normal direction of the polyhedron faces. However, care should be taken for the circular arc on the equator. Because some circular arc on the equator might pass through the zero point due to the parameterization. In this case we obtain:

$$A_{neqa} + A_{seqa} = 2R^2(t_2 - t_1 \pm 2\pi) \quad = 2R^2(t_2 - t_1) \pm 4\pi R^2 \; . \tag{J.51}$$

Eq.J.51 reminds us that the jump in the zero point does not influence the final calculation because we need to take the modulo with respect to the sphere surface area. After calculating the contribution from each individual circular arc, we need to take the modulo of the final summation as it is shown in the reference method, even though here the summation could be negative.

- Original curve.

  The original curve will intersect with the equator in this model. According to Eq.J.1, we force $\hat{z}(t) = 0$:

  $$\cos t = \cot\beta \cot\alpha \; . \tag{J.52}$$

  With Eq.J.52, we could easily determine t for the equator. Then with Eq.J.11, the contribution to the final area calculation from this point is solved. In addition, Eq.J.52 also reminds us that when $\beta = 0$, we do not need to consider the intersection between the circular curve and the equator.

Even for this method, we could still have some alternative method because the overlapping region between two different vector field is not necessarily the equator. For example, if we let the two vector field overlap for some latitude when $\alpha = \hat{\alpha}, \beta = 0, \pi$:

$$\begin{aligned} A_{neqa} &= R^2\bigg(-2\arctan\left(\frac{\cos\frac{\hat{\alpha}+\beta}{2}}{\cos\frac{\hat{\alpha}-\beta}{2}}\cot\frac{t}{2}\right) - t\cos\hat{\alpha}\bigg)\bigg|_{t_1}^{t_2} \\ &= R^2(-2\arctan(\cot\frac{t}{2})) - t\cos\hat{\alpha}|_{t_1}^{t_2} = R^2(t_2 - t_1)(1 - \cos\hat{\alpha}) \\ A_{seqa} &= R^2(t_2 - t_1)(1 + \cos\hat{\alpha}) \; . \end{aligned} \tag{J.53}$$

With Eq.J.53, we are able to evaluate the contribution from the circular arcs which crosses the latitude of the sphere. By varying $\hat{\alpha}$, the circular arcs might intersect with the latitude at new points. On top of that, we developed a new branch of methods for evaluating the area formed by these circular arcs. This method is inspired by the monopoles without strings [Preskill, 1984; Wu and Yang, 1975]. And when $\hat{\alpha} = \frac{\pi}{2}$, we have Eq.J.51.

Compared with the vector field with one singular point, this method guarantees that every point on the sphere is well defined. And from the description of the algorithm, it is also clear that we could directly evaluate the contribution of the final area calculation by individual circular arc. What needs to be done is to check whether a circular arc is intersecting with the equator or not. But it is worth showing that how the researches related with gauge fields [Wu and Yang, 1975] are closely related to the question we are discussing. In addition, all the algorithms presented are exact calculations, which are only limited by the machine precision. But these algorithms might inspire new approximation methods, which could achieve higher efficiency by sacrificing part of the accuracy.

Bibliography

W. Abdallah, J. S. Buckley, A. Carnegie, J. Edwards, B. Herold, E. Fordham, A. Graue, T. Habashy, N. Seleznev, C. Signer, et al. Fundamentals of wettability. *Technology*, 38(1125-1144):268, 1986.

A. Aharony and D. Stauffer. *Introduction To Percolation Theory*. Taylor & Francis, 2003. ISBN 9781135747831. URL `https://books.google.de/books?id=Dph5AgAAQBAJ`.

A. Al-Futaisi and T. W. Patzek. Impact of wettability alteration on two-phase flow characteristics of sandstones: A quasi-static description. *Water Resources Research*, 39(2), 2003.

M. Alava, M. Dubé, and M. Rost. Imbibition in disordered media. *Advances in Physics*, 53(2):83–175, 2004.

K. A. Alshibli and M. I. Alsaleh. Characterizing surface roughness and shape of sands using digital microscopy. *Journal of computing in civil engineering*, 18(1):36–45, 2004.

E. Amott et al. Observations relating to the wettability of porous rock. 1959.

W. G. Anderson et al. Wettability literature survey-part 1: rock/oil/brine interactions and the effects of core handling on wettability. *Journal of petroleum technology*, 38 (10):1–125, 1986.

M. Andrew, B. Bijeljic, and M. J. Blunt. Pore-by-pore capillary pressure measurements using x-ray microtomography at reservoir conditions: Curvature, snap-off, and remobilization of residual co 2. *Water Resources Research*, 50(11):8760–8774, 2014.

R. T. Armstrong and S. Berg. Interfacial velocities and capillary pressure gradients during haines jumps. *Physical Review E*, 88(4):043010, 2013.

R. T. Armstrong, M. L. Porter, and D. Wildenschild. Linking pore-scale interfacial curvature to column-scale capillary pressure. *Advances in Water Resources*, 46: 55–62, 2012.

J. S. Asvestas and D. C. Englund. Computing the solid angle subtended by a planar figure. *Optical Engineering*, 33(12):4055–4060, 1994.

A. J. Banchio and G. Nägele. Short-time transport properties in dense suspensions: from neutral to charge-stabilized colloidal spheres. *The Journal of chemical physics*, 128(10):104903, 2008.

G. K. Batchelor. *An Introduction to Fluid Dynamics*. Cambridge Mathematical Library. Cambridge University Press, 2000. doi: 10.1017/CBO9780511800955.

J. Bear. *Dynamics of fluids in porous media*. Courier Corporation, 2013.

J. Bear, B. Rubinstein, and L. Fel. Capillary pressure curve for liquid menisci in a cubic assembly of spherical particles below irreducible saturation. *Transport in porous media*, 89(1):63–73, 2011.

S. Berg, H. Ott, S. A. Klapp, A. Schwing, R. Neiteler, N. Brussee, A. Makurat, L. Leu, F. Enzmann, J.-O. Schwarz, et al. Real-time 3d imaging of haines jumps in porous media flow. *Proceedings of the National Academy of Sciences*, 110(10):3755–3759, 2013.

F. Bernardeau and R. van de Weygaert. A new method for accurate estimation of velocity field statistics. *Monthly Notices of the Royal Astronomical Society*, 279(2): 693–711, 1996.

M. V. Berry. Quantal phase factors accompanying adiabatic changes. *Proceedings of the Royal Society of London. A. Mathematical and Physical Sciences*, 392(1802): 45–57, 1984.

M. Bevis and J.-L. Chatelain. Locating a point on a spherical surface relative to a spherical polygon of arbitrary shape. *Mathematical geology*, 21(8):811–828, 1989.

J. Bico and D. Quéré. Precursors of impregnation. *EPL (Europhysics Letters)*, 61(3): 348, 2003.

J. Binysh and G. P. Alexander. Maxwell's theory of solid angle and the construction of knotted fields. *Journal of Physics A: Mathematical and Theoretical*, 51(38):385202, 2018.

M. Blunt, M. J. King, and H. Scher. Simulation and theory of two-phase flow in porous media. *Phys. Rev. A*, 46:7680–7699, Dec 1992. doi: 10.1103/PhysRevA.46.7680.

M. J. Blunt. *Multiphase flow in permeable media: A pore-scale perspective*. Cambridge University Press, 2017.

M. J. Blunt, B. Bijeljic, H. Dong, O. Gharbi, S. Iglauer, P. Mostaghimi, A. Paluszny, and C. Pentland. Pore-scale imaging and modelling. *Advances in Water Resources*, 51:197 – 216, 2013. ISSN 0309-1708. doi: https://doi.org/10.1016/j.advwatres.2012.03.003. URL `http://www.sciencedirect.com/science/article/pii/S0309170812000528`. 35th Year Anniversary Issue.

K. A. Brakke. The surface evolver. *Experimental Mathematics*, 1(2):141–165, 1992. doi: 10.1080/10586458.1992.10504253. URL `https://doi.org/10.1080/10586458.1992.10504253`.

S. R. Broadbent and J. M. Hammersley. Percolation processes: I. crystals and mazes. *Mathematical Proceedings of the Cambridge Philosophical Society*, 53(3):629–641, 1957. doi: 10.1017/S0305004100032680.

R. H. Brooks and A. T. Corey. Hydraulic properties of porous media and their relationship to drainage design. *Paper (American Society of Agricultural Engineers); no. 63-214*, 1963.

R. J. Brown, I. Fatt, et al. Measurements of fractional wettability of oil fields' rocks by the nuclear magnetic relaxation method. In *Fall Meeting of the Petroleum Branch of AIME*. Society of Petroleum Engineers, 1956.

S. Bucciarelli, J. S. Myung, B. Farago, S. Das, G. A. Vliegenthart, O. Holderer, R. G. Winkler, P. Schurtenberger, G. Gompper, and A. Stradner. Dramatic influence of patchy attractions on short-time protein diffusion under crowded conditions. *Science advances*, 2(12):e1601432, 2016.

S. E. Buckley, M. Leverett, et al. Mechanism of fluid displacement in sands. *Transactions of the AIME*, 146(01):107–116, 1942.

A. Carminati. Rhizosphere wettability decreases with root age: a problem or a strategy to increase water uptake of young roots? *Frontiers in plant science*, 4:298, 2013.

O. Chapuis, M. Prat, M. Quintard, E. Chane-Kane, O. Guillot, and N. Mayer. Two-phase flow and evaporation in model fibrous media: Application to the gas diffusion layer of PEM fuel cells. *Journal of Power Sources*, 178(1):258 – 268, 2008. ISSN 0378-7753. doi: http://dx.doi.org/10.1016/j.jpowsour.2007.12.011.

B. Chareyre, A. Cortis, E. Catalano, and E. Barthélemy. Pore-scale modeling of viscous flow and induced forces in dense sphere packings. *Transport in porous media*, 94(2):595–615, 2012.

S.-s. Chern. Characteristic classes of hermitian manifolds. *Annals of Mathematics*, pages 85–121, 1946.

M. Cieplak and M. O. Robbins. Dynamical transition in quasistatic fluid invasion in porous media. *Phys. Rev. Lett.*, 60:2042–2045, May 1988. doi: 10.1103/PhysRevLett.60.2042.

M. Cieplak and M. O. Robbins. Influence of contact angle on quasistatic fluid invasion of porous media. *Phys. Rev. B*, 41:11508–11521, Jun 1990. doi: 10.1103/PhysRevB.41.11508.

D. A. Clarke, A. J. Sederman, L. F. Gladden, and D. J. Holland. Investigation of void fraction schemes for use with cfd-dem simulations of fluidized beds. *Industrial & Engineering Chemistry Research*, 57(8):3002–3013, 2018.

E. Clement, C. Baudet, E. Guyon, and J. Hulin. Invasion front structure in a 3-d model porous medium under a hydrostatic pressure gradient. *Journal of Physics D: Applied Physics*, 20(5):608, 1987.

S. Coles, J. Bawa, L. Trenner, and P. Dorazio. *An introduction to statistical modeling of extreme values*, volume 208. Springer, 2001.

P. Concus and R. Finn. On the behavior of a capillary surface in a wedge. *Proceedings of the National Academy of Sciences*, 63(2):292–299, 1969. ISSN 0027-8424. doi: 10.1073/pnas.63.2.292. URL `https://www.pnas.org/content/63/2/292`.

M. L. Connolly. Analytical molecular surface calculation. *Journal of applied crystallography*, 16(5):548–558, 1983.

T. H. Cormen, C. E. Leiserson, R. L. Rivest, and C. Stein. *Introduction to algorithms*. MIT press, 2009.

G. M. Crippen, T. F. Havel, et al. *Distance geometry and molecular conformation*, volume 74. Research Studies Press Taunton, 1988.

L. P. Dake. *Fundamentals of reservoir engineering*, volume 8. Elsevier, 1983.

P.-E. Danielsson. Euclidean distance mapping. *Computer Graphics and image processing*, 14(3):227–248, 1980.

H. P. G. Darcy. *Les Fontaines publiques de la ville de Dijon. Exposition et application des principes à suivre et des formules à employer dans les questions de distribution d'eau, etc.* V. Dalamont, 1856.

S. S. Datta, J.-B. Dupin, and D. A. Weitz. Fluid breakup during simultaneous two-phase flow through a three-dimensional porous medium. *Physics of Fluids*, 26(6):062004, 2014.

P.-G. De Gennes. Wetting: statics and dynamics. *Reviews of modern physics*, 57(3):827, 1985.

P.-G. de Gennes. *La percolation: un concept unificateur (Percolation a unifying concept)*, pages 72–82. 2009. doi: 10.1142/9789814273817_0009. URL `https://www.worldscientific.com/doi/abs/10.1142/9789814273817_0009`.

T. J. Dekker. A floating-point technique for extending the available precision. *Numerische Mathematik*, 18(3):224–242, 1971.

C. Delaunay. Sur la surface de révolution dont la courbure moyenne est constante. *Journal de mathématiques pures et appliquées*, pages 309–314, 1841.

M. M. Dias and D. Wilkinson. Percolation with trapping. *Journal of Physics A: Mathematical and General*, 19(15):3131, 1986.

P. A. M. Dirac. Quantised singularities in the electromagnetic field. *Proceedings of the Royal Society of London. Series A, Containing Papers of a Mathematical and Physical Character*, 133(821):60–72, 1931.

M. P. Do Carmo. *Differential Geometry of Curves and Surfaces: Revised and Updated Second Edition.* Courier Dover Publications, 2016.

C. Domb, T. Schneider, and E. Stoll. Cluster shapes in lattice gases and percolation. *Journal of Physics A: Mathematical and General*, 8(9):L90, 1975.

E. C. Donaldson, R. D. Thomas, P. B. Lorenz, et al. Wettability determination and its effect on recovery efficiency. *Society of Petroleum Engineers Journal*, 9(01): 13–20, 1969.

M. Dong and I. Chatzis. The imbibition and flow of a wetting liquid along the corners of a square capillary tube. *Journal of colloid and interface science*, 172(2):278–288, 1995.

B. Drawert, S. Engblom, and A. Hellander. Urdme: a modular framework for stochastic simulation of reaction-transport processes in complex geometries. *BMC systems biology*, 6(1):76, 2012.

F. A. Dullien. *Porous media: fluid transport and pore structure.* Academic press, 2012.

F. A. Dullien, C. Zarcone, I. F. Macdonald, A. Collins, and R. D. Bochard. The effects of surface roughness on the capillary pressure curves and the heights of capillary rise in glass bead packs. *Journal of Colloid and Interface Science*, 127(2):362–372, 1989.

Y. Edery, S. Berg, and D. Weitz. Surfactant variations in porous media localize capillary instabilities during haines jumps. *Physical review letters*, 120(2):028005, 2018.

J. Eells. The surfaces of delaunay. *The Mathematical Intelligencer*, 9(1):53–57, 1987.

S. Engblom, L. Ferm, A. Hellander, and P. Lötstedt. Simulation of stochastic reaction-diffusion processes on unstructured meshes. *SIAM Journal on Scientific Computing*, 31(3):1774–1797, 2009.

R. Erban and S. J. Chapman. Stochastic modelling of reaction–diffusion processes: algorithms for bimolecular reactions. *Physical biology*, 6(4):046001, 2009.

M. A. Erle, D. Dyson, and N. R. Morrow. Liquid bridges between cylinders, in a torus, and between spheres. *AIChE Journal*, 17(1):115–121, 1971.

R. P. Ewing and B. Berkowitz. Stochastic pore-scale growth models of dnapl migration in porous media. *Advances in water resources*, 24(3-4):309–323, 2001.

L. Eyges. *The classical electromagnetic field.* Courier Corporation, 2012.

I. Fatt, W. A. Klikoff Jr, et al. Effect of fractional wettability on multiphase flow through porous media. *Journal of Petroleum Technology*, 11(10):71–76, 1959.

I. Fatt et al. The network model of porous media. 1956.

L. Fejes. Über die dichteste kugellagerung. *Mathematische Zeitschrift*, 48:676–684, 1942. URL `http://eudml.org/doc/169007`.

M. Ferer, C. Ji, G. S. Bromhal, J. Cook, G. Ahmadi, and D. H. Smith. Crossover from capillary fingering to viscous fingering for immiscible unstable flow: Experiment and modeling. *Physical Review E*, 70(1):016303, 2004.

M. Ferer, G. S. Bromhal, and D. H. Smith. Crossover from fractal capillary fingering to compact flow: The effect of stable viscosity ratios. *Physical Review E*, 76(4): 046304, 2007.

J. F. Fernández, R. Rangel, and J. Rivero. Crossover length from invasion percolation to diffusion-limited aggregation in porous media. *Physical review letters*, 67(21): 2958, 1991.

A. Ferreira, L. De Haan, et al. On the block maxima method in extreme value theory: Pwm estimators. *The Annals of statistics*, 43(1):276–298, 2015.

R. Fisher. On the capillary forces in an ideal soil; correction of formulae given by wb haines. *The Journal of Agricultural Science*, 16(3):492–505, 1926.

L. Fries, S. Antonyuk, S. Heinrich, and S. Palzer. Dem–cfd modeling of a fluidized bed spray granulator. *Chemical Engineering Science*, 66(11):2340–2355, 2011.

G. Gagneux and O. Millet. Analytic calculation of capillary bridge properties deduced as an inverse problem from experimental data. *Transport in porous media*, 105(1): 117–139, 2014.

S. Galindo-Torres. A coupled discrete element lattice boltzmann method for the simulation of fluid–solid interaction with particles of general shapes. *Computer Methods in Applied Mechanics and Engineering*, 265:107–119, 2013.

S. A. H. Gangaraj, M. G. Silveirinha, and G. W. Hanson. Berry phase, berry connection, and chern number for a continuum bianisotropic material from a classical electromagnetics perspective. *IEEE journal on multiscale and multiphysics computational techniques*, 2:3–17, 2017.

C. F. Gauss. Allgemeine theorie des erdmagnetismus. In *Werke*, pages 119–193. Springer, 1877.

M. N. Gladkikh. *A priori prediction of macroscopic properties of sedimentary rocks containing two immiscible fluids*. PhD thesis, 2005.

J. T. Gostick, M. A. Ioannidis, M. W. Fowler, and M. D. Pritzker. Wettability and capillary behavior of fibrous gas diffusion media for polymer electrolyte membrane fuel cells. *Journal of Power Sources*, 194(1):433–444, 2009.

P. Grassberger and I. Procaccia. Measuring the strangeness of strange attractors. In *The Theory of Chaotic Attractors*, pages 170–189. Springer, 2004.

D. J. Griffiths. Introduction to electrodynamics, 2005.

S. Gruener, Z. Sadjadi, H. E. Hermes, A. V. Kityk, K. Knorr, S. U. Egelhaaf, H. Rieger, and P. Huber. Anomalous front broadening during spontaneous imbibition in a matrix with elongated pores. *Proceedings of the National Academy of Sciences*, 109(26):10245–10250, 2012. ISSN 0027-8424. doi: 10.1073/pnas.1119352109. URL `https://www.pnas.org/content/109/26/10245`.

W. B. Haines. Studies in the physical properties of soil. v. the hysteresis effect in capillary properties, and the modes of moisture distribution associated therewith. *The Journal of Agricultural Science*, 20(1):97–116, 1930.

T. Hales. *Dense Sphere Packings: A Blueprint for Formal Proofs*. London Mathematical Society Lecture Note Series. Cambridge University Press, 2012. doi: 10.1017/CBO9781139193894.

Y. Han and P. A. Cundall. Lbm–dem modeling of fluid–solid interaction in porous media. *International Journal for Numerical and Analytical Methods in Geomechanics*, 37(10):1391–1407, 2013.

M. Hassanizadeh and W. G. Gray. General conservation equations for multi-phase systems: 1. averaging procedure. *Advances in water resources*, 2:131–144, 1979.

S. M. Hassanizadeh and W. G. Gray. Thermodynamic basis of capillary pressure in porous media. *Water resources research*, 29(10):3389–3405, 1993.

T. F. Havel. Distance geometry: Theory, algorithms, and chemical applications. *Encyclopedia of Computational Chemistry*, 120:723–742, 1998.

S. Hayryan, C.-K. Hu, J. Skřivánek, E. Hayryane, and I. Pokornỳ. A new analytical method for computing solvent-accessible surface area of macromolecules and its gradients. *Journal of computational chemistry*, 26(4):334–343, 2005.

I. Hecht and H. Taitelbaum. Roughness and growth in a continuous fluid invasion model. *Phys. Rev. E*, 70:046307, Oct 2004. doi: 10.1103/PhysRevE.70.046307. URL `https://link.aps.org/doi/10.1103/PhysRevE.70.046307`.

A. Heiko, C. Nicolas, D. Jack, G. Erik, H. Junehee, K. Matthias, K. Youngseuk, K. Fabian, L. Minhui, M. Claudio, M. Mike, M. Tapan, H. S. Erik, S. Ratnanabha, S. Nishank, R. Sarah, W. Andreas, and Z. Xin. Digital rock physics benchmarks—part i: Imaging and segmentation. *Computers & Geosciences*, 50:25–32, 2013. ISSN 0098-3004.

I. Hepburn, W. Chen, S. Wils, and E. De Schutter. Steps: efficient simulation of stochastic reaction–diffusion models in realistic morphologies. *BMC systems biology*, 6(1):36, 2012.

S. Herminghaus. Universal phase diagram for wetting on mesoscale roughness. *Physical review letters*, 109(23):236102, 2012.

S. Herminghaus, M. Brinkmann, and R. Seemann. Wetting and dewetting of complex surface geometries. *Annu. Rev. Mater. Res.*, 38:101–121, 2008.

J. Hilden and K. Trumble. Numerical analysis of capillarity in packed spheres: Planar hexagonal-packed spheres. *Journal of Colloid and Interface Science*, 267(2):463 – 474, 2003. ISSN 0021-9797. doi: https://doi.org/10.1016/S0021-9797(03)00683-0.

T. Hiller, J. Ardevol-Murison, A. Muggeridge, M. Schröter, M. Brinkmann, et al. The impact of wetting-heterogeneity distribution on capillary pressure and macroscopic measures of wettability. *SPE journal*, 24(01):200–214, 2019.

R. Holtzman. Effects of pore-scale disorder on fluid displacement in partially-wettable porous media. *Sci. Rep.*, 6, Feb 2016. doi: doi:10.1038/srep36221.

R. Holtzman and E. Segre. Wettability stabilizes fluid invasion into porous media via nonlocal, cooperative pore filling. *Phys. Rev. Lett.*, 115:164501, Oct 2015. doi: 10.1103/PhysRevLett.115.164501.

G. M. Homsy. Viscous fingering in porous media. *Annual review of fluid mechanics*, 19(1):271–311, 1987.

J. Hoshen and R. Kopelman. Percolation and cluster distribution. i. cluster multiple labeling technique and critical concentration algorithm. *Phys. Rev. B*, 14:3438–3445, Oct 1976. doi: 10.1103/PhysRevB.14.3438. URL `https://link.aps.org/doi/10.1103/PhysRevB.14.3438`.

R. Hu, T. Lan, G.-J. Wei, and Y.-F. Chen. Phase diagram of quasi-static immiscible displacement in disordered porous media. *Journal of Fluid Mechanics*, 875:448–475, 2019. doi: 10.1017/jfm.2019.504.

S.-G. Hwang. Cauchy's interlace theorem for eigenvalues of hermitian matrices. *The American Mathematical Monthly*, 111(2):157–159, 2004.

P. Iassonov, T. Gebrenegus, and M. Tuller. Segmentation of x-ray computed tomography images of porous materials: A crucial step for characterization and quantitative analysis of pore structures. *Water Resources Research*, 45(9), 2009.

S. A. Isaacson. A convergent reaction-diffusion master equation. *The Journal of chemical physics*, 139(5):054101, 2013.

S. A. Isaacson and C. S. Peskin. Incorporating diffusion in complex geometries into stochastic chemical kinetics simulations. *SIAM Journal on Scientific Computing*, 28(1):47–74, 2006.

S. A. Isaacson and Y. Zhang. An unstructured mesh convergent reaction–diffusion master equation for reversible reactions. *Journal of Computational Physics*, 374: 954–983, 2018.

J. Jang, Z. Sun, and J. C. Santamarina. Capillary pressure across a pore throat in the presence of surfactants. *Water Resources Research*, 52(12):9586–9599, 2016.

D. J. Jeffrey and A. D. Rich. The evaluation of trigonometric integrals avoiding spurious discontinuities. *ACM Transactions on Mathematical Software (TOMS)*, 20(1):124–135, 1994.

G. R. Jerauld and S. J. Salter. The effect of pore-structure on hysteresis in relative permeability and capillary pressure: Pore-level modeling. *Transport in Porous Media*, 5(2):103–151, 1990. ISSN 1573-1634. doi: 10.1007/BF00144600.

V. Joekar-Niasar, S. M. Hassanizadeh, and H. Dahle. Non-equilibrium effects in capillarity and interfacial area in two-phase flow: dynamic pore-network modelling. *Journal of Fluid Mechanics*, 655:38–71, 2010.

B. D. Jones and J. R. Williams. Fast computation of accurate sphere-cube intersection volume. *Engineering Computations*, 34(4):1204–1216, 2017. doi: 10.1108/EC-02-2016-0052. URL `https://doi.org/10.1108/EC-02-2016-005`.

M. Jung, M. Brinkmann, R. Seemann, T. Hiller, M. Sanchez de La Lama, and S. Herminghaus. Wettability controls slow immiscible displacement through local interfacial instabilities. *Phys. Rev. Fluids*, 1:074202, Nov 2016. doi: 10.1103/PhysRevFluids.1.074202.

K. Khare, M. Brinkmann, B. M. Law, E. L. Gurevich, S. Herminghaus, and R. Seemann. Dewetting of liquid filaments in wedge-shaped grooves. *Langmuir*, 23(24): 12138–12141, 2007.

C. Kloss, C. Goniva, A. Hager, S. Amberger, and S. Pirker. Models, algorithms and validation for opensource dem and cfd–dem. *Progress in Computational Fluid Dynamics, an International Journal*, 12(2-3):140–152, 2012.

B. A. Kopera and M. Retsch. Computing the 3d radial distribution function from particle positions: An advanced analytic approach. *Analytical chemistry*, 90(23): 13909–13914, 2018.

G. A. Korn and T. M. Korn. *Mathematical handbook for scientists and engineers: definitions, theorems, and formulas for reference and review*. Courier Corporation, 2000.

S. V. Kostinski, E. R. Chen, and M. P. Brenner. Characterization of patterns formed by shadows of spheres. *Phys. Rev. Lett.*, 112:235502, Jun 2014. doi: 10.1103/PhysRevLett.112.235502. URL `https://link.aps.org/doi/10.1103/PhysRevLett.112.235502`.

A. Kovscek, H. Wong, and C. Radke. A pore-level scenario for the development of mixed wettability in oil reservoirs. *AIChE Journal*, 39(6):1072–1085, 1993.

F. Lamarche and C. Leroy. Evaluation of the volume of intersection of a sphere with a cylinder by elliptic integrals. *Computer Physics Communications*, 59(2):359 – 369, 1990. ISSN 0010-4655. doi: https://doi.org/10.1016/0010-4655(90)90184-3. URL `http://www.sciencedirect.com/science/article/pii/0010465590901843`.

J. Lane, B. Magedson, and M. Rarick. An efficient point in polyhedron algorithm. *Computer Vision, Graphics, and Image Processing*, 26(1):118 – 125, 1984. ISSN 0734-189X. doi: https://doi.org/10.1016/0734-189X(84)90133-6. URL `http://www.sciencedirect.com/science/article/pii/0734189X84901336`.

P. Laplace. Mécanique celeste 10. *Supplement to the tenth edition*, 1806.

H. Lee, A. Gupta, T. A. Hatton, and P. S. Doyle. Creating isolated liquid compartments using photopatterned obstacles in microfluidics. *Physical Review Applied*, 7 (4):044013, 2017.

R. Lenormand. Différents mécanismes de déplacements visqueux et capillaires en milieu poreux: Diagramme de phase. *Comptes rendus de l'Académie des sciences. Série 2, Mécanique, Physique, Chimie, Sciences de l'univers, Sciences de la Terre*, 301(5):247–250, 1985.

R. Lenormand. Pattern growth and fluid displacements through porous media. *Physica A: Statistical Mechanics and its Applications*, 140(1-2):114–123, 1986.

R. Lenormand. Liquids in porous media. *Journal of Physics: Condensed Matter*, 2 (S):SA79, 1990.

R. Lenormand, C. Zarcone, and A. Sarr. Mechanisms of the displacement of one fluid by another in a network of capillary ducts. *Journal of Fluid Mechanics*, 135: 337–353, 1983.

R. Lenormand, C. Zarcone, et al. Role of roughness and edges during imbibition in square capillaries. In *SPE annual technical conference and exhibition*. Society of Petroleum Engineers, 1984.

R. Lenormand, E. Touboul, and C. Zarcone. Numerical models and experiments on immiscible displacements in porous media. *Journal of fluid mechanics*, 189:165–187, 1988.

R. Lenormand et al. Scaling laws for immiscible displacements with capillary and viscous fingering. In *SPE Annual Technical Conference and Exhibition*. Society of Petroleum Engineers, 1986.

M. Lessel, O. Bäumchen, M. Klos, H. Hähl, R. Fetzer, M. Paulus, R. Seemann, and K. Jacobs. Self-assembled silane monolayers: an efficient step-by-step recipe for high-quality, low energy surfaces. *Surface and Interface Analysis*, 47(5):557–564, 2015.

M. Leverett et al. Capillary behavior in porous solids. *Transactions of the AIME*, 142(01):152–169, 1941.

J. Li, H. Zhang, and W. Wang. Fast and robust point-in-spherical-polygon tests using multilevel spherical grids. In *International Workshop on Next Generation Computer Animation Techniques*, pages 56–66. Springer, 2017.

G. Lian, C. Thornton, and M. J. Adams. A theoretical study of the liquid bridge forces between two rigid spherical bodies. *Journal of colloid and interface science*, 161(1):138–147, 1993.

B.-Y. Liu, R. Seemann, L.-J. Chen, and M. Brinkmann. Directional liquid wicking in regular arrays of triangular posts. *Langmuir*, 35(50):16476–16486, 2019.

Y. Liu, D. Nolte, and L. Pyrak-Nolte. Hysteresis and interfacial energies in smooth-walled microfluidic channels. *Water Resources Research*, 47(1), 2011.

N. B. Lu, C. A. Browne, D. B. Amchin, J. K. Nunes, and S. S. Datta. Controlling capillary fingering using pore size gradients in disordered media. *Physical Review Fluids*, 4(8):084303, 2019.

Y. Lu, Z. Jing-Zhong, and B. Neumann. A generalisation to several dimensions of the neuberg-pedoe inequality, with applications. *Bulletin of the Australian Mathematical Society*, 27(2):203–214, 1983.

A. V. Lukyanov, M. M. Sushchikh, M. J. Baines, and T. G. Theofanous. Superfast nonlinear diffusion: Capillary transport in particulate porous media. *Phys. Rev. Lett.*, 109:214501, Nov 2012. doi: 10.1103/PhysRevLett.109.214501.

K. J. Måløy, J. Feder, and T. Jøssang. Viscous fingering fractals in porous media. *Physical review letters*, 55(24):2688, 1985.

B. B. Mandelbrot. *The fractal geometry of nature*, volume 173. WH freeman New York, 1983.

S. Markose and A. Alentorn. The generalized extreme value distribution, implied tail index, and option pricing. *The Journal of Derivatives*, 18(3):35–60, 2011.

G. Mason and N. Morrow. Meniscus configurations and curvatures in non-axisymmetric pores of open and closed uniform cross section. *Proc. R. Soc. Lond. A*, 414(1846):111–133, 1987.

J. C. Maxwell. *A treatise on electricity and magnetism*, volume 1. Oxford: Clarendon Press, 1873.

R. P. Mayer and R. A. Stowe. Mercury porosimetry—breakthrough pressure for penetration between packed spheres. *Journal of colloid Science*, 20(8):893–911, 1965.

J. E. McClure, R. T. Armstrong, M. A. Berrill, S. Schlüter, S. Berg, W. G. Gray, and C. T. Miller. Geometric state function for two-fluid flow in porous media. *Physical Review Fluids*, 3(8):084306, 2018.

S. R. McDougall, K. S. Sorbie, et al. The impact of wettability on waterflooding: pore-scale simulation. *SPE Reservoir Engineering*, 10(03):208–213, 1995.

E. Medici and J. Allen. Existence of the phase drainage diagram in proton exchange membrane fuel cell fibrous diffusion media. *Journal of Power Sources*, 191(2): 417–427, 2009.

K. Melnikov, R. Mani, F. K. Wittel, M. Thielmann, and H. J. Herrmann. Grain-scale modeling of arbitrary fluid saturation in random packings. *Physical Review E*, 92 (2):022206, 2015.

J. Melrose. Interfacial phenomena as related to oil recovery mechanisms. *Can. J. Chem. Eng*, 48(6):638–644, 1970.

J. Melrose et al. Role of capillary forces in detennining microscopic displacement efficiency for oil recovery by waterflooding. *Journal of Canadian Petroleum Technology*, 13(04), 1974.

K. Menger. Untersuchungen über allgemeine metrik. *Mathematische Annalen*, 100 (1):75–163, 1928.

J. Middleton, H. Averdunk, and A. Sheppard. Mango user guide for applied mathematics anu. 2007. URL `http://xct.anu.edu.au/mango`.

F. Moebius and D. Or. Interfacial jumps and pressure bursts during fluid displacement in interacting irregular capillaries. *Journal of colloid and interface science*, 377(1): 406–415, 2012.

K. K. Mohanty, H. T. Davis, L. E. Scriven, et al. Physics of oil entrapment in water-wet rock. *SPE Reservoir Engineering*, 2(01):113–128, 1987.

R. Moosavi, M. Schröter, and S. Herminghaus. Symmetric wetting heterogeneity suppresses fluid displacement hysteresis in granular piles. *Phys. Rev. Fluids*, 3: 024304, Feb 2018. doi: 10.1103/PhysRevFluids.3.024304. URL `https://link.aps.org/doi/10.1103/PhysRevFluids.3.024304`.

J. E. Morrison and J. A. Smith. Stochastic modeling of flood peaks using the generalized extreme value distribution. *Water Resources Research*, 38(12):41–1, 2002.

N. R. Morrow et al. The effects of surface roughness on contact: angle with special reference to petroleum recovery. *Journal of Canadian Petroleum Technology*, 14 (04), 1975.

N. R. Morrow et al. Wettability and its effect on oil recovery. *Journal of Petroleum Technology*, 42(12):1–476, 1990.

P. Mostaghimi, B. Bijeljic, and M. Blunt. Simulation of flow and dispersion on pore-space images. pages 4430–4448, 2010.

S. Motealleh, M. Ashouripashaki, D. DiCarlo, and S. Bryant. Mechanisms of capillary-controlled immiscible fluid flow in fractionally wet porous media. *Vadose Zone Journal*, 9(3):610–623, 2010. doi: 10.2136/vzj2009.0059.

S. Motealleh, M. Ashouripashaki, D. DiCarlo, and S. Bryant. Unified model of drainage and imbibition in 3d fractionally wet porous media. *Transport in porous media*, 99(3):581–611, 2013.

G. E. Mueller. Radial void fraction distributions in randomly packed fixed beds of uniformly sized spheres in cylindrical containers. *Powder technology*, 72(3):269–275, 1992.

P. P. Mukherjee, C.-Y. Wang, and Q. Kang. Mesoscopic modeling of two-phase behavior and flooding phenomena in polymer electrolyte fuel cells. *Electrochimica Acta*, 54(27):6861–6875, 2009.

J. Murison, B. Semin, J.-C. Baret, S. Herminghaus, M. Schröter, and M. Brinkmann. Wetting heterogeneities in porous media control flow dissipation. *Phys. Rev. Applied*, 2:034002, Sep 2014. doi: 10.1103/PhysRevApplied.2.034002.

J. L. Murison. Wetting heterogeneities in porous media. 2014.

D. Noble and J. Torczynski. A lattice-boltzmann method for partially saturated computational cells. *International Journal of Modern Physics C*, 9(08):1189–1201, 1998.

P. G. Nutting. Physical analysis of oil sands. *AAPG Bulletin*, 14(10):1337–1349, 1930.

C. Odier, B. Levaché, E. Santanach-Carreras, and D. Bartolo. Forced imbibition in porous media: A fourfold scenario. *Physical review letters*, 119(20):208005, 2017.

D. Or. Scaling of capillary, gravity and viscous forces affecting flow morphology in unsaturated porous media. *Advances in water resources*, 31(9):1129–1136, 2008.

D. Owen, C. Leonardi, and Y. Feng. An efficient framework for fluid–structure interaction using the lattice boltzmann method and immersed moving boundaries. *International Journal for Numerical Methods in Engineering*, 87(1-5):66–95, 2011.

P. Panizza, H. Algaba, M. Postic, G. Raffy, L. Courbin, and F. Artzner. Order-disorder structural transitions in mazes built by evaporating drops. *Physical review letters*, 121(7):078002, 2018.

L. Paterson. Diffusion-limited aggregation and two-fluid displacements in porous media. *Physical review letters*, 52(18):1621, 1984.

T. W. Patzek, W. Saputra, W. Kirati, and M. Marder. Generalized extreme value statistics, physical scaling, and forecasts of gas production in the barnett shale. *Energy & Fuels*, 2019.

T. W. Patzek et al. Verification of a complete pore network simulator of drainage and imbibition. In *SPE/DOE Improved Oil Recovery Symposium*. Society of Petroleum Engineers, 2000.

A. Payatakes. Dynamics of oil ganglia during immiscible displacement in water-wet porous media. *Annual Review of Fluid Mechanics*, 14(1):365–393, 1982.

D. Pedoe. An inequality for two triangles. In *Mathematical Proceedings of the Cambridge Philosophical Society*, volume 38, pages 397–398. Cambridge University Press, 1942.

R. Pini and S. M. Benson. Simultaneous determination of capillary pressure and relative permeability curves from core-flooding experiments with various fluid pairs. *Water Resources Research*, 49(6):3516–3530, 2013.

J. Preskill. Magnetic monopoles. *Annual Review of Nuclear and Particle Science*, 34 (1):461–530, 1984.

C. Priest, R. Sedev, and J. Ralston. Asymmetric wetting hysteresis on chemical defects. *Physical review letters*, 99(2):026103, 2007.

B. K. Primkulov, S. Talman, K. Khaleghi, A. Rangriz Shokri, R. Chalaturnyk, B. Zhao, C. W. MacMinn, and R. Juanes. Quasistatic fluid-fluid displacement in porous media: Invasion-percolation through a wetting transition. *Phys. Rev. Fluids*, 3:104001, Oct 2018. doi: 10.1103/PhysRevFluids.3.104001. URL `https://link.aps.org/doi/10.1103/PhysRevFluids.3.104001`.

B. K. Primkulov, A. A. Pahlavan, X. Fu, B. Zhao, C. W. MacMinn, and R. Juanes. Signatures of fluid–fluid displacement in porous media: wettability, patterns and pressures. *Journal of Fluid Mechanics*, 875, 2019.

H. Princen. Capillary phenomena in assemblies of parallel cylinders: Iii. liquid columns between horizontal parallel cylinders. *Journal of Colloid and Interface Science*, 34(2):171–184, 1970.

M. Prodanović and S. L. Bryant. A level set method for determining critical curvatures for drainage and imbibition. *Journal of colloid and interface science*, 304(2):442–458, 2006.

W. Purcell et al. Capillary pressures-their measurement using mercury and the calculation of permeability therefrom. *Journal of Petroleum Technology*, 1(02):39–48, 1949.

C. Quan and B. Stamm. Mathematical analysis and calculation of molecular surfaces. *Journal of Computational Physics*, 322:760 – 782, 2016. ISSN 0021-9991. doi: https://doi.org/10.1016/j.jcp.2016.07.007. URL `http://www.sciencedirect.com/science/article/pii/S0021999116302868`.

H. S. Rabbani, D. Or, Y. Liu, C.-Y. Lai, N. B. Lu, S. S. Datta, H. A. Stone, and N. Shokri. Suppressing viscous fingering in structured porous media. *Proceedings of the National Academy of Sciences*, 2018. ISSN 0027-8424. doi: 10.1073/pnas.1800729115. URL `http://www.pnas.org/content/early/2018/04/19/1800729115`.

M. Reyssat, L. Courbin, E. Reyssat, and H. A. Stone. Imbibition in geometries with axial variations. *Journal of Fluid Mechanics*, 615:335–344, 2008.

R. L. Ricca and B. Nipoti. Gauss'linking number revisited. *Journal of Knot Theory and Its Ramifications*, 20(10):1325–1343, 2011.

L. A. Richards. Capillary conduction of liquids through porous mediums. *Physics*, 1 (5):318–333, 1931.

T. J. Richmond. Solvent accessible surface area and excluded volume in proteins: Analytical equations for overlapping spheres and implications for the hydrophobic effect. *Journal of molecular biology*, 178(1):63–89, 1984.

K. F. Riley, M. P. Hobson, and S. J. Bence. *Mathematical methods for physics and engineering: a comprehensive guide.* Cambridge university press, 2006.

J. Roof et al. Snap-off of oil droplets in water-wet pores. *Society of Petroleum Engineers Journal*, 10(01):85–90, 1970.

M. Rücker, S. Berg, R. Armstrong, A. Georgiadis, H. Ott, A. Schwing, R. Neiteler, N. Brussee, A. Makurat, L. Leu, et al. From connected pathway flow to ganglion dynamics. *Geophysical Research Letters*, 42(10):3888–3894, 2015.

Z. Sadjadi, M. Jung, R. Seemann, and H. Rieger. Meniscus arrest during capillary rise in asymmetric microfluidic pore junctions. *Langmuir*, 31(8):2600–2608, 2015.

P. G. Saffman and G. I. Taylor. The penetration of a fluid into a porous medium or hele-shaw cell containing a more viscous liquid. *Proceedings of the Royal Society of London. Series A. Mathematical and Physical Sciences*, 245(1242):312–329, 1958.

M. Sahimi. *Flow and transport in porous media and fractured rock: from classical methods to modern approaches.* John Wiley & Sons, 2011.

R. Salathiel et al. Oil recovery by surface film drainage in mixed-wettability rocks. *Journal of Petroleum Technology*, 25(10):1–216, 1973.

M. Scheel, R. Seemann, M. Brinkmann, M. Di Michiel, A. Sheppard, B. B, and S. Herminghaus. Morphological clues to wet granular pile stability. *Nature Materials*, 7: 189–193, 10 2008.

S. Schlüter, S. Berg, M. Rücker, R. Armstrong, H.-J. Vogel, R. Hilfer, and D. Wildenschild. Pore-scale displacement mechanisms as a source of hysteresis for two-phase flow in porous media. *Water Resources Research*, 52(3):2194–2205, 2016.

H. G. Scholl. Experimentelle untersuchungen zum mehrphasenfluss in porösen medien. 2015.

C. Scholz and T. Pöschel. Velocity distribution of a homogeneously driven two-dimensional granular gas. *Physical review letters*, 118(19):198003, 2017.

C. Semprebon, M. Scheel, S. Herminghaus, R. Seemann, and M. Brinkmann. Liquid morphologies and capillary forces between three spherical beads. *Physical Review E*, 94(1):012907, 2016.

M. Sezgin and B. Sankur. Survey over image thresholding techniques and quantitative performance evaluation. *Journal of Electronic imaging*, 13(1):146–166, 2004.

J. Sherwood and J. Nittmann. Gradient governed growth: the effect of viscosity ratio on stochastic simulations of the saffman-taylor instability. *Journal de physique*, 47 (1):15–22, 1986.

H. Si. Tetgen, a delaunay-based quality tetrahedral mesh generator. *ACM Trans. Math. Softw.*, 41(2):11:1–11:36, feb 2015. ISSN 0098-3500. doi: 10.1145/2629697. URL `http://doi.acm.org/10.1145/2629697`.

D. Silin and T. Patzek. Pore space morphology analysis using maximal inscribed spheres. *Physica A: Statistical mechanics and its applications*, 371(2):336–360, 2006.

K. Singh, B. Bijeljic, and M. J. Blunt. Imaging of oil layers, curvature and contact angle in a mixed-wet and a water-wet carbonate rock. *Water Resources Research*, 52(3):1716–1728, 2016.

K. Singh, H. Menke, M. Andrew, Q. Lin, C. Rau, M. J. Blunt, and B. Bijeljic. Dynamics of snap-off and pore-filling events during two-phase fluid flow in permeable media. *Scientific reports*, 7(1):1–13, 2017a.

K. Singh, H. Scholl, M. Brinkmann, M. Di Michiel, M. Scheel, S. Herminghaus, and R. Seemann. The role of local instabilities in fluid invasion into permeable media. *Scientific Reports*, 7, 12 2017b.

K. Singh, M. Jung, M. Brinkmann, and R. Seemann. Capillary-dominated fluid displacement in porous media. *Annual Review of Fluid Mechanics*, 2019.

P. K. Sinha, P. P. Mukherjee, and C.-Y. Wang. Impact of gdl structure and wettability on water management in polymer electrolyte fuel cells. *Journal of Materials Chemistry*, 17(30):3089–3103, 2007.

J. P. Snyder. Map projections used by the us geological survey. Technical report, US Government Printing Office, 1982.

F. Soddy. The kiss precise, 1936.

M. D. Spivak. *A comprehensive introduction to differential geometry.* Publish or perish, 1975.

G. Strang. *Introduction to Linear Algebra.* Wellesley-Cambridge Press, 2016. ISBN 9780980232776. URL `https://books.google.de/books?id=efbxjwEACAAJ`.

S. Strobl, A. Formella, and T. Pöschel. Exact calculation of the overlap volume of spheres and mesh elements. *Journal of Computational Physics*, 311:158 – 172, 2016. ISSN 0021-9991. doi: https://doi.org/10.1016/j.jcp.2016.02.003. URL `http://www.sciencedirect.com/science/article/pii/S0021999116000577`.

J. Su, G. Chai, L. Wang, J. Yu, W. Cao, Z. Gu, C. Chen, and W. Meng. Direct numerical simulation of particle pore-scale transport through three-dimensional porous media with arbitrarily polyhedral mesh. *Powder Technology*, 2020.

Z. Sun and J. C. Santamarina. Haines jumps: Pore scale mechanisms. *Physical Review E*, 100(2):023115, 2019.

D. Svrtan and D. Veljan. Non–euclidean versions of some classical triangle inequalities. In *Forum geometricorum*, volume 12, pages 197–209, 2012.

J. Terning and C. B. Verhaaren. Resolving the weinberg paradox with topology. *Journal of High Energy Physics*, 2019(3):177, 2019.

I. Todhunter. *Spherical trigonometry, for the use of colleges and schools: with numerous examples.* Macmillan, 1863.

M. Trojer, M. L. Szulczewski, and R. Juanes. Stabilizing fluid-fluid displacements in porous media through wettability alteration. *Physical Review Applied*, 3(5):054008, 2015.

T. Tsuji, F. Jiang, and K. T. Christensen. Characterization of immiscible fluid displacement processes with various capillary numbers and viscosity ratios in 3d natural sandstone. *Advances in Water Resources*, 95:3–15, 2016.

P. H. Valvatne and M. J. Blunt. Predictive pore-scale modeling of two-phase flow in mixed wet media. *Water resources research*, 40(7), 2004.

A. van Blaaderen and P. Wiltzius. Real-space structure of colloidal hard-sphere glasses. *Science*, 270(5239):1177–1179, 1995.

A. Van Oosterom and J. Strackee. The solid angle of a plane triangle. *IEEE transactions on Biomedical Engineering*, (2):125–126, 1983.

D. Vassetti, B. Civalleri, and F. Labat. Analytical calculation of the solvent-accessible surface area and its nuclear gradients by stereographic projection: A general approach for molecules, polymers, nanotubes, helices, and surfaces. *Journal of Computational Chemistry*, 2020.

N. Wardlaw et al. The effects of geometry, wettability, viscosity and interfacial tension on trapping in single pore-throat pairs. *Journal of Canadian Petroleum Technology*, 21(03), 1982.

G. Webb, Q. Hu, B. Dasgupta, and G. Zank. Homotopy formulas for the magnetic vector potential and magnetic helicity: The parker spiral interplanetary magnetic field and magnetic flux ropes. *Journal of Geophysical Research: Space Physics*, 115 (A10), 2010.

R. N. Wenzel. Resistance of solid surfaces to wetting by water. *Industrial & Engineering Chemistry*, 28(8):988–994, 1936.

S. Whitaker. Flow in porous media i: A theoretical derivation of darcy's law. *Transport in porous media*, 1(1):3–25, 1986.

D. Wildenschild and A. P. Sheppard. X-ray imaging and analysis techniques for quantifying pore-scale structure and processes in subsurface porous medium systems. *Advances in Water Resources*, 51:217–246, 2013.

D. Wilkinson and J. F. Willemsen. Invasion percolation: a new form of percolation theory. *Journal of Physics A: Mathematical and General*, 16(14):3365, 1983.

C. D. Willett, M. J. Adams, S. A. Johnson, and J. P. Seville. Capillary bridges between two spherical bodies. *Langmuir*, 16(24):9396–9405, 2000.

T. A. Witten and L. M. Sander. Diffusion-limited aggregation, a kinetic critical phenomenon. *Phys. Rev. Lett.*, 47:1400–1403, Nov 1981. doi: 10.1103/PhysRevLett.47.1400. URL `https://link.aps.org/doi/10.1103/PhysRevLett.47.1400`.

J. Woodrow, H. Chilton, and R. Hawes. Forces between slurry particles due to surface tension. *Journal of Nuclear Energy. Part B. Reactor Technology*, 1(4):229–IN3, 1961.

C. Wu, J. Zhan, Y. Li, K. Lam, and A. Berrouk. Accurate void fraction calculation for three-dimensional discrete particle model on unstructured mesh. *Chemical Engineering Science*, 64(6):1260 – 1266, 2009. ISSN 0009-2509. doi: https://doi.org/10.1016/j.ces.2008.11.014. URL `http://www.sciencedirect.com/science/article/pii/S0009250908006258`.

T. T. Wu and C. N. Yang. Concept of nonintegrable phase factors and global formulation of gauge fields. *Phys. Rev. D*, 12:3845–3857, Dec 1975. doi: 10.1103/PhysRevD.12.3845. URL `https://link.aps.org/doi/10.1103/PhysRevD.12.3845`.

H. Yang, B. A. Baudet, and T. Yao. Characterization of the surface roughness of sand particles using an advanced fractal approach. *Proceedings of the Royal Society A: Mathematical, Physical and Engineering Sciences*, 472(2194):20160524, 2016.

L. Yang and J. Zhang. Metric equations in geometry and their applications. Technical report, International Centre for Theoretical Physics, 1989.

Y. C. Yortsos, B. Xu, and D. Salin. Phase diagram of fully developed drainage in porous media. *Physical review letters*, 79(23):4581, 1997.

Y. C. Yortsos, B. Xu, D. Salin, et al. Phase diagram of fully developed drainage: A study of the validity of the buckley-leverett equation. In *SPE Annual Technical Conference and Exhibition*. Society of Petroleum Engineers, 1998.

T. Young. Iii. an essay on the cohesion of fluids. *Philosophical transactions of the royal society of London*, (95):65–87, 1805.

C. Yuan, B. Chareyre, and F. Darve. Pore-scale simulations of drainage in granular materials: finite size effects and the representative elementary volume. *Advances in water resources*, 95:109–124, 2016.

I. Zacharoudiou, E. M. Chapman, E. S. Boek, and J. P. Crawshaw. Pore-filling events in single junction micro-models with corresponding lattice boltzmann simulations. *Journal of Fluid Mechanics*, 824:550–573, 2017.

I. Zacharoudiou, E. S. Boek, and J. Crawshaw. The impact of drainage displacement patterns and haines jumps on co 2 storage efficiency. *Scientific reports*, 8(1):1–13, 2018.

B. Zhao, C. W. MacMinn, and R. Juanes. Wettability control on multiphase flow in patterned microfluidics. *Proceedings of the National Academy of Sciences*, 113(37): 10251–10256, 2016.

D. Zwillinger. *CRC standard mathematical tables and formulae.* Chapman and Hall/CRC, 2002.